Retrieval of Atmospheric Structure and Composition of Exoplanets from Transit Spectroscopy

Submitted for the degree of Doctor of Philosophy

Jae-Min Lee

Wolfson College, University of Oxford

Michaelmas Term 2012

Abstract

Recent spectroscopic observations of transiting exoplanets have permitted the derivation of the thermal structure and molecular abundances of H_2O, CO, CO_2, CH_4, metallic oxides and alkali metals in these extreme atmospheres. Here, for the first time, a fully-fledged retrieval algorithm has been applied to exoplanet spectra to determine the thermal structure and composition. The development of a suite of radiative transfer and retrieval tools for exoplanet atmospheres is described, building upon an optimal estimation retrieval algorithm extensively used in solar system studies. Firstly, the collection of molecular line lists and the pre-tabulation of the absorption coefficients (k-distribution tables) for high temperature application are discussed. Secondly, the best-fit spectra for hot Jupiters are demonstrated and discussed case by case. Available sets of primary and secondary transit observations of exoplanets are used to retrieve atmospheric properties from these spectra, quantifying the limits of our knowledge of exoplanetary atmospheres based on the current quality of the data. The contribution functions and the vertical sensitivity to the molecules are fully utilised to interpret these spectra, probing the structure and composition of the atmosphere. Finally, the retrievals provide our best estimates of the thermal and compositional structure to date, using the covariance matrices to properly assess the degeneracy between different parameters and the uncertainties on derived quantities for the first time. This sheds light on the range of diverse interpretations offered by other authors so far, and allows us to scrutinise further atmospheric features by maximising the capability of the current retrieval algorithm and to demonstrate the need for broadband spectroscopy from future missions.

Acknowledgements

It was March 2010 when I met Pat Irwin and Leigh Fletcher. I could come out of unprecedented days because they helped me and led me to the new world of the planetary sciences. They also showed me a glimpse of how important it is to become a skilled and even morally right scientist. Thank you, Pat and Leigh.

The time with him has been so special to me even after his absence in this world. Actually it has got stronger. I have been truly proud of myself being a part of his academic career and of experiencing his knowledge and kindness. John Barnett, you cannot be with me now but I know your voices and care will remain with me.

The story of my life in UK was started in 2006 in the Jeju island, Korea, where I met Mike Lockwood for the first time. After one year in RAL, he helped me continuing my study in UK afterwards. We do not work together anymore, but, of course, he is still my mentor. His wife, Celia, is always good to my family and she helped Sookyung settling down to new culture during her first year in Oxford.

Undoubtedly, I know Sug-whan Kim's support for last few years has helped me to be where I am now. I strongly feel that he will just continuously give me courage to become a scientist, worthy of being beneficial to others. I still remember his way from my years in Yonsei to lead people around him with a great passion and initiative. That absolutely has been a great influence to me.

It was not only academic achievement through the last 4 years, but also amazing friends I found here: Sunjeong, Taysun and Jiyeon, Joongoo and Kyungmi, Kyungkyu, Sungkyun, Hyunjung, Yoonjoo, Seungyoung, Minsoo, Sangsuk, Eunhyuk and Songju's family. We spent unforgettable times together for meals, BBQs, punts, teas, coffees and even beers. I would like to take this chance to thank their friendship which has helped me go through difficult times. I wish you the best to achieve your own goals.

My friends from the department mean more than just friends to me. They warm welcomed and understood me as a foreign student. Ben Grandey, Ramin Lolachi, Jo Barstow, Richard Passmore, David Mullholand and Corwin Wright. I can not imagine my department life without them and need to give Jo great gratitude for her kindness and proofreading all the chapters.

There are more friends from South Korea who are always supportive, standing behind me, and cheering me up with hilarious and comforting text messages. Dooyoung, Seungyeob, Jaehee, Kyunghyun, Byungjin, Jihun, Soochan and Dongseob. They are the ones who call me first and show their interest in what I do and care about my life over all, whenever I go to Korea. I am not sure my support toward them is even near the way they showed to me, but I do appreciate your friendship and always think of you and your families.

SOLers workers, hard workers! Even at the time of writing these words, I can see them working hard in their office. I hope all the best for their academic and personal life. I specially thank for Hanshin's cheering that let me get through my hard days.

My parents, they are my biggest fans and sponsors with 100% love. I couldn't finish my thesis if there weren't my dad and mom's unlimited supports. Saranghaeyo (I love you) and Gomawoyo (Thank you).

My in-laws trusted me whenever I was in trouble. Their beliefs were great encouragement to me. I would be a your great "son". Trust me, again.

I also want to give my best regard to the rest of my family: my brother, Jaechan, sister, Seunghyun, her husband, Jaesung, brother in-law, Jaewoo and her wife, Wani. My first nephew, Aa-yoon, I haven't met her yet, but I can not wait to meet her! I am just grateful to be a family member of such loving and kind people.

Last but not least, my the other half, Sookyung and June, many thanks for encouraging me all the way to the final and simply being with me. There is no word to describe how thankful to you and how much I love you. Now it's my turn. I promise you that I'll be your good hubby and daddy. I am looking forward to next journey as your husband and father.

Contents

List of Figures

List of Tables

Chapter 1

Exoplanets

1.1 Beyond the First Exoplanet Observation

Since the first detection of a planet orbiting a Sun-like star (51 Pegasi) in 1995 (Mayor and Queloz, 1995), more than 750 planets of various types have now been discovered around main-sequence stars. The detection of these exoplanets has revolutionised our understanding of our solar system as one of many planetary systems in our galaxy. Encouragingly, the rate of discovery of exoplanets has increased dramatically in recent years[1] and detectable masses and sizes are now comparable to more or less Earth-mass (M_E) and size (R_E) (Mayor et al., 2009). Recently, the $Kepler$ telescope found >2000 exoplanet candidates, including tens of Earth-sized planets orbiting in the habitable zone (Borucki et al., 2011). It is expected that the next generation of telescopes being built within one or two decades will successfully detect tiny spectral signals from terrestrial exoplanets. In this sense, the objective for this study is to provide the novel tool for characterising the atmospheres hosted by these remote objects, and understanding the broad diversity of chemistry and thermal structure of planets.

A range of methodologies for discovering exoplanets has been established and advanced in many ways. Although direct imaging, which requires a very high contrast ratio and angular resolution of the instrument, is the most intuitive way, only a small number

[1] http://exoplanet.eu/index.php; http://exoplanets.org/planets.shtml

of exoplanets have been directly imaged. Thus only planets having large orbital distance (>5 AU) and large size (>Jupiter size) have been detected so far in this fashion (see Figure 1.1). Companions detected via this method are sometimes considered as cool brown dwarfs. Indirect techniques have been more commonly used, including astrometry, gravitational microlensing, radial velocity, and transit spectroscopy. This is because most of the exoplanet candidates orbit close to their parent star with short orbital periods, providing frequent opportunities to verify their existence within a short observation time. Also, high masses and sizes that are as large as Jupiter ($R_p \sim R_{Jupiter}$, $M_p \sim M_{Jupiter}$) help finding exoplanets by inducing higher fluctuation in the signals during their orbit. Therefore the Jupiter-sized planets ($\sim$100 M_E) with short orbital distance, generally called '$hot\ Jupiters$', in which the atmosphere easily heats up over a thousand K and that are thought to be completely tidally locked, are the first class of planets observed successfully. So far, most of the exoplanets measured by indirect methods, particularly transit spectroscopy, are of this type of class as seen in Figure 1.1. Hot Jupiters therefore have rigorously been investigated with different instruments and tools in literature, owing to relatively high detectability compared to the planets with smaller size and longer orbital period. Therefore, this study will utilise the measurements for hot Jupiters in order to validate the tools for characterising the atmospheres of exoplanets.

Before discussing our present knowledge of hot Jupiters, some detection methodologies will be introduced in the next section.

1.2 Detection Methods

1.2.1 Direct Imaging

Direct imaging is a useful technique for the observation of exoplanets with large semi-major axes of over five AU, the distance which is most likely considered as a limit of indirect measurements (Chauvin et al., 2004; Marois et al., 2008) (see Table 1.1). Spectroscopic and photometric data from direct imaging also make it possible to derive physical properties of exoplanets without any interference from the parent star. It requires

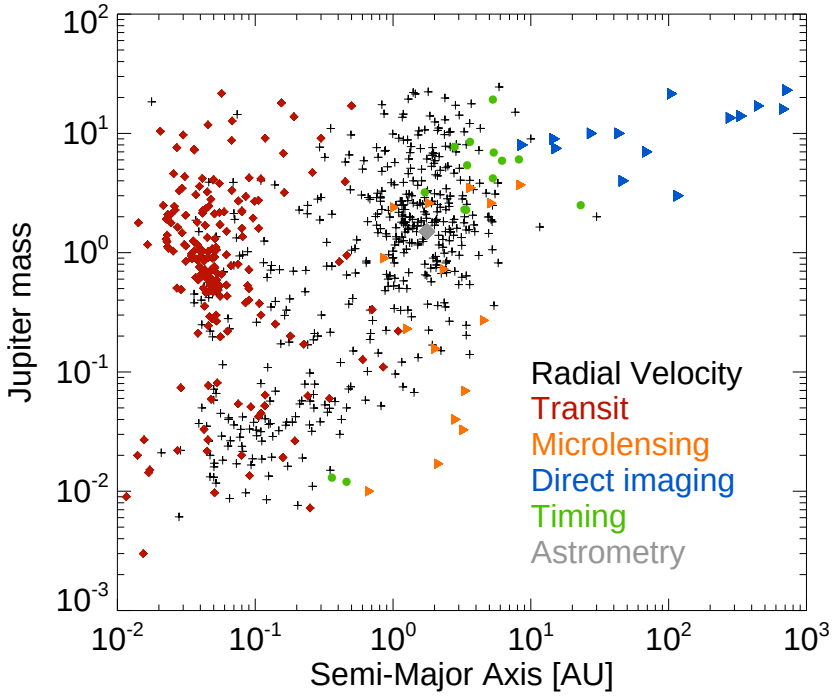

Figure 1.1: Detected and confirmed exoplanets by direct imaging, radial velocity (or astrometry), transit, microlensing and timing method. Data is taken from *http://exoplanet.eu*.

highly advanced observation and image processing technology to separate the exoplanets from the host star. For this reason, only ground based telescopes with very large apertures with adaptive optics and some of the space telescopes using coronagraphic techniques have succeeded in imaging exoplanets. In 2004, using the 8-m class ESO Very Large Telescope (VLT) in Chile, a companion of a young brown dwarf 2MASSWJ 1207334–393254, located $\sim$70 pc away from the Earth, was observed as the first directly imaged exoplanet. With the help of adaptive optics system called *Naos-Conica* (NACO) on the VLT, difficulties in sharpening a faint object could be successfully overcome during the observation (Chauvin et al., 2004). This observation enables us to derive the physical properties of a companion such as projected separation from the dwarf ($\sim$55 AU), mass (5 ± 2 M_{Jup}), and effective temperature (1250 ± 200 K).

Since the first imaging, the VLT/NACO has discovered 4 more exoplanets from different planetary systems, sometimes using a coronagraphy observation mode that allows enhancement of resolving power near the parent star by occulting the bright centre of the field (Chauvin et al., 2005; Lagrange et al., 2009; Neuhäuser et al., 2005; Schmidt et al., 2008, 2009). Other large ground telescopes such as the Keck (10-m class) and Gemini (8-m class) telescopes have also detected several giant planets (Lafrenière et al., 2010, 2011) including 4 planets co-orbiting around an A-type main sequence star, HR 8799 (Marois et al., 2008, 2010; Metchev et al., 2009). Table 1.1 shows the physical properties of directly imaged exoplanets to date.

Currently, ongoing observation programmes are limited to observing exoplanets that are large, bright, and well separated from the star. Technologies such as nulling interferometry for ground telescopes (Mennesson et al., 2006) are being developed for the observations requiring extremely high sensitivity. Also, space interferometers such as *Terrestrial Planet Finder Interferometer* (TPF-I, Henry et al., 2004) by NASA and *Darwin* (Fridlund, 2002) by ESA were planned to be launched within a decade, but their further study has been permanently postponed due to funding issues. However, future direct imaging focusing on two specific concepts is still ongoing: ground telescopes such as the *Giant Magellan Telescope* (GMT, Johns et al., 2004), *European Extreme Large*

Table 1.1: Candidates for directly imaged exoplanets. Data is taken from http://exoplanet.org and Neuhäuser and Schmidt (2012)

Planet	Distance[pc]	Semi-major Axis[AU]	Mass[M_J]	Reference
RXJ 1609 b	$\sim$145	$\sim$311	6–11	Lafrenière et al. (2010)
2M1207 b	52.4$\pm$1.1	40.5$\pm$1	3–10	Chauvin et al. (2004)
2M J044144 b		$\sim$15	7.5$\pm$2.5	Todorov et al. (2010)
AB Pic b	46.1$\pm$1.5	251.7$\pm$8.9	13.5$\pm$0.5	Chauvin et al. (2005)
β Pic b	19.4$\pm$0.05	$\sim$10	6–13	Lagrange et al. (2009)
CT Cha b	165$\pm$30	441$\pm$87	17$\pm$6	Schmidt et al. (2008)
GQ Lup b	$\sim$140	$\sim$100	1–42	Neuhäuser et al. (2005)
HIP 78530 b	157$\pm$13	710$\pm$60	19–26	Lafrenière et al. (2011)
HR 8799 b	39.4$\pm$1	$\sim$68	5–11	Marois et al. (2008)
c		$\sim$38	7–13	
d		$\sim$24	7–13	Marois et al. (2010)
e		14–15	$<$13	
SCR 1845 b			45$\pm$5	Biller et al. (2008)
UScoCTIO-108 b			6–16	Béjar et al. (2008)

Telescope (E-ELT, Gilmozzi and Spyromilio, 2008), and *Thirty-Metre Telescope* (TMT, Nelson and Sanders, 2008) pursuing 'extremely large' light collecting area, and 'space-borne' telescopes such as the *James Web Space Telescope* (JWST, Clampin, 2008), which will be launched in 2018. The programme is planned to be completed within the next one or two decades. The planets that have been and will be detected via direct imaging will become hundreds more potential targets available for characterisation via the tools developed in this study.

1.2.2 Pulsar Timing

As the first exoplanet discovery, three planets orbiting around a pulsar, PSR B1257+12, have been confirmed via pulsar timing (Wolszczan and Frail, 1992) method. A pulsar is a fast rotating neutron star, emitting a very short and regular signal (milliseconds to seconds) to an observer on the Earth. The signal is so precise and punctual for a long time scale so that an observer can detect the timing variation in the signal, if there is any companion like planets around the pulsar. The detectable mass and radius of planets via

pulsar timing can easily be smaller than one thousandth of the Earth's one. So far, five planets from two pulsars, PSR B1620-26 and PSR B1257+12 have been confirmed via this method.

1.2.3 Astrometry

Astrometry, simply positioning the celestial bodies on the sky, is the oldest astronomical technique and, also, is a useful tool to find exoplanets around nearby stars. In a planetary system, a star and a planet co-rotate around the centre of mass of the system, called the barycentre. Thus, a star would regularly wobble and show a periodic shift in position by hosting a planet, so stellar movement is able to provide physical information about exoplanets. Theoretically, it is considered that astrometry is one of the most sensitive methods to discover Earth-sized exoplanets and derive accurate exoplanet masses. Unlike other techniques, although a 'face-on' orbit of an exoplanet maximizes the parent star's movement, no special 'alignment' between objects is needed because most visible stars can be surveyed and astrometry is a complementary technique to transit and Doppler spectroscopy, which require 'edge-on' orbits to see the maximum amplitude in radial velocity. Technical difficulty, however, restricts observable targets to be low-mass, nearby stars to our solar system. The effectiveness of astrometry is essentially related to the stellar displacement determined by the mass ratio between star and planet, and distance from the observer.

There have been several astrometric experiments for detecting exoplanets around nearby stars (e.g. 61 Cygni and Barnard's star) and some seemed to have succeeded in detection (Strand, 1943; Van de Kamp, 1963). Their discoveries were not proven by successive observations with modern technologies. This is because astrometry for an exoplanet detection requires too high a precision of measurement (a few micro arcseconds), which is hard to achieve, to allow a frequent detection rate. In spite of the precision difficulty, in 2002, it was reported that observations by HST astrometrically estimated an accurate physical mass of an exoplanet (Gliese 876b), which was already confirmed via the Radial Velocity (RV) method (Benedict et al., 2002). Also, as the first discovery, a compan-

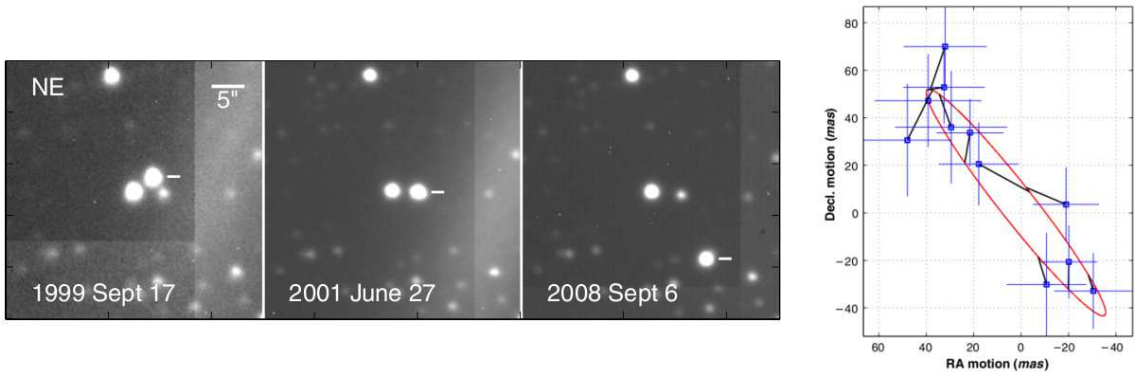

Figure 1.2: $(Left)$ Observed orbital motion of VB 10 is clearly shown on a series of pictures made for 9 years observation. $(Right)$ Its predicted orbit is displayed on RA and Dec plane (Pravdo and Shaklan, 2009).

ion orbiting VB 10 was successfully observed by Palomar telescope astrometry in 2009 (Figure 1.2) and its mass was announced as $\sim$7 M_{Jup} in the best estimation (Pravdo and Shaklan, 2009). Even though determination of absolute mass of course needs assumptions to be made, since only mass ratios are determined due to a lack of planetary information, this method provides better insight into mass determination than radial velocity because the inclination of the orbits can be seen during the measurements.

Atmospheric interference limits the accuracy of astrometric measurements from the ground. For this reason, a future space-borne instrument, ESA's *Gaia* (Gilmore et al., 1998), is designed to achieve unprecedented accuracy. *Gaia* is expected to detect gas giant exoplanets through sky surveys.

1.2.4 Gravitational Microlensing

In a situation of alignment between observer, foreground object (lens), and background object (source), the gravitational field of the lens distorts the path of the light from the source and then the observer experiences magnification of the brightness of the lens. This $gravitational\ lensing$ phenomenon, firstly predicted by Einstein (1936), was proposed as a detection method for exoplanets in 1991 (Mao and Paczynski, 1991). Gould and Loeb (1992) described the details of a microlensing event in a mathematical way. The brightness curve (A) in the course of the source passing across the lens would be expressed

as

$$A = \frac{u^2 + 2}{u\sqrt{u^2 + 4}}, \tag{1.1}$$

where u, a function of time, is the separation between the lens and the source on a projected plane, and is given by

$$u\left(t\right) = \sqrt{u_0^2 + \left(\frac{t - t_0}{t_E}\right)^2}, \tag{1.2}$$

where u_0 is the minimum separation, t_0 is the time of closest approach giving maximum brightness, and t_E is the Einstein time-scale, which accounts for the time taken to cross the Einstein ring (R_E) which gives the vicinity of an refracted light annulus around the lens image. For the case of a solar mass lens, t_E and R_E typically correspond to two months and four AU assuming 100 km/s transverse velocity of the Galactic centre relative to the lens star. This yields the magnification of microlensing of nearly 1.3.

If the lens star hosts planets, gravitational perturbations by planets, called 'the caustic', appear on the main symmetric line shape and provide the physical properties of the exoplanet. Figure 1.3 shows the measured brightness variation during a microlensing event, OGLE–2003–BLG–235 (or MOA–2003–BLG–53, Bond et al., 2004). Currently, the microlensing method, which term is applicable for a stellar mass foreground object, is considered as one of the most sensitive methods capable of the discovery of Earth-sized exoplanets in small orbital separation:$\sim$0.1 M_E and $\geq$0.5 AU in theory (Bennett, 2008).

As the occurrence of microlensing is unpredictable and relies on a proper alignment of the lens and the source on the line of sight, observations towards the Galactic bulge increase the detection probability because of its high density. Since the first detection in 2004, eight exoplanets reported by microlensing have been discovered with the bulge background. Also, a microlensing event normally lasts just a few hours for a terrestrial planet and a few days for a giant, so follow-up observations after the first detection should be required for its confirmation.

An unrepeatable characteristic of alignment makes observation of an exoplanet im-

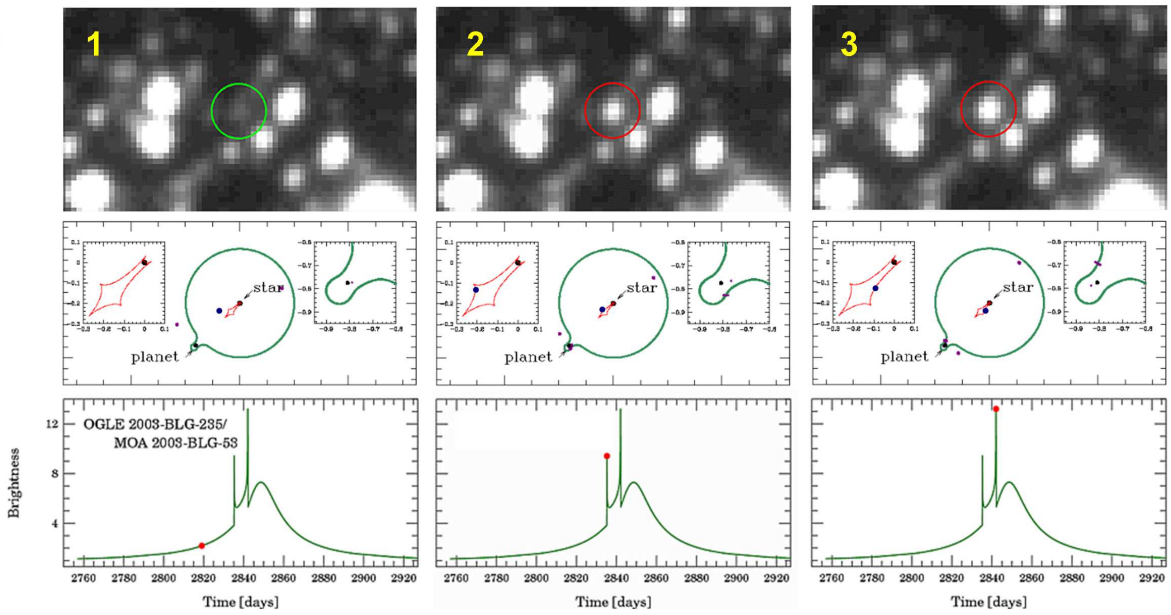

Figure 1.3: Images of time-dependent brightness change (1st row), schematic geometries (2nd row), and light curves (3rd row) of the lens during a microlensing event in OGLE–2003–BLG–235 (or MOA–2003–BLG–53). Through phase 1 (1st column) to 3 (3rd column), intrinsic peaks by the 'caustic' marked as a red shape near the 'Star' in 2nd row occur during the source passing the edges of caustic. Courtesy of B. Scott Gaudi.

probable and it requires long-term and continuous observations by network telescopes. There are two programmes mainly contributing monitoring microlensing events of exoplanets: *Optical Gravitational Lensing Experiment* (OGLE, Udalski, 2003), and *Microlensing Observations in Astrophysics* (MOA Bond et al., 2002) located on opposite sides of the Earth (Chile and New Zealand) so that real time survey is possible. In order to take advantage of the density of the Galactic bulge, telescopes are located in the Southern hemisphere. Once one of telescopes has initially succeeded in detecting an event by continuous monitoring, the follow-up observation via network telescopes follows immediately, which includes Robonet (Gomboc et al., 2006), *Microlensing Follow-Up Network* (MicroFUN Yoo et al., 2004), and *Probing Lensing Anomalies NETwork* (PLANET Dominik et al., 2002).

1.2.5 Radial Velocity

Since the first discovery, radial velocity (RV), also called Doppler spectroscopy, is a tool which has contributed to the detection of ∼600 exoplanets in ∼550 planetary systems, and is one of the most productive and effective methods currently known. As mentioned in section 1.2.2, a parent star wobbling around the barycentre makes changes in its position on the sky and, also, velocity in the radial direction with respect to the observer. If a system does not lie 'perfectly' face-on, a velocity vector of stellar movement back and forth is detectable and this yields displacements in spectral lines due to Doppler shift.

The shape of a RV curve depends on orbital parameters (Ohta et al., 2005): semi-major axis (a), orbital inclination (i), period (P), eccentricity (e), masses of star and planet (M and m), and argument of pericentre (ω) that is the longitude of the observer's line of sight with respect to the pericentre. In general, inclination of the orbital plane is not known, so only the minimum mass of the exoplanet ($m\sin i$) can be estimated by RV detection. Using some of orbital parameters, minimum mass, $m\sin i$ is written as (Gaudi and Winn, 2007)

$$m \sin i = K \left(1 - e^2\right) \left(\frac{P \left(m + M\right)^2}{2\pi G} \right)^{1/3}, \tag{1.3}$$

where K is the orbital velocity semi-amplitude in m/s and G is the gravitational constant. Assuming the star mass (M) is much larger than planet mass (m), then K is approximated as

$$K = \left(\frac{2\pi G}{P} \right)^{1/3} \frac{m \sin i}{M^{2/3}} \left(1 - e^2\right)^{-1/2}. \tag{1.4}$$

For convenience's sake, this equation can be expressed with familiar notation,

$$K = 0.089 \ \ m/s \left(\frac{P}{year} \right)^{-1/3} \left(\frac{m \sin i}{M_E} \right) \left(\frac{M}{M_S} \right)^{-2/3}. \tag{1.5}$$

For the case of planets orbiting the Sun, assuming i is zero, the maximum radial velocity would be 13 m/s with a period of twelve years for Jupiter and 0.089 m/s for the

Earth during one year. This means that long-term observation is essential for confirmation of exoplanets with broad orbital separation, and this fact tells us that most exoplanets discovered by the RV method have short periods (one day to ten years) with large mass ($\sim$ Jupiter mass) and narrow distance from the central star (0.01 to 6 AU).

Although the RV method is irrespective of orbital distance, it requires a high signal-to-noise ratio and is useful for nearby stars and massive planets orbiting with small separation, called hot Jupiters, as described in Section 1.1. Hot Jupiters orbit so close to their parent stars that these planets have effective temperatures easily exceeding 1,000 K.

In the RV method, the only thing measured is the Doppler shift of stellar spectral lines on the projected plane on the line of sight. This means that any atmospheric properties and bio-signatures comprised in the exoplanets are not observable via this method. Also, unlike astrometry, it has an edge-on advantage and only the minimum mass of exoplanet ($m\sin i$) can be estimated. The true mass of an exoplanet would be higher than estimated, only excepting the few that have $\sim$90 degree inclination. Simply, the observed planet mass ($m\sin i$) varies between m and zero. Therefore, combining observations with transit spectroscopy or astrometry, which give other physical parameters of exoplanets, enable us to improve the accuracy of mass estimation.

In order to achieve high precision in a RV measurement, state-of-the-art spectrographs on large ground telescopes are operating in different ground telescopes. Two spectrographs, the *High Resolution Echelle Spectrograph* (HIRES, Vogt et al., 1994) on the Keck telescope and the *High Accuracy Radial velocity Planetary Search project* (HARPS, Mayor et al., 2003) on ESO La Silla telescope, contribute to the search for exoplanets with 1 m/s precision in RV. The HARPS was successful in the discovery of a nearly Earth-sized exoplanet (1.94 M_E) orbiting around Gliese 581 (Mayor et al., 2009). Other current instruments such as the *high-resolution spectrograph* (HRS, Tull, 1998) on the *Hobby-Eberly Telescope* (HET), SOPHIE (Perruchot et al., 2008) and ELODIE (Baranne et al., 1996) on the telescope of *Observatoire de Haute-Provence*, and CORALIE (Weber et al., 2000) on the Euler Swiss telescope at La Silla are working and used for RV measurements of exoplanets.

1.2.6 Magnetospheric Emission

Like the Earth, planets comprising internal dynamo currents generate magnetic fields around the sphere. The shape and strength rely on the amount of iron and movement in the core and the solar wind effect which is the source of the magnetopause formation. Interaction between magnetic fields and the magnetised plasma in the solar wind, called electron cyclotron masers, produces energetic electrons (keV) in the radio band ranged from decametric to kilometric wavelength.

The radio luminosity is proportional to the solar wind power into the magnetopause. Therefore, the Earth emits more robust radio emission than Uranus and Neptune, even though their magnetic fields are stronger than that of the Earth. Exoplanets hosted by active stars are not easy to detect using other methods; magnetic emission, however, has an advantage in targeting these stars. In addition to this benefit, magnetic fields prevent the atmosphere and possible life on exoplanet from being exposed to energetic particles. This may support a hypothesis that detected magnetised terrestrial planets have better conditions for habitability.

Currently, efforts to detect magnetic emission from exoplanets have been increased. For decametre burst detection, several ground telescopes are ongoing, such as the *Long Wavelength Array* (LWA, Kassim and Erickson, 1998) in the Mexico, the *Low-Frequency Array* (LOFAR, Kassim et al., 2004) in the Netherlands and the *Square Kilometer Array* (SKA, Terzian and Lazio, 2006) in the Australia or South Africa. As a future space mission, NASA plans to build a telescope on the far side of the Moon for kilometric radiation detection from terrestrial exoplanets, because the Earth's ionosphere is generally opaque to the radiation above 30 m wavelength.

1.2.7 Transit Photometry and Spectroscopy

When a companion passes in front of (primary transit) or behind (secondary transit) the parent star (Figure 1.4), the combined light of the system is slightly decreased for a time, if the orbital plane lies in the line of an observer's sight. If the dimming is deep enough to

detect at regular intervals, it is deduced that there is a planet orbiting the parent star. Even though an orbital inclination must be quasi-random, a large number of transit light curves have been obtained from various planetary systems so far. Considering $Kepler$'s observations, $>\sim$2,000 candidates of transiting planets were detected, which are necessary to be confirmed as a $planet$ by follow-up observations (Batalha et al., 2012). Spectroscopically, transit curves at multiple wavelengths are directly interpreted as an atmospheric spectrum that includes a transmission spectrum (during primary transit when light is filtered through the upper levels of a planet's atmosphere), a thermal emission spectrum (during secondary eclipse when the emission is directly detected from a planet's atmosphere) and a reflected spectrum (out of transit when light is directly reflected by the clouds and surface). These complementary methods of spectroscopy provide improved confidence in the derived atmospheric properties.

Simply, the obtainable signals from the primary transit and secondary eclipse, and outside transit are (Seager, 2010)

$$Fraction\ of\ star\ obscured\ :\ \left(\frac{R_P}{R_S}\right)^2, \tag{1.6}$$

$$Emission\ flux\ ratio\ between\ planet\ and\ star\ :\ \left(\frac{T_P}{T_S}\right)\left(\frac{R_P}{R_S}\right)^2, \tag{1.7}$$

$$and\ Reflection\ flux\ ratio\ between\ planet\ and\ star\ :\ f\left(\frac{R_P}{a}\right)^2, \tag{1.8}$$

where T_P, T_S, f and a are effective temperature of planet and star, and planetary geometric albedo and planet-to-star distance, respectively. Here, we assume the atmosphere of planet is rather thin and negligible to detect. For the case of the hot Jupiters, each ratio is typically equivalent to the order of $\sim 10^{-4}$, $\sim 10^{-3}$ and $\sim 10^{-5}$ (Seager, 2008). As the only indirect detection method to take advantage of photometry and spectroscopy together, transit spectroscopy allows us to characterise exoplanet atmospheres in detail.

During primary transit, a photometric light curve in a given bandpass contributes to an estimation of the radius ratio of an exoplanet and host star (R_P/R_S). Assuming that the stellar radius is well known from its theoretical spectral type, the radius of exoplanet

can be determined from the light curve measured. The depth of transit at the middle of event then can be expressed as

$$Depth\ \ of\ \ transit = \left(\frac{R_P}{R_S}\right)^2. \tag{1.9}$$

Note that the 'Depth of transit' is shown in Figure 1.4 as 'A'. The transit curve shape (marked as 'B' in Figure 1.4) shows the amount of brightness obscuration along the transit path that indicates the limb darkening profile of the parent star (Seager and Mallén-Ornelas, 2003). The stellar light filtered through the atmospheric limb of the exoplanet is directly converted to the transmission spectrum, which can help to find either atmospheric scale height or the diverse molecular or atomic species present in the atmosphere.

During secondary eclipse, the disk-averaged emission of exoplanet can be measured by taking the difference between two spectra in-transit and out-of-transit. Spectral features of IR emission, where thermal radiation from the exoplanet is predominant, are highly useful for the detection of composition at certain pressure levels and the temperature structure of the exoplanet.

It has been also shown that the brightness change between primary transit and secondary eclipse makes it possible to deduce the relative longitudinal brightness of the exoplanet. This gives intriguing clues on the atmospheric dynamics of the exoplanet (Harrington et al., 2006; Knutson et al., 2007), by which the atmospheric circulation and energy distribution in extreme circumstance can be simulated. Figure 1.5 clearly shows HD 209458b's transit dimming (left) and simulated surface map (right), predicted from brightness change of the light curve during between primary and secondary transits.

The probability of transit is defined as a radius ratio between star and planetary orbit (R_S/a). This means that the more closely an exoplanet orbits around a host star, the higher possibility it has to be spotted. Namely, exoplanets having large orbital distance can only be detectable during a tiny fraction of orbital period. For example, the transit time of an Earth-like planet is approximately only 12 hours during 1 year, which is only 0.5% per orbital period. In this sense, overcoming the intrinsic limitation in detecting small

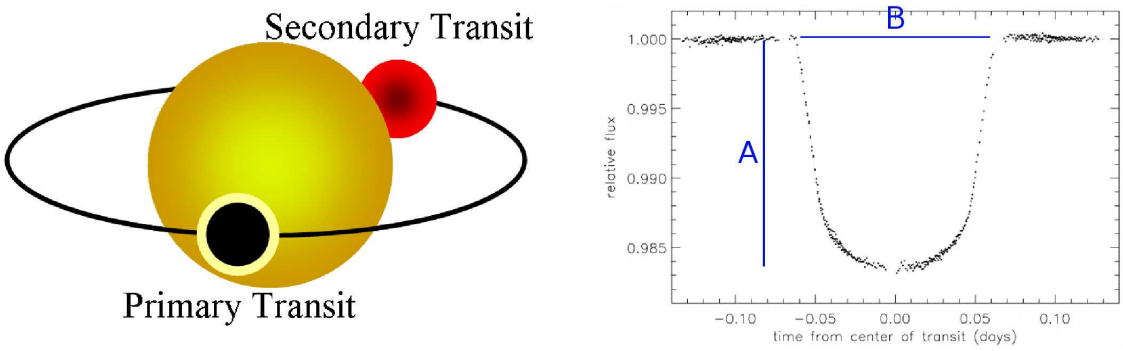

Figure 1.4: $(Left)$ A schematic diagram illustrating the geometry of a planetary system during primary and secondary transits, and $(Right)$ a light curve of HD 209458b during primary transit.

and long-period transiting exoplanets, NASA's *Kepler* mission (Borucki et al., 2003) has been performing a continuous observation of a fixed Cygnus-Lyra region with a wide $10^\circ \times 10^\circ$ field-of-view. It has detected $\sim$50 planet candidates in a habitable zone among detected candidates of $\sim$200 Earth-size, $\sim$700 super Earth-size, $\sim$1,200 Neptune-size, $\sim$200 Jupiter-size and $\sim$50 larger than the size of Jupiter from 100,000 nearby stars during its operation[2].

Global network projects use small ground based telescopes designed to observe transit photometry, covering a wide field-of-view of the sky. *The Trans-atlantic Exoplanet Survey* (TrES) project ran three 10 cm telescopes located at Lowell Observatory, Palomar Observatory, and the Canary Islands and it has confirmed five exoplanets (Alonso et al., 2004). In Hawaii, the two 200-millimetre telephoto binocular camera, called XO-$telescope$, found five transiting exoplanets from nearby stars (McCullough et al., 2005). The *Hungarian Automated Telescope Network* (HATNet) project consists of six fully automated 11 cm telescopes located at two Smithsonian Astrophysical Observatory (SAO) sites in Arizona and Mauna Kea, Hawaii (Bakos et al., 2002). So far more than 40 exoplanets including two multi-planetary system have been discovered via HATNet. *Super Wide Angle Search for Planets* (SuperWASP) can cover 500 square degrees of the sky using 8 multi-cameras built on one mount. SuperWASP's two telescopes placed at the Canary Islands and the South Africa have made 70 detections of Jupiter-size exoplanets

[2]http://kepler.nasa.gov/

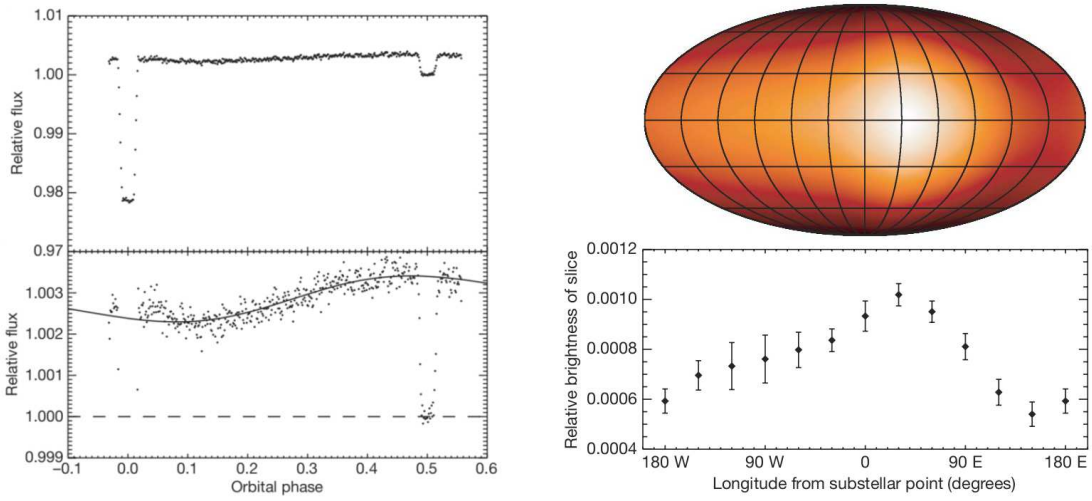

Figure 1.5: ($Left$) Light curve of combined light of HD 209458 during one orbital period. Brightness variation is clearly shown between transits and is led by the phase change of HD 209458b during orbit. ($Right$) Longitudinal brightness of HD 209458b can be mapped based on the light curve between two eclipses (Knutson et al., 2007).

(Street et al., 2003).

Transit spectroscopy for the atmospheres of exoplanets has been only being carried out using large ground based and space telescopes. Inaugural observations made by the VLT found an atmospheric feature of a sodium doublet line from the transmission spectrum of HD 189733b (Redfield et al., 2008). In the near IR, high flux ratios of the dayside emission spectrum of HD 189733b has been observed by IRTF (Swain et al., 2010). *Convection, Rotation and Transits* ($CoRoT$, Viard et al., 2007) has a low-resolution spectral dispersing prism that is able to provide RGB colours for simultaneous light curves, although $CoRoT$ mainly does photometry in the visible band. The $Spitzer$ telescope and the HST provide remarkable spectroscopic data, which is acquired from the IR instruments, i.e. Infrared Array Camera (IRAC, imager) and Infrared Spectroscoph (IRS) on $Spitzer$, and Near Infrared Camera and Multi-Object Spectrometer (NICMOS) on HST. Further noteworthy results on transit spectroscopy will be discussed in the next section and the detailed radiative transfer process during the transits will be described in Chapter 2.

1.3 Hot Jupiters

Current research of exoplanetary atmospheres is mostly based on transiting planets due to the fact that transit spectroscopy is the only indirect method for characterising the properties of these atmospheres. For this reason, there are a number of transiting exoplanets that have been observed in multiple wavelengths since the first transiting planet discovery in 1995. In particular, some of the close-in exoplanets have been intensively investigated due to their warm and inflated atmospheres and short orbital period, making them ideal for study via the transit technique. As a result of multi-observational data, transiting exoplanets have been shown to possess diverse characteristics of atmospheres depending on the planetary mass, orbital distance and spectral type of parent star. In this section, the atmosphere of hot Jupiters that will be examined throughout this study will be highlighted.

1.3.1 Theoretical Model for Hot Jupiters

Hot Jupiters have masses and radii similar to those of Jupiter, orbiting the parent star with a short semi-major axis ($<$0.1 AU) so a strong insolation impacts the dynamics and thermal conditions in the atmosphere. Among the detected hot Jupiters, HD 189733b and HD 209458b have successfully been studied since the first detections, due to the facts that these planets have a near edge-on orbital plane (i.e. $\sim$90° inclination) and the atmospheric features are different even though they have similar physical characteristics, making them more interesting in terms of exoplanet diversity. In this context, this study will examine the atmospheres of transiting exoplanets based on the measurements and the theoretical results of these two hot Jupiters.

Thermal Structure

In general, the atmospheres of exoplanets are modelled under the assumption of a stable atmosphere in hydrostatic equilibrium, achieved from the balance between the forces of gravity of the planet and atmospheric pressure. If the main heat source of the atmosphere comes from the planets' interiors like Jupiter or Saturn, vertical convection dominates the

energy transportation outward in the deep atmospheres where opacity is high. The convection zone continues until opacity becomes thin ($\sim$1 bar), called the radiative-convective boundary, and radiation, the flow of photons, is now predominant in transporting the outgoing energy. Unlike the gas giant planets in our solar system, strong irradiation from the parent star penetrates into the deep atmospheres of these hot Jupiters, which play a crucial role in determining the energy transportation above deep convection zones of hot Jupiters. As a result, strong incident flux from the parent star pushes the radiative-convective boundary down to the 100–1000 bar region and causes an isothermal layer above the convection zone (Fortney et al., 2008, 2010; Hubbard et al., 2001). Above the deep radiative zone, temperature is strongly connected with the chemical composition of atmosphere, which may show a temperature-decreasing, -increasing or isothermal layer.

Relying on what composition and temperature structure the atmosphere has, Fortney et al. (2008) classifies hot Jupiters into two different species, 'pM' class and 'pL' class planets, which are analogous to the 'M-type' and 'L-type' dwarf stars and are categorised by the level of incident flux from parent star. Firstly, in a 'pM' class planet that experiences an incident flux in an orbital distance less than 0.04 AU from the Sun, molecules such as titanium oxide (TiO) and vanadium oxide (VO) absorb strong optical radiation, leading to an inversion layer in the upper atmosphere (i.e. stratosphere), wherein temperatures increase with increasing altitudes. As a consequence the molecular emission lines from an inversion layer causes a high MIR flux level in the dayside emission spectrum. On the other hand, H_2O and alkalis show dominant absorptions in 'pL' class planets that have orbital distances greater than 0.05 AU in normalised distance, so these might show no stratosphere. The theoretical vertical temperature models for pM and pL class planets are displayed in Figure 1.6. Although the model by Fortney et al. (2008) is simplistic and will likely be ruled out as we obtain more data, it serves as a first guess for explaining and characterising the different spectra observed in hot Jupiters, and a hypothesis that should be tested from data.

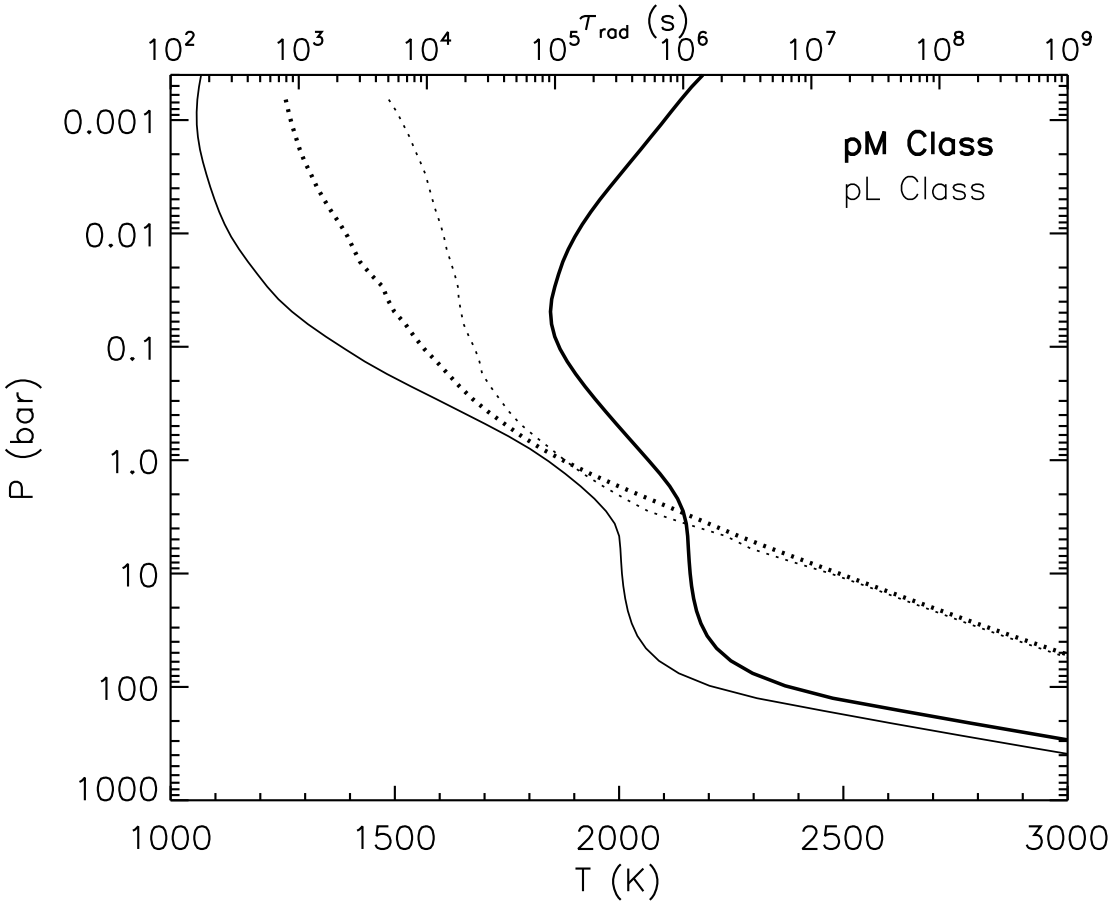

Figure 1.6: Temperature profiles of typical 'pM' and 'pL' class planets, taken from Fortney et al. (2008). Due to a strong irradiation from parent star, a deep radiative zone can be seen above a convection zone for both cases. For 'pM' class planets, an inversion is also shown in the atmosphere, caused by TiO/VO absorptions at visible wavelgnths.

Chemistry

In the atmospheres of hot Jupiters, hydrogen (H_2) and helium (He) are dominant as they are in the giant planets of our solar system. The fractions of these molecules are likely to be similar to their parent star value (Burrows and Sharp, 1999). Besides these two constituents, other molecules such as oxygen, carbon, and nitrogen species, hydrides and other elements are also predicted to be abundant in the atmospheres (Burrows and Sharp, 1999; Sharp and Burrows, 2007). The amounts and vertical distributions of composition are estimated by running photochemical and thermochemical models (Liang et al., 2003, 2004; Line et al., 2011; Moses et al., 2011). Given a composition of C, O and H with abundances identical to the parent star value, the photochemical models consider initially photolysis by radiation from the parent star and reactions between molecules and elements in the environment of the hot atmospheres, and then the initial abundances of each molecule can be calculated. The initial state of chemistry is now used to derive the final state of atmospheric composition from thermochemical models, which remain in the chemical equilibrium state (Liang et al., 2003, 2004; Line et al., 2011).

H_2O, one of stable molecules, is highly plausible in the atmospheres of hot Jupiters because H_2O is present when the planet has a close distance from the central star (about 1 AU orbit distance in case of the sun). As stable carbon carriers, CH_4 and CO are in thermochemical equilibrium by the following equation,

$$\mathbf{CO + 3H_2\,(at\ \ high\ \ T/low\ \ P) \rightleftharpoons CH_4 + H_2O\,(at\ \ low\ \ T/high\ \ P)}\,.$$

At high temperatures ($\geq$1200K), reactions towards the left side of the formula are more active and, at low temperatures ($\leq$800K) reactions towards the right side are more active (Swain et al., 2008a). Due to the $Le\ Chartelier$'s principle, the higher pressure that exists, the fewer molecules there will be to maintain equilibrium. Therefore CH_4 and CO production are simultaneously controlled by both temperature and pressure. The reactions between CO, H_2O and the hydroxyl radical (OH) explain the process of CO_2 production,

$$\mathbf{CO + H_2O \rightleftharpoons CO_2 + H_2}$$
$$\mathbf{CO + OH \rightleftharpoons CO_2 + H}.$$

Photolysis of H_2O is the primary source of OH (i.e. $H_2O + h\nu \rightarrow H + OH$), being active at high altitude, thus CO_2 steadily increases with altitude. Additionally, high fractions of H_2 and He exhibit strong absorption features in a wide region from 1 μm to the far IR which is called collisional induced absorption (CIA). CIA by these two molecules shows a strong continuum absorption in transmission and emission spectra as the absorption is efficient at high temperatures and pressures. Another continuum source, Rayleigh scattering, contributes to absorption in the visible band ($<1\mu$m). Other constituents dominating visible absorption are alkali metals and metallic oxides; alkali metal lines such as sodium (Na) and potassium (K) are prominent at 1000–1500K. In the case of very high temperature regions (2000$\sim$2500 K), Ti and V, mostly in gaseous TiO/VO, might play a critical role in forming the temperature inversion (Fortney et al., 2008, 2010).

For comparison, Sudarsky et al. (2000, 2003) suggested different classification of hot Jupiters: 'class IV' (900 K $\leq T_{eff} \leq$ 1500 K) planets have abundant alkali metals, where excess visible absorption reduces the bond albedo (i.e. dark in the visible), and H_2O, CO, a small fraction of CH_4, and no NH_3. A silicate cloud layer may form at low altitude. On the other hand, 'class V' ($T_{eff} \geq$ 1500 K) planets are bright in the visible due to high silicate/iron cloud. H_2O and CO are still abundant but CH_4 is depleted. Evaporation of oxides (TiO and VO) as well as hydrides such as CrH and FeH is also likely in very hot atmospheres ($T_{eff} \geq$ 2000 K), producing spectral features in the hottest planetary atmospheres. All the derivations of composition have been performed with a chemical equilibrium condition, but the studies predicted that photochemical products by nonequilibrium processes in the stratosphere may change the temperature profile to have an inversion layer at low pressure levels.

In the following sections, we will discuss previous attempts to characterise the atmospheres of two different types of transiting hot Jupiters, HD 189733b and HD 209458b, which represent either a pM and a pL class planets as defined by Fortney et al. (2008) or class IV and class V planets by Sudarsky et al. (2000, 2003). Here we will highlight find-

ings and issues that provided new milestones to understanding the atmospheric features of hot Jupiters.

1.3.2 HD 189733b

Transmission Spectrum

Since its discovery in 2005 (Bouchy et al., 2005), HD 189733b, 19.3 pc away from the Earth, is one of the most studied of all the exoplanets observed. It orbits a K-type star with separation of 0.031 AU and has slightly larger radius than Jupiter (1.13 R_J). Beaulieu et al. (2008); Tinetti et al. (2007a) deduced a high abundance of H_2O in the upper atmosphere from transmission spectra of HD 189733b acquired during primary transits (∵ transmission spectra are sensitive to terminator regions), which were observed by $Spitzer$ mid-IR (MIR) broadband photometry at 3.6, 5.8 and 8.0 μm. However, Ehrenreich et al. (2008) re-visited these observations and drew opposite conclusions (i.e. H_2O is no evidence for H_2O on this exoplanet). New observations from Agol et al. (2009), Knutson et al. (2007), Knutson et al. (2009) and Désert et al. (2009) showed that the flux ratios delivered from the IRAC measurements are highly dependent on the decorrelation methods applied for each study. A spectral feature of HD 189733b at 4.5 μm can be explained by the carbon bearing molecules of either CO_2 (Désert et al., 2009) or CO (Fortney et al., 2010), although it is still unclear due to the degeneracy of the solution. Swain et al. (2008b) reported strong absorption from CH_4 in the near-IR (NIR) at 2.0–2.5 μm using the HST/NICMOS spectrophotometry. However, Gibson et al. (2011,b) claimed that the NICMOS measurement did not provide hard evidence for CH_4 due to systematic errors of the instrument, and may support a thick haze layer of silicate grains. At visible wavelengths, a featureless spectrum detected by the HST/ACS and HST/STIS are thought to be caused by thick atmospheric hazes (Lecavelier Des Etangs et al., 2008; Pont et al., 2008; Sing et al., 2009, 2011) of silicate such as enstatite ($MgSiO_3$). Above a thick haze, strong lines of the alkali metal, Na, were reported using observations with the high resolution (R=60,000) ground spectrograph of the $Hobby–Eberly$ Telescope (Redfield et al.,

2008).

Emission Spectrum

Observations of secondary transits of HD 189733b by $Spitzer$/IRAC at 3.6, 4.5, 5.6, and 8.0 μm and MIPS at 24 μm showed that H_2O is abundantly present in the dayside atmosphere (Charbonneau et al., 2008; Deming et al., 2006), forming the main features of the emission spectrum and confirming some of the results from the primary transits[3] bf Grillmair et al. (2008) using the $Spitzer$/IRS spectrograph showed a flat spectrum between 5–10 μm that is characterised by a molecule formed in an isothermal layer, particularly H_2O in this atmosphere. In addition to the detection of H_2O, the HST/NICMOS measurements showed extra spectral features at 1.4–2.5 μm, indicating the presence of carbon bearing molecules such as CO_2, CO, and CH_4 (Line et al., 2011; Madhusudhan and Seager, 2009; Swain et al., 2009b). Also, Swain et al. (2009b) and Madhusudhan and Seager (2009) suggested that an atmosphere without a thermal inversion layer best represents the atmospheric structure of HD 189733b, for which a troposphere may be located between 0.01 and 1 bar pressure level. Thus one aim of this study is to retrieve the vertical temperature structure of the dayside HD 189733b within an optimal estimation scheme, and to quantify the true uncertainties on the compositional determinations proposed by previous studies.

1.3.3 HD 209458b

Transmission Spectrum

The other hot Jupiter, HD 209458b, has a radius 1.35 times greater than Jupiter, and was discovered for the first time using transit spectroscopy in 1999; it is the second-best observed of transiting exoplanets. This planet orbits a G-type star with a semi-major axis of 0.045 AU. Charbonneau et al. (2002) reported a sodium doublet feature at 589.6 and 589.9 nm from a transmission spectrum of HD 209458b. Some years later, Knutson

[3]Recent interpretation of the first two IRAC channels by Knutson et al. (2012) claimed that the flux ratio at 3.6 μm is needed to be down graded, indicating that there might not be a strong H_2O feature in the MIR.

et al. (2007) observed the transmission spectrum at the visible band between 300–770 nm, showing smoothed absorption features due to Rayleigh scattering by hydrogen molecules (Sing et al., 2008). Based on the observation of HST/STIS, Désert et al. (2008) suggested a possibility that there are features caused by metallic oxide lines from TiO and VO in 0.6–0.8 μm, which molecules play an important role in the occurrence of a temperature inversion in the pM class atmosphere (Fortney et al., 2008). In the ultraviolet (UV) region, Vidal-Madjar et al. (2003, 2004) using HST/STIS detected an evaporating atmosphere of Hydrogen (H), Oxygen (O), and Carbon (C) surrounding HD 209458b, which is believed to be due to strong irradiation from the parent star heating up the upper atmosphere. Beaulieu et al. (2010) analysed the $Spitzer$/IRAC photometry of HD 209458b during primary transit, and suggested the best-fitted spectrum based on H_2O transitions alone, showing an agreement with the measurements in the visible (Barman, 2007) and at 24 μm (Richardson et al., 2006). Snellen et al. (2010) discovered fast wind speeds at high altitude by measuring doppler shifts of 56 CO lines at high spectral resolution between 2.291–2.349 μm during primary transit. However, the retrievals for the atmosphere of terminator regions for HD 209458b will not be performed in this study due to the small number of measurements currently available, which may give a huge degeneracy between atmospheric parameters. We will leave this for one of future studies.

Emission Spectrum

Burrows et al. (2007) as well as Sudarsky et al. (2003) and Fortney et al. (2008) discussed in-depth the structure of the stratosphere and proposed the possibility of a thermal inversion layer in HD 209458b. A warm stratosphere has been generally accepted through significant and successive observations of the dayside emission taken by various instruments on board $Spitzer$ and HST (Burrows et al., 2007; Swain et al., 2010). Of all measurements of the secondary transit, the six $Spitzer$ broadband photometry channels ranging from 3.6 to 24 μm showed very high flux ratios that require a thermal inversion structure during retrieval (Knutson et al., 2009; Madhusudhan and Seager, 2009, 2010; Swain et al., 2009a). Despite the fact that all these studies claimed to find an inversion,

each produced an estimate of the size and altitude which was inconsistent with all the others. In this sense, one aim of this study is to test how robust such a conclusion actually is by quantifying the uncertainties in the temperature field based on the compositional degeneracy. Additionally, we will look for evidence of differences between HD 189733b and HD 209458b as a function of effective temperature and orbital separation.

1.3.4 Summary

According to the various theoretical models, the atmospheres of hot Jupiters HD 189733b and HD 209458b consist primarily of H_2 and He, forming a CIA continuum in the spectra, and prominent H_2O, CO_2, CO, and CH_4 features, showing deep troughs over the wavelengths for both transmission and emission spectra. The emission spectrum has only been measured in the infrared (IR) region (1–30 μm), where the flux ratio between parent star and planet rises appreciably. On the other hand, transmission spectra have also been measured at shorter wavelengths where Rayleigh scattering and alkali metals are thought to be highly dominant in the optical ($\leq 1\mu$m). However, for both primary and secondary transits, many authors have focussed on very narrow wavelength ranges with a sparse number of data points to draw their conclusions.

Previous attempts to scrutinize each atmosphere from transit spectroscopic data have either not used retrieval techniques to study these atmospheres, instead relying on forward models, or not quantified the uncertainties caused by the compositional and temperature degeneracy. Given low measurement S/N and the small number of data available, these limitations may lead us to misinterpretations of the properties of these planetary atmospheres. Therefore, the next section will discuss the current understanding of how to characterise the exoplanets listed in previous sections, based on their various modelling methods, and then the motivation of this study.

1.4 Current Issues in Characterisation of Exoplanetary Atmospheres

The retrieval of atmospheric properties from remotely sensed measurements of solar system planets has been developed over many decades (Goody and Yung, 1989) and has become a common tool for the study of planetary atmospheres. Radiances measured (either photometry or spectroscopy) by an instrument contain information about the atmosphere, including the specific vertical structure of constituents and temperature. However, our incomplete knowledge limits our ability to reproduce the measured radiances from the target atmosphere entirely due to the $inverse\ problem$–The values of the parameters in the atmospheric model can reproduce the values of the parameters in the observed atmospheres. This must be done based on a physical theory between the observed values and the parameters defining the atmospheric system. However, the complete theory is not known in general due to our insufficient knowledge of physics linking the observation and atmospheric system. The $inverse\ problem$ therefore is caused when we extract the atmospheric information from the observation.–During the retrieval process, measured spectra are compared to synthetic spectra that are integrated based on the best-known properties, $a\ priori$. Varying and perturbing the atmospheric properties, the retrieval solves the $inverse\ problem$ to find the most likely solution, which allows us to constrain the atmospheric temperature and composition.

In general, the retrieval process faces two inevitable problems. Firstly, the information we can deduce from the atmosphere consists of a combination of many individual parameters such that a small number of measurement constraints are insufficient to determine continuous profiles from a limited set of radiances, i.e. the problem is $ill-posed$. Secondly, small changes in the measurements can potentially have a disproportionately large effect on the solution and hence the retrieval may end up with unrealistic vertical atmospheric profiles in which the retrieval is $ill-conditioned$. Therefore, we can say that the retrieval process is a way to overcome the given impediments in an efficient way to constrain physically-realistic solutions and a range of uncertainty.

Exploiting data from telescopes and spacecraft over the last few decades, diverse retrieval techniques have succeeded in characterising the atmospheres in our solar system using spectroscopic measurements with high spectral resolution and low uncertainties. Exoplanetary atmospheres, however, have been recently understood from a few spectroscopic data points taken during primary transits and secondary eclipses. This is why meaningful retrievals have been performed only for few exoplanets so far and used to constrain atmospheric properties such as temperature and major molecules. Moreover, it is known that these model fits suffer from excessively large measurement errors that lead to extreme degeneracy between retrieval parameters. In this sense, current retrieval models are principally focused on how to describe the correlation between the parameters by exploring the solution space wherein each fit is converted into a statistically meaningful value. In this context, this chapter will introduce the retrieval techniques that have been used up to date. The pros and cons of each method will be followed by the motivation of this study and a detailed description of optimal estimation retrieval, which will be used throughout the next chapters.

1.4.1 Retrieval Studies of Exoplanetary Atmospheres

Previous studies, such as those by Tinetti et al. (2007b) and Swain et al. (2008b, 2009b), utilised a forward model, which takes into account the end-to-end radiative transfer calculation addressing all the physics involved therein, so as to determine a best-fit to the data, and constrained the range of molecular abundances of transiting exoplanets. This process can be done by running forward models based on theoretical pressure-temperature (P-T) profiles. For instance, fitting to the dayside emission spectrum of HD 209458b, Swain et al. (2009b) showed the effect of theoretical P-T profiles to the spectrum integration. By doing so, Swain et al. (2009b) suggested that there is a possibility of a stratosphere in HD 209458b, which can be placed at a certain pressure level between 10^{-1} and 10^{-3} bar. The uncertainty of the thermal inversion layer is due to the degeneracy problem between temperature and molecular abundances. The forward modelling technique with theoretical P-T profiles is, however, hard to 1) test the reliability of the resulting solu-

tion, owing to not solving the inherent inverse or forward problem, 2) find truly unbiased solution towards previous model-based knowledge of P-T profile and 3) demonstrate the degeneracy range of retrieval parameters.

On the other hand, Sing et al. (2008), who also adopted the forward modelling method, applied different P-T profiles and molecular abundances in a parameterised space, wherein calculated spectra were again compared with observations in terms of the goodness-of-fit, and their runs enabled them to constrain the given parameters as well as showing the best-fit spectrum for visible transmission of HD 209458b. Similarly, but in a more general way, Christiansen et al. (2010); Madhusudhan and Seager (2009); O'Donovan et al. (2010); Stevenson et al. (2010) exploited freely roaming parameterised P-T profiles and molecular abundances as an alternative forward modelling approach. Their enormous numbers of runs ($>$one million) with a broad range of the parameters, which were established in advance of the retrieval, physically constrained by hydrostatic equilibrium and global energy balance, can characterise the hot Jupiter's P-T profile and molecular abundances in terms of statistics. In particular, their comprehensive computations allowed them to illustrate the uncertainty of the retrieval parameters occurring from the strong degeneracy problem. Therefore, this method can suggest more realistic solutions and information from the measured data than any other studies before. The cost-ineffective radiative transfer calculation, however, makes it difficult to add new parameters to those from previous model runs, which requires one complete numerous iteration again. Although these forward modelling techniques provide valuable insights, their methods are based on line-by-line radiative transfer models, which are very slow when large numbers of synthetic spectra are to be calculated over a wide wavelength range.

In order to reduce computational cost and to seek plausible solutions in an efficient way, a number of studies (Anderson et al., 2011; Blecic et al., 2011; Christiansen et al., 2011; Demory et al., 2011; Désert et al., 2011; Knutson et al., 2011; Madhusudhan and Seager, 2010, 2011; Madhusudhan et al., 2010, 2011; Nymeyer et al., 2011; Smith et al., 2012), as an improved version of Madhusudhan and Seager (2009), extensively applied the Markov chain Monte-Carlo (MCMC) method for constructing the contours

of goodness-of-fit in parameter space, where each sampled model is defined by certain atmospheric parameters. Using four and six $Spitzer$/IRAC measurements, Madhusudhan and Seager (2010) discussed the plausibility of a thermal inversion layer in hot Jupiter atmospheres. Also, this method has been applied to the other transiting planets including relatively small objects (e.g. Neptune class planet by Knutson et al. (2011); Madhusudhan and Seager (2011)) observed recently, to estimate the characteristics of each planet's atmosphere from a small number of data points. Hence, retrieval with the MCMC technique and parametric variables in grid space has become a popular method due to its ability for finding the best estimate and full exploration of degeneracy problem. In principle, a MCMC method finds the best estimate solution with a well-defined $Markov\ chain$, which is consist of a series of random variables, where the newly proposed state relies on the previous state. The proposed state is accessed based on the goodness-of-fits between the spectra of the current state and previous state, which determines the acceptance of a new state. However, this "random-walk" method still requires a number of steps to give sufficient reliability to converged retrievals, which is an intrinsic limit of the MCMC technique. In addition, in order to check the degeneracy between the parameters, it is still essential that radiative transfer calculations should be carried out on all the grid points as done by the previous version.

Taking the benefit of existing methods into account, Benneke and Seager (2012) reported an advanced retrieval method that incorporated the MCMC model with the Bayesian approach, the $Metropolis\text{-}Hastings$ (M-H) algorithm. This combination was initially introduced to the exoplanetary retrievals in Madhusudhan and Seager (2010), but Benneke and Seager (2012) developed and firmly applied it to finding the best-fit solution to the measurements. Unlike classical sampling, a series of samples in the M-H algorithm is generated from the probability distribution with which the Bayesian theorem can be efficiently applied to the retrievals. In a chain of the states, whether or not the proposal state is acceptable is determined depending on either the proposal state conditions, where it shows a reduced goodness-of-fit, or higher prior probability than previous state. In the case of which any condition is not fulfilled, it is only accepted when the jump probability

between previous and proposal states, $P(x_n)$ and $P(x')$, are high enough, which can be expressed as (Benneke and Seager, 2012)

$$P(x_{n+1} = x') = exp\left[-\frac{\chi^2(x') - \chi^2(x_n)}{2}\right]\frac{P(x')}{P(x_n)}, \tag{1.10}$$

where χ^2 describes the goodness-of-fit between the measurement and the spectrum reproduced by a state vector. This helps to search for the posterior probability distribution and find the best-fit spectrum more quickly than the MCMC alone. Benneke and Seager (2012), however, constrained the degeneracy uncertainties on individual parameters by marginalising the probability distribution and assuming no prior information for the atmospheric state available. Instead, this method was performed running the multiple retrievals in parallel with a different starting point, called the $parallel\ tempering$ scheme as defined in Gregory (2007), in order to let the current state not biased towards prior information. Probability of the abundances of all molecules included in the forward model is also equally distributed in a plausible range (10^{-12}-1 in mixing ratio) to remove any previous knowledge. By doing so, this model is enabled to obtain the non-Gaussian probability of each parameter uncertainty. Given the unique constraints determining the shape of the calculated synthetic spectrum (e.g. the transit depth shape by specific spectral features, slope due to Rayleigh scattering or relative depths of the spectrum caused by the same molecule), the method provided the possibility to constraining the mixing ratio for active and even inactive gases, surface pressure level, and mean molecular mass from the observed transmission spectra. As an attempt to reduce computational time, its forward model adopted an approximate radiative transfer calculation, interpolating the pre-calculated cross-sections of molecules on a temperature and pressure grid. Despite uniquely explaining the state of the atmosphere with a small number of measurements, this retrieval model still has the limitation on its speed of forward model equivalent to the predecessors.

By contrast, we (also, Lee et al., 2012) have developed a non-linear optimal estimation technique based on Rodgers (2000) and demonstrated robustness of optimal estimation in

terms of rapid convergence and high reliability for the first time. An inverse method solves inverse problem by updating the state vectors, directly addressing the information from the measurement and priors, which is one of different features from the previous MCMC methods. Also, Lee et al. (2012) showed that the retrievals can be achieved by minimising a $cost\ function$ that determines the $optimal\ state$, accounting for the balance between measurements and any prior information we may know. This Bayes' theorem-based retrieval study clearly indicated that optimal estimation is a significantly more efficient technique than the previous MCMC method in searching for the statistical minimum, and its analytical approach to the problem enables us to maximise information content from the atmosphere by utilising the $Jacobian$s (i.e. the rate of change of radiance with each model parameter), each calculated during the retrieval process. In general, our prior knowledge on exoplanets doesn't exist in most cases so allowing a large error range assigned to $a\ priori$ and performing multiple retrievals with various retrieval starting points spread widely in parameter space enables us to explore a sufficient coverage of the degeneracy topology between variables. Consequently, Lee et al. (2012) constrained the vertical thermal profile and individual molecular abundance of the dayside of HD 189733b from HST and $Spitzer$ emission spectra. The detailed process of optimal estimation will be presented in Chapter 4. Subsequently, Line et al. (2012) utilised the optimal estimation technique to determine the best fit P-T profile and molecular abundances from the HST/NICMOS data only. However, the numerically calculated derivatives of the elements in the $Jacobian$ matrix during their iterative retrieval steps are primary causes for increasing computational time as well as its slow line-by-line calculation.

1.4.2 Research Objectives

The retrieval methods referred to above showed that an optimal estimation retrieval is a robust tool to solve the limitations of previous studies, including 1) a lack of tools to understand the sensitivity of spectra to retrieval parameters to see what atmospheric information can be provided by individual data points, 2) unsolved inverse problem that is a requisite process for all retrieval studies and 3) strictly selected data points in a narrow

wavelength range that increases degeneracy uncertainties. In addition, a fast correlated-k technique overcomes problems such as 1) inefficient forward model with a standard line-by-line radiative transfer computation, and 2) slow quantification of parameter uncertainty due to the degeneracy problem. Hence the goal of this study is to apply an optimal estimation theory (Goody and Yung, 1989) to the retrieval of exoplanetary atmospheres, overcoming limitations in previous methods. The optimal estimation retrieval model enables us to quantify the best estimates for the temperature and composition of the atmospheres of close-in transiting exoplanets by solving the inverse problem and quantifying the errors on properties from all available spectroscopic measurements (Irwin et al., 2008).

In other words, the optimal estimation retrieval algorithm, NEMESIS (Irwin et al., 2008) that will be extensively used in this study solves the inverse problem using an iterative scheme, rather than simply minimising the deviation between data and model by calculating millions of individual synthetic spectra (the forward model), and uses the correlated-k technique (Lacis and Oinas, 1991) in its radiative transfer model, which rapidly integrates synthetic spectra using k-distribution tables pre-calculated from line databases (Goody and Yung, 1989) (see Chapter 4). Since its birth, the combination of the correlated-k forward model, which is orders of magnitude faster than a line-by-line model, with an optimal estimation retrieval scheme (Irwin et al., 2008) has been used to successfully investigate planetary atmospheres in our own solar system. By adapting this rapid retrieval architecture to exoplanets and considering all the measurements available over a wide wavelength range, it is capable of formally addressing the uncertainties and degeneracies inherent in previous studies. Moreover, understanding of the detailed correlations between the derived P-T profile and atmospheric compositions can be achieved from the covariance matrices which are calculated using this method, and which quantify the correlations between the retrieved values of different properties.

In summary, the retrieval model in this study can provide the solutions to the limitations of previous retrieval architectures by

- Applying a fast correlated-k technique to the radiative transfer calculation, with pre-

tabulated k-distributions, that is fully applicable to a high temperature application,

- Yielding fast-computed partial derivatives using an analytic method for each step of optimisation,
- Exploiting sensitivity matrices such as covariance matrices and functional derivative (Jacobian) matrices to scrutinize the correlation between spectra and atmospheric parameters with the pressure levels and across wavelengths,
- Performing multiple retrievals of temperature with gridded spaces for different molecules in order to determine the plausible error range due to the degeneracy problem instead of taking the Gaussian error shape.
- Addressing all the available measurements between visible and FIR in order to break the degeneracy and to maximise the information we can extract available in the present data.

Ultimately, using full retrieval theory, we are able to quantify the uncertainties on the characterisations that have been presented in the literature so far in order to answer the intrinsic question of $what\ lessons\ can\ we\ learn\ from\ the\ exoplanet\ spectra\ available\ to\ date?$ Moreover, given the previous data and theoretical results, this study will answer the question of $can\ we\ confirm\ the\ atmospheric\ features\ estimated\ by\ the\ literature\ using\ given\ measurements?$. The results from this study will provide good inputs for the models to answer the question of $what\ additional\ measurements\ do\ we\ need\ from\ future\ observation\ programmes?$ In terms of information quantity, the study here will mainly focus on examining the atmospheres of transiting exoplanets via a conventional retrieval architecture. This includes re-analysis of the various sets of measurements to investigate the diverse scenarios made to date, and to deduce further feasible aspects of atmospheric systems. As a result of this study, we have been able to build a canonical model that will be a foundation for forthcoming exoplanetary retrievals in a decade when spectroscopic data with high resolution and low error may become available.

Chapter 2

Retrieval

An optimal estimation retrieval finds the best balanced state (i.e. optimised solution) between constraints from measurements and prior information by iterating a forward model that includes the physics between atmosphere and measured signal and its error. A forward model includes a radiative transfer calculation for an atmosphere that we are interested in, which can be calculated differently depending on the viewing geometry. In this chapter, we will describe radiative transfer calculations for the atmospheres in transiting planets, which will be followed by discussion of retrievals with an optimal estimation technique.

2.1 Forward Model – More about Transit Spectroscopy

When looking at the atmospheres of planets, we observe the emergent spectrum, contributed to by three different mechanisms: absorption, emission and reflection (or scattering). When the continuous blackbody radiation is emitted from the inside of the planet, the cool gases in the upper atmosphere absorb at wavelengths where molecular and atomic transitions are present, forming the 'absorption spectrum'. The absorbed irradiation excites the molecules and atoms in the cool atmosphere and they re-emit the radiation into the atmosphere or space with a local temperature, forming the 'emission spectrum'. The irradiation from a star in the visible or near infrared is reflected or scattered by the cloud

layers or constituents in the planetary atmosphere, forming a 'reflection spectrum'. The reflection spectrum is, however, defined by various aspects of scattering such as Rayleigh scattering by molecules, refraction and diffraction of scattering particles and particle optical properties. Therefore it is complicated to model the reflection spectrum with a simple calculation. In this sense, we will only consider the extinction effect by single scattering calculations under Mie theory rather than account for all the aspects of multiple scattering. Given this basic idea for the emergent spectrum from planet, we review the spectroscopic techniques needed to characterise the atmospheric structure of an exoplanet.

2.1.1 Radiative Transfer for Non-Scattering Atmospheres

Assuming that light travels along the slant path from z_0 to z_1, and scattering effects by any particle in the atmosphere are negligible, the spectral radiance at z_1 $(I_{z_1,\lambda})$ with an angle θ is calculated as

$$I_{z_1,\lambda} = I_{z_0,\lambda}\, exp\left(\frac{-\tau_\lambda\left(z_0, z_1\right)}{\mu}\right), \tag{2.1}$$

where $\tau_\lambda\left(z_0, z_1\right)$ is the optical thickness of a slab atmosphere at wavelength λ and μ is cos θ. The exponential term on the righthand side is the transmission (T_λ) of the slant path with θ between z_0 and z_1. Considering a thick slab atmosphere that can be split into number of thin layers each having thickness dz, a thin layer of atmosphere at z emits thermal radiation into the next layer that finally contributes to $I_{z_1,\lambda}$ at z_1 after attenuation by the layers above. Thus, the spectral radiance at z_1 by the contribution to the emergent spectrum by a particular emission layer at z is then

$$dI_{z_1,\lambda} = B_\lambda\left(z\right)\, exp\left(\frac{-\tau_\lambda\left(z, z_1\right)}{\mu}\right) = B_\lambda\left(z\right) dT_\lambda\left(\mu, z, z_1\right), \tag{2.2}$$

where $B_\lambda\left(z\right)$ is the Planck function at λ and z. Consequently, the emergent spectrum at altitude z_1 is the sum of the transmitted radiance from the bottom of the atmospheric model and the transmission-weighted sum of contributions from each of the individual

layers. Thus this can be given by Irwin et al. (2008)

$$I_{z_1,\lambda} = I_{z_0,\lambda} T_\lambda (\mu, z_0, z_1) + \int_{z_0}^{z_1} B_\lambda (z) \frac{dT_\lambda}{dz} dz, \tag{2.3}$$

where dT/dz is the $transmission\ weighting\ function$, which describes the rate of change of atmospheric transmission with height. BdT/dz is generally called the $contribution\ function$ that describes the radiance measured in each wavelength originating from different levels within the atmosphere. Now Equation 2.3 is a basic description of atmospheric radiation, wherein each term represents a physical process of transmission and emission in atmosphere.

2.1.2 Secondary Eclipse

During secondary eclipse, the thermal emission leaving the top of an exoplanet atmosphere can be acquired by measuring the total flux from the planet-star system before, during and immediately after the planet is eclipsed by the host star and taking the difference between in and out of eclipse. Because the blackbody radiations of star and planet, which have different effective temperatures, peak at different wavelengths, the ratio between the hemispherically disk-averaged fluxes of planet and star steeply rises at wavelengths long ward of 1 μm for typical hot Jupiters around Sun-like stars. This high contrast flux ratio at infrared wavelengths enables us to detect strongly absorbed and emitted molecular features in the dayside atmospheres.

The flux ratio between two objects is then

$$Flux\ ratio,\ \frac{F_{P,\lambda}}{F_{S,\lambda}} = \frac{\pi R_P^2\, I'_{P,\lambda}}{\pi R_S^2\, I'_{S,\lambda}} = \left(\frac{R_P}{R_S}\right)^2 \left(\frac{I'_{P,\lambda}}{I'_{S,\lambda}}\right), \tag{2.4}$$

where $I'_{P,\lambda}$ and $I'_{S,\lambda}$ are the disk-averaged spectral radiance of planet and star. To compute $I'_{P,\lambda}$, the radiance $I_{P,\lambda}$ first needs to be integrated over a hemisphere and all directions of emission from the surface ($0<\mu\leq 1$). Before integration, Equation 2.3 can be re-written

with a new coordinate of τ that is the optical depth of a path length z,

$$I_{z_1,\lambda} = I_{z_0,\lambda} e^{-\tau_0/\mu} + \int_0^{\tau_0} B_\lambda(\tau)\, e^{-\tau/\mu} \frac{d\tau}{\mu}. \tag{2.5}$$

We can now integrate $I_{z_1,\lambda}$ over the solid angle of a hemisphere and μ, and find the emitted flux at the top of atmosphere $F_{z_1,\lambda}$.

$$F_{z_1,\lambda} = \int I_{z_1,\lambda}\, \mu\, d\Omega = 2\pi \int_0^1 I_{z_1,\lambda}\, \mu\, d\mu, \tag{2.6}$$

where $d\Omega$=$\int\int_s sin\theta d\theta d\phi$=$-2\pi d\mu$ ($\because d\mu = -sin\theta d\theta$). Using Equation 2.5, $F_{z_1,\lambda}$ can be given by

$$F_{z_1,\lambda} = 2\pi I_{z_0,\lambda} \int_0^1 e^{-\tau_0/\mu}\, \mu d\mu + 2\pi \int_0^{\tau_0} B_\lambda(\tau) \int_0^1 e^{-\tau_0/\mu} d\mu\, d\tau. \tag{2.7}$$

Here the integrals that involve an exponential term are solved using an exponential integral $E_n(x)$ (Goody and Yung, 1989), where

$$E_n(x) = \int_1^\infty \frac{e^{-xt}}{t^n} dt = \int_0^1 \mu^{n-2} e^{-x/\mu} d\mu, \tag{2.8}$$

if t=$1/\mu$. In principal, the derivative of E_n is equal to $-E_{n-1}$. Now Equation 2.8 can be obtained,

$$F_{z_1,\lambda} = 2\pi I_{z_0,\lambda} E_3(\tau_0) + 2\pi \int_{E_3(\tau_0)}^{0.5} B_\lambda(\tau)\, dE_3(\tau), \tag{2.9}$$

where $E_3(0)$=0.5 ($\because E_n(0)$=$\frac{1}{n-1}$). For the accurate calculation of the flux, the function $E_n(x)$ must be calculated with optical depth to a high precision. Consequently, the disk-averaged spectral radiance of the planet $I'_{P,\lambda}$ can be obtained by applying the planet projected solid angle of π to the denominator of Equation 2.9 (i.e. $I'_{P,\lambda}$=$F_{z_1,\lambda}/\pi$) to convert the unit to W cm^{-2} (cm^{-1})$^{-1}$ sr^{-1} or W m^{-2} μm^{-1} sr^{-1}. Unlike the case for the planetary atmosphere, the disk-averaged radiance of the parent star $I'_{S,\lambda}$ can be computed from the total sum of irradiance of all the annuli that form the stellar disk, by considering the stel-

lar limb darkening effect (Kurucz, 2006). Given an effective temperature, metallicity, and surface gravity, the stellar fluxes are conveniently taken from the radiative transfer models for stellar atmospheres such as ATLAS (Kurucz, 2006) and PHOENIX (Hauschildt, Baron, and Allard, 1997). All models incorporate the transfer process of electromagnetic radiation propagating from the centre to the outer boundary (photosphere and chromosphere) of the star.

Considering a simple approximation, we assume that a planet and star emit perfect blackbody radiation with effective temperatures, T_{EP} and T_{ES}, and then we can re-write Equation 2.4 using the Planck function B_λ, i.e.

$$\frac{F_{P,\lambda}}{F_{S,\lambda}} = \left(\frac{R_P}{R_S}\right)^2 \frac{B_\lambda\left(T_{EP}\right)}{B_\lambda\left(T_{ES}\right)} = \left(\frac{R_P}{R_S}\right)^2 \frac{exp(hc/\lambda k T_{ES}) - 1}{exp(hc/\lambda k T_{EP}) - 1} \tag{2.10}$$

where h and c are the Planck constant and the speed of light, respectively. For long wavelengths where the Rayleigh-Jeans approximation is valid, $\exp(hc/\lambda k T_E) \sim (1 - hc/\lambda k T_E)$ because $hc/\lambda k T_E$ is much smaller than 1. As a result, Equation 2.10 can be simplified as

$$\frac{F_{P,\lambda}}{F_{S,\lambda}} = \left(\frac{R_P}{R_S}\right)^2 \left(\frac{T_{EP}}{T_{ES}}\right). \tag{2.11}$$

For a typical hot Jupiter with $T_{EP} \sim$ 1,000 K orbiting around a Sun-like star ($T_{ES} \sim$ 6,000 K), the flux ratio becomes $\sim$0.001. This number drops rapidly for eclipsing planets with a smaller radius and a wider orbital separation. To describe the flux ratio more closely to the real world, the effective temperature in Equation 2.11 needs to be converted into the wavelength dependant brightness temperature $T_{B,\lambda}$. In this sense, the thermal emission spectrum during secondary eclipse directly gives the brightness temperature of a planetary atmosphere at wavelength λ, and the thermal emission is therefore strongly linked to not only the vertical structure of the temperature, but also the vertical distribution of molecular species. The determination of the dayside temperature profile is also useful to see whether specific thermal structures such as inverted, isothermal, and adiabatic layers are present in the atmosphere.

The disk-averaged emission spectrum calculation introduced in this section will be

adopted to build a forward model for retrievals of the dayside atmospheres of HD 189733b and HD 209458b in Chapters 4 and 6. The vertical structure of the atmospheres and the molecular abundances for different species will be discussed.

2.1.3 Primary Transit

Assuming that the orbital inclination of an exoplanet is nearly 90 degrees ($\mu \simeq 1$), the transit depth at λ in the middle of primary transit is equivalent to the ratio of the stellar fluxes; 1) emitted from the cross sectional area of the parent star disk (πR_S^2); and 2) obscured by the optically thick disk of the exoplanet a_P ($= \pi R_P^2$) and filtered through the atmospheric annulus a_n ($= 2\pi R_P A_H$), where A_H is the thickness between the reference altitude and the top of atmosphere. The area of the atmospheric annulus is a function of wavelength. Therefore, (Seager, 2010)

$$Transit\ \ depth,\ \ \frac{a_P\, I_{S,\lambda} + a_{n,\lambda}\, I_{P,\lambda}}{\pi R_S^2\, I_{S,\lambda}} = \left(\frac{R_P}{R_S}\right)^2 + \frac{2R_P\, A_H}{R_S^2}\frac{I_{P,\lambda}}{I_{S,\lambda}}. \tag{2.12}$$

Here $I_{S,\lambda}$ and $I_{P,\lambda}$ are the stellar radiance at the stellar surface and the radiance filtered by the atmospheric annulus of planet at wavelength λ. The first term in Equation 2.12 describes the transit depth by the optically thick disk only and the second term describes the part of the transit depth due to the atmospheric limb of the planet.

Considering that the stellar light passing through the planetary limb is much brighter than the emission along the paths in the atmosphere, transmission of the atmospheric annulus at λ can be computed without the second term in Equation 2.3 and be expressed with the integration of transmission of the annulus along the path l_h that is placed at tangential height h from the reference altitude (h=0). Thus, using Equation 2.3 and 2.12,

$$I_{P,\lambda} = I_{S,\lambda}\, T_\lambda\,(l_h) \tag{2.13}$$

$$A_H\, I_{P,\lambda} = I_{S,\lambda} \int_0^{A_H} T_{\lambda,l_h}\, dh \tag{2.14}$$

$$\left(\frac{R_P}{R_S}\right)^2 + \frac{2R_P\, A_H}{R_S^2}\frac{I_{P,\lambda}}{I_{S,\lambda}} = \left(\frac{R_P}{R_S}\right)^2 + \frac{2R_P}{R_S^2}\int_0^{A_H} T_{\lambda,l_h}\, dh. \tag{2.15}$$

Ultimately, the absorption depth of a primary transit varies with the physical parameters of the star, and planet and the atmospheric transmission of the day/night terminator region. Moreover, as seen in Equation 2.15, the parent star spectrum is not significantly involved in calculating the transit depth because we assume reasonably that the stellar spectrum is stable for all wavelengths considered during the transit period[1]. In particular, the depths measured in multiple bandpasses are akin to the transmission spectrum of the atmosphere, and thus it can characterise a specific atmospheric pressure level and height in the terminator, where a molecular absorption feature is shown. However, uncertainties in the reference level of the model can lead to large-scale uncertainties in the final solution. This effect on the retrieval will be discussed further in Section 4.7 (secondary eclipse of HD 189733b), 5.5 (primary transit of HD 189733b) and 6.7 (secondary eclipse of HD 209458b).

In general, the transit depth can be replaced by the radius ratio between planet and star by replacing the planetary radius R_P to the effective radius $R_{EP,\lambda}$. Then by taking the square root of Equation 2.15, we can obtain

$$Radius\ \ ratio,\ \ \frac{R_{EP,\lambda}}{R_S} = \frac{\sqrt{R_P^2 + 2R_P \int Tdh}}{R_S} \tag{2.16}$$

Variations in the effective radius are a function of the opacity of the atmosphere, due to extinction by absorption and scattering along the limb paths, as well as the pressure level at which the molecules are effectively distributed. Throughout the study here, both the transit depth and radius ratio will be used depending on the units of data taken.

For a typical Jupiter-size exoplanet, considered by Seager (2008), in which the size of an atmosphere would be approximately five scale heights thick ($A_H I_{P,\lambda} \simeq 5HI_{S,\lambda}$), Equation 2.15 can be written as

$$\left(\frac{R_P}{R_S}\right)^2 + \frac{2R_P a_H}{R_S^2}\frac{I_{P,\lambda}}{I_{S,\lambda}} \simeq \left(\frac{R_P}{R_S}\right)^2 + \frac{10HR_P}{R_S^2}. \tag{2.17}$$

[1]This is not applicable to the cases with strong stellar surface activity (e.g. stellar spots), of which effect may change the overall depth of transit (e.g. Pont et al., 2008).

Typically, H ∼500 km for a hot Jupiter having effective temperature ∼1000 K (Seager, 2008), and therefore the absorption during transit can be ∼1 $\%$. For different classes of exoplanet, this would be ∼0.1 $\%$ for a hot Neptune, ∼0.01 $\%$ for a Super-Earth, all orbiting Sun-like (G-type) stars. The absorption is increased with increasing ages of main sequence stars from F-type (larger size) to M-type (smaller size). The depth of planet's transmission spectrum is therefore a function of the scale of atmosphere, which can be depicted by the scale height $H = kT/mg$, where k, m and g are the Boltzmann constant, the molecular mass of atmosphere and the gravitational acceleration of planet at the reference altitude. By definition, the temperature intrinsically determines the scale height. In this sense, the P-T profile mainly characterises the overall depth of the transmission spectrum across the wavelengths whereas compositional abundances play a critical role in the formation of spectral features in transmission (Tinetti et al., 2007b). The planetary transmission spectra are therefore robust footprints to determine the molecular or atomic abundances in the upper atmospheres of exoplanets. Moreover, the contributions of clouds and hazes (i.e. attenuation and scattering of light) are detectable via this method. Although there exists a significant degeneracy between parameters used to define its optical properties, the characteristics of condensates/clouds/hazes that are likely to be present in various exoplanetary atmospheres are prominently detectable during primary transit. We will discuss this issue more detail in Chapter 5.

Based on the transmission spectrum calculation described in this section, we will build a forward model for the atmospheres in the terminator regions of HD 189733b and characterise the atmospheric composition in Chapter 4. By running and iterating a forward model during the retrieval process, which will be introduced in the next sections, the abundances of different molecules and the properties of haze/cloud will be discussed based on the measurement constraints and the result will be compared with its dayside result to suggest the general atmospheric state for HD 189733b.

2.1.4 Phase curve

During being outside transit and eclipse, the phase curve of a planet is measurable in various wavelengths, where the observation in the visible directly informs us the geometric and Bond albedo and even the energy balance of a planet, and the IR observation enables us to scrutinise the vertical atmospheric circulation at different pressure levels. Since a strong irradiation from the parent star is main driving force of the atmospheric dynamics of hot Jupiter, determining the energy distribution across the planet is extremely important, which can be known from the phase curves at different wavelengths. For a tidally-locked hot Jupiter, the permanent dayside atmosphere emits thermal IR radiation to the space and allows us to observe different thermal conditions in pressures, therefore, which have a strong connection with atmospheric circulation patterns. The phase curve can provide 3-dimensional information for the circulation pattern of planet. The amplitude of the phase curve in between transit and eclipse is approximately 10^{-5} for a typical hot Jupiter (Seager, 2008), meaning that measuring with a high precision is still challenging for most hot Jupiters.

2.1.5 Scattering Calculation

To complete a radiative transfer calculation, we need to constrain scattering effects by particles in the Equation 2.3. However, full scattering calculations are time-consuming and greatly increase the amount of input information that defines scattering characteristics. Hence, the atmospheric effect of single and multiple scattering will not be regarded in our model. This assumption is reasonable for a transmission spectrum because considering the extinction effect as calculated by Mie theory is a good approximation for the atmospheres of transiting planets due to the fact that the scattered light contribution to out of sight is nearly negligible (Hubbard et al., 2001; Lecavelier Des Etangs et al., 2008). Recently, de Kok and Stam (2012) showed that the forward-scattered light may significantly change the transmission spectrum if the optical thickness of the path is larger than unity. In our case, as seen in Chapter 5, the required optical depths to fit the transmission

spectrum of HD 189733b are low ($\sim$0.05) enough not to adopt a forward scattering calculation. Although Mie theory might not be the best solution for the dayside atmospheres but, as a useful start, we will only consider the extinction effect of condensates. This will be discussed in Chapter 5 again. Rayleigh scattering for molecules and condensates using Mie theory will be contained in the radiative transfer models in this study.

Rayleigh Scattering

Rayleigh scattering becomes efficient when the wavelength of light is much larger than the particle size. For Earth, the molecules of N_2 and O_2 are dominant sources for Rayleigh scattering whereas high volume mixing ratios of H_2 ($\sim$0.91) and He ($\sim$0.09) are responsible for Rayleigh scattering in hot Jupiter atmospheres. The probability of Rayleigh scattering by a molecule is defined by the cross-section (cm^2) (Goody and Yung, 1989),

$$\sigma_R(\lambda) = \frac{8\pi}{3}\left(\frac{2\pi}{\lambda}\right)^4 \alpha^2, \tag{2.18}$$

where α is the polarizibility, which is a function of the refractive index of molecule (m) and the number density of molecules (N), i.e. $\alpha = (m-1)/2N\pi$. Therefore Equation 2.18 can be written as

$$\sigma_R(\lambda) = \frac{1}{\lambda^4}\frac{32\pi^3(m-1)^2}{3N^2}. \tag{2.19}$$

Here we can find the dependence of Rayleigh scattering on λ^{-4} so the Rayleigh scattering optical depth due to molecules tends to be strong at shorter wavelengths.

Mie Theory

Mie theory describes the extinction optical depth by scattering and absorption of spherical particles. Given scattering particles that are spherical and have a comparable size with the wavelength, Mie theory can explain an absorption and a scattering event in an atmosphere. For larger particle sizes, the phase function in Mie theory tends to follow geometric optics and to be strongly forward scattering due to diffraction. For smaller particle size, on the

other hand, Mie theory tends towards the Rayleigh regime. Using Mie theory, the phase function (p), the single scattering albedo for particle (ω), and the extinction cross section (σ_{ext}) can be calculated with the complex particle refractive index and size parameter, $x = 2\pi r/\lambda$, where r is the radius of particle. There are different analytical forms of phase functions depending on the scattering particle characteristics. In this study, we assumed a single particle size to define a phase function for Mie calculation. The single scattering albedo (ω) is defined as $\omega = scattering\ cross\ section$ (σ_{scat}) / $extinction\ cross\ section$ (σ_{ext}). The extinction cross section is the sum of cross sections by scattering (σ_{scat}) and absorption (σ_{abs}). From Goody and Yung (1989), σ_{abs} can be

$$\sigma_{ext} = \frac{2\pi r^2}{x^2} \sum_{n=1}^{\infty} (2n+1)\left(a_n + b_n\right), \tag{2.20}$$

$$\sigma_{scat} = \frac{2\pi r^2}{x^2} \sum_{n=1}^{\infty} (2n+1)\left(|a_n|^2 + |b_n|^2\right), \tag{2.21}$$

$$\sigma_{abs} = \sigma_{ext} - \sigma_{scat} \tag{2.22}$$

where a_n and b_n are the coefficients for electric and magnetic multipole radiation that are related with the Riccati–Bessel functions and the spherical Bessel functions. Assuming the single scattering atmosphere, we only need to consider the extinction effect by the molecules and condensates in non-scattering radiative transfer calculations. Without a sufficient understanding of these complicated parameters, it is difficult to define multiple scattering atmospheres and non-spherical particles so more detailed scattering models will be contained in future studies.

2.1.6 Summary

In summary, we discussed the physics of radiative transfer in the forward models for transmission and emission spectrum. The atmosphere of a transiting planet is characterised by two different spectra, i.e. a transmission spectrum from the terminators and an emission spectrum from the dayside. Using primary transit spectroscopy, we measure the filtered stellar spectrum through the transparent limb paths of planet, with which we can

obtain information on the abundances of different gases and haze/cloud properties. From secondary transit spectroscopy, we measure the disk-averaged emission spectrum of the planet's dayside, which provides evidence for vertical thermal structure and composition. Therefore we will discuss two different aspects of atmospheres of two hot Jupiters and characterise the best atmospheric states in Chapter 4, 5 and 6. In the following section, a retrieval technique based on an optimal estimation theory method will be introduced.

2.2 NEMESIS – Non-linear Optimisation Retrieval Algorithm

The NEMESIS code has been initially developed for the retrieval of the atmosphere of Saturn and its biggest moon, Titan, measured from the CIRS instrument in the Cassini spacecraft. The algorithm has been being successfully contributed to understanding of the chemistry (e.g. phosphine) and dynamics by constraining the latitudinal and vertical structure of the thermal structure and molecular features of planet. After the triumph with the Cassini mission, the NEMESIS has been implemented to many other applications (i.e. different planets and different geometries) and now becomes one of leading retrieval code for the solar system planets of Mars, Venus, Jupiter, Uranus and Neptune.

The NEMESIS algorithm uses two novel tools for an efficient retrieval of the atmospheric properties: a non-linear optimal estimation scheme and a fast forward model taking advantage of the correlated-k approximation and k-distribution look-up tables. NEMESIS solves the inverse problem using a method based on a Bayesian and maximum-likelihood approach incorporating $a\ priori$ information (Rodgers, 2000). NEMESIS solves numerically non-linear inverse problem based on a Newtonian method, which might be slow for some cases. Therefore, the optimal state in the algorithm is accomplished after a moderate number of iterations, whose scheme is based on the Marquardt-Levenberg principle (Levenberg, 1944; Marquardt, 1963), which improves the convergence remarkably. The algorithm calculates synthetic spectra using the correlated-k method, which calculates finite resolution spectrum by ranking the individual line strengths in

terms of their intensity within a particular bin. This method has been shown to be fast, reliable, and sufficiently accurate compared to a line-by-line calculation (see Chapter 3). Moreover, the optimal estimation retrievals permit an extension of previous retrieval results by other authors and formal quantification of errors and uncertainties. In addition, the functional derivatives that are analytically-computed partial derivatives allow analysis of the vertical contribution of the constituents in each observation channel.

2.2.1 Cost Function Minimisation

In the optimal estimation algorithm, the optimisation of the state vector $\mathbf{x}$ can be achieved via Bayes' theorem. If we assume that the error shape follows Gaussian probability distribution functions (PDFs), P, then the optimal state of $\mathbf{x}$ (or $a\ posteriori$) by the Bayes' theorem is

$$P(\mathbf{x}|\mathbf{y}) = \frac{P(\mathbf{y}|\mathbf{x})\,P(\mathbf{x})}{P(\mathbf{y})}, \tag{2.23}$$

where $\mathbf{y}$ is the measurement vector, $P(\mathbf{x})$ the PDF of the prior state vector, i.e. $a\ priori$, and $P(\mathbf{x}|\mathbf{y})$ and $P(\mathbf{y}|\mathbf{x})$ mean the conditional PDF of $\mathbf{x}$ and $\mathbf{y}$ with given $\mathbf{y}$ and $\mathbf{x}$, respectively. To present the $a\ posteriori$ in practical form, we express the terms in the numerator in Equation 2.21 to be the Gaussian PDFs for a vector that can be written as

$$P(\mathbf{y}|\mathbf{x}) = \frac{1}{\sqrt{2\pi}}\mathbf{S}_{\varepsilon}^{-\mathbf{1}}\,exp\left[-\frac{1}{2}(\mathbf{y}-\mathbf{K}\mathbf{x})^{T}\mathbf{S}_{\varepsilon}^{-\mathbf{1}}(\mathbf{y}-\mathbf{K}\mathbf{x})\right] \tag{2.24}$$

$$P(\mathbf{x}) = \frac{1}{\sqrt{2\pi}}\mathbf{S}_{\mathbf{a}}^{-\mathbf{1}}\,exp\left[-\frac{1}{2}(\mathbf{x}-\mathbf{x}_{\mathbf{a}})^{T}\mathbf{S}_{\mathbf{a}}^{-\mathbf{1}}(\mathbf{x}-\mathbf{x}_{\mathbf{a}})\right] \tag{2.25}$$

where $\mathbf{x_a}$ is the $a\ priori$ state vector, $\mathbf{S_a}$ is the covariance matrix of $a\ priori$ in which the diagonal and off-diagonal elements are the errors of the $a\ priori$ and the vertical correlation, and $\mathbf{S}_{\varepsilon}$ is the measurement covariance matrix in which the diagonal elements include the sum of measurement errors, forward model errors [i.e. being caused by incorrect physics (Rodgers, 2000)], and also errors like missing or inaccurate line data to consider both effects into the output together. The term $\mathbf{Kx}$, where $\mathbf{K}$ denotes the matrix

of functional derivatives or the Jacobian, is equivalent to the calculated spectrum. Since the optimal state is achieved with its Gaussian probability distribution when $P(\mathbf{x}|\mathbf{y})$ approaches to its maximum, the negative exponential term of $P(\mathbf{y}|\mathbf{x})$ and $P(\mathbf{x})$ should be close to its minimum. Using logarithms, Equation 2.22 and 2.23 become

$$-2\,lnP(\mathbf{y}|\mathbf{x}) = (\mathbf{y}-\mathbf{Kx})^T\,\mathbf{S_\varepsilon}^{-1}(\mathbf{y}-\mathbf{Kx}) + \mathbf{c_1} \tag{2.26}$$

$$-2\,lnP(\mathbf{x}) = (\mathbf{x}-\mathbf{x_a})^T\,\mathbf{S_a}^{-1}(\mathbf{x}-\mathbf{x_a}) + \mathbf{c_2}. \tag{2.27}$$

Then the optimal state can be

$$-2\,lnP(\mathbf{x}|\mathbf{y}) = (\mathbf{y}-\mathbf{Kx})^T\,\mathbf{S_\varepsilon}^{-1}(\mathbf{y}-\mathbf{Kx}) + (\mathbf{x}-\mathbf{x_a})^T\,\mathbf{S_a}^{-1}(\mathbf{x}-\mathbf{x_a}) + \mathbf{c_3}. \tag{2.28}$$

Terms on the right hand side, except the constant that is independent of state vector $\mathbf{x}$, determine the optimal state of retrieval. Hence we have the formalism that minimises $P(\mathbf{x}|\mathbf{y})$,

$$\phi = (\mathbf{y}-\mathbf{Kx})^T\mathbf{S_\varepsilon}^{-1}(\mathbf{y}-\mathbf{Kx}) + (\mathbf{x}-\mathbf{x_a})^T\mathbf{S_a}^{-1}(\mathbf{x}-\mathbf{x_a}) \tag{2.29}$$

which is named the $cost\ function$. The first term of the function represents the minimisation of the residual between model and data, whilst the second term constrains the solution $\mathbf{x}$ to lie close to the $a\ priori$ value $\mathbf{x_a}$. The NEMESIS retrieval algorithm thus finds the optimal solutions numerically and iteratively to minimise the deviation between the measurements and the model spectrum.

There are various types of definition for $a\ priori$ in NEMESIS, which are applicable for different types of variables, e.g., vertically well mixed profile, continuously vertically varying profile, pre-defined shapes in different pressures, etc. Since our prior knowledge on the exoplanets that will be investigated in this study is not available, we only choose a scaling factor, f, as a state vector for molecular abundance x, where a well-mixed vertical profile is assumed, in order to marginalise the number of fitting variables. In particular, in order to prevent the value of any state vector from becoming negative, the prior scaling

factor is converted to the log value ($log\ f$), and the input error, ε, is considered to be a fractional error (ε/f), all which are now the relevant numbers in the measurement vectors. The log scaling factor then is utilised to multiply the reference value of exponent, $e^{logf'}$, where f' is the state vector at each retrieval stage. The $a\ priori$ is defined by a Gaussian PDF centred at the logarithm of the value of scaling factor to base e with its 1-σ error ε/f (i.e. the 1-σ range of x = [$x \times e^{(logf-\varepsilon/f)}$, $x \times e^{(logf+\varepsilon/f)}$].

2.2.2 Convergence based upon Marquardt-Levenberg Scheme

For a non-linear inverse problem, Equation 2.27 should become zero to approach to the maximum probability state. Applying the derivative of Equation 2.27 to the Newtonian iteration, the state vector and the Jacobian (now $\mathbf{x_n}$ and $\mathbf{K_n}$ replace $\mathbf{x}$ and $\mathbf{K}$ from the previous section) are iteratively updated from non-linear optimal equation (Rodgers, 2000),

$$\mathbf{x_{n+1}} = \mathbf{x_a} + \mathbf{S_x K_n^T} \left(\mathbf{K_n S_x K_n^T} + \mathbf{S}_\varepsilon\right)^{-1} (\mathbf{y} - \mathbf{y_n} - \mathbf{K_n} (\mathbf{x_a} - \mathbf{x_n})), \tag{2.30}$$

where $\mathbf{y_n}$ is the calculated spectrum at nth iteration. Here, the $a\ priori$ vector $\mathbf{x_a}$ always participates in each calculation so that the derived state vector $\mathbf{x_{n+1}}$ remains close to the $a\ priori$ state. To achieve fast convergence to the minimum $cost\ function$ in NEMESIS, $\mathbf{x_{n+1}}$ is tested before the subsequent iteration whether it needs to be modified to the trial state vector $\mathbf{x'_{n+1}}$, which yields a closer spectrum to the measured vector $\mathbf{y}$ than $\mathbf{x_{n+1}}$ does. Based on the Marquardt-Levenberg scheme (Levenberg, 1944; Marquardt, 1963), $\mathbf{x'_{n+1}}$ is defined as

$$\mathbf{x'_{n+1}} = \mathbf{x_n} + \frac{\mathbf{x_{n+1}} - \mathbf{x_n}}{\mathbf{1} + \lambda}, \tag{2.31}$$

where λ is an adjustable parameter for each iteration, which determines convergence speed and pattern of retrieval. If the new trial state vector $\mathbf{x'_{n+1}}$, which is calculated from $\mathbf{x_n}$ and $\mathbf{x_{n+1}}$ returns a reduced $cost\ function$ than the one with $\mathbf{x_{n+1}}$ then state vector $\mathbf{x_{n+1}}$ is updated to be $\mathbf{x'_{n+1}}$. Otherwise, the calculated spectrum with the new state

vector $\mathbf{x'_{n+1}}$ and new λ which is increased or decreased is compared with previous iteration. If the reduction in the $cost\ function$ is less than the pre-defined reduction rate limit, then the iterations cease. The state vector $\mathbf{x_{n+1}}$ becomes $\mathbf{x'_{n+1}}$ when λ approaches to zero, which means that the optimal estimation state is now achieved. The optimal state in the NEMESIS algorithm is typically accomplished after a moderate number of iterations (approximately 10–20).

For the cases where the expected solution is not very well known, there is not enough information to be used as $a\ priori$, and there may exist only the predicted model profile from theoretical studies. In addition, if the given measurements are insufficient for strong constraints and have large errors, $a\ priori$ errors should be carefully determined in order to prevent the retrieval from becoming ill-conditioned or over-constrained. Therefore $a\ priori$s in this context are used to provide a smoothing constraint, keeping the solutions physically realistic whilst not over-constraining them. Also, smoothed profiles with reasonable errors can be achieved by making a balance between $a\ priori$ error and the measurement covariance error $\mathbf{S}_\varepsilon$. As described in Irwin et al. (2008), this balance can be found via test retrievals with various constraint degrees and choosing the best constraint between the results, which is weighted equally by the $a\ priori$ and the measurement. In the cases with exoplanets, however, we may have no reliable prior information, so our task is to find which atmospheric parameters can be determined without excessive bias to our $a\ priori$ assumptions.

In Chapter 3, we will now investigate the spectral modelling method in our forward model, along with comparisons between the spectra calculated by line-by-line and correlated-k methods. The line databases for molecules and atoms will also be introduced.

Chapter 3

Spectral Modelling

The computation of a planet's emergent spectrum by line-by-line and correlated-k techniques will be described in this chapter. We will compare calculated spectra from both methods in terms of accuracy and speed. In addition, demonstrating the molecular and element line lists applied for hot Jupiter atmospheres, we will discuss how important a selection of proper line lists is for a high temperature application. Finally, the error sources inherent in spectral calculation will be presented at the end of this chapter.

3.1 Line-by-Line Model

The optical depth τ_ν between z_0 and z_1 in Equation 2.1 is written as

$$\tau_\nu\left(z_0, z_1\right) = \int_{z_0}^{z_1} k_\nu \rho_a dz, \tag{3.1}$$

where k_ν and ρ_a are the monochromatic absorption coefficient [m^2 molecule^{-1}] and the absorber mean number density [m^{-3}]. The line strength and shape determine k_ν, which is essential in calculating the opacity of a path of atmosphere. The total sum of k_ν over frequency, is equal to the line strength,

$$S = \int_0^\infty k_\nu \, d\nu, \tag{3.2}$$

namely $k_\nu = S\, g_\nu$, where g_ν describes the shape of the single spectral line. Therefore, it is essential that both the line strength and line shape fitting in high temperature applications should be taken into account in advance of integrating the transmission and emission spectra of the atmospheres of transiting hot Jupiters.

3.1.1 Spectral Line Strength

Spectral line lists for molecules and elements must be selected with careful consideration of the temperature range being observed. In many cases, this means that we must employ line data at much higher temperatures than typically applicable to planetary atmospheres in our own solar system. Also, the cut-off level for the lowest intensity spectral lines primarily decides the completeness of a line list. Therefore, the line strength is a key factor determining if a given line list is suitable for the study with a required temperature range. Fundamentally, a spectral line is induced by a transition between lower and upper energy states (E_L and E_U in cm^{-1}) and each state is defined by upper($'$) and lower($''$) states of vibrational and rotational quantum numbers, which means that a line strength becomes a function of factors describing each energy state. The spectral line strength in cm species^{-1} is defined as (Sharp and Burrows, 2007)

$$S = \frac{\pi e^2 g_L f_{LU}}{m_e c^2} \frac{e^{-hcE_U/kT}}{Q\left(T\right)} \left[1 - e^{-hc(E_U - E_L)/kT}\right], \tag{3.3}$$

where g_L, f_{LU} and $Q\left(T\right)$ are the statistical weight of a given energy level, the oscillator strength of a transition to upper level and the partition function, which is the sum of all the microstates of the system. Also, the parameters, e, m_e, h, k and c are the electron charge, the electron mass, the Planck constant, the Boltzmann constant and the speed of light, respectively.

HITRAN (Rothman et al., 2009) and GEISA (Jacquinet-Husson et al., 2008) are commonly used molecular line lists for radiative transfer calculations and these compilations hold vast line lists for molecules. For the HITRAN databases, the line strength is standardised at a reference temperature of 296 K (T_0). Given the temperature range covered

by the atmosphere in question, S at a certain temperature T can be calculated as

$$S\left(T\right)=S\left(T_0\right)\left[\frac{Q\left(T_0\right)}{Q\left(T\right)}\right]e^{-hcE_L/k\left(\frac{1}{T}-\frac{1}{T_0}\right)}\frac{1-e^{-hc\nu/kT}}{1-e^{-hc\nu/kT_0}}, \tag{3.4}$$

where ν is wavenumber in cm^{-1}. Therefore, we can calculate the line strength at any temperature given appropriate expressions for a lower energy state E_L and a partition function at a temperature T. The partition functions can be gathered from different sources and will be detailed in Section 3.5.

3.1.2 Spectral Line Shape

Given atmospheric conditions, the line shape g_ν is dominated by physical processes between gases, which cause the line broadening centred at a particular frequency, ν. Depending on the dominant process, the broadening equation follows either the Lorentzian profile, arising due to the gas collisional effect under high pressure, or the Doppler profile, arising due to the velocity distribution of gases with warm thermal conditions. Since this study will involve atmospheres over a broad range of pressures and temperatures, the appropriate expression for the line broadening shape would be a combination of these two shapes, i.e. the Voigt line shape (Goody and Yung, 1989),

$$\begin{aligned} g_\nu &= \frac{y}{\gamma_D\pi^{3/2}}\int_{-\infty}^{\infty}\frac{e^{-t^2}}{(x-t)^2+y^2},dt \\ y &= \frac{\alpha_L}{\alpha_D},\ \ x=\frac{\nu-\nu_0}{\alpha_D}\ \ and\ \ \gamma_D=\frac{\alpha_L^2}{\alpha_D}, \end{aligned} \tag{3.5}$$

where α_L and α_D are the Lorentzian and Doppler broadening widths. The Voigt profile provides a good approximation of the broadening effect for molecules. Alkali metals, on the other hand, require theoretical treatments of broad line wings for a different solution of line shape. Nevertheless, as no unique solution is yet available, the Voigt profile is adopted to explain the broad line wings of alkali metals. As suggested in Lodders (1999), the Lorentzian shape is assumed to be an adequate line shape for low abundance alkali metals, where the Voigt shape is mostly equivalent to the Lorentzian due to negligible

broadening by Doppler shifts.

3.1.3 Radiative Transfer for High Temperature Applications

According to Equation 3.4, because the line strength S increases dynamically with temperature, lines having a weak strength at low temperature make a notable contribution to the total opacity at high temperature ($>$1000 K). Therefore, in order to add the opacity due to the weak lines we must ensure that the line database being used at high temperature includes a number of transitions between high energy states, for which the exponential term in Equation 3.4 is kept small, consequently, leading to a weak line strength. Although the databases such as HITRAN and GEISA are sufficient for integrating spectral lines for terrestrial atmospheres, they favour low temperatures where weak line strengths are still not substantial, meaning that lines in these databases are insufficient for application to hot Jupiter atmospheres. As a result, the line databases needed for high temperature conditions must contain many weak lines unavailable in commonly used line lists. However, a line-by-line radiative transfer calculation with such a database containing an enormous number of transitions requires extreme computational resources and, therefore, line-by-line techniques are inappropriate and inefficient for a iterative forward model calculation during the retrieval process.

If we require only the averaged spectral intensity in given wavelength bins (at a particular resolution), then the position and strength of every line in each bin does not need to be considered during the calculation of the transmission. Thus a pre-calculated absorption coefficient, k, for each bin can be used instead. This fact allows a reduction in the computational resource demanded for the iterative radiative transfer calculation even with low model error, and the size of the error is much smaller than the one inherent in the current measurements. In this sense, approaches such as band models and correlated-k models can be alternatives to the line-by-line models and allow us to deal with countless lines at high temperatures over a wide wavelength range. Band models take advantage of the mean absorption coefficient by simply adding up all the line strengths in the interval. Due to its fast integration, band models are suitable for computations which need only

low resolution and low accuracy, taking advantage of the Curtis-Godson approximation (Curtis, 1952; Godson, 1955), which allows the transmissions in inhomogeneous paths. Band models, however, cannot include scattering calculations due to the limitation of the Curtis-Godson approximation, which cannot be used to calculate scattering in an inhomogeneous atmospheric path. Hence, we adopt correlated-k models to benefit from speed, accuracy and calculations in the scattering atmospheres.

3.2 Correlated-k Model

Correlated-k models (Goody and Yung, 1989) have a high computational speed comparable to the band model, and have been shown to be reliable, fast and sufficiently accurate for finite resolution spectral calculations (Lacis and Oinas, 1991). Unlike band models, these models calculate transmissions for single and multiple scattering atmospheres in the inhomogeneous path. Although the spectral correlation between high and low absorption in the band can be also found in the k-distributions, by splitting the inhomogeneous path into a number of subpaths, correlated-k models integrate the mean transmission from the multiplication of k-distribution in each subpath, which is called the correlated-k approximation. This is conceptually similar to monochromatic calculations for the transmission of the inhomogeneous path.

The correlated-k models use spectral frequency space re-distributed into a fraction of the frequency domain containing absorption coefficients between k and k+dk. It is sufficient to know what proportion of a particular bin contains lines of a particular intensity, without needing to know how they are distributed with wavelength within the bin, therefore avoiding the need for repetitive line-by-line calculations. As a result, the line-by-line calculation is required only once to tabulate k-distributions.

The mean transmission of the absorber amount m, $\bar{T}(m)$, over the interval $\Delta\nu$ from ν_0, is expressed as

$$\bar{T}(m) = \frac{1}{\Delta\nu} \int_{\nu_0}^{\nu_0+\Delta\nu} \exp\left(-k_\nu m\right)\, d\nu. \tag{3.6}$$

Using a fraction of the frequency space, $f\,(k)\,dk$, Equation 3.6 is now re-written as

$$\bar{T}\,(m) = \int_0^{\infty} f\,(k) \exp\,(-km)\;\, dk, \;\; where \;\; f\,(k) = \frac{1}{\Delta\nu} \sum \left| \frac{d\nu}{dk} \right|. \tag{3.7}$$

Here a cumulative function of the fraction of the frequency interval, $g\,(k)$, is defined as,

$$g\,(k) = \int_0^{k} f\,(k')\;\, dk'. \tag{3.8}$$

A cumulative function $g\,(k)$ has an inverse function $k\,(g)$ called a k-distribution function, and $g\,(k)$ approaches unity when k goes to infinity. Therefore, $\bar{T}\,(m)$ in Equation 3.7 becomes a function of g:

$$\bar{T}\,(m) = \int_0^{1} exp\,(-k\,(g)\,m)\;\, dg. \tag{3.9}$$

From the above equation, it is known that a well-defined $k\,(g)$ with sufficient intervals of g can be used to precisely calculate the mean transmission. With discrete quadrature points, N, Equation 3.9 is written as

$$\bar{T}\,(m) = \sum_{i=1}^{N} exp\,(-k_i m)\;\, \Delta g_i \tag{3.10}$$

where k_i and Δg_i are the k-coefficients and quadrature weights at each quadrature point. The number of quadrature points N determines the performance of the approximation form, and N=20 is applied in this study based on experience with solar system radiative transfer studies. Assuming that gas absorptions are uncorrelated with each other in a given wavelength range, the mean transmission of a mixed gas atmosphere in Equation 3.10 is then the sum of k-distributions from each gas. Therefore, k-distributions for individual gases are calculated from line databases over a range of temperatures and pressures expected in the exoplanet atmospheres and tabulated in advance of the retrieval so that a fast forward model calculation is possible during each iteration of the model. In this study, a grid of 18 temperatures between 400–2950 K and 12 pressures between 1.388×10^{-11}

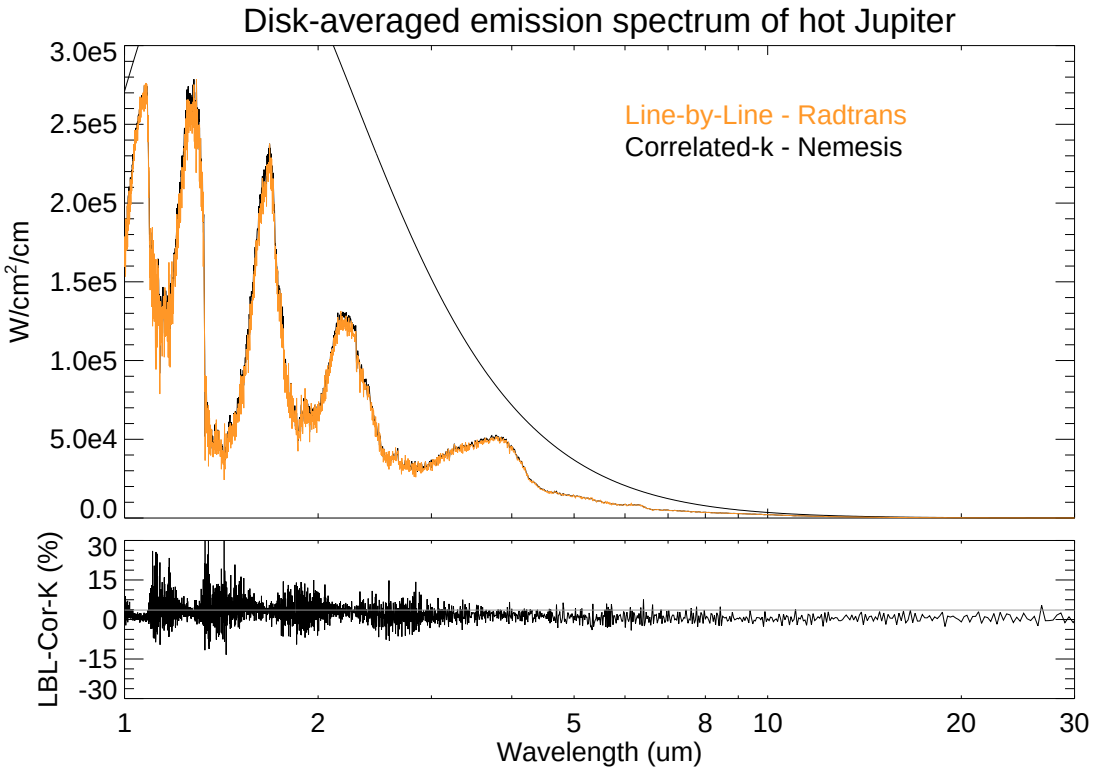

Figure 3.1: Spectral irradiance of the disk-averaged emission spectrum of a hot Jupiter. The spectra are calculated based on the vertical structure of the $P-T$ profile and molecular abundances for H_2O, CO_2, CO and CH_4, which come from Tinetti et al. (2007a). The blackbody radiation for a temperature of 1990 K is overplotted in grey colour. The averaged spectral difference between line-by-line and correlated-k methods is 4.8 % (grey line) as seen in the bottom panel.

(e^{-25}) and 20.085 (e^3) bar are chosen in order that the large range of temperatures and pressures in known exoplanets are fully covered. In Figure 3.1, the disk-averaged emission spectra for a model hot Jupiter that are computed using line-by-line and correlated-k approaches show a good agreement for overall wavelength range, giving a reliability to the utilisation of correlated-k method for transit spectroscopy. Small differences between two spectra come from the inherent uncertainty of a correlated-k model that can be improved by applying a larger g-ordinate number.

3.3 Treatment of Spectral Line

The parameters used for spectral line treatment must be carefully determined before the k-coefficient calculation. These parameters define how to calculate the absorption (or transmission) at output wavelengths having separation **DELV**. To include the contribution of wings of lines centred outside the spectral range of interest, the total wavelength range considered is defined as a range between $\mathbf{V}_{MIN}$ (minimum output wavelength)–$\mathbf{V}_{REL}$ and $\mathbf{V}_{MAX}$ (maximum output wavelngth)+$\mathbf{V}_{REL}$, where $\mathbf{V}_{REL}$ defines an extra interval, in which line wing contributions extend into $\mathbf{V}_{MIN}$–$\mathbf{V}_{MAX}$. The total spectral interval is then sub-divided into **WING**-sized wavelength bins, where line data is stored. Absorption at a particular output wavelength is then calculated by considering lines stored in the adjacent bins and the bin in the middle. Wing contributions from the lines centred outside these bins are calculated at the middle and bin ends using a quadratic polynomials (because the wing shape follows the Lorentzian), and added on the absorption at an output wavelength. For each line calculation, a line wing outside a **CUTOFF** length, which defines the distance from the centre of a spectral line to the edge of line, is ignored. After monochromatic calculations, absorption is integrated and convolved over width **FWHM** (i.e. resolution) centred on an output wavelength. Figure 3.2 demonstrates the parameters used for the definition of spectral line handling.

Here we select 5 cm^{-1} and 5 nm for output wavenumber and wavelength interval (**DELV**), 1.5 cm^{-1} for bin width (**WING**), 10 cm^{-1} for resolution (**FWHM**), 25 cm^{-1} for extra intervals ($\mathbf{V}_{REL}$), and 25 cm^{-1} for line wing cut-off (**CUTOFF**), respectively. For the alkali lines, particularly, $\mathbf{V}_{REL}$ and **CUTOFF** are chosen to be 6000 cm^{-1} so that the opacity due to their broad line wings are sufficiently integrated in the synthetic spectrum. In the next section, the k-distribution tables calculated for the molecules and elements will be demonstrated and compared with line-by-line calculations.

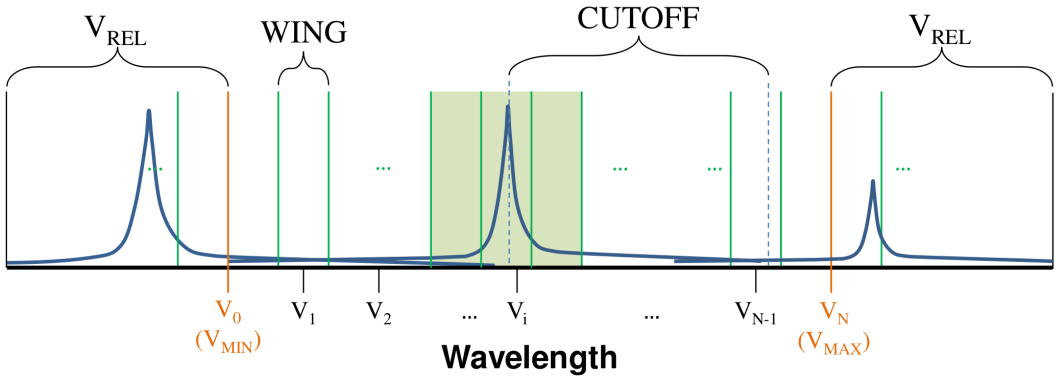

Figure 3.2: The parameters used for spectral line treatment define how to calculate the absorption at a certain wavelength, V_i, from overlapped lines in a given wavelength range from V_{MIN} to V_{MAX}. Given $\mathbf{V}_{REL}$, defining extra intervals to include the wing contribution of lines centred outside the spectral range of interest, the lines contained in between V_{MIN}–V_{REL} and V_{MAX}+V_{REL} are calculated. The total spectral interval is divided into N bins with **WING** width, in which line data is stored. For absorption at an output wavelength V_i, the lines stored the adjacent bins and the bin in the middle (shaded in green) are only considered and the wing contribution from the lines outside these bins are added on. A line wing outside a **CUTOFF** length from the line centre is not included. Spectral resolution is determined from width **FWHM**, with which absorption at an output wavelength is integrated.

3.4 Line Lists for k-distribution

As mentioned in Section 3.1.3, the line databases that are used for terrestrial atmospheres are limited to show enough opacity information in the absence of weak lines. Hence valid molecular line databases suitable for high temperature applications are required for the retrievals in this study, which are listed in Appendix A. Because some of the lists in Appendix A are not conveniently tabulated as the existing compilations are, line strengths and broadening widths should be calculated either by theoretical models or experiments. Given parameters for lines, we chose to convert all the line lists into a HITRAN format for ease of use, and detailed work for each line list will be discussed first and then the method used to derive partition functions for each species will be presented in the following sections.

3.4.1 Water

H_2O, which shows strong absorptions throughout exoplanet spectra, is one of the most important gases in the atmospheres of exoplanets. It has been predicted that H_2O opacity is the most dominant feature in atmospheres of close-in exoplanets (Liang et al., 2003, 2004; Line et al., 2010; Seager and Sasselov, 2000). The latest edition of HITRAN (Rothman et al., 2009) considers transitions between rotational quanta less than J''=32, excluding line strengths weaker than 10^{-32} cm molecule^{-1}. Less than 70,000 lines are available in total, hence radiative transfer with this HITRAN version may be suitable only for low temperatures (less than a few hundred K). One of the most complete lists for H_2O, a line list by Barber et al. (2006) (hereafter BT2) that is a calculated line list based on a quantum mechanical approach rather than a measured one, is selected in this study. This line list covers wavelengths between 0 cm^{-1} and 30000 cm^{-1} and includes most of the transitions between roto-vibrational quantum numbers ($J'' \leq 50$) so line contributions from $J'' > 50$ are missed, only $\sim$0.02 % even at 4,000 K. The list uses 221,097 energy levels, containing over half a billion transitions, a size 7,000 times greater than the latest HITRAN version.

In general, lots of weak lines in BT2 certainly show no contribution at room temperature because the line strength cut-off in BT2 goes down to $\sim 10^{-100}$. Their features, however, become noticeable at a temperature larger than 1000 K (Figure 3.3). The BT2 list has been recently chosen for the latest HITRAN compilation for high temperature calculation (HITEMP) (Rothman et al., 2010) and tabulated in the typical format of HITRAN. Using air broadening widths available for low $J'' < 20$ from measurements (Gamache and Hartmann, 2004) and theoretical calculations (Gamache and Laraia, 2009), Rothman et al. (2010) estimated the air broadening widths for high J'' by extrapolating with third-order polynomials. Current existing widths data for H_2O, however, were acquired under the assumption that the broadening is dominantly driven by the Earth atmosphere composition of nitrogen and oxygen. This could be a potential error source during retrieval for a hydrogen and helium atmosphere but we will leave this issue for the future studies.

In Figure 3.4, transmission spectra created by a line-by-line calculation and a correlated-k model are compared using the 43 layered hot exoplanet atmospheres, in which temper-

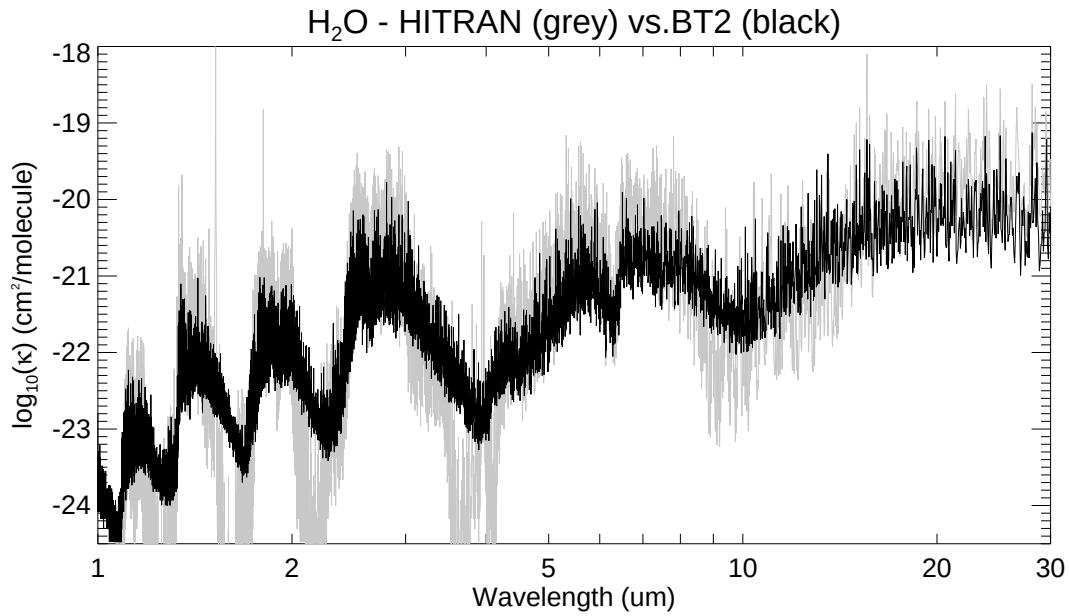

Figure 3.3: The latest HITRAN (grey) and Barber et al.(2007)[BT2] (black) version of H_2O line opacity at 1 atm and 1500 K. H_2O of HITRAN version underestimates absorption coefficients at some wavelength ranges (e.g. 4–5 μm due to lack of weak lines).

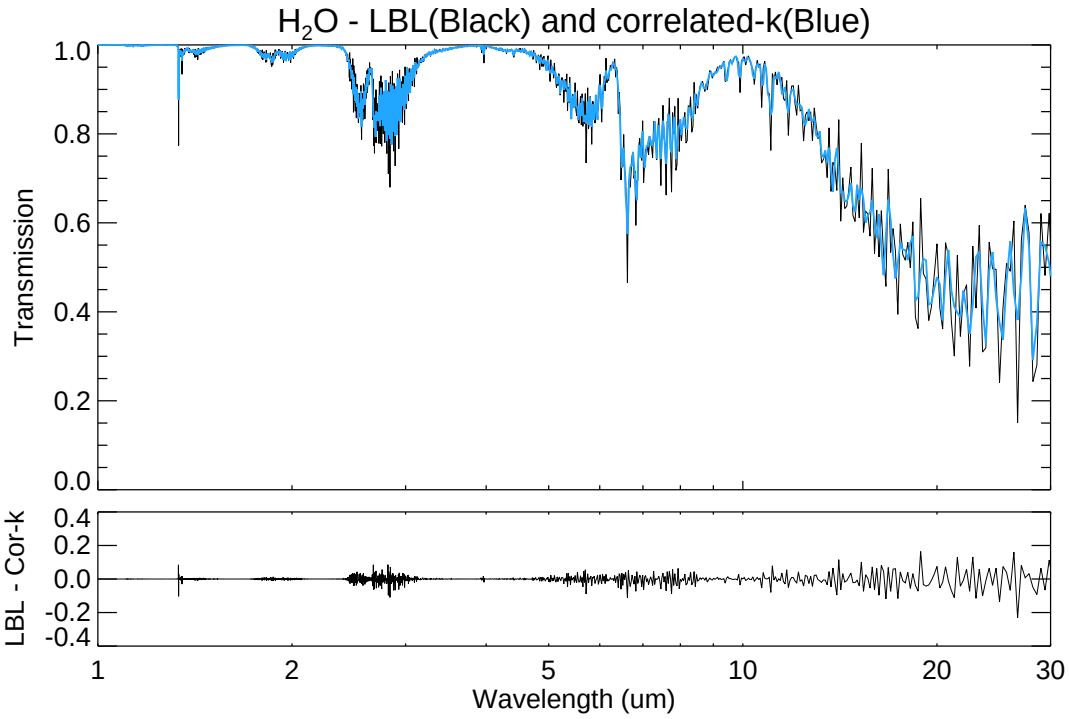

Figure 3.4: H_2O transmission spectra of 43 hot atmospheric layers calculated by line-by-line (black) and correlated-k approximation (blue). The difference between line-by-line and correlated-k methods is smaller than 5% on average.

atures are distributed from 1800 K at 10 bar to 800 K at 10^{-10} bar. The spectral difference between two approaches is small for most wavelengths except ranges where a high population of lines and a high fluctuation in transmission exist. The overall difference is less than 5% on average over 1–30 μm, which is smaller than the range of uncertainties on available exoplanet measurements.

3.4.2 Carbon Dioxide

One complete version for CO_2 available at high temperatures is the Carbon Dioxide Spectroscopic Databank (CDSD, Tashkun et al., 2003). There are several versions of CDSD that are suitable for different temperature levels: CDSD-296 and -1000. Here each number refers to a reference temperature applied to calculate line strengths and each version has different numbers of lines, implying that we can choose a version depending on the application we should consider (e.g. CDSD-296 is a good line list for a room temperature calculation). Recently, a new version of HITEMP CO_2 line list that is mostly based on CDSD-1000 version has been released[1], and the lines are broadly distributed between 0 cm^{-1} and 12,500 cm^{-1} (Rothman et al., 2010). The line list provides also air- and self-broadening data that have been calculated from a semi-empirical approach (Tashkun et al., 2003)

According to Rothman et al. (2010), the CO_2 HITEMP has been tested for high temperatures to 1950 K and they have found only a small deviation from the reference observation data. Even if the temperatures we consider for hot Jupiter atmospheres ($\leq$2500 K) are somewhat higher than the tested temperatures, we adopted the recent HITEMP CO_2 line list for this study. This is because the opacities from two line lists that are suitable for low and high temperatures are similar at wavelengths where high CO_2 absorption coefficients are dominant, and the differences in spectra are mostly shown in regions of low absorption (Figure 3.5). In other words, additional weak lines in a line list more suitable for higher temperatures may only show small changes in low opacity regions. Moreover,

[1]The HITEMP version of CO_2 is identical to the CDSD-HITEMP version, which is available to download via ftp://ftp.iao.ru/pub/CDSD-HITEMP.

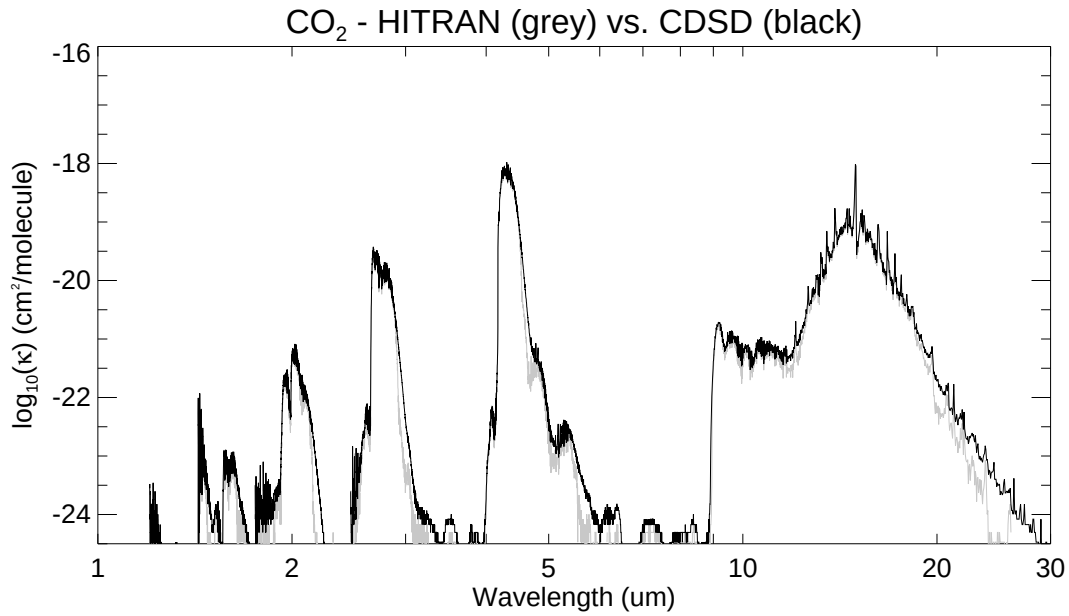

Figure 3.5: The latest HITRAN (grey) and CDSD (black) version of CO_2 line opacity at 1 atm and 1000 K. CO_2 in HITRAN underestimates absorption coefficients at some wavelength ranges (e.g. 20–30 μm) due to lack of weak lines.

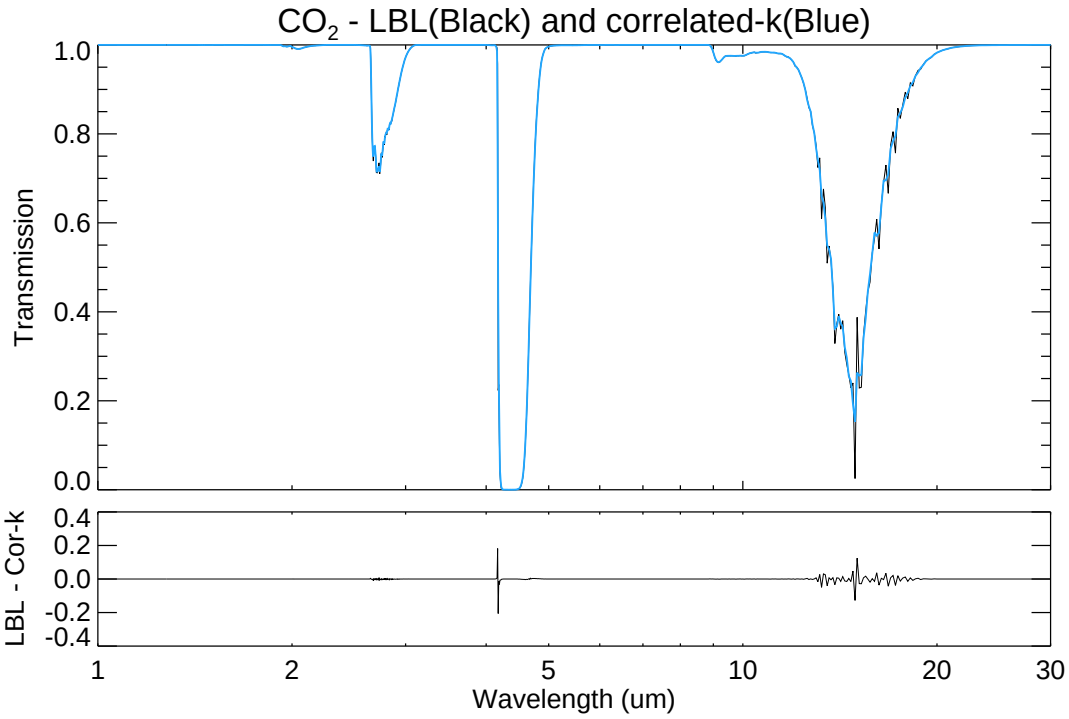

Figure 3.6: CO_2 transmission spectra of 43 hot atmospheric layers calculated by line-by-line (black) and correlated-k approximation (blue). Here, transmission spectra calculated by the line-by-line and correlated-k methods are nearly identical except the region showing spiky shapes an 4.1 μm and between 10–20 μm, where the lines are associated with the main absorption of CO_2 at 15 μm.

since the CO_2 weak absorption bands do not appear prominently in exoplanet spectra due to strong absorption bands from other molecules, we assume that the errors due to deficiency in weak lines are insignificant during retrieval. For future studies, however, we will adopt a new version of CDSD (CDSD-4000, Tashkun and Perevalov, 2011) in order to reduce any small errors might be arise from line selection.

Figure 3.6 demonstrates transmission spectra in the hot atmosphere used in the previous section, which are calculated by line-by-line and correlated-k methods. The figure shows that the difference in spectra between two methods is small (less than 5% on average) except the region where the lines are associated with the main absorption of CO_2 at 15 μm.

3.4.3 Carbon Monoxide

As the most abundant molecule next to H_2O in the atmospheres of theoretical hot Jupiters, CO plays an important role in atmospheric chemistry between carbon bearing molecules (Liang et al., 2003, 2004; Line et al., 2010). Commonly used line lists for CO are versions of HITRAN, GEISA (Jacquinet-Husson et al., 2008), and HITEMP (Rothman et al., 1995). A new HITEMP compilation also provides a CO line list (Rothman et al., 2010), of which line data originates mostly from the old HITEMP version (Rothman et al., 1995). Its wavelength range is 3 to 8465 cm^{-1} and this range is much broader than the previous version. Maintaining the parameters used for the old HITEMP version, including air- and self-broadening widths, the new HITEMP version contains additional lines available after the old version release. Figure 3.7 illustrates the absorption coefficients calculated using the old and new CO HITEMP and there is a negligible gap between two spectra. For this study, the old version of HITEMP (Rothman et al., 1995) is chosen and converted to k-coefficients.

Figure 3.8 shows a comparison of transmission spectra integrated by line-by-line and correlated-k models. The difference between two models is small ($<$5% on average) as for other molecules except several regions showing a steep change in transmission (e.g. 5.3 μm).

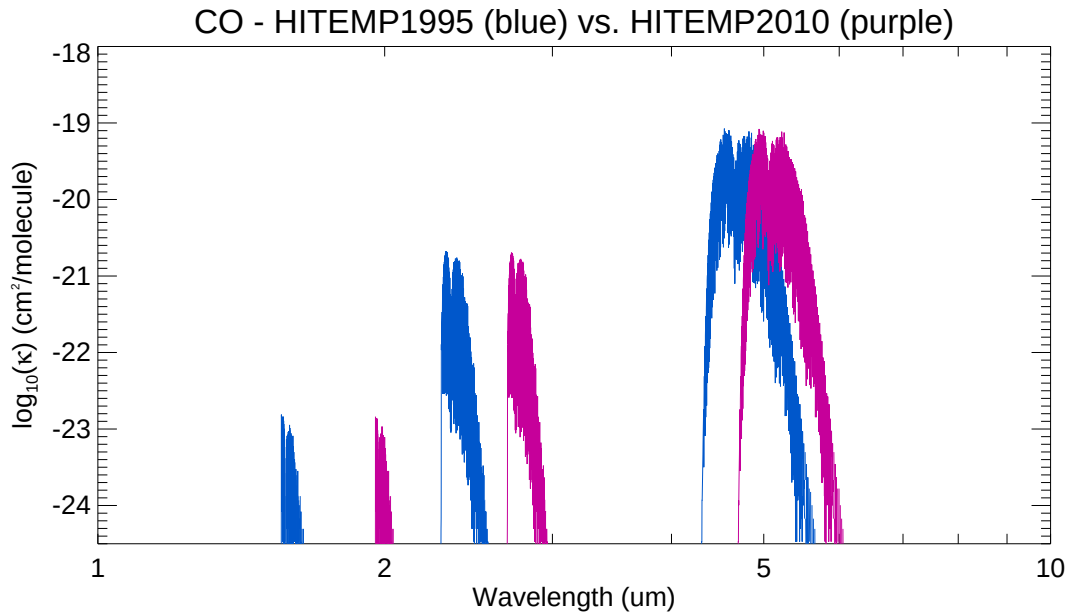

Figure 3.7: The CO opacity from the old HITEMP (1995) (blue) adopted for this study and new HITEMP (2010) (purple) at 1 atm and 1000 K. For clarity, the spectrum with new HITEMP version is shifted longward by $\log_{10}2$. Two spectra are nearly identical for all wavelengths.

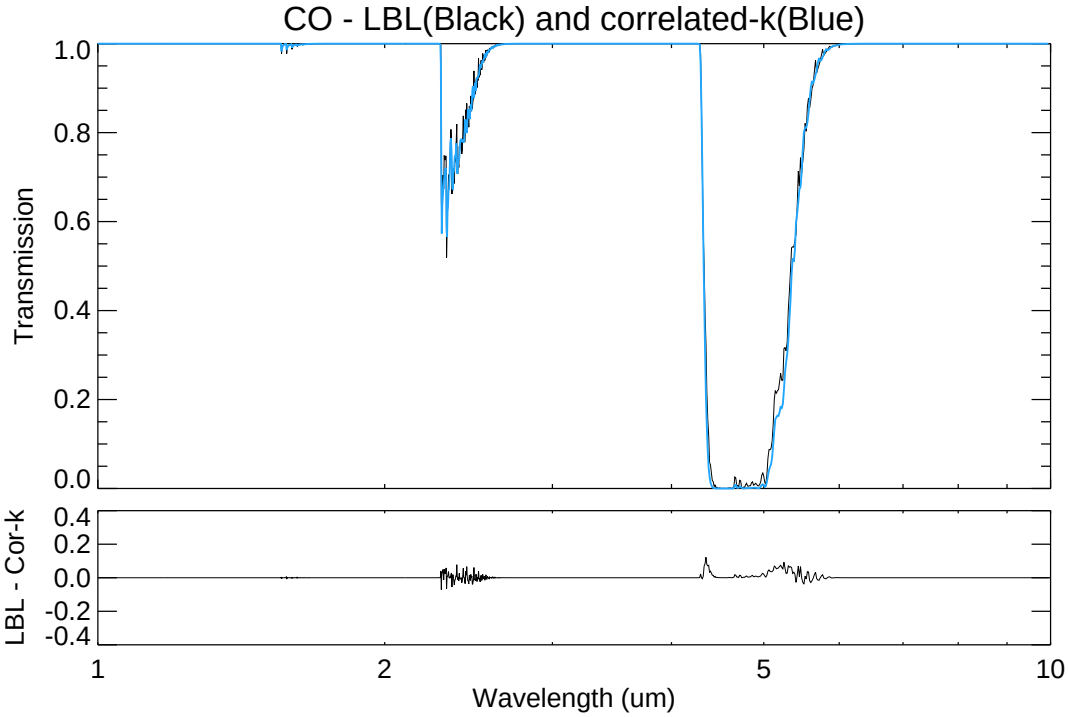

Figure 3.8: The CO transmission spectra of 43 hot atmospheric layers calculated by line-by-line (black) and correlated-k models (blue), showing that they are nearly identical except a few regions (e.g. 5.3 μm).

3.4.4 Methane

The CH_4 lines are broadly distributed and are distinct between the NIR and FIR. However, a database suitable for high temperatures ranging over the entire infrared ($>1\mu$m) is not yet available. As the most complete line list, Sharp and Burrows (2007) stitched together four databases from diverse sources (Borysow et al., 2003; Brown et al., 1997; Karkoschka, 1994; Strong et al., 1993) so as to make up a single list of CH_4, and Nassar and Bernath (2003) experimentally measured CH_4 line strengths between 2000–6400 cm^{-1} at high temperatures (800, 1000, and 1273 K). In this study, a theoretical line list by the University of Bourgogne for spherical top molecules, called Spherical Top Data System (STDS, Wenger and Champion, 1998), is selected for CH_4 due to its broad spectral coverage (0–6500 cm^{-1}) and a large number of weak lines included. The complete line list is delivered from numerous calculations provided by the website[2], and is converted into the HITRAN format. As a result, the list contains approximately 9 million CH_4 lines up to 6500 cm^{-1} ($J'' \leq 50$) and the line strength cut-off reaches less than 10^{-79} cm molecule^{-1}. The CH_4 show the weak transitions at $>$6500 cm^{-1} ($<$1.538 μm), whose lines can be obtained from a few individually tabulated line lists (e.g. Karkoschka (1994)), mostly suitable for low temperatures. However, there will be no strong requirement for these weak lines at shorter wavelengths in this study due to the fact that 1) the dayside emission spectroscopy for hot Jupiters only extends to as low as 1.476 μm and 2) a high opacity at <1 μm of the transmission spectrum of HD 189733b is likely due to extinction by condensates, and molecular absorption except H_2O is unlikely to contribute significantly. Figure 3.10 shows CH_4 opacity at 1 atm and 1000 K calculated from STDS and the latest HITRAN version. Large differences are shown across the wavelengths due to a deficiency in weak lines.

Due to the absence of broadening widths in the STDS line list, air- and self-broadening widths for CH_4 are directly extracted from the HITRAN database, in which the widths are available for transitions up to J''=31. These widths are extrapolated to estimate the widths for transitions up to J''=50 (Figure 3.9). The CH_4 transmissions in the hot atmosphere

[2]http://icb.u-bourgogne.fr/omr/SMA/SHTDS/STDS.html

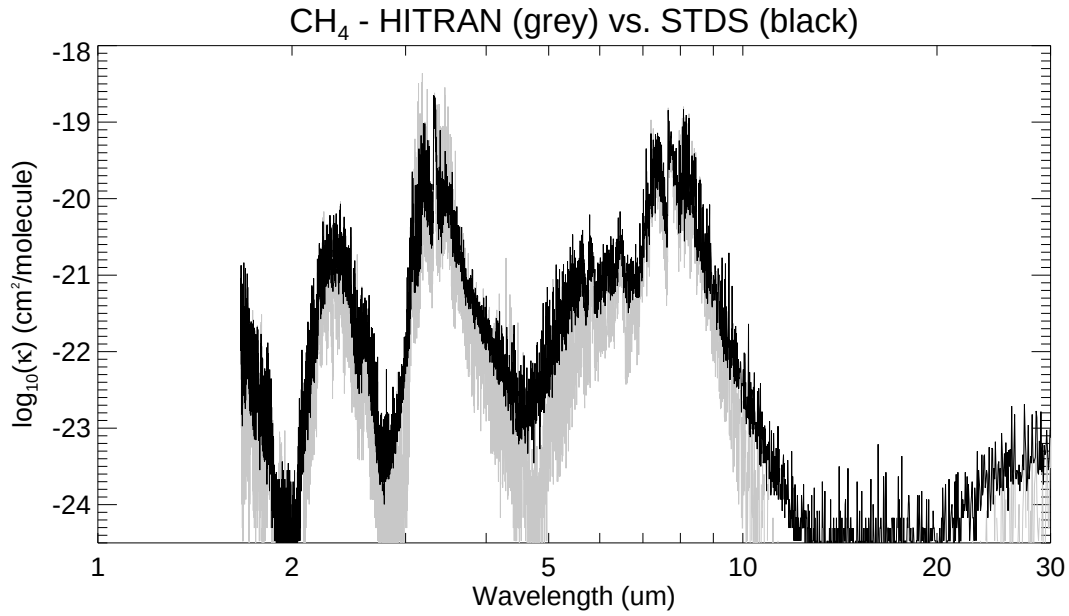

Figure 3.9: The CH_4 opacity at 1 atm and 1000 K are calculated from the STDS (black) and HITRAN (grey) database. Due to a deficiency in weak lines in HITRAN list, significant differences between spectra are clear across all wavelengths.

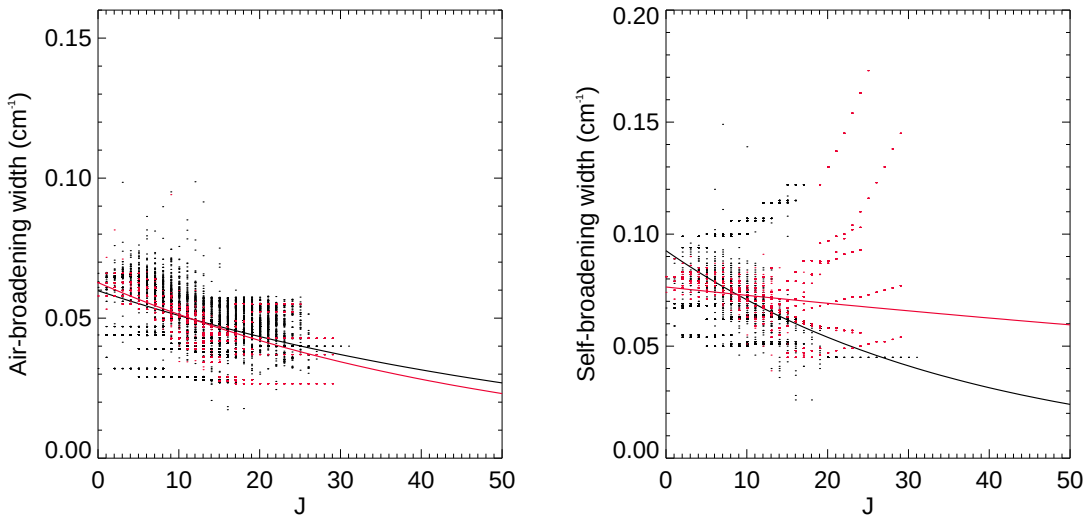

Figure 3.10: The $(left)$ air- and $(right)$ self-broadening widths of $^{12}CH_4$ (blue) and $^{13}CH_4$ (red). The extrapolated broadening widths (solid lines) are also presented separately for $^{12}CH_4$ and $^{13}CH_4$.

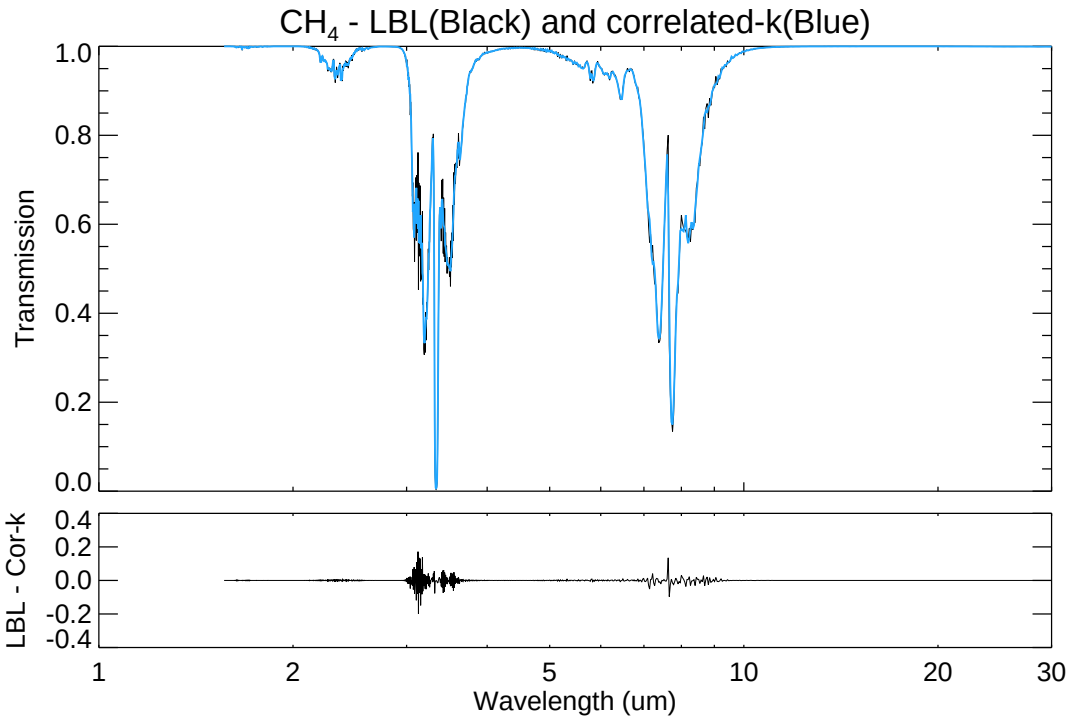

Figure 3.11: The CH_4 transmission spectra of 43 hot atmospheric layers calculated by line-by-line (black) and correlated-k methods (blue). The transmission spectra by two methods are nearly identical.

calculated by line-by-line and correlated-k methods are shown in Figure 3.11 and it is found that the difference in spectra between two methods is smaller than 5% on average. Low accuracy in k-distribution can be particularly found only in a few wavelength ranges where a high fluctuation is discovered (e.g. 3–4 μm and 7–9 μm).

3.4.5 Alkali Metals

The low ionisation energy makes the alkali metals dominant absorbers in the visible and NIR. A few alkali metal lines can obscure the features of gases such as H_2O due to their extreme broadening at the far wings, which is caused by the collisions with H_2 and He. In the case of atmospheres with hot temperatures, sodium (Na) doublet lines at 589.0 nm and 589.6 nm and potassium (K) doublet lines at 766.5 nm and 769.9 nm are considered as predominant features over the whole visible region. Unlike molecules, the alkali line properties can be taken from an element line database such as either The Opacity

Project database (TOPbase, Cunto and Mendoza, 1992; Cunto et al., 1993), NIST Atomic Spectroscopy Database (Fuhr and Wiese, 1998) or Vienna Atomic Line Database (VALD) (Kupka et al., 2000). The all databases provide a position and a strength for the required lines. Here we used VALD for this study so that we can calculate the line strength for each line in the units used in the HITRAN format (cm molecule^{-1}) with the provided properties. The air-broadening width of alkali metals by a perturber (e.g. another species such as H_2) in the atmosphere the broadening widths were arbitrarily set to 0.075 cm^{-1} atm^{-1} based on experience with terrestrial radiative transfer studies, and that these assumptions will be updated as new line broadening measurements are available.

The transmission spectra of Na and K in the hot atmosphere calculated by line-by-line and correlated-k models are presented in Figure 3.12 and Figure 3.13. The line wings of Na and K doublet at 589.0 and 589.6 nm and 766.5 and 769.9 nm are dominant and broadly extend throughout the visible wavelengths. The mean difference in spectra between line-by-line and correlated-k models is nearly identical compared to the molecular cases, which is due to the fact that only a small number of alkali lines are prominent in transmission spectra.

3.4.6 Metallic Oxides

At T $\geq$ 1000 K, metallic oxides such as TiO and VO are expected to be strong candidates for generating a thermal inversion in HD 209458b by absorbing light at visible wavelengths and heating up the stratosphere (Fortney et al., 2008). For TiO and VO, there exists no commonly available line list. Hence these have been acquired from R. S. Freedman for TiO and VO (private communication). The databases were listed in the HITRAN format and the broadening widths were reasonably guessed by the provider. The wavelength coverage for TiO ranges from 0 to 20000 cm^{-1} while the VO lines cover between 3850–25950 cm^{-1}. The partition functions for both molecules are also obtained from Sauval and Tatum (1984). Figure 3.14 and Figure 3.15 show TiO and VO transmission spectra in a single atmosphere at 1 atm and 1000 K. For both TiO and VO cases, the difference between spectra between line-by-line and correlated-k models is less than 5% on

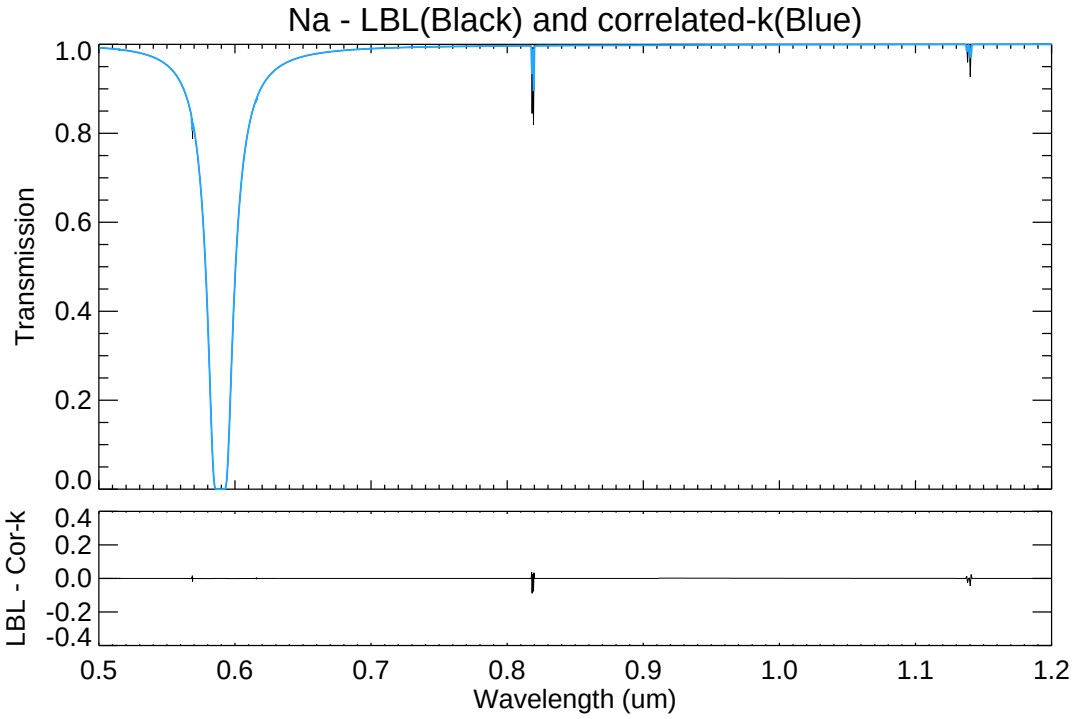

Figure 3.12: Comparison of Na transmissions in the 43-layered hot atmosphere. Broad wings of doublet lines of Na at 589.0 nm and 589.6 nm are predominant mostly in the visible. The spectrum difference between line-by-line and correlated-k models are nearly negligible.

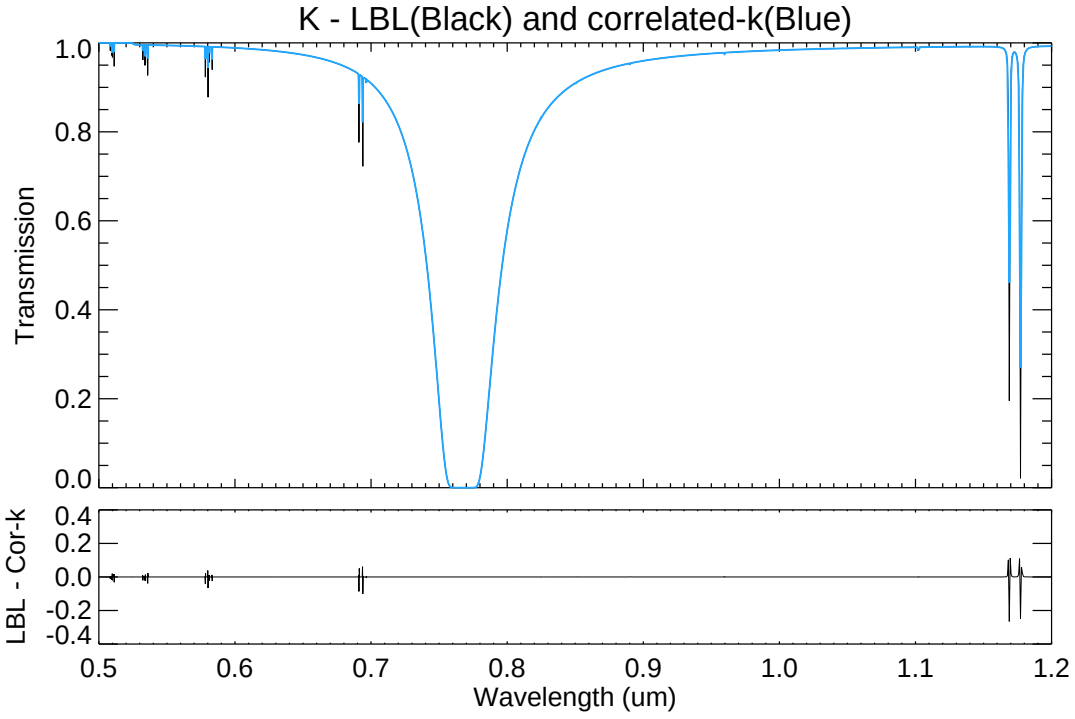

Figure 3.13: Comparison of K transmissions in the 43-layered hot atmosphere. Broad wings of doublet lines of K at 766.5 nm and 769.9 nm are predominant mostly in the visible. The spectrum difference between line-by-line and correlated-k models are nearly negligible.

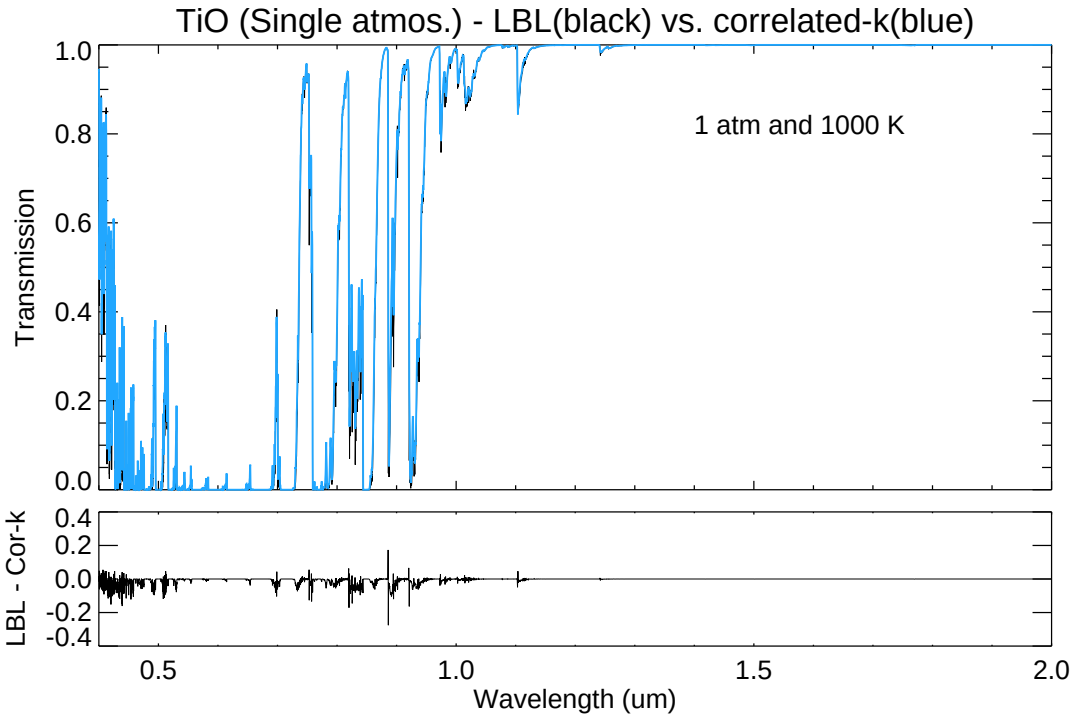

Figure 3.14: TiO single atmosphere transmission comparisons at 1 atm and 1000 K. The k-distributions show low accuracy at wavelengths where dense lines exist. The mean spectra difference is less than 5%.

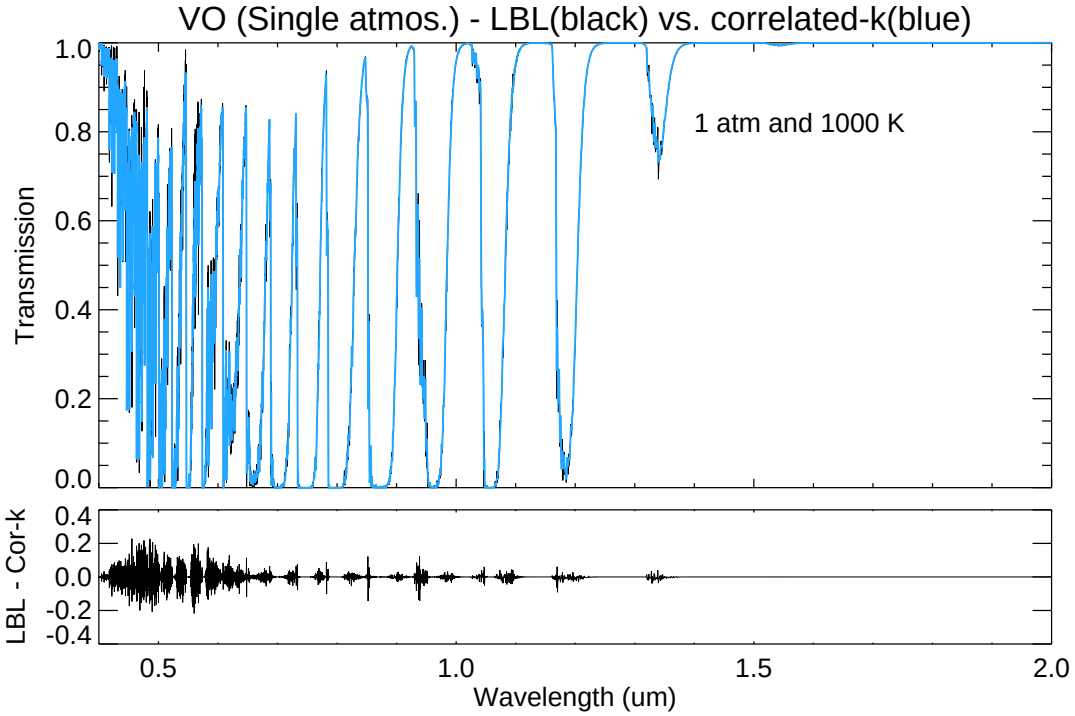

Figure 3.15: VO single atmosphere transmission comparisons at 1 atm and 1000 K. Likewise, the k-distributions show low accuracy at wavelengths where dense lines exist. The mean spectra difference is less than 5%.

average except the wavelengths where dense lines are shown.

3.5 Partition Function at High Temperature

The partition function, which describes the probability of finding the molecule or element in the quantum state with energy E_i, is temperature dependent and is fitted with polynomials rather than its original complicated equation. For molecules, we fit a 3^{rd} order polynomial to the Total Internal Partition Sums (TIPS, Laraia et al., 2011, and, references therein) and apply to every isotope included in the lists. The temperature coverage ranges from 30 to 3000 K for H_2O, CO_2 and CO. Due to fluctuations of the fitted curve, the partition function for CH_4 is split into 3 temperature ranges (400–1000 K, 1000–2000 K and $\geq$2000 K) and polynomial coefficients for each range are obtained, respectively. The partition function polynomials are written as

$$Q\left(T\right) = \sum_{i=0}^{3} a_i T^i, \tag{3.11}$$

The TIPS databases do not include partition functions for alkali metals and metallic oxides. As described in Sharp and Burrows (2007), the metallic oxides partition function therefore can be acquired from a different form of polynomials, with tabulated data by Jørgensen (1997) and the approximated equation, which is made up of electronic, vibrational, and rotational contribution term, as described in Huber and Herzberg (1979). Given molecular spectroscopic data in Huber and Herzberg (1979), polynomial coefficients for these two sets of non-HITRAN gases partition functions are derived by Sauval and Tatum (1984). The polynomial expressions provided by these authors development is slightly different from the polynomials used for molecules and can be expressed as

$$log_{10}Q\left(T\right) = \sum_{i=0}^{4} a_i l_\theta^i, \tag{3.12}$$

where l_θ is $log_{10}\left(\frac{5040}{T}\right)$. Sauval and Tatum (1984) provide the coefficients for many elements in various excited states. Here, only the first excited level of Na and K is taken

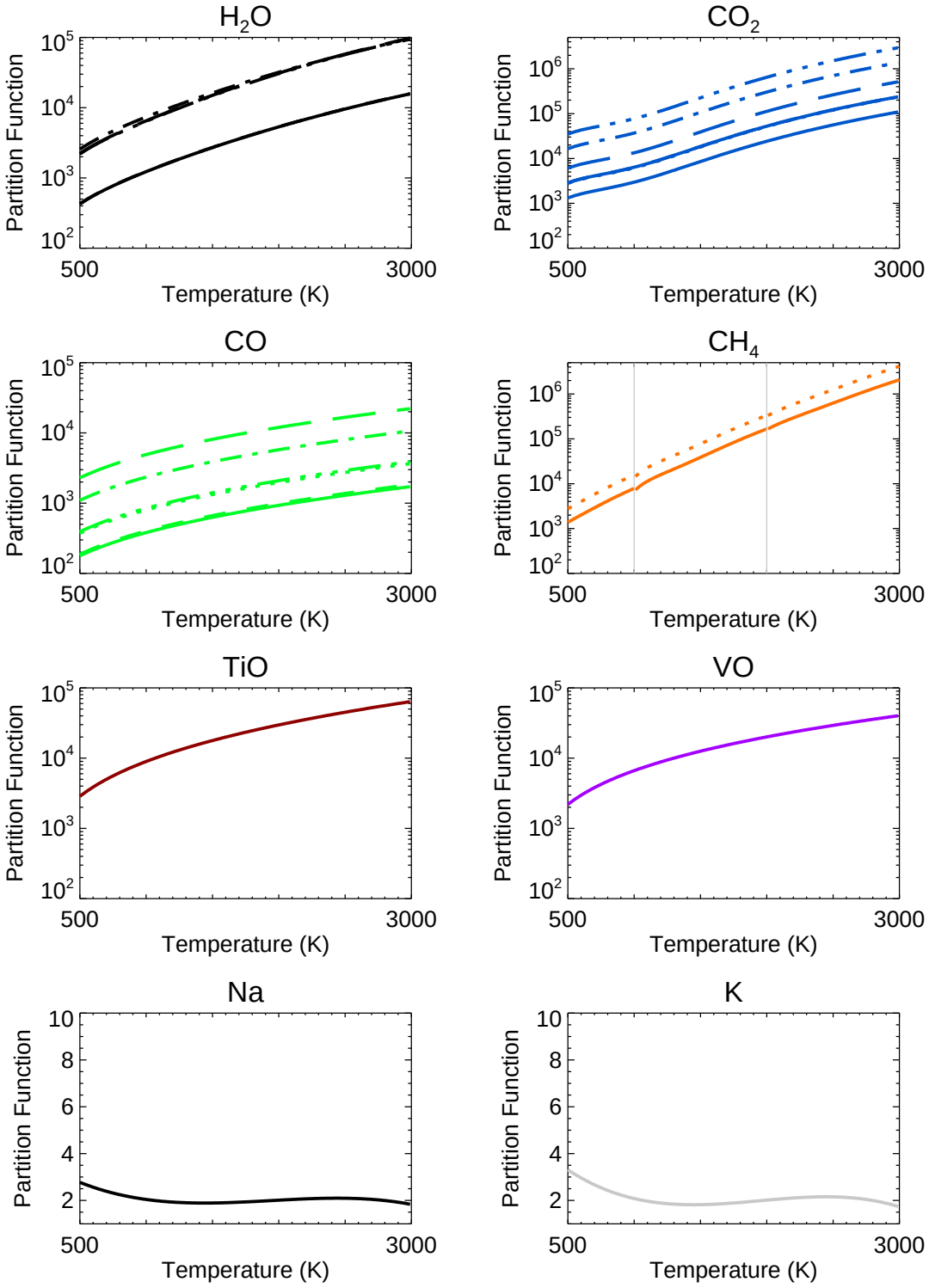

Figure 3.16: Adopted partition functions for H_2O, CO_2, CO, CH_4, TiO, VO, Na and K in this study. Each line style in same plot represents different isotopes whose lines are contained in the line list. For CH_4, the partition functions are presented in three temperature regions, which are 400 K $< T <$ 1000 K, 1000 K $< T <$ 2000 K and $T >$ 2000 K.

Table 3.1: Calculated k-distribution tables[a]

Molecule/Element	Wavelength Coverage (μm)[b]	Wavenumber Coverage (cm^{-1})[c]
H_2O	0.3–30	300–20000
CO_2	1–30	300–10000
CO	1–10	1000-10000
CH_4	1.55–30	300–6500
Na	0.4–1.4	7000–22000
K	0.4–1.4	7000-22000
TiO	0.3–30	300–30000
VO	0.4–2.5	4000–25000

[a] 400 K $\leq$ T $\leq$ 2950 K, 1.39×10^{-11} bar $\leq$ P $\leq$ 20.09 bar
[b] Resolution=0.005 μm, FWHM=0.01 μm
[c] Resolution=5 cm^{-1}, FWHM=10 cm^{-1}

into consideration. Based on Equation 3.12, the fitted quadratic partition functions for each constituent are plotted in Figure 3.16 and the polynomial coefficients are listed in Appendix B.

Given the line lists described above, the k-distribution tables for each molecule and element are calculated in both wavelength and wavenumber spaces. Table 3.1 lists the complete k-distribution for the molecules and metals described in the last sections.

3.6 Collisional Induced Absorption

Collisions between the nonpolar molecules of H_2 and He induce a temporary dipole moment so that numerous transitions arise at wavelengths >1 μm. Here pairs of H_2-H_2 and H_2-He are dominant sources of collision-induced opacity. In general, the metallicities of exoplanets are thought to be similar to their parent stars (Burrows and Sharp, 1999), and hence the atmospheres may consist of large fractions of H_2 and He gases. Therefore collision-induced absorption (CIA) certainly forms a continuum in giant exoplanets.

The database of CIA can be obtained from Borysow (2002); Borysow and Frommhold

(1990); Zheng and Borysow (1995) for H_2-H_2 and Borysow and Frommhold (1989); Borysow et al. (1989) for H_2-He. Transitions of all bands for H_2-H_2 and H_2-He including roto-transitional and roto-vibrational band are computed using the provided routines by A. Borysow[3], and are available for temperatures <5000 K. Collisions between H_2-CH_4 are not regarded here due to the small abundance of CH_4 (q[CH_4]/q[H_2] $\leq 10^{-5} \sim 10^{-6}$). For a typical hot Jupiter atmosphere, the combined CIA shows the largest absorption at 2.3 μm and decreases from 6$\sim$7 μm to longer wavelengths. The top panel of Figure 3.17 demonstrates the CIA transit depths in the reference atmosphere of the terminators in HD 189733b and the opacity peaks at 2.3 μm and propagates towards longer wavelengths up to FIR ($\sim$30 μm). The CIA opacity for both transmission and emission cases increases gradually from 1 μm and varies smoothly at the longer wavelengths of 2.3 μm.

3.7 Current Issues in Spectral Modelling

The transmission and emission spectrum of a hot Jupiter during transits are shown in Figure 3.17, demonstrating the wavelength regions where the contributions of different species, weighted by their molecular abundances, are evident. Distinct features of a spectrum (e.g. alkali doublets in transmission or CH_4 at 3–4μm in emission) may allow us to investigate its chemical characteristics in the atmosphere and, even, the atmospheric thermal structure. However, spectral features in regions of overlapping gases (e.g. CO and CO_2 at 4–5μm in transmission and emission) may produce severe degeneracies that can be only resolved by higher spectral resolution measurements and more accurate spectral modelling.

Spectral modelling for atmospheres of exoplanets evidently relies on the line lists available for hot temperatures. The absorption coefficients for the extreme atmospheric temperatures found within exoplanetary atmospheres are continuously being improved, so the retrievals are considerably limited by the quality of the available spectroscopic data, broadening widths, or partition functions for molecules and atoms. In particular, the

[3]http://www.astro.ku.dk/ aborysow/programs/index.html

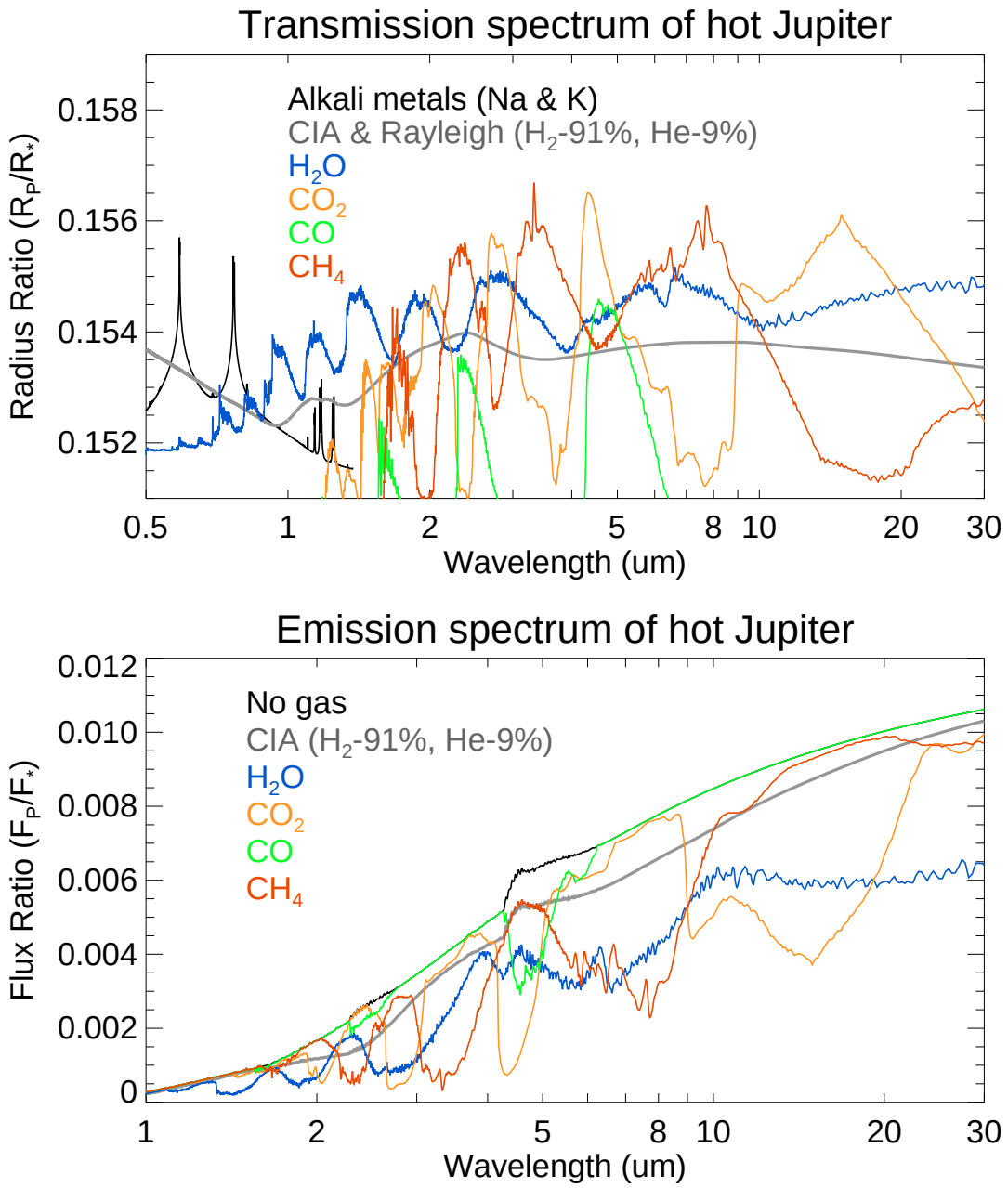

Figure 3.17: (*Top*) Transmission and (*Bottom*) disk-averaged emission spectrum of the 43 layered atmosphere of a hot Jupiter. We applied the P-T profile of HD 189733b taken from Tinetti et al. (2007a). Each spectrum in the panels, calculated with the atmosphere containing the composition of the same colour, represents explicitly the wavelength-dependant opacity of each gas. For the emission spectrum case with 'No gas' in bottom panel, we can still see a spectral feature in between 3–5 μm due to a CO absorption from the K-type stellar spectrum.

air-broadening widths, which are available at present, were measured or calculated in a terrestrial atmosphere, which possesses an utterly different composition compared to that of a hot Jupiter. Hence, we can expect that the sum of uncertainties coming from the line databases is folded into the retrieval errors, although current line databases cannot precisely quantify uncertainties on the spectroscopic parameters. Therefore, the reliability of any findings for exoplanets will ultimately be improved when new line lists become available for high temperatures. This study has made use of the best available spectroscopic parameters at the time of writing, and our line database will be updated as new sources of data become ready. In addition, the inclusion of other molecules such as NH_3, H_2S, or other carbon bearing molecules will be very important for the future development in this field.

In the next chapter, the sources of opacity described in this chapter will be combined with the retrieval architecture from Chapter 2 to determine new temperature profiles and compositions from exoplanet spectroscopic measurements.

Chapter 4

Secondary Eclipse of HD 189733b

Previous studies have suggested that although the spectra measured in various channels show evidences for the molecules in dayside atmosphere of HD 189733b, it has not been confirmed firmly by successive observations yet and that its temperature structure has either a stratosphere where temperatures decrease with height, or isothermal layer above troposphere (Seager and Deming, 2010, and references therein). According to theoretical studies (Fortney et al., 2008; Hubbard et al., 2001; Sudarsky et al., 2000, 2003), HD 189733b could be a typical pL or class IV planet, where the effective temperature is not as warm as a pM or class V planet, so a stratospheric inversion is unlikely to be present due to a lack of optical absorbers at altitudes. However, the retrieval of the temperature and compositions of the dayside hemisphere of HD 189733b is ill-posed due to an insufficient number of measurements. Therefore this study will determine the details of the thermal and chemical conditions in the dayside atmosphere of HD 189733b using all the spectroscopic data publically available, and discuss how reliably we can determine each characteristic under investigation. For comparison, we will refer to previous results constrained from the studies by a forward modelling (Madhusudhan and Seager, 2009; Swain et al., 2009b, hereafter, MS09 and S09b) and an optimal estimation retrieval (Line et al., 2012).

In the following sections, we will introduce the datasets and models used for the retrieval of the dayside atmosphere of HD 189733b.

4.1 Data

To retrieve the P-T profile and compositional abundances, three measurement sets of the secondary eclipse for HD 189733b are used, representing all of the available infrared dayside eclipse measurements at the present time, ranging over a wide wavelength range from 1.45 μm to 24 μm: 1) eighteen HST/NICMOS (Swain et al., 2009b) channels covering the range 1.45–2.5 μm; 2) forty seven $Spitzer$ IRS (Grillmair et al., 2008) channels covering the range 5–14.5 μm and one IRS photometry (Charbonneau et al., 2008) channel at 16 μm that has been re-analysed from the one by Deming et al. (2006); and 3) four $Spitzer$ IRAC (Infrared Array Camera) and one MIPS (Multiband Imaging Photometer for $Spitzer$) (Charbonneau et al., 2008) photometry channels at 3.6[1], 4.5, 5.8, 8.0, and 24 μm. The measurement errors on the three observational datasets are directly obtained from the studies referenced above. The bin width of each channel used for flux integration are 1) filter widths taken from the literature for $Spitzer$ broadband channels (Deming et al., 2006; Fazio et al., 2004; Rieke et al., 2004); 2) HST/NICMOS widths of $\sim$10 nm at 2 μm; and 3) $Spitzer$/IRS widths of $\sim$100 nm at 8 μm. The reference stellar spectrum for HD 189733 is taken from the Kurucz grid model (Kurucz, 2006) based on the stellar parameters listed in Table 4.1. Here we omitted the dataset from the IRTF in the NIR (Swain et al., 2010), which shows extremely high flux ratios at wavelengths between 2.4 and 5.2 μm. This is because as Swain et al. (2010) and Thatte et al. (2010) suggested, the IRTF measurement may be fitted with the models capable of calculating atmospheres in non-local thermodynamic equilibrium (NLTE) conditions, which we do not presently handle in our model. Furthermore, the accuracy of ground-based observations in this region of telluric water and methane absorption have yet to be fully verified. Figure 4.1 demonstrates the datasets used for this study.

Despite the substantial efforts towards finding and reducing the errors from the data, uncertainties on the given datasets still remain and are widely distributed over the wavelengths due to various error sources. First of all, techniques to decorrelate a transit light

[1]Recently, Knutson et al. (2012) re-analysed this point and found substantially degraded flux ratio, which may change the retrieval results significantly. This will be discussed in Chapter 7 again.

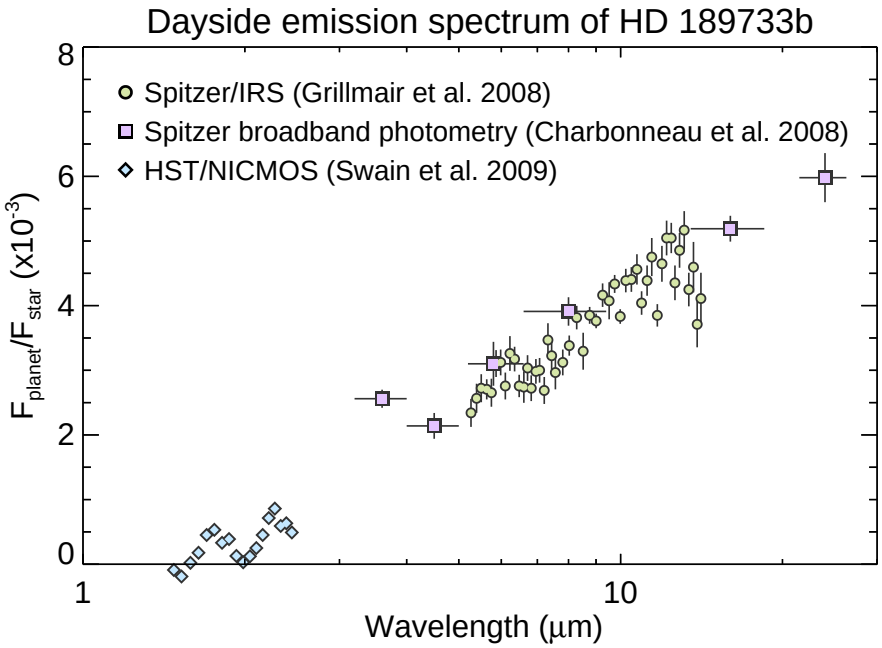

Figure 4.1: Datasets used for the retrieval of the dayside of HD 189733b, measured in the HST/NICMOS spectrophotometry (cyan diamond) (Swain et al., 2009b), $Spitzer$ broadband photometry (violet square) (Charbonneau et al., 2008) and $Spitzer$/IRS spectrograph (green circle) (Grillmair et al., 2008).

curve from the combined light of a planetary system are not consistent with each other [e.g. Swain et al. (2008a) vs. Gibson et al. (2011,b)]. The effects of underestimated errors on the dayside spectra will be discussed in Section 4.3.2. Also, systematic errors inherent in the observations themselves could be a strong error source. These two facts may cause the planet-star flux ratio to be dependent on the data reduction process. Non concurrent observations for different wavelengths could cause large variations in the measured flux between observations if there is any significant temporal variability in the atmosphere of HD 189733b. Moreover, the problems in inter-instrument calibration cause considerable uncertainty when combining different datasets. Therefore, all these sources of potential error could lead to substantial inconsistencies between the datasets taken from different studies, instruments, and observation times. Although this study does not intend to revisit the decorrelation procedures with this analysis, the aim of the retrieval is to show the limitations of the spectra available at the present epoch under the assumption that the measurements are an accurate representation of the mean planetary flux.

4.2 Model

The $a\ priori$ dayside atmosphere of HD 189733b extends from 10^{-9} to 10 bar. For initial modelling it is assumed that all species are well-mixed throughout the atmosphere and the molecular abundance is defined in terms of a single scaling parameter. This is because the retrieval of a continuous profile of composition would be under-constrained, leading to non-physical oscillations in the retrieved profile. In our forward model, the prior for a single scaling parameter has its error range, which has a gaussian distribution. So the $a\ priori$ scaling parameter is assumed to have a large uncertainty in logarithmic scale (1-σ $>$ e^{10}) so that retrieved values are not weighted by initial guesses since a simple scaling parameter already includes vertical smoothing. For the temperature, we assumed that the $a\ priori$ is a layered profile, where the temperature varies vertically and the initial error is assigned to each layer. However, the profile has to be adjusted to achieve the optimal balance between the quality of the fit to the measured data and the vertical smoothing. This will be further discussed in Section 4.3.1 The mole fractions of H_2 and He are supposed to be related to the fractions of atomic H and He, which are assumed to be close to the typical solar value of 9.10×10^{-1} and 8.87×10^{-2} each (Burrows and Sharp, 1999). The implications of this assumption will be tested in Section 4.6. The system properties used for the planet and star are listed in Table 4.1.

Scattering by clouds and hazes has been reported from HST observations at visible wavelengths, yielding a featureless transmission spectrum of HD 189733b (Pont et al., 2008; Sing et al., 2011). Recently, Heng et al. (2012) showed that the effect of scattering by clouds and hazes modifies the inferred temperature profile and that an isothermal temperature structure above an adiabatic troposphere could also be caused by a cloud-top or haze layer. Here it is considered, however, that the inclusion of scattering clouds and hazes in the retrieval model is beyond the scope of the present study for a number of reasons: 1) the scattering properties of possible clouds and hazes are insufficiently known; 2) adding such particles would greatly enlarge an already large and poorly constrained parameter space and; 3) modelling scattering processes will significantly increase the computation time. In summary, the addition of scattering would increase the complexity of the model

Table 4.1: The system properties for HD 189733 and HD 209458 and their planets (Fortney et al., 2010; Torres et al., 2008).

	HD 189733	HD 209458
$Spectral\ Type$	K1.5V	G0V
T_{eff}(K)	5050	6100
$log(g)$	4.53	4.38
$log[Fe/H]$	-0.03	+0.00
R_*	0.756 $R_\odot$	1.155 $R_\odot$
R_p/R_*	0.151	0.118

and does not appear to be warranted by the dayside emission spectra studied here. Assessing the likely effects of scattering on our modelling of hot Jupiters will follow in future studies.

4.3 Best-fitting Solution for the Dayside Spectrum of HD 189733b

Giving the minimum goodness-of-fit (χ^2), the best-fitting solution demonstrates the most plausible state of the atmospheric parameters consistent with retrieval probability distribution, which is calculated by the convolution of the PDFs of the $a\ priori$ and measurements. This will be the initial point of constraining the uncertainties for temperature and molecules (cf. Section 4.4). In this chapter, the best-fitting solution for the dayside emission spectrum of HD 189733b will be discussed by investigating the best-fit temperature (Section 4.3.1), compositions (Section 4.3.3) and spectrum (Section 4.3.6).

4.3.1 Best-fitting P-T Profile

Previously P-T profiles of HD 189733b have been estimated based on theoretical models or parametric retrievals that generate many thousands of model spectra to compare

with observations. However, this forward modelling approach does not explicitly solve the inverse problem during the constraining process and thus it is unclear if the solutions are biased towards theoretical expectations rather than being driven by the measurements themselves. For this reason, we derive temperatures using several different $a\ priori$ profiles to show that the retrieved temperature converges to a reproducible profile in the altitude range covered by the contribution functions. Because a biased P-T profile would vary with the $a\ priori$ assumptions, the model looks for an appropriate $a\ priori$ error and its vertical shape in order that the same P-T profile can be retrieved irrespective of the shape of the $a\ priori$ profile. Figure 4.2(a) presents the retrieved P-T profile and its error for a range of selected temperature $a\ priori$. For all cases, the P-T profiles share a common shape between 0.1 mbar and 1 bar, demonstrating the validity of the temperature retrieval over this range. It is shown that even with the simplest possible assumption such as an isothermal temperature throughout the atmosphere [blue line in Figure 4.2(a)], the measurements still produce a similar thermal profile as the other retrievals. As a further test, we take an $a\ priori$ structure from the retrieved profile in the previous step, offset it by a temperature 400 K, and repeat the temperature retrieval again. Figure 4.2(b) shows that the P-T profile is still sufficiently constrained by the measurements, even if there are large shifts at levels not covered by the contribution functions, where the solutions relax back to their different priors. It is concluded here that the available dayside emission spectra can constrain an unbiased atmospheric structure over the levels probed by the contribution functions (see Section 4.3.4).

As a result, it is found that the temperature decreases adiabatically from 2100 K at 700 mbar to $\sim$1250 K at 100 mbar, then becomes isothermal up to the upper atmosphere ($\sim$0.1 mbar). These adiabatic and isothermal layers in the thermal structure are dominant features of heat transfer by convection and radiative cooling, respectively. For comparison, S09 claimed a decreasing temperature layer between 10 mbar and 1 bar to model the HST/NICMOS measurements, making an adiabatic layer $\sim$10 times thicker than our estimation, and theoretical models showed also an adiabatic layer in the troposphere (Burrows et al., 2008; Fortney et al., 2006; Showman et al., 2008). The isothermal tempera-

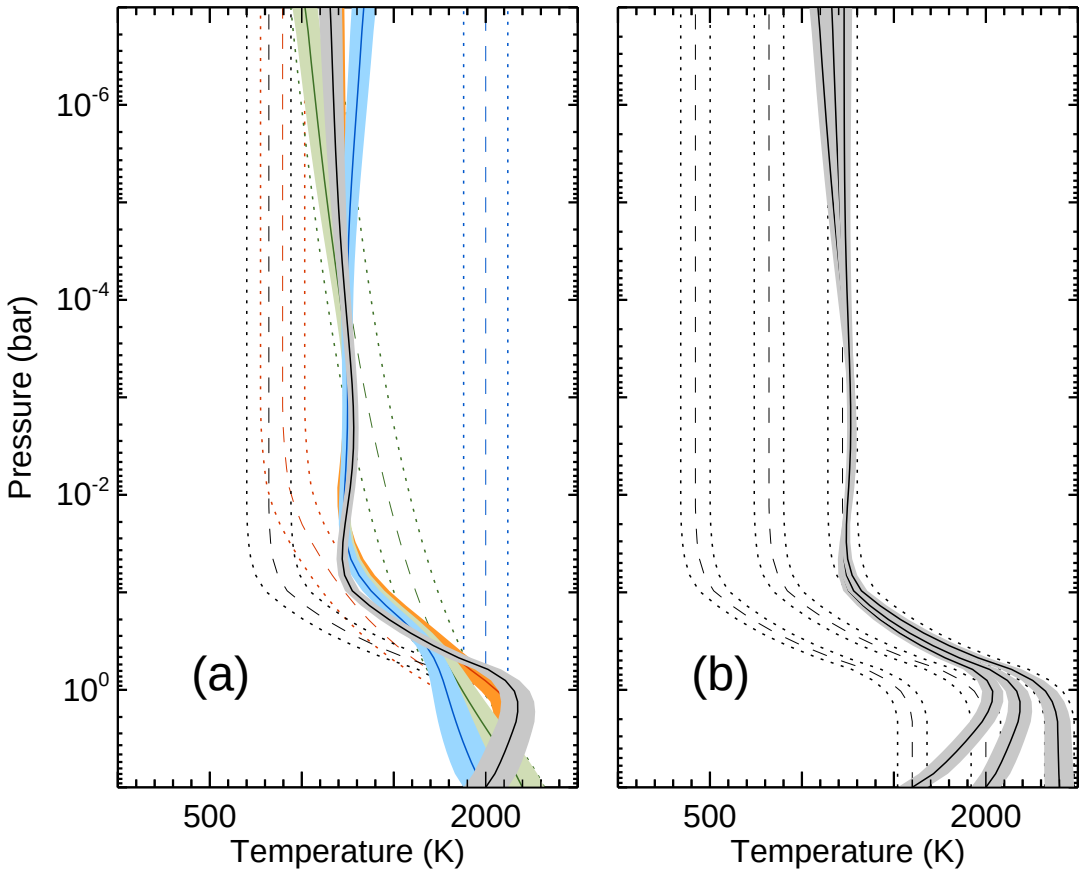

Figure 4.2: (a) Retrieved P-T profiles of the dayside of HD 189733b from a range of diverse *a priori* profiles. The different lines show: *a priori* P-T profiles (dashed), retrieved P-T profiles (solid) and their errors (dot-dashed and dotted). This plot shows the pressure range over which the P-T profile is retrievable from these measurements. (b) Retrieved P-T profiles from the same *a priori* profile shape, but offset from each other with baseline temperatures at 1600 K, 2000 K, and 2400 K at 10 bar.

tures ($\sim$1250 K) of the dayside hemisphere at pressure levels above the troposphere (100 mbar) are possibly maintained by efficient energy re-distribution throughout the whole planet system as suggested by the observations in the $Spitzer$/IRAC channels (Charbonneau et al., 2008; Knutson et al., 2007). Various circulation models (Dobbs-Dixon and Lin, 2008; Showman et al., 2008) predict that the heat transports between the dayside and nightside lead to the isothermal structure at mid and low pressure ($<$100 mbar) in the dayside atmosphere.

In summary, the broad wavelength range of available measurements has provided a strong constraint on the vertical P-T profile (an adiabatic troposphere and isothermal stratosphere) without excessive sensitivity to the $a\ priori$ assumptions, and without reliance on theoretical modelling or parameterised profiles.

4.3.2 Required Molecules to Reproduce the Data

The molecular composition of the dayside atmosphere of HD 189733b is generally accepted to be a mixture of H_2O, CO_2, CO, and CH_4. These molecules have been discovered based on various spectroscopic measurements, listed in Chapter 2. However, given the large uncertainties in the available data and the degeneracy between retrieved parameters, the existence of some of these species is called into question. Therefore it was decided to statistically test whether the presence of each molecule is truly warranted by the data. Using a statistic, the change in the goodness-of-fit parameter (χ^2) between a range of simple and complex models was evaluated. Successively more complexity was added to the model (i.e. additional molecules to the H_2/He atmosphere) and the improvement in χ^2 was evaluated for the best-fitting spectrum. This test was then used to assess whether the inclusion of a particular molecule was required to fit the data.

The test indicates that an atmospheric composition for HD 189733b containing H_2O and CO_2 above the H_2/He model is highly plausible, giving distinctive improvement in χ^2 [from 401.4 (H_2/He only)to 285.3 (H_2/He + H_2O) and 354.6 (H_2/He + CO_2)]. The presence of these two molecules is required to obtain a reasonable fit to the available data. However, insignificant improvement is found when the complexity of the model is

increased by adding CO, CH_4 or a combination of the two to the simple model containing H_2, He, H_2O and CO_2. In other words, CO and CH_4 provide negligible enhancements to the fitting quality and are not required to fit the dayside emission measurements to within the stated error bars (although upper limits on these species can certainly be derived).

Additionally, the implications of Gibson et al. (2011b) are considered, who claimed larger uncertainties in the HST/NICMOS data by re-processing its transmission spectrum (Swain et al., 2008a). If the same conclusions are applicable to the secondary eclipse emission spectrum, then the measurement error on the NICMOS data must be increased similarly by a factor of five. This leads to even smaller confidence levels on the more complex models, and the solutions are found to be even more degenerate. In this case, evaluating χ^2 using a variety of models still suggests that both H_2O and CO_2 are required to reproduce the dayside emission spectra, but makes the presence of CO and CH_4 even more uncertain.

Therefore it is concluded that, irrespective of the uncertainties on the HST/NICMOS data, current datasets are unable to constrain CO and CH_4 on the dayside of HD 189733b with statistical certainty, while the transmission spectrum of this planet provide strong evidence for CH_4. We will discuss this more detail in Chapter 5. Nevertheless, upper limits on the abundances of these molecules can be obtained (see Section 4.4.2), and all four molecules will be included in our subsequent study.

4.3.3 Best-fitting Molecular Abudances

Despite the molecular degeneracies described above, the dayside emission spectra can be used to place crude estimates on the abundances in addition to the vertical temperature structure. Each gas is assumed to be well-mixed with a constant mole fraction with height. However, it is known that the functional derivatives are only sensitive to a limited pressure range and thus our retrieved abundances represent mean concentrations only at the pressure levels which show the highest sensitivity (see Figure 4.4). The best-fitting molecular abundances are determined from the retrieval accompanying the best-fitting P-T profile given in Section 4.3.1 and it is found that those are 4.0×10^{-4} (H_2O), 3.8×10^{-3} (CO_2),

and 8.9×10^{-3} (CO), respectively. Due to its tiny contribution to the spectrum, the best estimation of CH_4 should be considered as an upper limit only, and the CO abundance is poorly constrained by the available data (see Figure 4.8). Additionally, the inferred C/O ratio of HD 189733b (0.75) is found to be a bit larger than the solar value ($\sim$0.6).

4.3.4 Contribution Functions

The radiance measured in each channel originates from different pressure levels within the atmosphere. This is generally described using a contribution function, which is the product of the Planck function at the local temperature in the atmosphere and the transmission weighting function, which describes the rate of change of atmospheric transmission with height. The contribution functions are dependent on the best-fitting profiles for the atmospheric structure and abundances. Thus the calculated contribution functions indicate the pressure levels at which thermal emission from the atmosphere contributes most to the radiance observed in each channel. Figure 4.3 shows the contribution functions for all channels of the $Spitzer$ IRS, IRAC, and MIPS, and HST/NICMOS.

The six $Spitzer$ broadband photometry channels in the range 3.6–24 μm have broadly-distributed contribution functions whose peak pressures range from 0.1 to 500 mbar. The contribution functions for the IRAC channels (3.6, 4.5, 5.8, and 8 μm) and MIPS (24 μm) are located in the deeper atmosphere and provide strong constraints for the temperature between 40–500 mbar. The contribution function of the IRAC 4.5 μm channel has a second and third peak at high altitude (3–5 mbar and $\sim$0.1 mbar), being close to the peak of the IRS 16 μm channel at 4–5 mbar. Hence, the temperature at pressures as low as 0.1 mbar can be retrieved from the IRAC channels, but only if the temperature of the deep atmosphere is well constrained from the other measurements. The 47 $Spitzer$ IRS spectroscopy channels between 5 and 14.5 μm have closely-spaced overlapping contribution functions, with peaks ranging from 0.4 to 250 mbar. The radiance from the lower atmosphere ($\sim$100 mbar) contributes to the channels in the range 5–9 μm, whereas radiance from the upper atmosphere (higher altitudes than $\sim$10 mbar) contributes longward of 9 μm. Unlike the MIR and FIR channels on $Spitzer$, the HST/NICMOS NIR 1.45–2.5

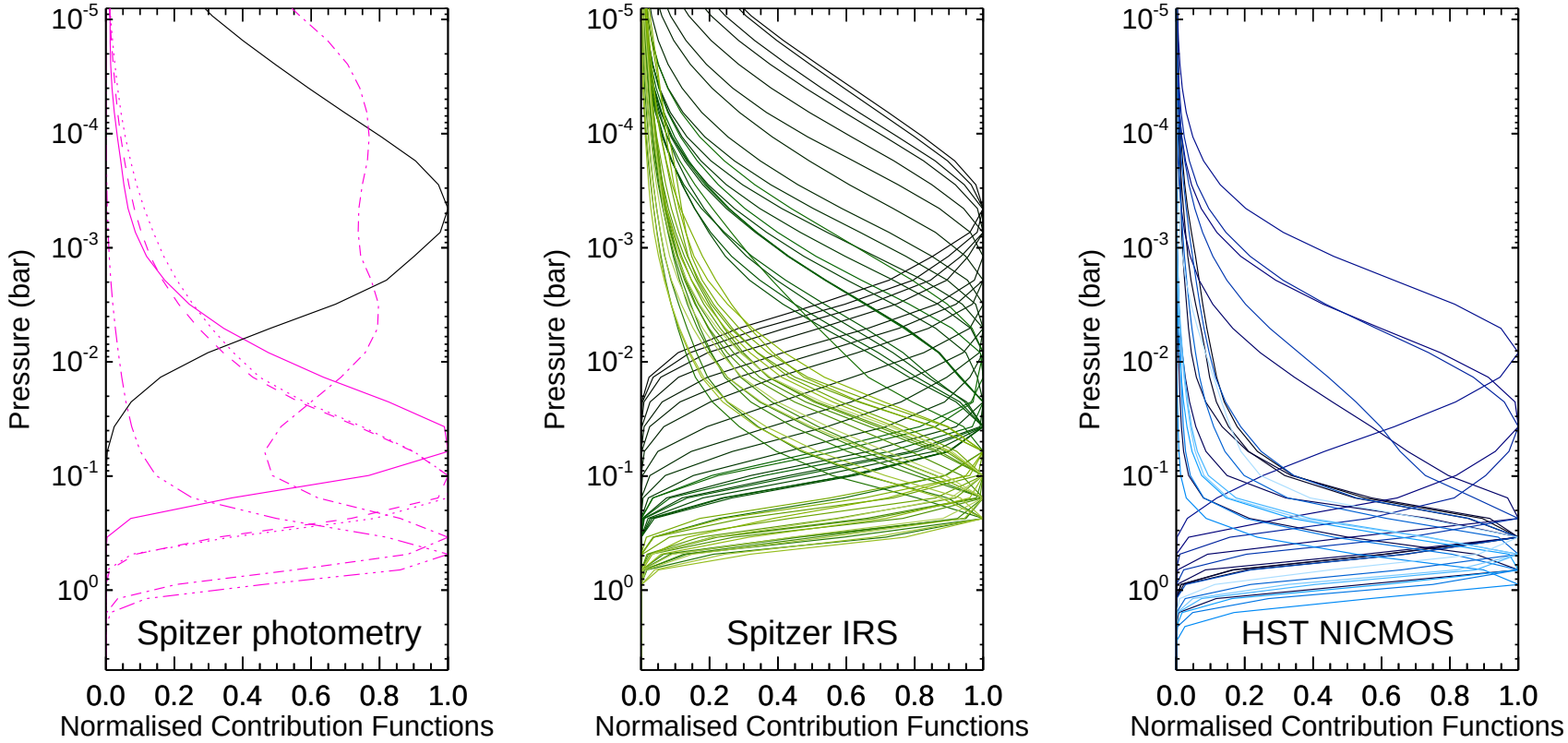

Figure 4.3: Contribution functions for the *Spitzer* broadband photometry (left), IRS spectroscopy (middle), and the *HST*/NICMOS spectrophotometry (right) channels. For the *Spitzer* photometry channels, each line pattern means MIPS 24 μm (solid), IRS 16 μm (solid-black), IRAC 8.0 μm (dotted), 5.8 μm (dashed), 4.5 μm (dot-dashed), and 3.6 μm (triple dot-dashed). For the *Spitzer* IRS and the *HST*/NICMOS channels, the brighter colours denote the channels at the shorter wavelengths. For all cases, emission from the lower atmosphere tends to dominate the shorter wavelength channels.

μm channels can measure the emission from the deeper atmosphere down to 950 mbar and their contribution functions are partly distributed over the pressure levels that are not covered by the $Spitzer$ measurements.

In summary, the contribution functions show that the P-T profile over a broad range of pressures from 0.1 to 950 mbar can be constrained by retrieving from the $Spitzer$ and HST measurements together. On the other hand, studies that focus on a single narrow wavelength range are sensitive to only a narrow altitude range, with potential degeneracies between temperatures at high and low altitudes. Thus, by considering all available datasets simultaneously, this study can provide stronger constraints on the retrieved thermal properties than in previous studies.

4.3.5 Functional Derivatives

The functional derivatives are defined to be the partial derivatives of the radiance (or any spectral output in the forward model) with respect to any given atmospheric parameters. By calculating the functional derivatives for molecular abundances, it can be seen which measurements are sensitive to the molecular abundance and at which pressure levels. Figure 4.4 shows the functional derivatives for the 4 molecules considered in this study. For ease of comparison, these are normalised to the peak of the functional derivatives for each measurement set. Using Figure 4.4 the sensitivity can be interpreted in two directions: Each row indicates which pressure levels show high sensitivity to a given molecule in each channel, and each column indicates how molecular sensitivity is distributed through pressure levels in a given set of measurements. In all cases, the derivatives are negative because an increasing abundance increases the atmospheric absorption (in the absence of a thermal inversion on this planet) and decreases the ratio of the disk-averaged planetary flux with respect to the host star since the P-T profile has a temperature-decreasing layer with height.

High sensitivity to the abundance of H_2O is seen in all channels, with the exception of the 1.93–2.16 μm channels of HST/NICMOS, 4.5 μm channel of $Spitzer$/IRAC, 9–14.5 μm and 16 μm channels of the $Spitzer$/IRS, in which regions the modelled radiance is

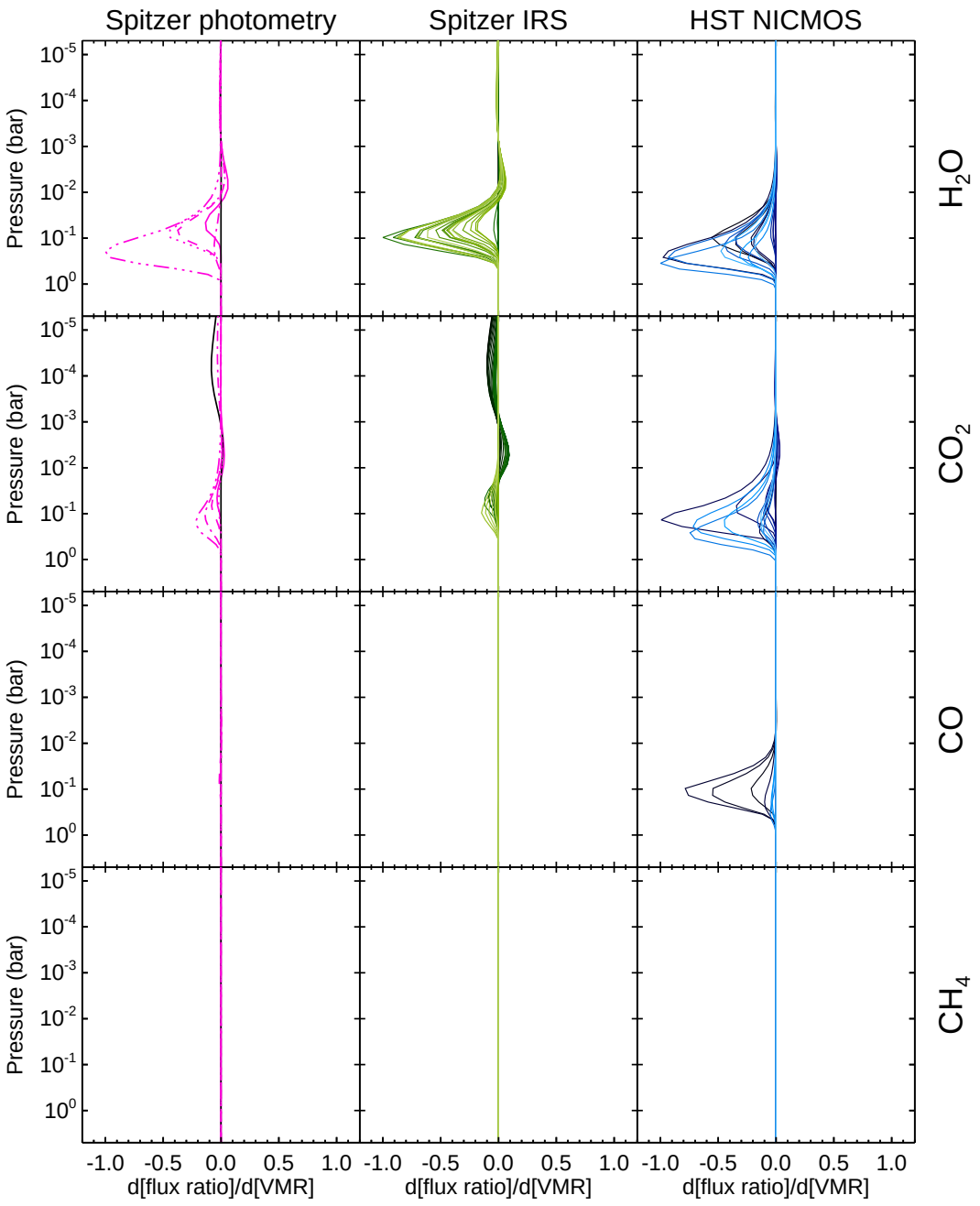

Figure 4.4: Normalised functional derivatives of radiance with respect to molecular abundances in $Spitzer$ and HST channels. The applied colours are the same as those described in Figure 4.3. Each row shows the vertical sensitivity of radiance with respect to the abundances H_2O, CO_2, CO, and CH_4 (from top to bottom). This figure shows the pressure levels at which molecular abundance can be retrieved (row direction) from which channel (column direction).

dominated by CO_2 absorption, as explained below. The H_2O functional derivatives all peak in the ∼50–500 mbar region, showing that the measurements can only constrain the H_2O abundance in this altitude range. In contrast, the CO_2 functional derivatives are divided into two separate pressure levels (peaks between ∼100 mbar and ∼0.1 mbar) as are clearly shown in the second row of Figure 4.4. The HST/NICMOS channels between 1.584–1.698 and 1.929–2.216 μm are only sensitive to the CO_2 abundance at altitudes below 100 mbar whereas the $Spitzer$ broadband photometry and IRS spectroscopy are sensitive to the CO_2 in the ∼0.1 mbar region as well. Despite this sensitivity to a range of altitudes for CO_2, a combination of these channels, however, may not determine CO_2 abundance at both levels due to the small sensitivity in the upper atmosphere (cf. Section 4.4.2). CO can only be detected in four HST/NICMOS channels in the range 2.33–2.45 μm at 100 mbar, and these channels have been extensively used to constrain the CO mixing ratio (S09 and MS09). The sensitivities for CH_4 are so marginal, as seen in the fourth row, that constraining its abundance may not be possible from the given measurements.

In summary, the functional derivatives indicate the altitudes and channels showing sensitivity to each particular molecule. The sensitivities to the molecules are mostly clustered in the lower atmosphere (∼100 mbar), and, in particular, CO_2 shows an additional peak at ∼0.1 mbar. Therefore the molecular abundances can only be constrained in the deep atmosphere (troposphere), with less sensitivity to the upper atmosphere. Finally, these functional derivatives show that the spectrum is sensitive to all the molecular abundances except CH_4 over a broad range in most of the measured channels, implying an inherent degeneracy between temperatures and the abundance of all molecules in these observations.

4.3.6 Best-fitting Solution

Using the NEMESIS algorithm, the best-fitting dayside spectrum of HD 189733b was retrieved, incorporating both the $Spitzer$ and HST observations as stated in Section 4.1. Figure 4.5 demonstrates the best-fitting spectrum to these measurements, and the retrieved

atmospheric P-T profile and molecular abundances for H_2O, CO_2, and CO except CH_4. This is because adding CH_4 to the model was found to worsen the quality of the fitting, as described in previous sections. Each panel will be explained below.

Figure 4.6 shows the contributions from the four main gases included in our model. This figure also shows the wavelength ranges where the molecular contributions are distributed by co-plotting the computed synthetic spectra with high and low abundances for each molecule. Spectral features of H_2O and CO_2 affect the spectrum at all wavelengths. CO has absorption features at 1.6 –1.7, 2.3–2.5, and 5.0–5.5 μm, while CH_4 features can be seen at 1.7, 2.2–2.5, 3–4, and 7–9 μm. A striking feature of the best-fitting spectrum is a deep IR absorption by CO_2 at 9–24 μm, which is rather different from the fitting by other studies (MS09; Charbonneau et al., 2008; Fortney and Marley, 2007; Grillmair et al., 2008), who concluded that the features at the longer wavelengths of IRS are caused mainly by H_2O, of which absorption is also dominant at the shorter wavelengths of 5–9 μm. Although the low CO_2 hypothesis seemed to give a good reproduction of the long-wave $Spitzer$ data, it fails to reproduce the shorter wavelengths covered by HST. As seen here, one of the benefits of this approach is that the use of a broad range of IR wavelengths allows us to break some of the degeneracies inherent in modelling a small number of data points (cf. Section 4.4).

In this study, the high CO_2 abundance causes a sharp drop at 9 μm and then a flat and featureless spectrum between 9–24 μm. H_2O still contributes to the spectrum at 5–9 μm and $>$20 μm as well as a small feature from a vibrational transition at 6–6.5 μm, which is one of the H_2O features highlighted by Grillmair et al. (2008). The spectrum fits the high planet-star flux ratio for the $Spitzer$/IRAC 3.6 μm channel with greater than 2-σ level. This result can be interpreted in two ways: 1) if the IRAC channel at 3.6 μm was determined as precise as the IRTF measurement (Swain et al., 2010), the large 3.25 μm emission of CH_4 in non-local thermodynamic equilibrium (NLTE) conditions can explain its high flux ratio (Swain et al., 2010; Thatte et al., 2010). 2) However, if the flux ratio of this IRAC channel is not repeatable as the recent observation has shown (Knutson et al., 2012), we can suppose that there might be a non-negligible time variability in

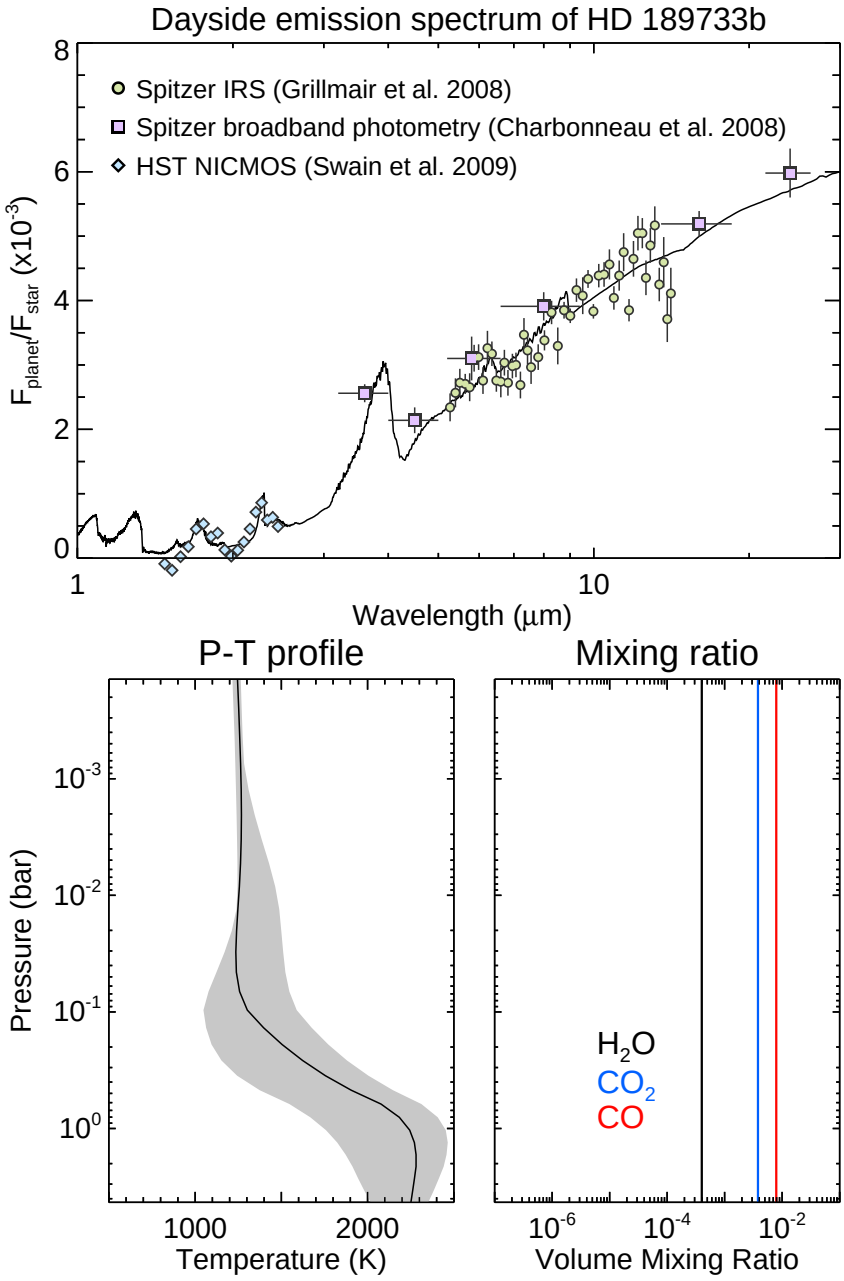

Figure 4.5: The best-fitting spectrum and atmospheric properties retrieved by the NEMESIS algorithm. In the top panel, the best-fitting dayside emission spectrum of HD 189733b is displayed as a black line. The green, purple with red, and cyan symbols are the measured planet-star flux ratio from the *Spitzer*/IRS spectroscopy (Grillmair et al., 2008), the *Spitzer* broadband photometry (Charbonneau et al., 2008), and the *HST*/NICMOS spectrophotometry (Swain et al., 2009b) (cf. Section 4.1), respectively. The retrieved best-fitting *P-T* profile in the bottom-left panel is shown in a black solid line with grey-coloured uncertainties due to the molecular degeneracy (cf. Section 4.4.1). In the bottom-right panel, retrieved best-fitting molecular mixing ratios for H_2O, CO_2, and CO are demonstrated with different colours. Each abundance is assumed to be fixed with height in order to minimise the number of retrieval variables (cf. Section 4.2). Here CH_4 is omitted in the figure due to its negligible enhancement to the fitted spectrum.

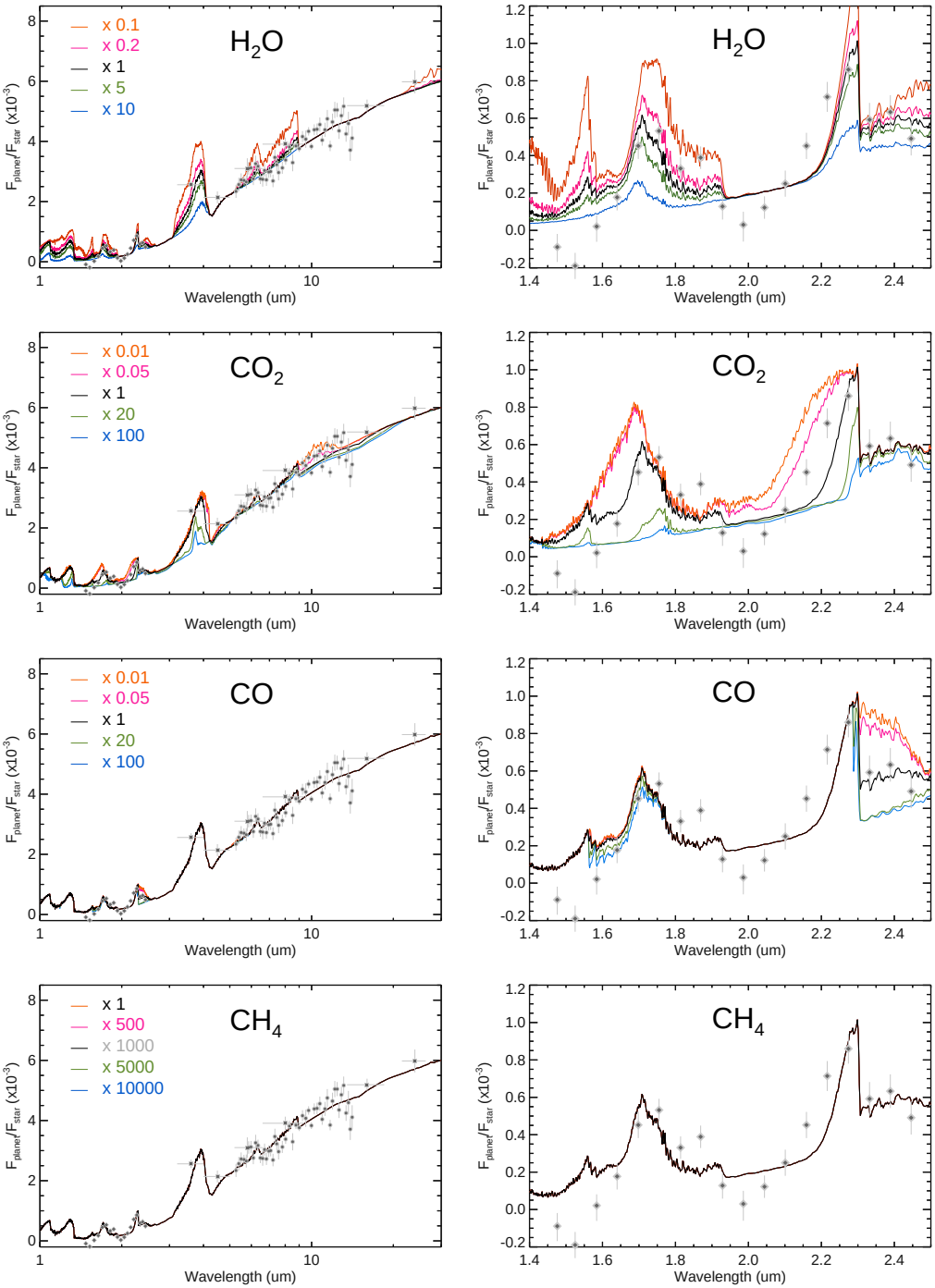

Figure 4.6: Fitted dayside emission spectra of HD 189733b. The orange, purple with red, and green symbols are the measured planet-star flux ratio from the *HST*/NICMOS (Swain et al., 2009b) spectrophotometry, the *Spitzer*/IRS spectroscopy (Grillmair et al., 2008), and the *Spitzer* broadband photometry (Charbonneau et al., 2008; Deming et al., 2006), respectively. The best-fit spectrum retrieved by the NEMESIS algorithm is displayed as a black line in all figures. Also calculated spectra with various molecular abundances are shown here in order to understand the contributions of different molecules to the best-fit spectrum. For H_2O, molecular abundances are varied 0.1, 0.2, 5.0, and 10.0 times from the abundance leading to the best-fit spectrum, 0.01, 0.02, 20.0, and 100.0 times for CO_2 and CO, and 500, 1000, 2000, and 10000 times for CH_4.

the dayside hemisphere or that the flux measurement by Charbonneau et al. (2008) is overestimated. More discussion will be presented in Chapter 7. For the HST/NICMOS channels between 1.45–2.5 μm, the measurements are fitted using a high amount of CO_2 as suggested in MS09 ($\sim 7 \times 10^{-4}$) rather than in S09 whose model suggested low CO_2 mixing ratio (10^{-7}–10^{-6}). This discrepancy is not yet fully resolved, but, as Shabram et al. (2011) stated, this may come from the difference in the forward models and assumed line data used for each study. In the best-fit spectrum, the channels at 1.584, 1.869, 2.159–2.216 μm, however, are underestimated by the high CO_2 abundance, leading to a decrease in the quality of the fit to the data. The sharp edge present in the synthetic spectrum at 9 μm, where a sudden CO_2 line weakening is shown (Tashkun et al., 2003), is caused by a strong CO_2 absorption. We consider that this spectral feature is related to the limited number of gases included in our model or the absence of aerosols considered during modelling. For clear understanding, this issue must be re-discussed with the reduced measurement errors.

4.4 Retrieval of Atmospheric Properties

4.4.1 Temperature Degeneracy

In general, the best-fitting P-T profile from the retrieval is a non-unique solution. This means that there is potentially a large family of solutions for the P-T profile that could fit the measured spectrum equally well within the same error range. In many retrievals, there may also exist cross-correlation with other fitted quantities, indicated by covariances that are larger than zero. The covariance matrix is advantageous because the matrix is computed as a part of the retrieval process and can be used in assessing the degeneracies between variables at the end of retrieval.

For the dayside spectrum of HD 189733b, the degeneracy between the molecular abundances and the P-T profile is significant at some pressure levels and bandpasses (S09 and MS09) because our unknown temperature and composition information can be adjusted to fit the spectrum. However, a detailed analysis of these correlations has

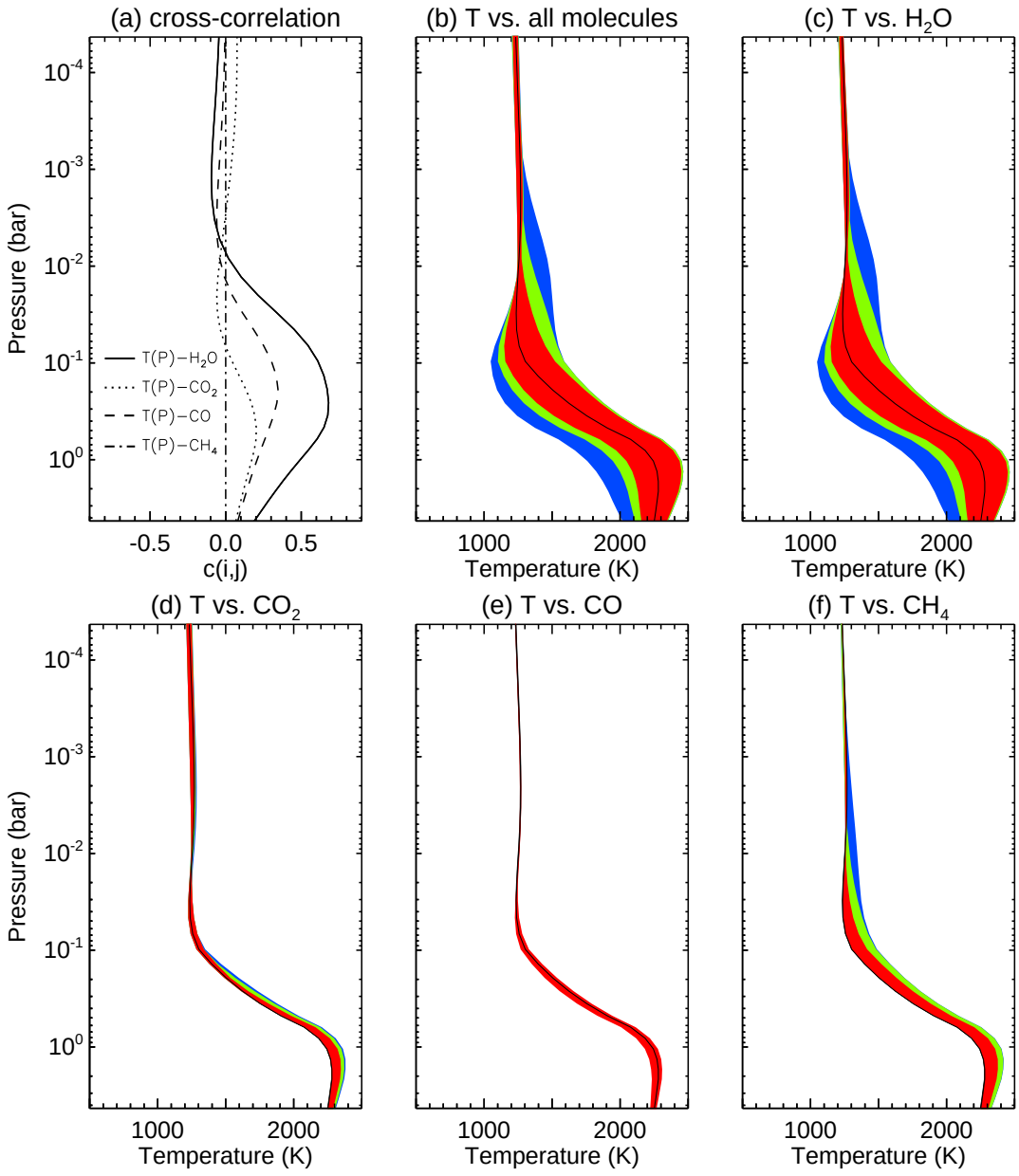

Figure 4.7: (a) The vertical structure of the cross-correlation functions. The high correlation with H_2O and CO_2 dominates the degeneracy of temperature at most pressures. (b-f) The retrieved P-T profiles of the dayside HD 189733b with various mixing ratios for each molecule are presented with $\Delta\chi^2$/N ranges. Each colour demonstrates $\Delta\chi^2$/N$<$0.5 (red), $<$1.0 (green), and $<$2.0 (blue), respectively. As a result, the large uncertainties of P-T profile are broadly distributed between the deep and middle atmosphere. On the other hand, narrow uncertainty at 0.2 mbar implies an isothermal structure in the upper atmosphere of the dayside of HD 189733b.

not previously been presented. Here, the cross-correlation functions $c(i,j)$ (i.e. the off-diagonal elements of the correlation matrix) are examined in order to determine the degree of degeneracy between elements i and j of the state vector. By definition, $|c(i,j)|$=1.0 represents a perfect correlation between variable i and j, and it is considered that $|c|$=0.5 is a limitation for quasi-independent retrievals of different variables. The profiles in Figure 4.7 (a) show the vertical structure of cross-correlation functions between the molecular abundances and the temperature at different pressure levels. It can be seen that the P-T profile is significantly correlated with molecular abundances at some levels, being most correlated with the H_2O abundance between 200–400 mbar and with CO_2 for altitudes above the 0.3 mbar pressure level.

To determine the degeneracy of the temperature profile from Figure 4.7 (a), multiple retrievals were performed, where individual molecular abundances were fixed at a particular value and all other variables retrieved. The weighted mean least square, χ^2/the number of measurements (N) of the solution, was then assessed as a function of the fixed molecular abundance. This is compared with the minimum χ^2/N (χ^2_{min}/N) of the best-fitting retrieval, and determined the range of temperatures for which the change $\Delta\chi^2$/N=χ^2/N-χ^2_{min}/N was less than 0.5, 1.0, and 2.0, respectively.

Figure 4.7 (b) shows the ranges in the retrieved P-T profile for different values of $\Delta\chi^2$/N due to the molecular degeneracy. At each pressure level, allowed temperature ranges are determined by varying the molecular abundance with which the temperature is most strongly correlated. The temperature uncertainties for $\Delta\chi^2$/N$<$1.0 calculated in this way are 540 K at 800 mbar, 490 K at 100 mbar, and 50 K at 2 mbar. The temperature uncertainties at altitudes below 1 mbar are caused mainly due to the degeneracy with the H_2O abundance and those at altitudes above 1 mbar are degenerate with the CO_2 abundance. On the other hand, the degeneracies between temperature and the abundances for CO and CH_4 are small because they affect only a small region of the spectrum. Therefore it can be seen that although some uncertainty in the deeper P-T profile exists due to molecular degeneracy, the small degree of degeneracy at lower pressures supports our conclusion that HD 189733b has an isothermal structure at the upper atmosphere.

4.4.2 Retrieval of Molecular Abundances

By looking at the covariance of our retrieved solution it is found that the cross-correlation between the different molecular abundances is rather small ($c < 0.1$) for all the molecular combinations. However, there remains some degeneracy due to the main correlation with temperature. To quantify this $\Delta\chi^2$/N is calculated for each gas by changing the abundance of a molecule and retrieving all other parameters including temperature. The variation of $\Delta\chi^2$/N with abundance for all four gases is shown in Figure 4.8. It is found that the following abundance ranges have $\Delta\chi^2$/N<0.5: (4–600)$\times10^{-5}$ for H_2O, (2–300)$\times10^{-4}$ for CO_2, and $<6\times10^{-5}$ for CH_4, respectively. The error ranges for the abundance of CO were so broad that we cannot provide meaningful estimates from the dayside spectra alone, hence they are absent from Table 4.2. The retrieved abundances of the other species for $\Delta\chi^2$/N<1.0 and 2.0 are also shown in Table 4.2 and are compared with the expectations of a thermo- and photo-chemistry model (Line et al., 2010), with previous forward model studies (S09 and MS09) and the other optimal estimation retrieval study (Line et al., 2012). As it was found in Section 4.3.3, the data only constrain the upper bound of the mixing ratio for CH_4 and do not offer useful constraints on the abundance of CO because the disk-averaged planet-star flux ratio shows only a small sensitivity to their abundances (Figure 4.4) and their contributions to the emission spectrum appear in only few bandpasses. Consequently, variation of these two gases leads to a tiny change in $\Delta\chi^2$/N where the abundances are lower than the best-fitting estimation. It is concluded that it is not possible to constrain the abundances of CO and CH_4 with a reasonable error range based on these datasets alone as previous studies have attempted.

All channels of *Spitzer* and *HST* are capable of constraining the H_2O mixing ratio as presented in the functional derivatives, and the constrained H_2O is consistent with other estimations. For CO, the strongest constraints are taken from the *HST*/NICMOS data (MS09) and it is found that the dayside emission spectra can offer no meaningful constraints on the abundance of this species. A relatively small abundance of CH_4 has been estimated by previous studies in Table 4.2, except for the large abundance range ($\sim10^{-2}$) derived from the *Spitzer*/IRS spectroscopy at 7.6 μm (MS09) and from the

Table 4.2: Estimated and retrieved mixing ratios and the C/O in the dayside of HD 189733b.

	H_2O (10^{-4})	CO_2 (10^{-4})	CO (10^{-4})	CH_4 (10^{-4})	C/O	Data Source
Line et al. 2010	6–13	0.0047–0.016	2–9	0.0026–6.758		Thermoschemistry
	$\sim$6.36	0.004–$\sim$0.1	$\sim$8.4	$\sim$0.4		Photochemistry
Line et al. 2012	0.529–2.67	16.9-67.2	36.0–364	$<$97.7		HST/NICMOS
Swain et al. 2009	0.1–1	0.001–0.01	1–3	$<$0.001	0.5–1	HST/NICMOS
Madhusudhan & Seager 2009	0.01–1000	...	...	$<$100	...	$Spitzer$ IRS
	0.1–10	0.007–0.7	...	$<$0.02	0.007–1	$Spitzer$ photometry
	$\sim$1	$\sim$7	2–200	$<$0.06	0.5–1	HST/NICMOS
This study	Best-fit value					
	4.0	38	89	...	0.75	All measurements
	Possible fit range					
	0.4–60	2–300	...	$<$0.6	0.5–1	$\Delta\chi^2$/N$<$0.5
	0.1–200	0.007–700	...	$<$2	0.4–1	$\Delta\chi^2$/N$<$1.0
	$>$0.005	...	...	$<$30	0.2–1	$\Delta\chi^2$/N$<$2.0

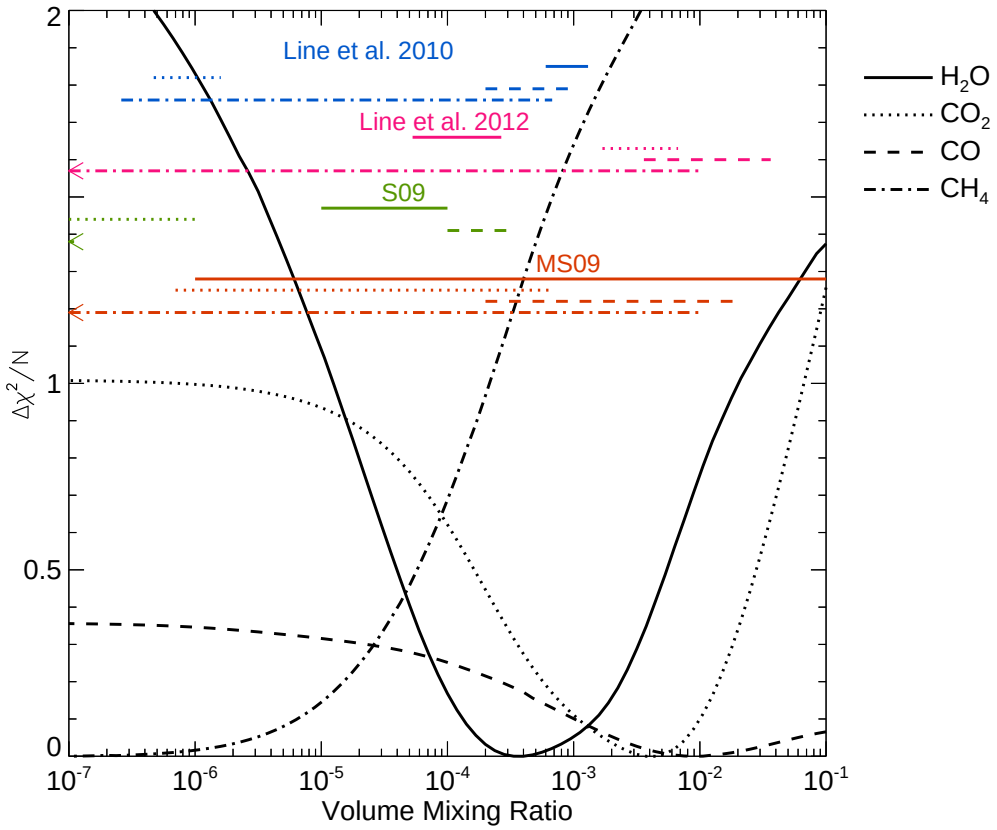

Figure 4.8: The degeneracy ranges of the molecular mixing ratios for H_2O, CO_2, CO, and CH_4. Each line shows resultant $\Delta\chi^2$/N with respect to given abundances. The results from the previous studies are displayed in blue (Line et al., 2010), magenta (Line et al., 2012), green (Swain et al., 2009b) and red (Madhusudhan and Seager, 2009). The $\Delta\chi^2$/N constrains the uncertainties of the molecular abundances which are distributed around the best-fitting abundance of H_2O (4.0×10^{-4}), CO_2 (3.8×10^{-3}), and CO (8.9×10^{-3}), respectively. Lower bounds of CO and CH_4 uncertainties are unconstrained because of their small contribution to the spectrum.

HST/NICMOS (Line et al., 2012), which is not consistent with this study. The derived abundance of CO_2 (2–300)$\times10^{-4}$ is 2–3 orders of magnitude larger than previous studies by a chemical model ($\sim10^{-7}$–$\sim10^{-5}$) (Line et al., 2010), S09 (10^{-7}–10^{-6}), and MS09 (using *Spitzer* photometry, (7–700)$\times10^{-7}$) for all $\Delta\chi^2$/N ranges and thus the retrieved CO_2 abundance in this study is only consistent with the *HST*/NICMOS estimation by MS09 and Line et al. (2012). Indeed, it is the *HST*/NICMOS channels that constrain the retrieved CO_2 abundance to be larger than previous studies ($\sim10^{-3}$), whereas the *Spitzer*/IRAC channels at 4.5 and 16 μm could be fitted with either low or high abun-

dances of this molecule.

To test the sensitivity to CO_2 in the upper atmosphere, the best-fitting spectra were compared to test cases with a range of upper atmospheric abundances of this molecule (i.e. allowing the abundance to vary with altitude). The CO_2 mixing ratio was fixed at a certain value up to a pre-defined pressure level, and then declined linearly into the upper atmosphere with a slope determined by a fractional scale height (the ratio of the scale height of the gas to the scale height of the atmosphere). This allows us to demonstrate the effect of different mixing ratios with height, but avoiding the need to introduce a complete vertical profile of CO_2 (and hence a large number of additional parameters in our state vector). In Figure 4.9, the retrieval with the new CO_2 vertical profile that decreases from 3.8×10^{-3} at 100 mbar to 1.0×10^{-7} at 0.1 mbar, produces a very similar spectrum to the well-mixed high-CO_2 case, leading to an insignificant improvement in terms of the χ^2/N. This is because the CO_2 sensitivity at the $Spitzer$ bandpasses is too low to adequately constrain its abundance in the upper atmosphere (0.1–1 mbar), whereas the strong constraints of the HST/NICMOS and $Spitzer$/IRS channels between 9–16 μm allow us to constrain the abundance in the lower atmosphere ($\sim$100 mbar). In contrast, a small abundance of CO_2 (10^{-7}) with a well-mixed vertical profile is unable to reproduce the measured spectrum. These results suggest that a large amount of CO_2 ($\sim10^{-3}$) exists at $\sim$100 mbar but that the abundance at 0.1–1 mbar is unconstrained by current measurements.

4.5 Lapse Rate

The retrieved thermal structure is a useful tool for further understanding of dynamic processes in the atmosphere. As a description of atmospheric stability, the lapse rate ($\Gamma = dT/dz$, the rate of change of temperature with respect to the height) is shown in Figure 4.10. An increase in the lapse rate indicates that there is an adiabatic layer beneath the $\sim$100 mbar level ($\sim$1400 km above from the level of 10 bar), and that the lapse rate tends to zero for pressure levels above $\sim$30 mbar ($\sim$2100 km) where the temperature pro-

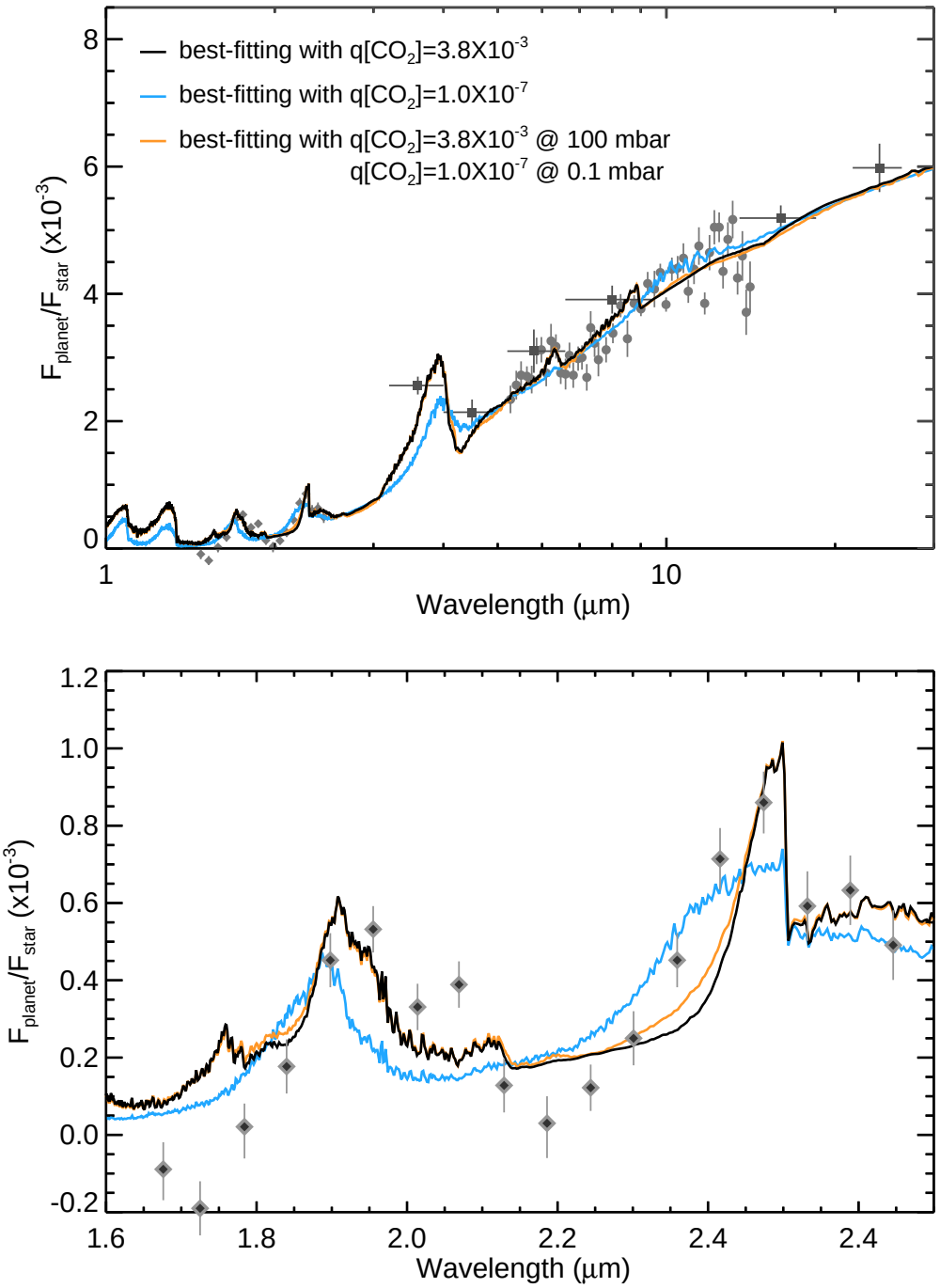

Figure 4.9: Synthetic emission spectra of the dayside of HD 189733b with different CO_2 abundances. The three lines show the spectrum with a well-mixed abundance of 3.8×10^{-3} (black); well-mixed at 1.0×10^{-7} (cyan) and the case with CO_2 varying with altitude from 3.8×10^{-3} at 100 mbar to 1.0×10^{-7} at 0.1 mbar (orange). The latter case is almost indistinguishable from the first scenario.

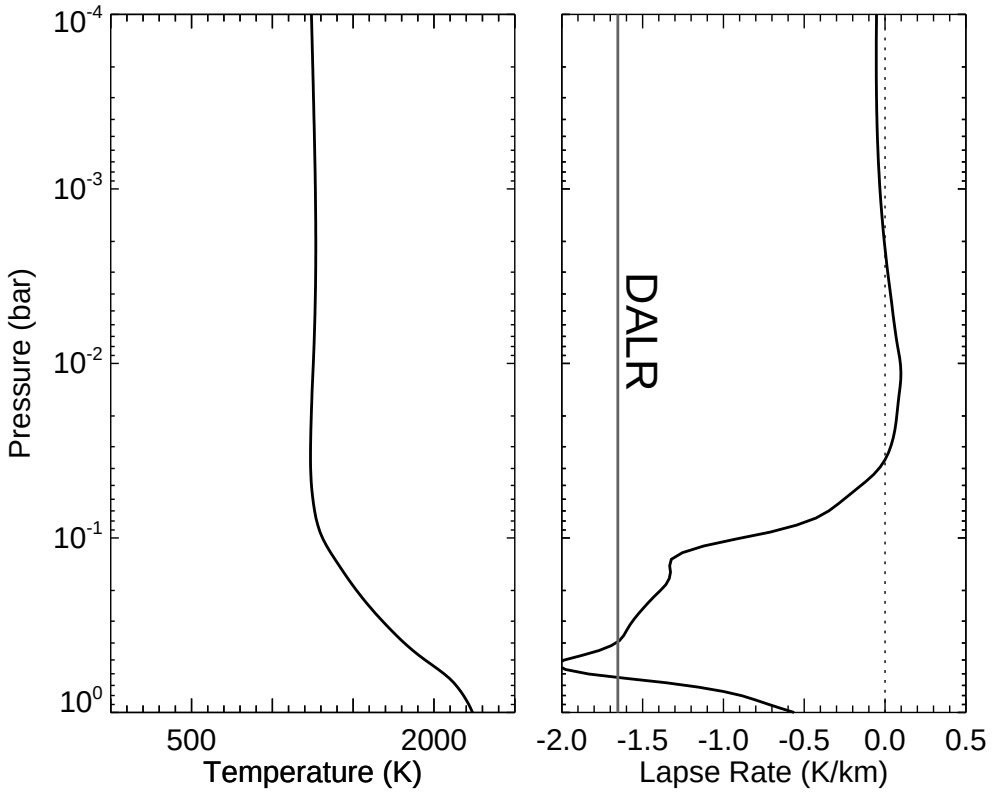

Figure 4.10: Disk-averaged dayside lapse rate of HD 189733b ($right$) from the derivative of the P-T profile ($left$). The given pressures correspond to the levels mostly covered by the contribution functions. Also the dry adiabatic lapse rate (DALR) is displayed in grey, assumed to be a constant over this pressure range.

file tends to an isotherm. We calculated the dry adiabatic lapse rate (DALR), assuming an uniform atmosphere composed of H_2 and He only and a fixed gravity with height (g = 21.2 m^2/s^2). The measured lapse rate is similar to DALR at the 400 mbar pressure level, and is overlain by a sub-adiabatic layer extending up to 30 mbar, similar to the atmospheric thermal structures seen in the upper tropospheres of the giants planets of our solar system.

4.6 Additional Sources of Degeneracy

In the sections so far, conclusions about the atmospheric temperatures and composition based on a series of underlying assumptions have been derived, which have not been quantified by previous authors. Here additional degeneracy tests are performed to quantify the uncertainties on temperature and composition caused by the uncertainty of the amount

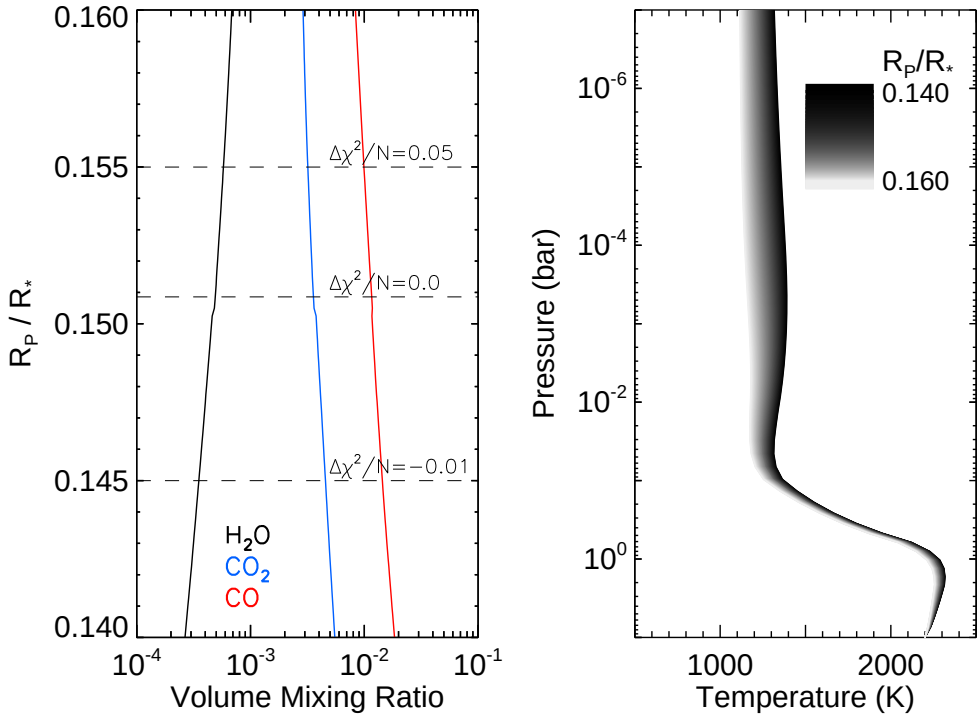

Figure 4.11: Uncertainty of composition (left) and temperature (right) being induced by the variation of planet-star radius ratio (R_p/R_*). Due to ∼15 per cent increment in R_p/R_*, the temperature profile shifts towards lower ∼220 K at isothermal stratosphere (1 mbar) whereas the fitting quality, $\Delta\chi^2$/N increases by <0.3.

of H_2 and He and the radius ratio between planet and star (R_p/R_*). The abundances of H_2 and He are generally considered to be more or less the same as in the parent star. However, the helium abundance in the giant planets of our own solar system deviates considerably from solar, and this could provide an additional source of error in the retrieval of the vertical temperature structure. However, it is found that the change in mole fraction of H_2 (assumed to be 1-q[He]) between 0.8–1.0 gives a negligible effect on the retrievals of temperature and composition from the dayside spectra at all pressure levels, suggesting that the emission spectrum of HD 189733b (which is dominated by the features of H_2O) is not particularly sensitive to variations of H_2 and He compared to the host star.

On the other hand, variations of the planet-star radius ratio, which determines the bottom level of the model atmosphere, has a significant effect on the flux ratio. If the effect of varying the radius ratio over the range $0.140<R_p/R_*<0.160$ (Agol et al., 2010; Fortney et al., 2010; Torres et al., 2008) is considered, then it is found that the best-fitting molecu-

lar abundances vary over the ranges: H_2O (2.7–6.8$\times10^{-4}$), CO_2 (2.9–5.5$\times10^{-3}$), and CO (8.4–20$\times10^{-3}$), respectively (Figure 4.11). The figure indicates that the temperature profile over the pressure range becomes $\sim$220 K cooler at 1 mbar when R_p/R_* is enhanced by 0.02 ($\sim$15 per cent increase in the radius of the planet). As an increase in R_p/R_* enhances the flux ratio across all wavelengths, the model tends to select a correspondingly low temperature profile that decreases the flux ratio.

Finally, as described in Section 4.2, the scattering and absorption processes have been omitted due to the presence of clouds and hazes in this hot Jupiter atmosphere, choosing to focus on a clear atmosphere for this initial exercise. Given the present quality of the dayside emission spectra, the more complex model with scattering hazes is not needed to reproduce the data (although hazes are clearly needed to reproduce transmission spectra of the terminator region), and would lead to a significant rise in the number of model parameters. However, the omission of aerosols could lead to significant changes to our derived temperatures and molecular abundances, and future work will aim to quantify these uncertainties to further explore the atmospheres of hot Jupiters.

4.7 Conclusion

Using the optimal estimation retrieval algorithm retrieval, it was shown that the current set of observations of the dayside spectrum of HD 189733b are enough to constrain the thermal structure at some pressure levels and the mixing ratios for H_2O, CO_2, CO, and CH_4 with its uncertainties. We found that the thermal structure and chemistry show the characteristics of theoretical models for HD 189733b. Furthermore, the ability to calculate the cross-correlation function allows us to assess the degeneracies between the various modelled parameters in the state vector.

With the retrieval method presented here, three major findings are derived from the available measurements given in this study. Firstly, the retrieved thermal structure of the dayside HD 189733b shows that the constraints in the NIR and MIR lead to an adiabatically decreasing temperature between 100 mbar–1 bar. In addition, strong constraints

from the *Spitzer*/IRS measurements in the 9–16 μm range suggest that the temperature structure in the mid and upper atmosphere (0.1–100 mbar) seems to be isothermal with a uniform temperature ($\sim$1250 K), which does not show an inverted layer at any pressure levels. This structure resembles thermal structures from theoretical models of a typical pL and class IV planet, where no stratospheric absorbers exit. One explanation for the isothermal layer is that super-rotating jets blowing from night- to dayside play a critical role of an efficient energy re-distribution over the whole planet and it may be responsible for maintaining the high temperature in the upper atmosphere (Knutson et al., 2007; Showman et al., 2008).

Secondly, the functional derivatives for the molecules show that the measurements at the NIR (1.45–2.1 μm), MIR (4.5 μm), and FIR (9–16 μm) spectral ranges independently constrain CO_2 abundance at $\sim$100 mbar and 0.1–10 mbar. Its abundance in the lower atmosphere is responsible for the spectral flatness at 9–16 μm, where previous studies assumed H_2O to be the dominant constituent. The vertical sensitivity of CO_2 abundance is determined by comparing the retrievals with abundant (3.8×10^{-3}) and scarce CO_2 (10^{-7}), and height-dependant CO_2 profile. The functional derivatives for CO_2 show low sensitivity at $\sim$0.1 mbar, which means that, in the upper atmosphere, the mixing ratio of CO_2 remains unconstrained and the spectrum looks the same irrespective of the chosen value of CO_2 at this pressure level. In contrast, high sensitivity of CO_2 at the lower atmosphere (100 mbar) indicates high abundance of CO_2 at this pressure level. The constrained molecular abundances also show that abundant H_2O and CO, and a CH_4 deficiency in the dayside hemisphere of HD 189733b are one of chemical characteristics for a typical class IV planet, whereas the high amount of CO_2 is not predicted by the models, which is possibly due to a higher concentration in the lower atmospheres (Madhusudhan and Seager, 2009).

Thirdly, the degeneracies between the atmospheric properties are quantified using the cross-correlation functions. The correlations between molecular abundances and temperature exhibit sizeable degeneracies, in particular, between temperature and H_2O abundance at 470 mbar. The temperature uncertainty at different pressure levels is determined by cal-

culating the statistics of the retrievals with the variation of each molecular mixing ratio and, as a result, this confirms the isothermal structure in the stratosphere. In the same way, the molecular abundances are also constrained by demonstrating that the uncertainty of retrieved parameters, based on the available measurements and the degeneracy with the temperature profile is much larger than previous studies have suggested. Therefore, additional data is clearly required to break the degeneracy between temperature and compositions, particularly H_2O. As long as the number of retrieval variables for the molecular abundance are kept to a small number, the cross-correlation functions are not significant between molecules. If we were forced to use a more detailed representation of the vertical distributions of the gases, then the degeneracies would grow more substantial.

In following chapters, the results from the dayside emission spectrum will be used as the prior for the study of the transmission spectrum of this planet in Chapter 5, and that the results again will be compared to a different type of hot Jupiter (i.e. HD 209458b) in Chapter 6.

Chapter 5

Primary Transit of HD 189733b

In this chapter, we will revisit the atmosphere of HD 189733b by considering the additional constraints offered by primary transit spectroscopy of the day/night terminator region. The main objective of the study in the following sections is to retrieve the best-fit model atmosphere consistent with all three sets of transmission spectrum, one taken from HST/ACS (0.55–1.05 μm) and two from NICMOS (1.45–2.5 μm), which were previously interpreted as having evidence for the presence of silicate haze/cloud or molecules (Gibson et al., 2011; Pont et al., 2008; Swain et al., 2008b). We hope that the simultaneous fitting of the broad spectral range of the primary transit spectrum of HD 189733b will provide new insights into the nature of the aerosols and gaseous species contributing to the terminator spectrum.

5.1 Data

The terminator region of HD 189733b is one of the best studied atmospheres among the known exoplanets in terms of number of measurements. The measurements range from 0.29 to 24 μm, obtained from both ground- and space-based telescopes. During the primary transit of HD 189733b, the radius ratio (defined as R_p/R_*) at mid-infrared wavelengths were measured in the four $Spitzer$/IRAC channels at 3.6, 4.5, 5.8, and 8.0 μm (Agol et al., 2009; Beaulieu et al., 2008; Désert et al., 2009), and, in the far-infrared,

Knutson et al. (2007) obtained an absorption depth in the 24 μm MIPS channel. There is a disagreement between the $Spitzer$/IRAC measurements that Beaulieu et al. (2008) showed the deeper spectrum compared with the one shown by Désert et al. (2009), which was due to their different data reduction processes (Fortney et al., 2010). In the NIR, Swain et al. (2008b) reduced the fifteen data points from the HST/NICMOS measurement using a linear light curve decorrelation method, while Gibson et al. (2011,b) reanalysed the NICMOS spectrum obtained by Swain et al. (2008b) utilising a full decorrelation method and stellar spot correction, for which they find a larger measurement error. Sing et al. (2009) re-visited the transmission spectrum using the NICMOS channels at 1.66 and 1.87 μm. Currently, the Wide-Field Camera 3 (WFC3), an instrument in operation on HST since 2009, has been producing spectra at wavelengths between 1.1–1.6 μm (Gibson et al., 2012). In the visible range at 0.55–1.05 μm and the UV at 0.29–0.57 μm, Pont et al. (2008) and Sing et al. (2011) acquired continuous absorption depths using ACS and STIS respectively on HST.

Only the HST/ACS (Pont et al., 2008) and NICMOS (Gibson et al., 2011; Swain et al., 2008b) observations will be taken into account in this study (see Figure 5.1). Due to the need for adjustment by the appropriate spot corrections between datasets made at different periods, the transmission spectrum with all currently available measurements are not available for retrieval. The rest of the data sets therefore are not regarded here in order to avoid a high degree of discrepancy between various observations and to find a first general solution for HST/ACS and NICMOS, which will play a critical role in the future study of the transmission spectrum with entire datasets. In this context, the objective of this study is to find the optimum solution explaining the HST/ACS and NICMOS measurements together before extending the study towards the shorter (HST/STIS, 0.29–0.57 μm) and longer ($Spitzer$/IRAC at 3.6, 4.5, 5.8, and 8.0 μm and MIPS at 24 μm) wavelengths. Presently, these HST/ACS and NICMOS datasets have not been characterised by any compatible scenarios; the ten HST/ACS data points were considered to provide a strong evidence for thick hazes or clouds at the terminators (Lecavelier Des Etangs et al., 2008; Pont et al., 2008; Sing et al., 2011) while the eighteen NICMOS channels were

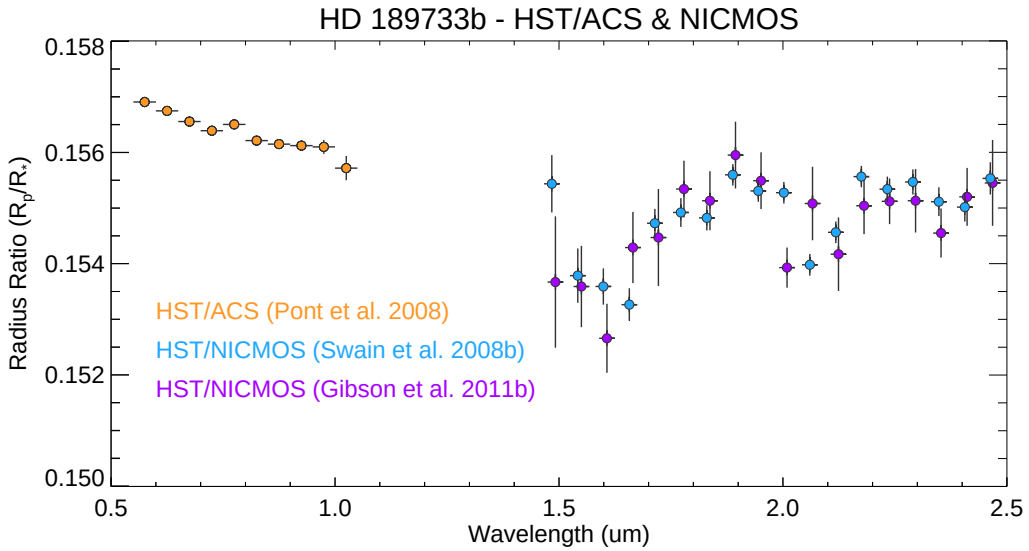

Figure 5.1: Datasets used for the retrieval of the terminator regions of HD 189733b, measured in the *HST*/ACS (orange) (Pont et al., 2008) and NICMOS (cyan and violet) (Gibson et al., 2011; Swain et al., 2008b).

either interpreted as having molecular absorption features of H_2O and CH_4 including the collisional induced absorption of hydrogen and helium (Beaulieu et al., 2008; Fortney et al., 2010; Swain et al., 2008b) or considered to provide evidence for the haze/cloud scenario (Gibson et al., 2011,b; Sing et al., 2009). Moreover, the *Spitzer* broadband measurements in the MIR are not consistent between studies (cf. Figure 7.2). This will be discussed more in Chapter 7.

5.2 Model

In general, it is extremely difficult to derive information on the atmospheric temperatures and aerosol content from a primary transit spectrum (Fortney et al., 2006; Marois et al., 2010; Seager, 2011, and references therein) due to the limited information available in the spectrum. It is therefore necessary to make some assumptions before performing a retrieval. Firstly, since temperature shows a low sensitivity with vertical variation and only affects the scale height (Tinetti et al., 2007b), the transmission spectrum may not provide strong constraints for a P-T profile retrieval, hence it is assumed here that the terminator region of HD 189733b has a similar thermal structure to the dayside of the atmosphere

(Lee et al., 2012). However, according to the observation at 8 μm of the $Spitzer$ IRAC channel (Knutson et al., 2007), the light curve of the brightness of HD 189733b showed that the planet's thermal structure in the dayside and nightside seems asymmetric, which is likely to be driven by the energy re-distribution mechanism between both hemispheres. This seems to cause the dark side to be cooler than the bright side, leading to non-uniform thermal structures across the globe and terminators. Therefore plausible temperatures must be considered for future retrieval studies. The $a\ priori$ P-T profile is therefore directly taken from the retrieved P-T profile of the secondary eclipse of HD 189733b [Figure 4.5 (a)]. The temperature structure is a fixed variable in this primary transit study. As described in previous chapters, the reference atmosphere covers a pressure range between 10^{-9}–10 bar. The collisional induced absorption opacity contributes at wavelengths greater than 1 μm, based on the interactions of H_2–H_2 and H_2–He.

The absorber species included are selected depending on the wavelength range covered by the measurement set involved in each retrieval process. Also, silicate grains of enstatite ($MgSiO_3$), a strong potential candidate for condensates in hot Jupiter atmospheres (Fortney, 2005; Helling and Woitke, 2006; Lecavelier Des Etangs et al., 2008), that is persistently produced by the reactions between SiO gas and forsterite (Mg_2SiO_4) (Visscher et al., 2010), are contained in the model so that the smoothly decreasing HST/ACS measurements with wavelength can be characterised by the extinction optical depth due to Rayleigh scattering of the haze/cloud. The real and imaginary parts of the refractive index for $MgSiO_3$ are taken from Scott and Duley (1996). The alternative Rayleigh scattering candidate suggested by Lecavelier Des Etangs et al. (2008), molecular hydrogen (H_2), is less likely. This is because the pressure required to explain Rayleigh scattering by H_2 is high ($\sim$400 mbar), which does not match up with pressures in upper atmospheres. The primary transit needs to be sensitive to the upper atmosphere as the spectrum obtained by HST/ACS shows high radius ratios at 0.5–1 μm, which means that a high opacity by any absorber is required to be present in the upper atmosphere. Due to the large number of parameters necessary to define haze/cloud properties, considering all the parameters to be retrievable variables would lead to extreme degeneracies and no meaningful conclusion

(i.e. too large uncertainties). A subset of haze parameters is used to choose the plausible solutions for the retrieval of the terminator of HD 189733b. More details will be described in Section 5.3.

To obtain the optimal solution for the HST observations, retrievals are performed in two successive steps: Firstly, the HST/ACS data points are fitted with a layer of haze/cloud having various thicknesses, along with H_2O, Na, and K, which show distinctive spectral features at 0.55–1.05 μm. The haze/cloud properties such as particle size (r_c), layer thickness (ΔP), and lower deck pressure (P_d) are defined in the parameter space used for the retrieval. Here it is assumed that the distribution of particle size has a very narrow Gaussian shape, allowing only one size for each case. Carbon bearing molecules that have no opacity sources in the ACS bandpass are not considered for this step. The prior information for H_2O is set to 10^{-4} with a scaling factor, 1, and its error, 20 (1-σ range = [2×10^{-13}, 5×10^{4}]). The abundances of Na and K are set to solar values (1.87×10^{-6} and 1.23×10^{-7} with error, i.e., 1-σ range = each value $\times$ $e^{\pm0.1}$) as their $a\ priori$ values (Anders and Grevesse, 1989). For Na and K retrieval, we give a small prior error range, which may not be variable over a wide range of mixing ratio if there isn't any strong measurement constraints. But the errors are subject to minimum in order to reject any scenarios fitted with a broad wings of Na and K, where their mixing ratios are unphysical, sometimes larger than 1, which is not plausible. Secondly, based on the solutions found in the first step, the HST/ACS points are retrieved again with either the HST/NICMOS data points by Swain et al. (2008b) or Gibson et al. (2011), increasing the spectral range to 0.55–2.5 μm. The different levels of confidence for the two versions of the NICMOS data result in two different interpretations. The molecular abundances for H_2O, CO_2, CO, and CH_4 are constrained in this step by the molecular absorption features in the NICMOS and ACS data.

5.3 Retrievals

5.3.1 HST/ACS - Extinction by Rayleigh Scattering

Pont et al. (2008) reported a near-linear decrease in the depth of primary transits with increasing wavelengths in the visible (0.55–1.05 μm), thought to be due to scattering by a haze/cloud composed of small silicate grains (particle size $<0.1\mu$m) rather than H_2 (Lecavelier Des Etangs et al., 2008). However, there is a debate on the wavelength region affected by the scattering of thick or thin hazes (Beaulieu et al., 2008; Gibson et al., 2011,b, 2012; Sing et al., 2008). As predicted in a theoretical model of a hot Jupiter (Sharp and Burrows, 2007), the opacity at wavelengths less than 1 μm is dominated by strong features of broad alkali metal (Na and K) lines and Rayleigh scattering by H_2 and He, which cannot provide enough opacity to fit the ACS dataset. However, additional scattering by a large amount of haze may blanket these spectral features and is able to fit the HST/ACS measurement as mentioned in various studies (Gibson et al., 2011b; Lecavelier Des Etangs et al., 2008; Pont et al., 2008; Sing et al., 2008, 2011).

Here, the HST/ACS transmission spectrum of HD 189733b (Pont et al., 2008) is initially used for the retrieval of haze/cloud properties. Due to the degeneracy between the given properties of haze and abundances of alkali metals and H_2O, fitting to the HST/ACS measurement is performed for all points in a grid space of haze particle size (0.003–1 μm) and number density (10^5–10^{18} g^{-1}) (Figure 5.2), and the best-fit retrieved for each grid point. The retrievals are performed for these grid points again with different layer thicknesses (compact layer to 8 dex in pressure) and haze/cloud deck pressure levels (10 bar – 10^{-5} bar) in order to find the most plausible aerosol properties of the atmosphere by fitting spectra to the ten HST/ACS data points with different acceptance criteria, as represented by χ^2/N_{obs} values of 1, 2, and 5 (5 being the most uncertain). This allows us to constrain reasonable ranges of atmospheric properties such as haze layer thickness, required nadir optical depth, particle size and the abundance of species (i.e. H_2O, Na, and K) with spectral features at these wavelengths.

As a result, Figure 5.2 illustrates a set of fits, plotted in a series of solutions along a

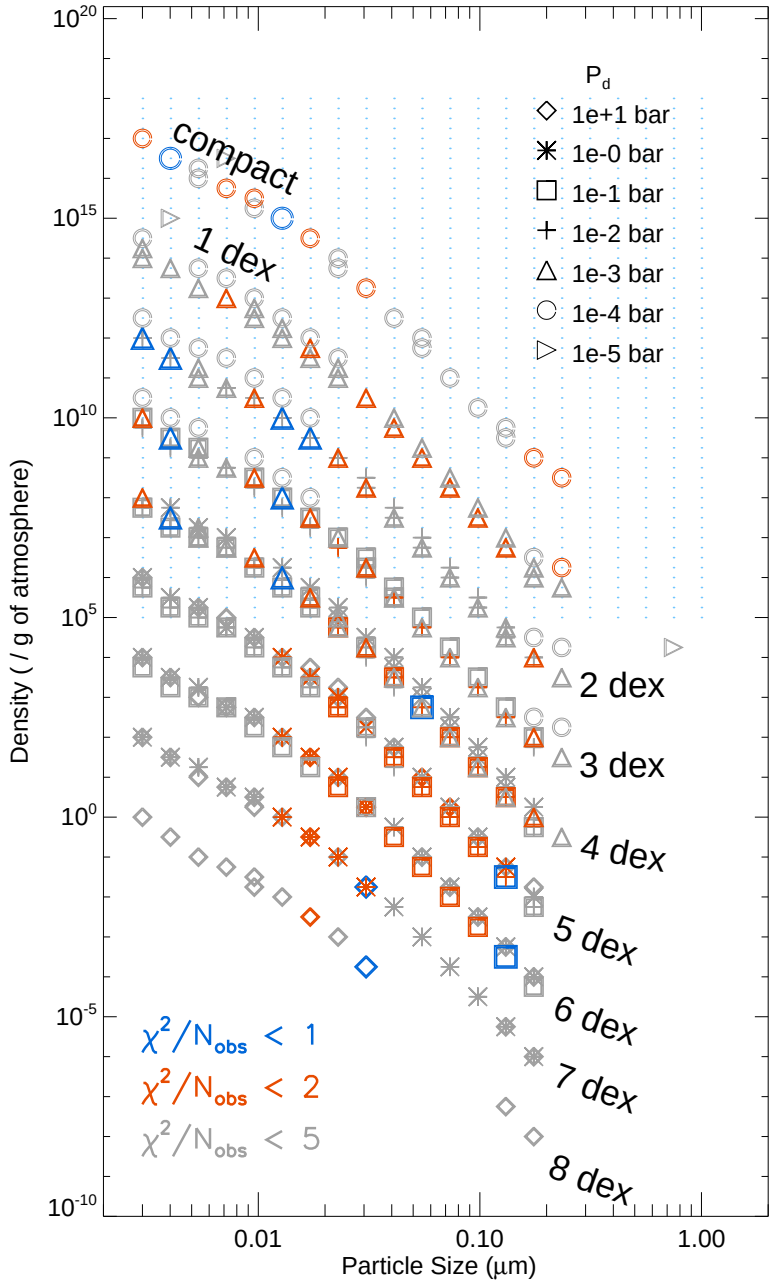

Figure 5.2: Subsets of hazes/clouds solution for the HST/ACS transmission spectrum of HD 189733b by Pont et al. (2008). Various scenarios, which are defined by the lower deck pressure, P_d (varying from the bottom of the atmosphere, 10 bar, to 0.01 mbar) and its thickness (from compact layer to ΔP = 8 dex), provide multiple fits to the ACS data points for χ^2/N <1 (blue), 2 (red), and 5 (grey). For clarity, a set of solution for each thickness scenario is shifted down by a factor of 0.01. It is found that the density (ρ) and particle size (r_c) are extremely correlated, leading to non-unique solutions for two parameters. Instead, we can say that only the particle size smaller than 0.25 μm is plausible to fit the measurements except a few fits by the hazy layer with P_d = 0.01 mbar and ΔP = 2 dex. The retrievals are performed for all grid points, marked in small blue dots. Note that this plot shows clearly that we can rule out the scenarios outside the fits presented. The corresponding spectra for the solutions are demonstrated in Figure 5.4.

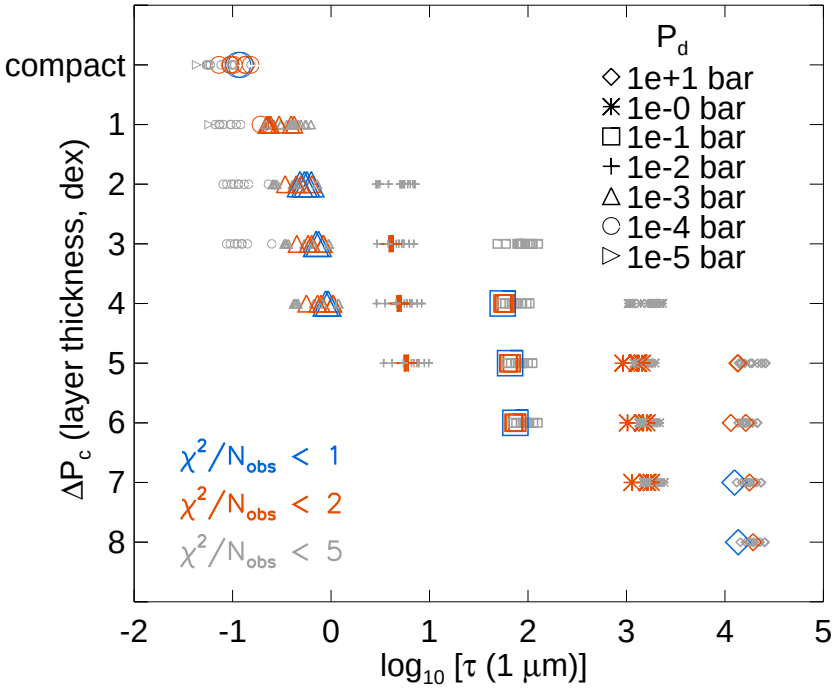

Figure 5.3: The nadir optical depths of the atmosphere corresponding to the points presented in Figure 5.2. The fits with a haze layer in same deck pressure (P_d), for most cases, give a unique optical depth, irrespective of the layer thickness (ΔP).

track for a given hazes/clouds thickness, retrieved by the various particle size and density with all hazes/clouds lower deck pressures. In general, it is found that good fits (χ^2/N<5) draw a track having a certain shape along diagonal direction, clearly demonstrating that any hazes/clouds density greater than $\sim 10^5$ g^{-1} is able to fit the ACS spectrum, regardless of any spatial conditions of the layer. Moreover, the degeneracy between density and grain particle size is extremely high, leading to large uncertainty. On the other hand, it is very clearly shown that the required particle size should be <0.25 μm and there is no solutions outside the diagonal track in the plot–the scenarios with low density and small particle or with high density and large particle whose cross-sections are too high or too low are certainly ruled out.

We calculate the corresponding optical depth (τ) at 1 μm to all the solutions plotted in Figure 5.2 and Figure 5.4 shows a set of the plausible optical depths for a layer of hazes/clouds against its thickness. The correlation between optical depth, layer thickness and even lower deck pressure is so strong that we are only able to determine the optical

depth with a large range (0.1–10000). The lower deck pressure (ΔP) of the solutions determines the overall optical depth of the hazes/clouds if the layer extends higher than the pressure level where it gives an equivalent radius ratio that corresponds to the ACS measurement (here it is $\sim$1e-4 bar). It is found that the plots in Figure 5.5, in which the spectra correspond to the grid points marked in Figure 5.4, show two groups of scenarios, spectrally defined by different constituents, where we can classify them with optical depth, i.e. optically thick, $\tau(1\mu m)>1$ and optically thin, $\tau(1\mu m)\leq 1$. The wavelength 1 μm is a reasonable point for the categorisation of the solutions because the spectrum at this wavelength is clearly reproduced by H_2O or extinction depending on the level of optical depth of hazes/clouds.

For the first group of spectra with optically thin layer, we see that the H_2O absorption is able to fit a sudden drop in R_p/R_* at 0.95–1.05 μm and a flat spectrum between 0.8–1.0 μm, whilst the broad wings and strong doublets of alkali metals define the spectrum shortward of 0.8 μm and a peak at 0.766 μm and 0.589 μm; the fitted spectra are slanted across the wavelength range due to atmospheric hazes with an optical depth at 1 μm less than unity. In particular, it is found that most of the good fits are obtained from the models with a compact haze/cloud layer crossing 0.1 mbar, by comparison with the pressures at the terminators corresponding to the HST/ACS radius ratios between 0.1 and 5 mbar as demonstrated in the first panel of Figure 5.4. Hence, when a haze layer is placed at either same or higher altitudes than the 0.1 mbar level, the fitted spectra are predominantly characterised by the features of H_2O and alkali metals above a steep opacity slope by hazes, whereas a layer at an order of magnitude higher pressure than 0.1 mbar suggest any plausible solution.

On the other hand, scenarios with an optically thick haze/cloud layer overlays compositional spectral features at most wavelengths and shows a smoothly decreasing extinction effect to fit the data, which shape is akin to the solution suggested by Gibson et al. (2011); Lecavelier Des Etangs et al. (2008); Sing et al. (2011). Each spectrum group in both plots provide evenly reliable fitting quality to the measurements, which implies that two hazes/clouds scenarios constrained from our retrieval can equally well explain the ACS

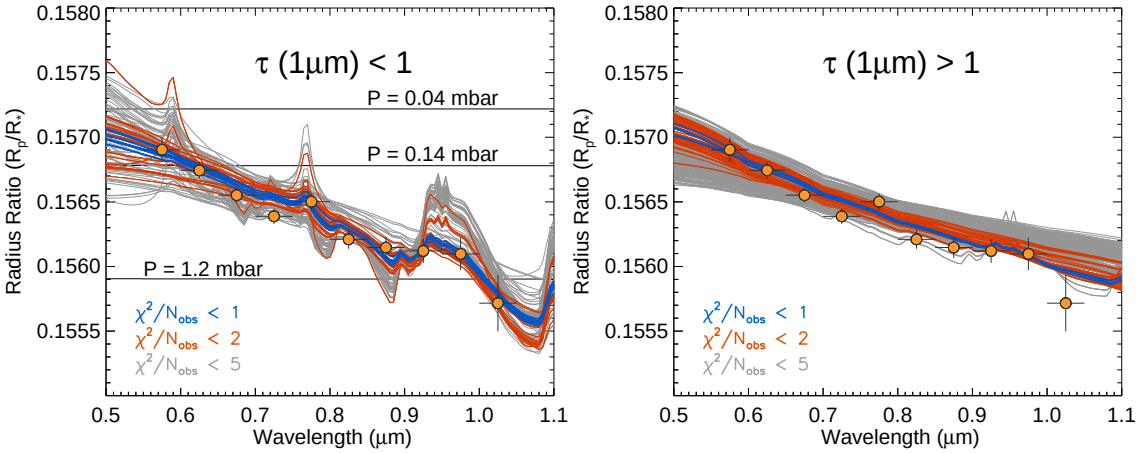

Figure 5.4: Each panel shows the fitted spectra to the HST/ACS data points with two different haze scenarios–an optically thin haze layer, $\tau(1\mu m) < 1$, and an optically thick haze layer, $\tau(1\mu m) > 1$). Each coloured spectrum corresponds to χ^2/N_{ACS} less than 1 (blue), 2 (red) and 5 (grey). With an optically thin hazes/clouds layer, most spectra show a hint of alkali metal lines (Na at 0.589 μm at and K at 0.766 μm) and the H_2O features at $\sim$0.7 μm and between 0.8 and 1.1 μm, whereas the overall shape of the fitted spectra with an optically thick haze/cloud layer is smoothly decreasing across the wavelength, where Mie scattering is predominant.

measurements and that are not enough constraints to propose more plausible one for the terminators. Fitting the ACS spectrum, the retrieved H_2O abundance ranges have (0.017–16)$\times10^{-4}$ for $\chi^2/N_{obs}<1$, (0.014–110)$\times10^{-4}$ for $\chi^2/N_{obs}<2$, and (6.8$\times10^{-5}$–350)$\times10^{-4}$ for $\chi^2/N_{obs}<5$, respectively. We can also constrain tightly the alkali metal abundances to (1.6–2.1)$\times10^{-6}$ for Na and (1.0–1.3)$\times10^{-7}$ for K with $\chi^2/N_{obs}<5$. But its ranges do not significantly vary from their $a\ priori$ values (1.85$\times10^{-6}$ for Na and 1.21$\times10^{-7}$ for K) due to their small prior error.

The scenarios giving acceptable quality of fitting found from the retrieval in this stage become the initial state vectors of the further retrieval with additional HST/NICMOS measurements. The constrained abundance of H_2O for each hazes/clouds scenario is adopted as the prior information for further retrieval with large error as it was in the first case. The procedure and results will be explained in the next section.

5.3.2 HST/ACS + NICMOS - Haze and Molecules

Swain et al. (2008b) suggested combined absorption features of H_2O and CH_4 in the

terminators of HD 189733b to explain the deep transmission features measured by HST/NICMOS. Given the best fit spectrum shown in Swain et al. (2008b), abundant H_2O was predicted as the predominant opacity source to explain spectral features between 1.45–2.5 μm, and a high absorption at 2.1–2.4 μm was likely to be yielded by a considerable amount of CH_4; this is deemed acceptable in a relatively low temperature region of a hot Jupiter's atmosphere and CO would be expected to be the most stable reservoir of carbon at the higher temperatures [e.g. Burrows et al. (2007)]. Swain et al. (2008b) applied a linear correlation method to the dataset so that they decorrelated the absorptions in eighteen channels from the measured stellar light curves. However, Gibson et al. (2011,b) argued that the removal of the systematics of HST data is rather challenging and requires a more sophisticated decorrelation technique due to its complexity. Among their various trials for the HST/NICMOS measurement, the Gaussian process method applied to the spectrum in Gibson et al. (2011) showed error bars at least twice as large for all channels and absorption features deeper than the one provided by Swain et al. (2008b). With a new light curve decorrelation method, Gibson et al. (2011) proposed that the NICMOS measurement might provide no robust evidence for the molecules of H_2O and CH_4. Since the reliability of the decorrelation methods suggested by the two groups is beyond the scope of this study, here each HST/NICMOS measurement is considered to provide an equally reliable constraint that can be applied to the further retrievals. The reason for separation of the two NICMOS results is to maximise the obtainable information from different constraints.

For the second retrieval stage with the additional HST/NICMOS constraints, the haze/cloud properties and alkali abundances are assumed to be equal to those determined from the HST/ACS data in the first stage. In particular, the fits retrieved at $\chi^2/N_{ACS}<10$ are chosen for further retrievals to allow the retrieval process to find fits for the ACS and NICMOS spectrum at $\chi^2/N_{NICMOS+ACS}<5$ using the haze layer, along with the molecules and atoms. Here again, the temperature structure is taken from the best fit case of the retrieval for the emission spectrum of HD 189733b (Lee et al., 2012). The molecules of H_2O, CO_2, CO and CH_4 are now considered to be retrieval variables for

the fitting of the NICMOS channels. The constrained H_2O abundances from the ACS retrievals become the prior information with a large assigned error. For other molecules, the nominal value of the volume mixing ratio, 10^{-4} and a large error (1-σ=$[a\ priori]\times$50), is assumed to be its prior information.

Case 1. HST**/ACS + NICMOS by Swain et al. (2008b)**

As the first case, secondary retrievals are performed with 28 data points where including the HST/ACS (0.55–1.05 μm) and the NICMOS data (1.45–2.5 μm) that was acquired by Swain et al. (2008b). Figure 5.6 demonstrates two sets of the retrieved spectra to the data sets across visible to NIR, in which each spectrum is assessed according to $\chi^2/N_{ACS+NICMOS}$. In general, it is shown that the atmosphere holding optically thin hazes/clouds (i.e. $\tau(1\mu m)\leq 1$) explains the NICMOS spectrum with deep molecular features, leaving the attenuation by a haze/cloud layer to fit the high ACS transit depths at shorter wavelengths. On the other hand, strong opacity by the hazes/clouds (i.e. $\tau(1\mu m)>1$) decreases smoothly up to 1.7 μm, where the H_2O feature is not prominent whereas CH_4 is able to explain the spectrum between 2.1–2.5 μm. Synthesising the results from the both cases, we only acquire $\chi^2/N_{ACS+NICMOS}<5$ and any scenarios cannot suggest good description on the NICMOS data at 1.5–1.7, 2.05 and 2.2 μm. As a result, the bad fits for these data points are the primary reason for the large goodness-of-fit. For the solutions retrieved with $\chi^2/N_{ACS+NICMOS}<5$, H_2O and CH_4 are necessary to fit to the transit depths at 1.5–2.1 and 2.1–2.5 μm and an opacity slope by extinction accounts for the ACS spectrum. Also, a tiny contribution of CO_2 and CO are seen at 2.0–2.1 and 2.3–2.5 μm.

Consequently, both silicate grains and molecules are required to fit the transmission spectrum of HD 189733b including the NICMOS spectrum from Swain et al. (2008b) within $\chi^2/N_{obs}<5$. However, we are unable to find a fit to this particular combination with $\chi^2/N_{obs}<2$, which is mainly due to the unfitted NICMOS channels at 1.5–1.7, 2.05 and 2.2 μm.

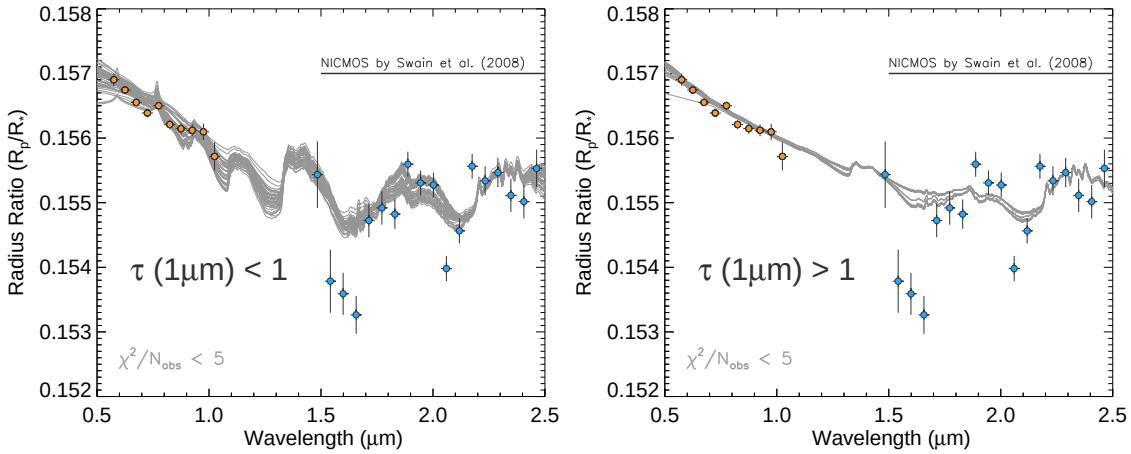

Figure 5.5: The fitted spectra to the data points of HST/ACS and NICMOS by Swain et al. (2008b) using optically thin ($left$) and thick haze layers ($right$). The spectrum colours refer to the fitting quality, $\chi^2/\mathrm{N}_{obs} < 5$ (grey), and we found no fit with $\chi^2/\mathrm{N}_{ACS+NICMOS} < 2$. For the spectrum shape at < 2 μm, the absorptions by two different opacity sources are complementary each other, leading to a high degree of degeneracy between H_2O and haze. For all cases, the fitted spectra show fitting quality worsened compared to the HST/ACS retrieval cases.

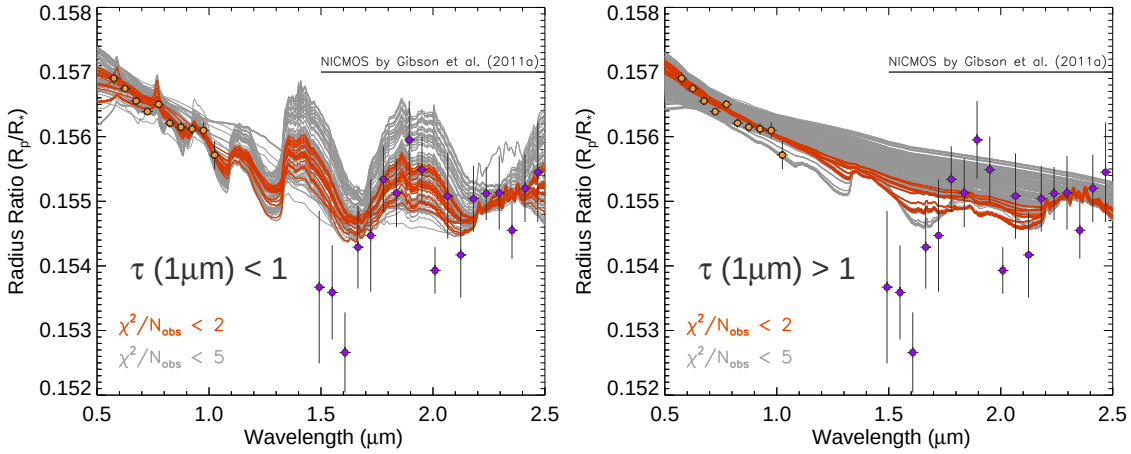

Figure 5.6: The fitted spectra to the data points of HST/ACS and NICMOS by Gibson et al. (2011) using optically thin ($left$) and thick haze layers ($right$). The spectrum colours refer to the fitting quality, $\chi^2/\mathrm{N}_{ACS+NICMOS} < 2$ (red) and 5 (grey). For most of cases, the overall quality of the fitting is worsened compared to the cases with the HST/ACS measurement only but are improved over the previous Swain et al. (2008b) retrieval, of course, owing to the 3–4 times enhanced error bars assigned from the systematics.

Case 2. HST/ACS + NICMOS by Gibson et al. (2011)

Unlike the NICMOS interpretation by Swain et al. (2008b), Gibson et al. (2011) found large uncertainties on the HST/NICMOS measurement, which are a factor of $\sim$2 larger than given by Swain et al. (2008b) (cf. Figure 5.1). Since the overall shape of the spectra analysed by two studies is similar, it is expected that the retrieved spectra will be more or less alike (i.e. R_p/R_* is low at shorter wavelengths, high R_p/R_* at middle wavelengths and mid R_p/R_* at longer wavelengths). Figure 5.7 clearly shows this trend that fitting is accomplished with either deep molecular features of H_2O and CH_4 (red in the left plot) or a high opacity of grains with deep CH_4 and blurred H_2O spectrum. A few times larger uncertainties assigned to the Gibson's data than the Swain's one allow more solutions, where an optically thick hazes/clouds smooths out all other spectrum at $<$2.1 μm that are identical to the ones proposed by Gibson et al. (2012); Lecavelier Des Etangs et al. (2008); Sing et al. (2009, 2011). However, this fact leads us to fitting the spectrum with a much broader range of potential atmospheric compositions and thus we encounter a broader range of uncertainties in the mixing ratios. Although the Gibson's NICMOS data points seem to allow for much more improved fitting, this certainly comes from the larger systematic errors. As a result, the one-to-one comparison for any results from the two NICMOS data are irrelevant in this study (i.e. Answering a question such as 'which data set is more plausible?' is not appropriate in this study). Since the aim of the study is to explore the plausible hazes/clouds solutions and to provide sensible scenarios explaining the ACS and NICMOS spectrum together which are extremely unclear, we will leave a statistical treatment of the measurement errors governed by different analysis tools for future work.

Consequently, the Gibson's NICMOS data provides various scenarios characterising the terminators with an optically thick or thin haze/cloud layer as we showed with the Swain's NICMOS data. We can also find some spectra decreasing to NIR, which are equal to the analytically calculated spectrum in previous studies. Therefore, our work is able to find all possibilities for the terminators, including the scenarios that suggested in literature. The larger systematic errors allow for improved fits but, this certainly increases

the possible range of the constrained molecular abundances. This will be discussed in the next section.

5.3.3 Retrieval of Molecular Abundances

Based on the fitting results from the one HST/ACS and two NICMOS datasets, we can constrained the range of the compositional abundances so that we represent the uncertainties of the molecular abundances. This is a similar technique to the method used for constraining abundances and temperatures from the dayside emission spectra in Chapter 4 and 6, being implemented by performing multiple retrievals. As clearly shown in Figure 5.4, 5.5 and 5.6, various hazes cenarios enable fitting to the measured transmission spectrum from HST/ACS and a combination of HST/ACS and NICMOS together at $\chi^2/N_{obs}<2$, if the HST/NICMOS measurement is taken from Gibson et al. (2011).

For $\chi^2/N_{obs}<2$, as seen in Figure 5.7 (also see Table 5.1), the H_2O volume mixing ratio from HST/ACS is constrained to (0.014–110)$\times10^{-4}$ and the H_2O and CH_4 from a combined measurement of HST/ACS and NICMOS by Gibson et al. (2011) are (0.0017–3.4)$\times10^{-4}$ and (0.031–0.18)$\times10^{-4}$, respectively. For all cases, the values are consistent or reduced compared with the previous results suggested by Swain et al. (2008b) (5×10^{-4} for H_2O and 5×10^{-5} for CH_4) and MS09 [(5–1000)$\times10^{-4}$ for H_2O and (0.1–3000)$\times10^{-4}$ for CH_4], which is possibly due to the fact that this study used a fixed P-T profile and an additional opacity from hazes, which can lead to an alternative composition to H_2O and CH_4 during the fitting. Also, it is possible to constrain the other molecules at $\chi^2/N_{obs}<5$, which produces (0.000068–350)$\times10^{-4}$ for H_2O with ACS only, $<3.8\times10^{-3}$ for H_2O, $<10^{-4}$ for CO_2, CO, and CH_4 with ACS and NICMOS by Gibson et al. (2011). The retrievals with the NICMOS measurement by Swain et al. (2008b) enable us to estimate the abundances to be (0.085–30)$\times10^{-4}$ for H_2O, $<3.3\times10^{-6}$ for CO_2, $<1.3\times10^{-6}$ for CO, and (2.5–5.8)$\times10^{-5}$ for CH_4, which are smaller ranges due to the smaller (e.g. underestimated) uncertainties on the Swain's data than Gibson's data. The amounts of CO_2 and CO were not reported in the earlier studies using ACS or NICMOS data. One number available for direct comparison is the CO volume mixing ratio in the equilibrium chemistry

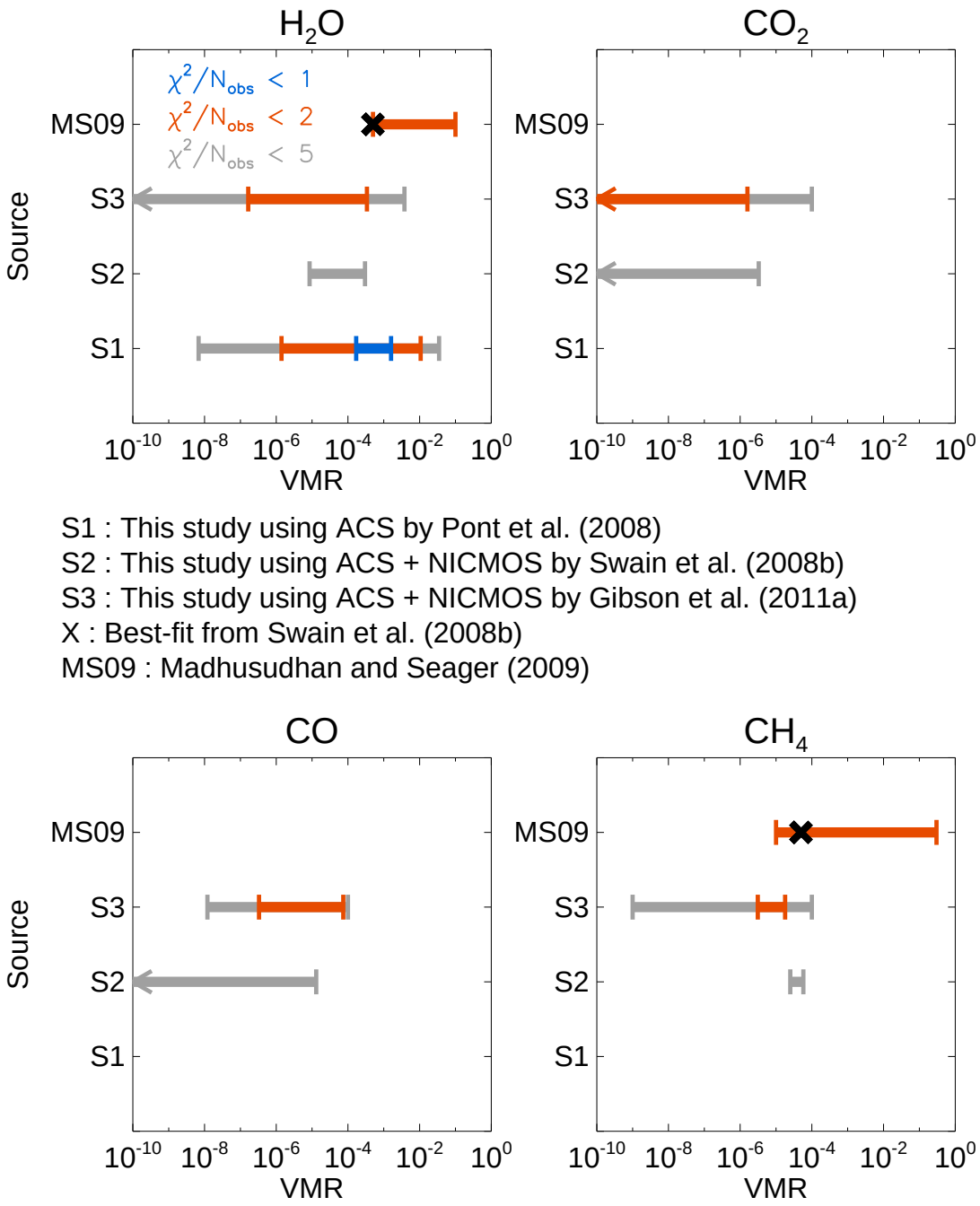

Figure 5.7: Each panel here illustrates the constrained molecular abundances for H_2O, CO_2, CO and CH_4 from this study with different measurement combinations, Swain et al. (2008b) and Madhusudhan and Seager (2009). The colours refer to the fitting quality, $\chi^2/N_{obs} < 1$ (blue), 2 (red) and 5 (grey). The lower bound of abundances less than 10^{-10} is marked with arrows. The abundance ranges for molecules corresponds to the ranges in Table 5.1.

Table 5.1: Constrained molecular mixing ratios and the C/O in the terminator region of HD 189733b.

	H_2O (10^{-4})	CO_2 (10^{-4})	CO (10^{-4})	CH_4 (10^{-4})	data source
Swain et al. (2008b)	5	-	-	0.5	HST/NICMOS
Madhusudhan and Seager (2009)	5–1000			0.1–3000	HST/NICMOS by Swain et al. (2008b)
This study	Best-fit value				
	1.4	8.5×10^{-5}	8.6×10^{-4}	0.41	HST/ACS + NICMOS (Swain et al., 2008b)
	1.2	3.2×10^{-4}	1.4×10^{-3}	0.048	HST/ACS + NICMOS (Gibson et al., 2011)
	Possible fit range				
	HST/ACS (Pont et al., 2008)				
	1.7–16				$\chi^2/\mathrm{N} < 1.0$
	0.014–110				$\chi^2/\mathrm{N} < 2.0$
	6.8×10^{-5}–350				$\chi^2/\mathrm{N} < 5.0$
	HST/ACS + NICMOS (Swain et al., 2008b)				
	...	...	...	...	$\chi^2/\mathrm{N} < 1.0$
	...	...	...	...	$\chi^2/\mathrm{N} < 2.0$
	0.085–30	<0.033	<0.013	0.25–0.58	$\chi^2/\mathrm{N} < 5.0$
	HST/ACS + NICMOS (Gibson et al., 2011)				
	...	...	...	...	$\chi^2/\mathrm{N} < 1.0$
	0.0017–3.4	<0.016	0.0033–0.74	0.031–0.18	$\chi^2/\mathrm{N} < 2.0$
	<38	<1.0	<1.0	<1.0	$\chi^2/\mathrm{N} < 5.0$

model by Fortney et al. (2010), determined to be 5×10^{-4} at higher altitudes than the 1 bar level based on the $Spitzer$/IRAC channel at 4.5 μm, which is a factor of $\sim$100 higher than the highest value estimated here. This is because Fortney's model assumed clear sky, which has no extra opacity source in the NIR except molecules, whereas the model in this study utilises CO to fit the NICMOS datasets, adding an additional opacity by haze/cloud. However, the CO sensitivity in the retrieval only appears in a narrow wavelength range (2.3–2.5 μm) and is too low to be constrained reliably (i.e. low sensitivity as seen in the functional derivatives in Figure 5.9). Therefore, the mixing ratio retrievals of CO and CO_2 should be derived using further measurements, either with very high resolution spectroscopy accompanying with a high signal-to-noise ratio or by including a broader range of wavelengths in the retrievals.

The retrieved abundances of carbon bearing molecules from the transmission spectrum of HD 189733b differ from those from the dayside emission in Section 4.4.2, which are a few orders of magnitude smaller than ones from the dayside retrieval. As demonstrated in Figure 5.9, only a limited number of the HST/NICMOS channels are available for the retrieval of CO_2 and CO, and the contributions to the fitting are small, leading to huge degeneracy ranges (see Section 4.4.2) with other parameters. Thus their abundances may have large uncertainties, which limits the direct comparison to the secondary eclipse results. The CH_4 abundance ($\sim10^{-6}$–$\sim10^{-5}$ for the best-fit primary transit spectra) that shows a high contribution over the wavelength range of spectrum is consistent with the degeneracy range ($\Delta\chi^2$/N) of less than 2.0 for CH_4 ($<2\times10^{-6}$) in the dayside atmosphere (Figure 4.8). Likewise, there is a good agreement in the H_2O abundance in the two atmospheres [$(0.002–3)\times10^{-4}$ from terminators (with Gibson's NICMOS) and $(0.15–600)\times10^{-4}$ from dayside], implying that H_2O is abundant and likely to be constant globally in HD 189733b. We will discuss about the chemistry of HD 189733b in Section 5.6.

Some of the HST/NICMOS transmission channels at 1.5–1.7 and 2.0–2.2 μm cannot be fitted well. These channels were not also fitted by any models in MS09 whereas Swain et al. (2008b) showed a well fitted spectrum to these channels. This discrepancy

is possibly due to gaps of the molecular line lists including the CH_4 list used for each study, which is one of the crucial uncertainties in radiative transfer calculations at high temperatures.

Although each of the H_2O and CH_4 abundances were obtained from different measurement combinations, the uncertainty ranges were not considerably different from each other. This means that the retrieval performed here is in agreement with the previous results on molecules in the terminator region, without any significant addition or reduction from the molecular abundances constrained by other studies. The haze/cloud properties derived by this study can also explain the decreasing visible opacity at high altitude. However, even if the calculated spectra agree well with the measurements, there is still a discrepancy between these results and others for the haze/cloud properties in the terminator regions, where various studies (Gibson et al., 2011,b, 2012; Lecavelier Des Etangs et al., 2008; Sing et al., 2009, 2011) postulated Rayleigh scattering, originating with thick hazes of silicate. Thus more measurement constraints and lower errors are required to confirm the most likely haze/cloud scenario for the terminator region in HD 189733b. Further retrievals with additional measurements will be shortly discussed and proposed for one of the future work items in Chapter 7.

5.4 Best-fit Spectrum

Figure 5.8 shows the fitted transmission spectra of HD 189733b among the solution found in the previous section. The two sets of best-fit molecular abundances of H_2O, CO_2, CO and CH_4 are 1.4×10^{-4}, 8.5×10^{-9}, 8.6×10^{-8} and 4.1×10^{-5}, fitted to the datasets of HST/ACS and NICMOS by Swain et al. (2008b) and 1.2×10^{-4}, 3.2×10^{-8}, 1.4×10^{-7} and 4.8×10^{-6}, fitted to the datasets of HST/ACS and NICMOS by Gibson et al. (2011). Although a more extended haze/cloud layer (0.1–1 mbar) with larger particle size (0.031 μm) is required for fitting to the HST/ACS and NICMOS measurement by Swain et al. (2008b) than the fit (a compact haze layer at 0.1 mbar and 0.003 μm) with the NICMOS measurement by Gibson et al. (2011), the optical depths for the two scenarios are

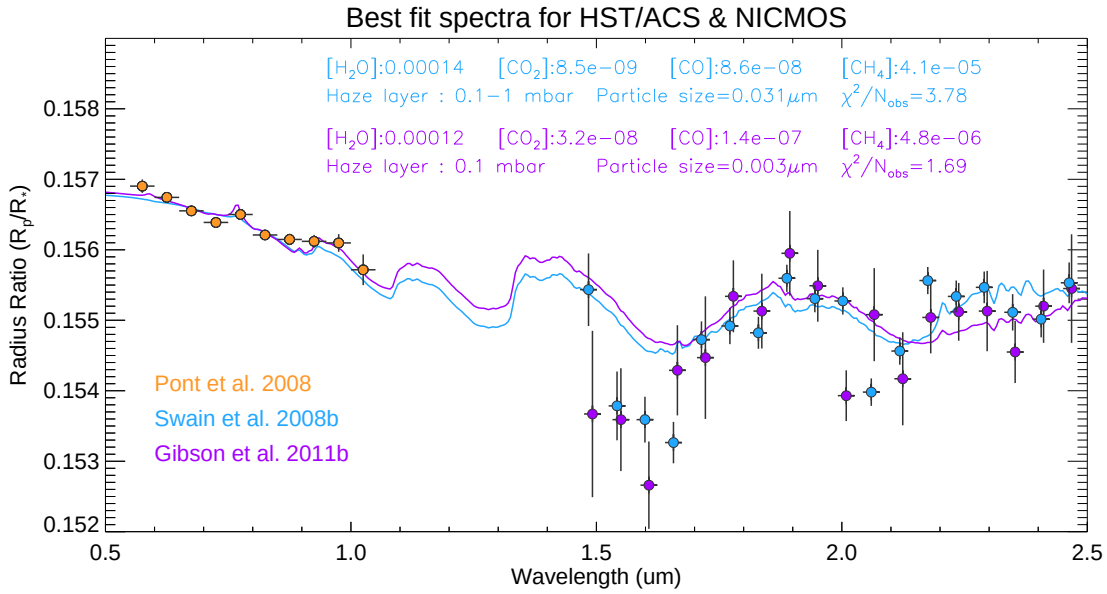

Figure 5.8: Transmission spectra fitting to the *HST*/ACS and NICMOS measurements of HD 189733b. Spectral features by Na and K each centred at 0.589 and 0.766 μm are just visible at < 0.8 μm. Continuous transit depths between 0.55–1.05 μm (Pont et al., 2008), and two NICMOS measurements between 1.5–2.5 μm by Swain et al. (2008b) and Gibson et al. (2011) are shown in orange, blue, and violet colour. The opacity by the haze extinction of Rayleigh scattering (< 1.0 μm) fits the ACS measurement. The spectral features by abundant H_2O and CH_4 are predominant at the NICMOS wavelengths.

consistent (0.061 and 0.071 each), which are sufficient to yield a smoothly decreasing *HST*/ACS spectrum at <1 μm and show a negligible opacity at the NICMOS band-passes. Moreover, owing to the optical depths as well as the H_2O abundances retrieved, both best fits show a similar spectral shape over wavelengths except >2.1 μm, where a clear distinction between two best-fit spectra are shown. This is because Swain's spectrum in this band requires an order of magnitude greater CH_4 abundance than Gibson's one, leading to a difference in the retrieved CH_4 abundance between the two fits. The difference in the CO_2 and CO abundance does not result in a prominent change in the spectra due to a small contribution to the fitted spectra.

5.4.1 Functional Derivatives

The eighteen measurements of the *HST*/NICMOS channels have a high dependence on H_2O absorption and, in addition, transit depths between 2.1–2.5 μm can be explained via

a high amount of CH_4. The abundances of CO, CO_2, and even NH_3 in the spectral model enable improvement in fitting the measurements at some channels (Swain et al., 2008b) but their contributions are visible in a few channels only. The primary transit spectra are therefore unable to provide strong constraints for their abundances. In Figure 5.9, the functional derivatives relevant to the best fit to Gibson's NICMOS data are displayed as a two-dimensional plot (pressure vs. wavelength). The figure demonstrates the corresponding pressures where the sensitivity to each retrieval variable is shown. The sensitivity of the spectrum to a haze/cloud layer of $MgSiO_3$ at 0.1 mbar is broadly stretched up to 2.5μm, showing the highest sensitivity at $<$1 μm and fitting the low radius ratios of the NICMOS measurements with molecular features. The spectra are sensitive to temperature and H_2O over a wide range of pressures. However, they are extremely correlated over the wavelengths, meaning that the retrieval must be performed with care to derive their values with more constraints. This justifies the reason why this study fixed the temperature at the dayside value. The CO_2 and CO have marginal sensitivity except at a wavelength region between 2.3 and 2.5 μm for CO whereas CH_4 is highly sensitive at 2.1–2.5 μm, where a low correlation with other parameters is present, indicating that the abundance of CH_4 is independently retrievable.

5.5 Additional Sources of Degeneracy

During secondary transit, it was shown in Chapter 4 that the assumption of the planet-star radius ratio (R_p/R_*) has a critical systematic effect on the retrieved temperature and compositions for the dayside atmosphere. For primary transits, the measured radius ratio at a certain wavelength is interpreted as the pressure level of the atmosphere where opacity sources that are able to fit the radius ratio exist (see Chapter 2). Hence, the uncertainty of the bottom level of the model atmosphere (here R_p at 10 bar level) gives a significant degeneracy problem for the retrievable factors. It is found that if the radius of the 10-bar level is increased by a certain amount, the pressure level of cloud layer that could fit the measurements in the visible in Figure 5.8 will be lowered by several scale heights.

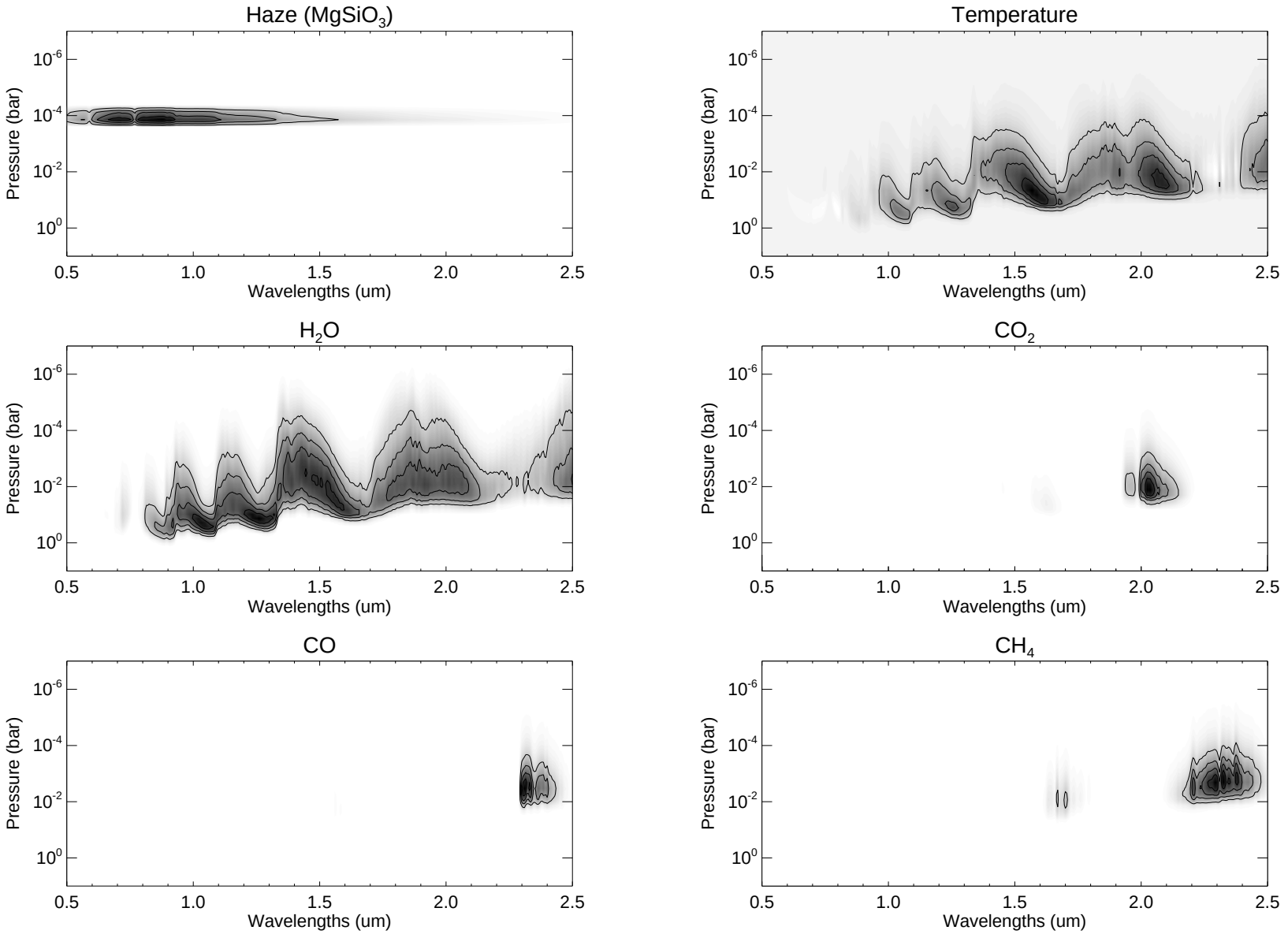

Figure 5.9: Two dimensional functional derivatives for haze/cloud, temperature, H_2O, CO_2, CO, and CH_4. All panels have been derived from the best fit to Pont's ACS and Gibson's NICMOS spectrum (violet spectrum in Figure 5.8). The sensitivities are plotted against pressure and wavelength.

Since the opacity by the haze/cloud layer is highly correlated with the temperature and pressure levels, we find that the retrieval with different haze/cloud scenarios will explain the datasets of HST/ACS and NICMOS. For a detailed description for the degeneracy caused by the R_p uncertainty, further investigations should be performed for all possible R_ps within its uncertainty range by defining the P-T profile, which originates from the dayside retrieval with a new R_p value, and, again, finding the best-fits for each R_p.

5.6 Discussion

5.6.1 A Note on the Global Haze Solution for HD 189733b

It is expected that the atmospheric states of the dayside atmosphere and terminator region of hot Jupiters is possibly explained by different chemical compositions governed by factors such as thermo- and photo-chemistry, global heat redistribution, cloud opacity etc. (Seager, 2011). However, the current measurements only provide enough constraints for broadly characterising the entire atmosphere of the planet. In this context, it is sensible to suggest a global haze/cloud solution for the whole atmosphere of the planet under the assumption that the haze/cloud characteristics are constant over HD 189733b. We find that the disk-averaged emitted radiance is not affected by an optically thin haze/cloud layer whereas an extra opacity coming from a thick haze/cloud layer blankets the dayside emission spectrum at <2 μm and 7–9 μm, where $MgSiO_3$ shows a high opacity. Therefore, no significant change in the spectrum was found, and there are still good fits to the whole emission spectra. Consequently, the measurements of the emission spectrum of HD 189733b does not contradict evidence for the haze/cloud scenarios constrained from the transmission spectrum. In other words, the hazes/clouds in the dayside atmosphere is plausible, meaning that an optically thin or thick haze/cloud layer that consists of small grains of $MgSiO_3$ can be one of the global solutions for the atmosphere of HD 189733b.

5.6.2 Terminator vs. Dayside

Chemistry Observations for the primary transit and secondary eclipse allowed us to constrain the molecular abundances and their uncertainties in the atmosphere of the terminators and dayside. For both atmospheres, the molecular constituents retrieved include H_2O, CO_2, CO and CH_4. Among them, H_2O shows deep absorption features in both spectra and the abundance of H_2O seems to be abundant evenly across the globe ($\sim 10^{-4}$). This is consistent with the theoretical chemical models, suggesting that the amount of H_2O is predominantly governed by metallicity of atmosphere, regardless of its temperature (e.g. Line et al., 2010; Moses et al., 2011), leading to a small difference in mixing ratio between terminators and dayside. Retrievals are also shown that CH_4, however, is not prominent in the dayside atmosphere, while it is a prominent species in the terminator atmosphere. Various studies indicate that CH_4 becomes more abundant at lower temperatures (nightside) than at higher temperatures (dayside) because its abundance is likely to be determined by 1) the temperature-sensitive transport-induced quenching[1] and by 2) photolysis at high altitude (Line et al., 2010; Moses et al., 2011; Visscher and Moses, 2011). Therefore our retrieved CH_4 abundances (low in the dayside and high in the terminators) can be explained well by the current theoretical chemistry of this planet. Unlike the retrievals for H_2O and CH_4, the uncertainties of CO (in both terminators and dayside) and CO_2 (in terminators) abundances are so large that a direct comparison between dayside and terminators will only become available with more observational constraints.

Thermal Structure The retrievals in this study have been conducted under the assumption that the thermal structures of the terminators are similar to the one in the dayside due to the low sensitivity of the transmission spectrum to the vertical thermal structure. However, this must be re-considered again for further studies. This is because the full light curve of HD 189733b that has been measured at 8 μm of the $Spitzer$ IRAC channel showed that the brightness of the day and night side is asymmetric, driven by the energy

[1]This is the value at the turning point of the vertical profile of CH_4, where the thermochemistry becomes disequilibrium. For a low temperature atmosphere, the quenching point is deeper and its mixing ratio is larger than the case at high temperature (see Figure 7. in Moses et al., 2011)

re-distribution mechanism between both sides, leading to the dark hemisphere being less warm than the bright hemisphere (Knutson et al., 2007). Although the thermal structure in the terminator regions is not yet well understood, plausible temperature profiles should be applied to the future retrievals so that we can characterise realistically the atmospheres based on current transit methodology.

5.7 Conclusion

During primary transit, transit depths of HD 189733b at visible wavelengths (0.55–1.05 μm) measured in HST/ACS were thought to be due to the extinction by hazes/clouds composed of $MgSiO_3$ (Lecavelier Des Etangs et al., 2008). On the other hand, the HST/NICMOS spectrum at NIR wavelengths (1.5–2.5 μm) were used to support two different scenarios; 1) a H_2O-rich atmosphere, including abundant CH_4 (Swain et al., 2008b) and 2) a hazy atmosphere, but the measurements provide no strong evidence for molecular features at NIR (Gibson et al., 2011,b; Sing et al., 2009). Here the main objective of our study were to retrieve plausible states of the atmosphere by fitting three sets of the HST measurements to constrain haze/cloud scenarios for the terminator region of this planet. To that end, we applied extinction opacity to a cloud-free atmosphere, which is caused by a haze/cloud layer characterised by four properties (single particle size, hazes/clouds density, lower deck pressure and thickness), whose values are defined in a parameter space. With different haze/cloud scenarios, we conducted consecutive retrievals using the ACS measurement and two different NICMOS measurements. A family of haze/cloud solutions for the ACS dataset were adopted as the first guesses of retrievals with the datasets in the visible and NIR together. By controlling the fitting and free parameters for each retrieval stage, this provides an efficient way to find global solutions for the atmosphere of terminator regions that show a strong extinction effect in the visible and even NIR. We conclude that the solutions for two different combined datasets are characterised by either optically thin or thick hazy atmospheres composed of small-sized particles, that also includes molecules of H_2O and CH_4 can reproduce the spectrum at >1.7 μm. Our approach

gives insight to constraining of haze and cloud properties from the transit measurement with a low S/N ratio, utilising two steps of retrievals.

Retrievals using the HST/ACS data were, firstly, performed for a grid space of different particle size and density. It was assumed that the haze/cloud primarily consisted of $MgSiO_3$, which was suggested as a strong candidate for condensates in the atmospheres of hot Jupiters (Helling and Woitke, 2006) and HD 189733b (Lecavelier Des Etangs et al., 2008), and that the layer is thin and placed at a certain pressure level rather than being vertically uniform. Using a fixed temperature profile that was retrieved from the dayside emission spectrum, we estimated the haze/cloud deck pressure levels and nadir optical depths of the atmosphere giving best-fits to the HST/ACS measurement. Secondly, using the plausible haze/cloud solutions from HST/ACS, retrievals were made to fit the HST/ACS data plus the NICMOS data at longer wavelengths. Successive retrievals with two different versions of the NICMOS data [i.e. Swain et al. (2008b) and Gibson et al. (2011)] were used to understand the implications of the different measurement uncertainties quoted by different decorrelation methods.

Four major findings can be determined from the transmission spectrum of HD 189733b. First of all, any nadir optical depth of a haze/cloud layer of $MgSiO_3$ is able to fit the HST/ACS measurements within fitting criteria due to the degeneracies between the properties of hazes/clouds and even compositions. In particular, we categorise the solutions into two groups in terms of optical thickness of haze/cloud layer, where the layouts of fitted spectra are clearly distinguishable. The ACS data is reproducible with a combination of absorptions by H_2O, K and Na as well as an additional opacity from an optically thin hazes/clouds whereas optically thick hazes/clouds provide an extinction slope. The categorisation is also valid in the successive retrieval stage with the NICMOS data sets. Given an optically thin hazes/clouds, extinction by $MgSiO_3$ weakens longward of 1.5 μm, leading to molecular absorptions becoming dominant at the NICMOS wavelengths. Extinction yielded by an optically thick hazes/clouds is efficient up to the mid wavelength of NICMOS, which also suggest a subset of reliable solutions for both NICMOS measurements. The results from two retrieval stages confirm that the measurements provide too

weak constraints to eliminate one of the solution groups that is less likely and that we can see the relationship between particle size and density, permitting us to reduce solutions in the parameterised space.

Secondly, a correlation between molecules and haze/cloud occurs much broader uncertainty of the molecular mixing ratios of H_2O and CH_4 than those by the previous studies (Madhusudhan and Seager, 2009; Swain et al., 2008b), in which the fittings were only made for the NICMOS channels analysed by Swain et al. (2008b). These results imply that although the radius ratio of the NICMOS spectrum is primarily achievable with any haze/cloud scenarios, molecular absorptions are necessary with broad uncertainties due to strong constraints at longer wavelengths. This fact therefore allows us to conclude that the addition of H_2O and CH_4 into the atmospheric model can improve fitting to the HST/ACS and NICMOS data sets compared to the model with haze/cloud only. Although the physics of a hazes/clouds layer are not yet clearly explained–this is because our understanding of condensation process in high temperature atmospheres is still not fully matured–the suggested scenarios of hazes/clouds and molecular features are fully consistent with the available data.

Thirdly, the constrained particle size of hazes/clouds is consistent with the analytic solutions suggested in previous studies. Lecavelier Des Etangs et al. (2008) state that among condensate candidates, $MgSiO_3$ gives the best fit refractive index properties to explain the decreasing visible opacity, and the particle size should lie between 0.01–0.1 μm for a temperature range of 1390$\pm$150 K, which values are consistent with the values retrieved from this study (i.e. particles smaller than 0.25 μm for an effective temperature $\sim$1250 K of this planet). These conclusions may not significantly change even though a different composition such as Mg_2SiO_4 is applied, owing to the fact that the absorption by hazes consisting of small particle sizes tends to the Rayleigh scattering limit.

Fourthly, the hazes/clouds solutions give a small influence on the dayside emission spectrum of HD 189733b. Any optical depths we find result in either a negligible effect on the spectrum or smearing the spectrum at wavelengths where a high extinction efficiency of $MgSiO_3$ exists, presenting that an insignificant change in the thermal structure and

composition compared with the retrieval with a cloud-free atmosphere. For comparison, a semi-analytical model of haze/cloud by Heng et al. (2012) provided evidence for a haze layer placed at $P < 1$ mbar in both the dayside and terminators of HD 189733b. However, their models predicted a shallow inversion between 1–100 mbar, caused by warming from the scattering of haze in short wavelengths at the given pressures, which was not clearly observed in this study. As suggested in Heng et al. (2012), more observations are required to confirm the suggested scenarios.

Despite the results that an extinction by silicate hazes/clouds gives a good explanation for the high absorptions at visible, more data with a high spectral resolution and signal-to-noise ratio are certainly required to break the degeneracy between fitting and free parameters involved in the retrieval. This suggests that future transit observations must be reproducible and improved enough to provide reliable evidences for haze/cloud characteristics and molecular abundances. The solutions provided by the novel retrieval method in this study will suggest a good starting point of the further retrieval with other primary transit observations for HD 189733b, e.g., a complete compilation of transmission spectrum between UV and FIR, conventionally synthesised by Pont et al. (2012). We hope that the simultaneous fitting of the broad spectral range of the primary transit spectrum of HD 189733b will provide new insights into the nature of the hazes/clouds and gaseous species contributing to the terminator spectrum.

Chapter 6

Secondary Eclipse of HD 209458b

Theoretical models predicted that the effective temperature of HD 209458b, which is a few hundred degrees warmer than that of HD 189733b, causes the planet to exhibit different chemistry and thermal conditions from those in HD 189733b, which categorises this planet as a pM or class V planet (Fortney et al., 2008; Hubbard et al., 2001; Sudarsky et al., 2000, 2003) that holds an inverted thermal structure in stratosphere. As suggested by follow-on studies, one plausible candidate for causing temperature inversion is strong UV or visible absorption by TiO and VO, the presence of which might be detectable during primary transit (Burrows et al., 2007, 2008; Désert et al., 2008; Fortney et al., 2008). Although the limited observations have been used to constrain distinguishable features from the dayside of HD 209458b such as a temperature inversion in the stratosphere, this has not been definitively probed (Madhusudhan and Seager, 2009, 2010; Swain et al., 2009a) and is still debated. Therefore, this study will use all available measurements of the hot Jupiter across a broad spectral range and will explain the thermal structure of the dayside atmosphere of HD 209458b, along with the molecular abundances including TiO/VO. Furthermore, we will discuss how the retrieved properties are different from other authors and what characteristics we can compare with those from HD 189733b. Ultimately, this comparison of the two benchmark hot Jupiters will allow us to understand how the proximity to the parent star influences atmospheric composition and thermal structure.

In the following sections, we will introduce the observations used and how we model the dayside atmosphere of HD 209458b.

6.1 Data

Unlike HD 189733b, fewer measurement sets are available for the dayside emission spectrum of HD 209458b. During the secondary eclipse, HD 209458b has been measured by three instruments, covering a wavelength range from 1.5 to 24 μm: 1) the four broadband channels of $Spitzer$/IRAC (3.6, 4.5, 5.8 and 8 μm) (Knutson et al., 2007) and the 24 μm $Spitzer$/MIPS channel (Deming et al., 2006); 2) the 16 μm $Spitzer$/IRS channel (taken from MS09) and the fifteen $Spitzer$ IRS (7.46–15.25 μm) channels (Swain et al., 2008b); 3) additionally, the sixteen HST/NICMOS (1.5–2.5 μm) channels (Swain et al., 2009a, hereafter S09b). There is no data available for the secondary eclipse at wavelengths shorter than 1.5 μm. The bin width used for each channel for flux integration are same as set for the HD 189733b retrieval study: 1) filter widths taken from the literature for $Spitzer$ broadband channels (Deming et al., 2006; Fazio et al., 2004; Rieke et al., 2004); 2) HST/NICMOS widths of 25 cm^{-1} ($\sim$10 nm at 2 μm); and 3) $Spitzer$/IRS widths of 15 cm ($\sim$100 nm at 8 μm). Also, the reference stellar spectrum for HD 209458 is taken from the Kurucz grid model (Kurucz, 2006) based on the stellar parameters listed in Table 4.1.

6.2 Model

The $a\ priori$ atmosphere model for HD 209458b is comparable to those applied for HD 189733b. This is because they are expected to be physically alike, having Jupiter-like mass and radius, high effective temperature, small orbital distance, and similar major composition. As used in the atmosphere of HD 189733b, the vertical range of the $a\ priori$ temperature profile is also sufficient to cover the full photosphere of the dayside atmosphere of HD 209458b over 10^{-9} to 10 bar. All constituents are assumed to be well-

mixed and each abundance is simply explained by a single scaling parameter. In the same manner, the fraction of H_2 and He are constrained to be the solar value (0.91 and 0.0887). However, one major difference between the two hot Jupiters is that the metallic oxides such as TiO and VO may play an important role in generating a thermal inversion and stratosphere on HD 209458b (Burrows et al., 2008; Fortney et al., 2008). The TiO and VO opacities may not impact the retrievals because the most of the TiO and VO lines occur at the shorter wavelengths, $<$1.5 μm (see Figure 3.14 and 3.15), which explain why these molecules become strong candidates for optical absorbers at stratosphere. More details on the test for the constrainability of TiO and VO will be discussed in Section 6.3.2. Again, the physical properties of HD 209458b used here are displayed in Table 4.1.

6.3 Best-fitting Spectrum of the Dayside of HD 209458b

The best-fitting solution gives the most statistically-plausible description for the state of the atmosphere and is a useful starting point to determine the range of uncertainties for temperature and molecules by finding the range of goodness-of-fit (χ^2) around the best-fit solution. Hence, in this section we determine the best-fit spectrum and atmosphere for the dayside of HD 209458b based on the best-fitting temperature (Section 6.3.3) and molecular abundances (Section 6.3.4).

6.3.1 Case study - Measurement Bias

The retrieval of the dayside emission spectrum of HD 209458b is more challenging than the one for HD 189733b due to the difficulty in fitting all available measurements simultaneously. As reported formerly, there are several plausible explanations for this problem: there may exist 1) atmospheric variability in HD 209458b, leading to a large fluctuation between different measurements (S09b), 2) data reduction diversity among the groups (MS09), or 3) complications in the calculation of a disk-averaged spectrum in which a single P-T profile may not represent the whole dayside hemisphere, i.e., dramatic dynamics on the hot (day) side. Here retrieval studies are carried out on an instrument-by-

instrument basis in order to see what each instrument contributes to our knowledge of the atmosphere, and whether the inference of a thermal inversion is supported by multiple studies, or just one alone. Four cases among various measurement combinations are displayed in Figure 6.1.

Case (a). The $Spitzer$/IRS Figure 6.1 (a) shows that the selected fifteen IRS channels between 7 and 15 μm can be fitted with a flat spectrum by H_2O absorption, which is produced by an isothermal layer at $\sim$10 mbar, rather than emissions by CH_4 and CO_2. Swain et al. (2008b) concluded that the IRS flat spectrum supports non-isothermal structure of temperature, who explained using emission features. These channels, however, do not provide enough constraints to determine a full vertical temperature profile and show no strong evidence for an inverted or a tropospheric temperature.

Case (b). The $Spitzer$/IRAC, MIPS and IRS In Figure 6.1 (b), all $Spitzer$ channels are used to constrain the temperatures between 0.1 and 10 mbar, producing an inversion layer at 1 mbar. Here the CO_2 and CH_4 emission features depart from the H_2O continuum to fit the 3.6, 4.5 and 8.0 μm IRAC and 14.3 μm IRS channels. In particular, this study is unable to find a proper scenario for a high flux ratio of the IRAC channel at 5.8 μm because of an absence of molecular features in our simple model which could produce this feature. To date, no viable candidates have been suggested which can successfully reproduce this spectral feature, except only S09b, whose spectra have deep absorption and emission features of H_2O, CO_2 and CH_4, which are not clearly produced in our model (see Section 6.5).

Case (c). The HST/NICMOS A retrieved P-T profile from the HST/NICMOS channels at 1.5–2.5 μm in Figure 6.1 (c) displays two constrained layers in the lower (0.1–1 bar) and upper (1 mbar) atmospheres. A troposphere with an adiabatically-decreasing temperature with altitude at 0.1–1 bar is constrained by a complicated combination of absorptions by the four molecules at 1.6–2.0 μm. The channels at 2.2–2.45 μm, where a CH_4 emission is shown, provide strong measurement constraints for the temperatures in

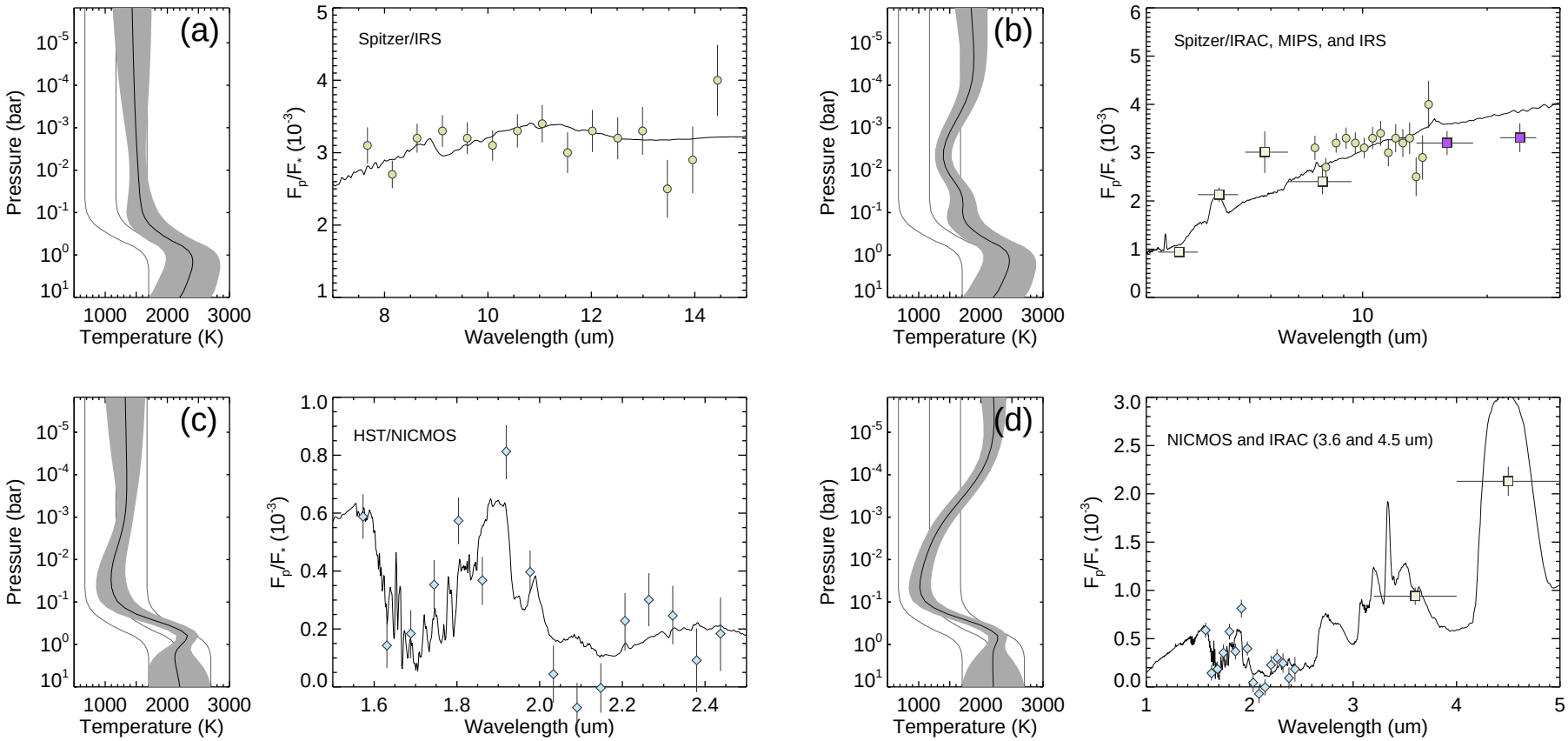

Figure 6.1: Retrieved P-T profiles and the best-fit spectra of the dayside HD 209458b using four different measurement combinations. Diverse combinations are used: (a) *Spitzer* IRS; (b) *Spitzer*/IRAC, MIPS, and IRS; (c) *HST*/NICMOS; and (d) *HST*/NICMOS and *Spitzer* IRAC (3.6, 4.5 μm only) channels.

the upper atmosphere (1 mbar). However, no strong evidence for a thermal inversion is suggested by the HST/NICMOS data alone.

Case (d). The HST/NICMOS and $Spitzer$/IRAC (3.6 and 4.5 μm) In Figure 6.1 (d), strong emission features of CH_4 and CO_2 fit the 3.6 and 4.5 μm $Spitzer$ IRAC channels, leading to a temperature inversion layer placed between 0.1–1 mbar (outside photosphere). As suggested in Case (c), the HST/NICMOS channels at 2.2–2.45 μm are characterised by the emission of CH_4. These results are consistent with those by S09b, where the NICMOS and IRAC measurements were used to support the presence of troposphere and stratosphere.

In summary, it is found that the $Spitzer$/IRAC channels at 3.6 and 4.5 μm and IRS channels at 7.7, 8.1 and 14.3 μm seem to provide no evidence for a thermal inversion in the photosphere of the dayside of HD 209458b, where previous studies proposed at altitudes higher than the 1 mbar. However, the rest of the $Spitzer$/IRS channels offer weak constraints for an isothermal structure at pressure levels between 10–100 mbar, which is needed to produce the flat H_2O spectrum at 9–13 μm. The HST/NICMOS channels between 1.6–2.0 μm constrain an adiabatically decreasing temperatures at low altitude ($\sim$100 mbar). On the other hand, we cannot reproduce the unusually large emission from 5.8 μm with any of the species considered in this study, as previous studies except S09b suggested before. A high flux ratio at 5.8 μm could indicate a possible thermal inversion at high altitude (Burrows et al., 2008; Knutson et al., 2007), but it is still not clarified by the observations yet. Therefore, we choose to omit the 5.8 μm $Spitzer$/IRAC channel from the remainder of this retrieval study. In Section 6.3.3 and 6.3.4, to confirm that increasing temperature with height at high altitude($>$1 mbar) is only produced by certain channels, we will show how contribution functions and functional derivatives change depending on the choice of $a\ priori$ P-T profile and in what way they can help us elaborate on the best-fitting spectrum.

6.3.2 Required Molecules to Reproduce the Data

The constituents of the dayside HD 209458b spectrum are typically thought to consist of absorptions by four major molecules of H_2O, CO_2, CO, and CH_4. As predicted and tested by several authors (Burrows et al., 2007, 2008; Crossfield et al., 2012; Désert et al., 2008; Fortney et al., 2008; Showman et al., 2009), metallic oxides such as TiO and VO are also expected at high altitude, absorbing stellar flux to produce the temperature inversion on HD 209458b (if it is indeed supported by the data). To investigate the plausibility of the molecules in the atmosphere, we controlled the number of priors so that retrievals are performed for various compositional combinations of these molecules. The atmospheric model containing both CO_2 and CH_4 certainly better reproduces the dayside flux ratios of HD 209458b compared to the models with H_2/He only, which is confirmed by considerably lowered χ^2 [from 197.8677 (H_2/He only) to 141.2688 (H_2/He + CO_2 and CH_4]. However, the addition of H_2O and CO produces only a small improvement in the χ^2 compared to atmospheric models with either H_2/He [from χ^2=197.8677 to 193.7112 (H_2/He + H_2O) and 190.5929 (H_2/He + CO)] or CO_2 and CH_4 [from χ^2=141.2688 to 136.5977 (H_2/He + H_2O + CO + CO_2) and 137.8922 (H_2/He + H_2O + CO + CH_4)]. Therefore, the inclusion of CO_2 and CH_4 is requisite for fitting the dayside emission measurements for HD 209458b but H_2O and CO are not critical molecules giving an enhancement in the fitting quality, which are not required to fit the data within the errors. Therefore, the abundance of H_2O and CO is not determined definitively by the given measurements, even when the full spectral range from 1.5 to 24 μm is taken into account.

Metallic oxides, suggested as potential candidates for strong optical absorbers in pM class (Fortney et al., 2008) and class V (Sudarsky et al., 2000, 2003) planets, may drive a thermal inversion in the dayside atmosphere of HD 209458b. Here we tested with only the measurements used in Case (d) in Section 6.3.1 because the TiO and VO opacities are mostly high at wavelengths shorter than a few microns. We conducted the retrieval with additional $a\ priori$ TiO and VO volume mixing ratios (10^{-5} with large errors) in the model atmosphere so that the constrained P-T profile and the fitted spectrum can be compared with those from Case (d). Figure 6.2 shows that there is no significant change

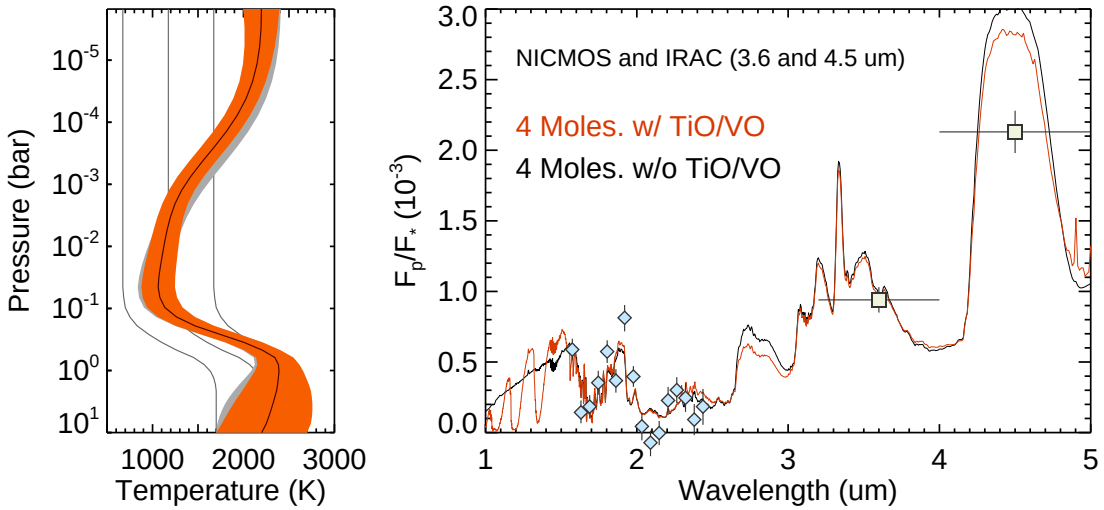

Figure 6.2: The retrieved P-T profile with additional TiO and VO (orange) above 1 bar shows a near-identical shape with the profile taken from Case (d) in Figure 6.1 (grey). Fitted spectra by these two atmospheric models give also similar flux ratios at all channels so the measurements do not provide enough constraint to determine TiO and VO with reliability. A wavelength range between 1 and 1.5 μm, where spectral features of VO are expected to be present, may be a useful bandwidth to be selected for future observation.

in the retrieved P-T profiles due to the metallic oxides, which are fitted with 5×10^{-9} for TiO and 4×10^{-7} for VO, and enhancement in spectral fitting quality is so marginal [from χ^2=45.92 (excluding TiO/VO) to 45.61 (including TiO/VO)] that the abundances of TiO and VO cannot be constrained with the datasets adopted in this study. As a result, Figure 6.2 exhibits the need for observations at $<$1.5 μm where we may find better constraints for metallic oxides in the dayside of HD 209458b. Further dayside observations or primary transit observations, as done by Désert et al. (2009), should be also required at the shorter wavelengths.

6.3.3 Best-fitting P-T Profile

Although different measurement constraints have been applied for different studies, there have been many observational evidence to support an inversion in the dayside atmosphere of HD 209458b. Knutson et al. (2007) and Burrows et al. (2008) proposed that there is a possibility of a steep temperature inversion at high altitude that is able to fit a high flux

ratio of $Spitzer$ IRAC channel at 5.8 μm. Using the $Spitzer$/IRAC, IRS, and MIPS, and HST/NICMOS observations, S09b suggested four plausible scenarios with and without an inversion layer, and concluded that a stratosphere with a temperature increase of 500–700 K is possibly located somewhere between 1–100 mbar. Moreover, MS09 and Madhusudhan and Seager (2010, hereafter MS10) demonstrated, using only the six $Spitzer$ photometry channels, that a thermal inversion is more likely to explain the observations with smaller fitting uncertainties than the fitting without an inversion, and suggested that a stratosphere can be placed at $\sim$30–500 mbar.

Our aim in retrievals of temperature profiles from exoplanet spectra is to limit the bias towards the $a\ priori$ atmospheric structures while achieving the closest possible reproduction of the spectra. To that end, we performed thermal retrievals with a variety of different initial temperature structures to test the sensitivity to the $a\ priori$, which are illustrated in Figure 6.3 (a) as an isothermal (pink) or a linearly-decreasing temperature profile (brown) throughout the atmosphere, a linearly-increasing temperature profile above the troposphere (blue), an isothermal layer to the top above the troposphere at 10 mbar (green) or at 100 mbar (orange), and an isotherm and a decreasing layer above the troposphere (grey). Various initial conditions for the retrievals are tested and each of these cases give the similar quality of fit to the data. Figure 6.3 (a) indicates that the retrieved P-T profiles commonly show an adiabatically decreasing layer up to 100 mbar that is akin to the dayside HD 189733b case, and a temperature increase above a quasi-isothermal layer at 1–100 mbar. The oscillations at 1–100 mbar seem to be unrealistic, which is due to the large error, initially assigned to the $a\ priori$. These non-physical oscillations can be narrowed by applying the reduced temperature prior error [Figure 6.3 (b)]. Temperature retrievals are then performed again, starting with a series of profiles, all inverted at high, isothermal at middle and decreasing at low altitudes from the 1 bar region, which were 400 K offset from each other, and these profiles still give only a tiny change in the fitting quality. Recalling from Section 4.4, the retrieved temperature profile is only valid for the pressure range where the contribution functions are sufficiently distributed. Thus the temperatures at altitudes beneath the 1 bar pressure level and above the 0.1 mbar pressure

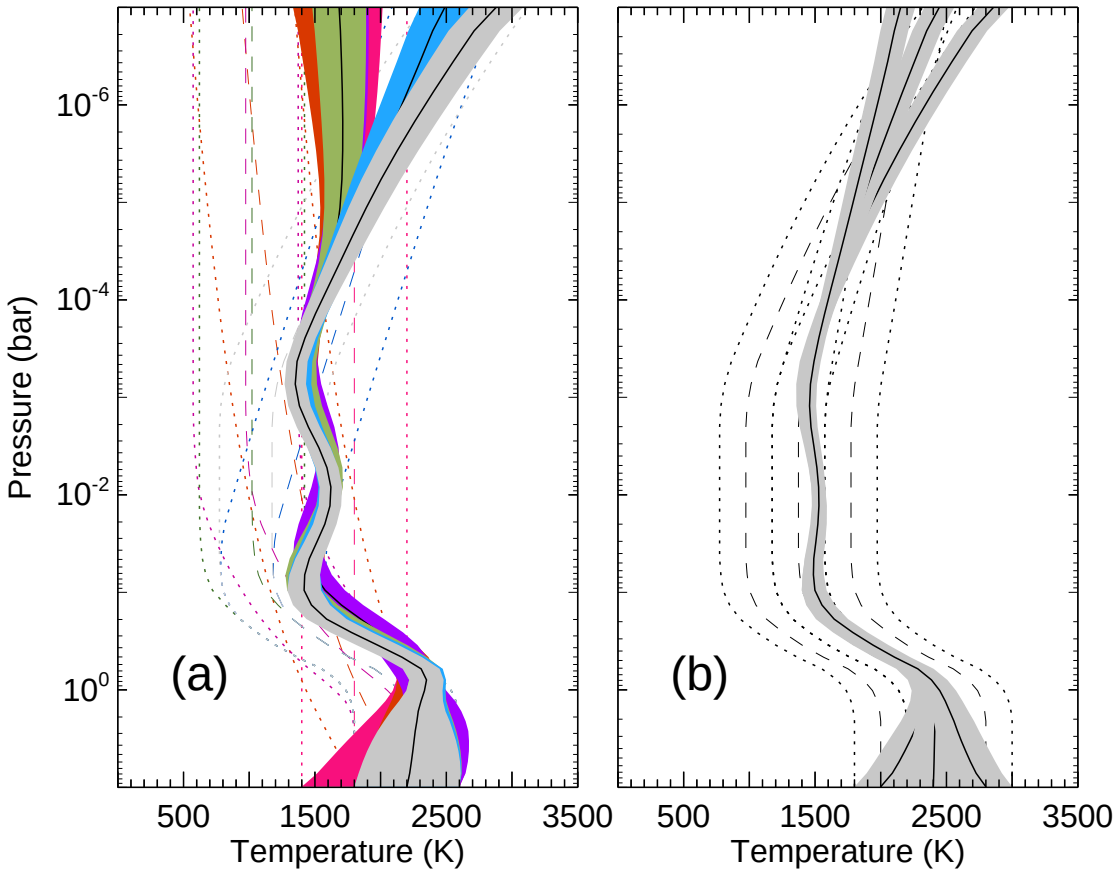

Figure 6.3: (a) Retrieved P-T profiles of the dayside of HD 209458b from a range of diverse prior profiles. The different lines show: $a\ priori$ P-T profiles (dashed), retrieved P-T profiles (solid) and their errors (dot-dashed and dotted). This plot shows the pressure range over which the P-T profile is retrievable from these measurements. (b) Retrieved P-T profiles from the same $a\ priori$ profile shape, but offset from each other with baseline temperatures at 1500 K, 1900 K, and 2300 K at 10 bar.

level show a large retrieval error and relax back to the $a\ priori$ profile.

As a result, the best-fit P-T profile has a temperature which decreases in the troposphere from 2400 K at 1 bar to 1500 K at 100 mbar and an isothermal layer at 1500 K that extends from 100 mbar to 1 mbar. Inverted temperatures between 0.1 and 1 mbar are also provided by the channels at 3.6, 4.5, 7.7, 8.0 and 14.3 μm. In Section 6.4, the uncertainty of the retrieved P-T profile will be discussed in detail.

6.3.4 Best-fitting Molecular Abundances

The best estimation for the volume mixing ratios for H_2O, CO_2, CO and CH_4 corresponding to the best-fitting model in Section 6.3.5 are reported in Table 6.1, along with the retrieval results from MS10 and S09b. The best-fitting model requires the inclusion of 1.9×10^{-6} for H_2O, 8.7×10^{-5} for CO_2, 2.0×10^{-2} for CO, and 4.0×10^{-3} for CH_4, respectively. It seems that the CO abundance is more enhanced than the CH_4 abundance, which is plausible scenario in such a hot temperature atmosphere unless there is very strong vertical mixing bringing CH_4 up as a disequilibrium species. However, since the CO abundance is weakly constrained and the retrieved uncertainty is much larger than CH_4, the conclusion on CO>CH_4 must be drawn with more datasets. Given the abundance of the carbon bearing molecules, the constrained C/O value for HD 209458b (C/O=1.2) is much higher than the one for HD 189733b (0.75), which is possibly driven by the different thermal structures of these two hot Jupiters. The uncertainty of the molecular abundances due to the degeneracy will be discussed in Section 6.4.

6.3.5 Best-fitting Spectrum

Figure 6.4 illustrates the best-fitting P-T profile and spectrum. It is shown that the best-fit spectrum of the dayside HD 209458b is characterised by both absorption at NIR (<2.5 μm) and emission at MIR and FIR (>2.5 μm). In the NIR, a high CH_4 abundance produces a deep absorption at 1.6–1.9 μm and a broad emission at 1.9–2.4 μm with CO_2 absorption, which is consistent with the results shown in S09b. To fit the $Spitzer$/IRAC

measurements, S09b suggested deep H_2O absorption features with emissions by CO_2 at 4.5 μm and CH_4 at 3.3 and 7.7 μm, which are not reproduced by our model (see Section 6.5). Instead, this study, taking advantage of a flat continuum coming from an isothermal layer above troposphere, fits the MIR broadband channels by considering a large amount of CO_2, CO, and CH_4, at the altitudes of $>$1 mbar, where the temperature increases with height. In this case, strong emission features departing from the continuum are produced by CO_2 at 4.5 μm, CH_4 at 3.3 and 7.7 μm, and CO at 4.5 μm. For $Spitzer$/IRS, S09b showed that absorption and emission by CO_2 that comes from troposphere and stratosphere each characterise all flux ratios except the channels at 7.5–8 μm. On the other hand, the calculated spectrum in this study rises in the MIR to fit flux ratios peaked at 7.7 and 14 μm but is unable to fit flux ratios at 8.15–10.57 μm with a flat spectrum.

Consequently, the best-fitting temperature of the dayside of HD 209458b shows an increasing temperature at 1 mbar, which is not shown in the case for HD 189733b. This is because the spectrum seems to be sufficiently sensitive to the thermal structure that a P-T profile without a temperature increase at very high altitude forms a dramatically different spectrum than the one with an inversion layer (Figure 6.4). As a result, the emission features of carbon bearing molecules originating in the stratosphere allow us to fit closely the flux ratios of channels at 3.6, 4.5, 7.7 and 14.3 μm. Details will be re-discussed in Section 6.4 and 6.5. Figure 6.5 demonstrates the contributions of H_2O, CO, CO_2 and CH_4 to the spectrum and that the CO_2 and CH_4 features are widely distributed across the wavelengths. This confirms that H_2O and CO play a smaller role in forming the spectral features.

6.3.6 Contribution Functions

Inversion vs. No Inversion at $>$1 mbar

The contribution functions vary depending on the retrieved P-T profiles. Here we compare two sets of contribution functions calculated from a non-inverted and an inverted

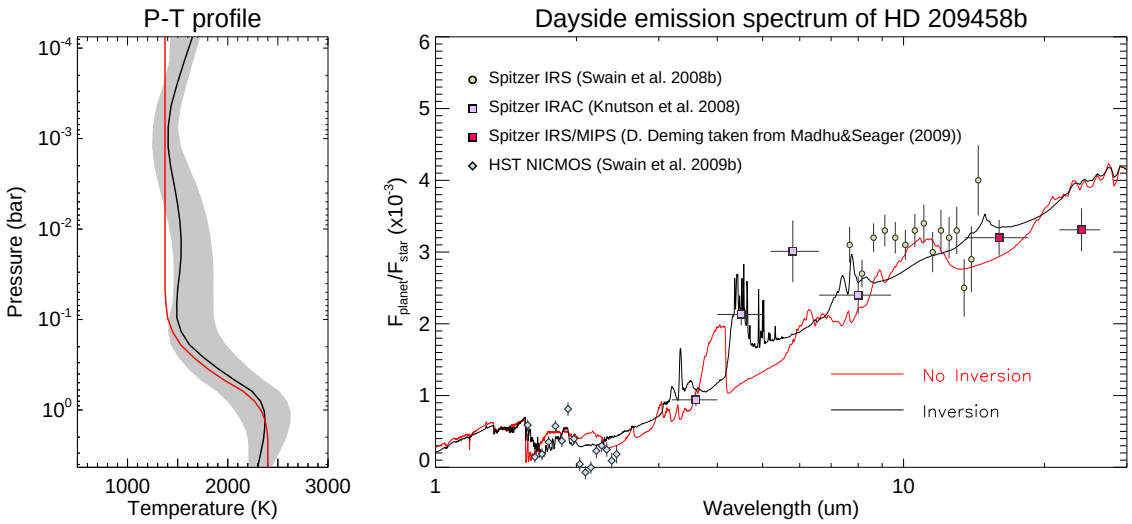

Figure 6.4: Retrieved best-fit P-T profile of the dayside HD 209458b in the left panel demonstrates an adiabatic troposphere and a weak thermal inversion at $>$1 mbar. The uncertainty range of temperature is displayed in grey colour. The best-fit spectrum in the right panel is constrained from 36 channels of all measurements except the 5.8 μm $Spitzer$/IRAC channel which provides no contribution to the retrieval. The green, purple and red, and cyan symbolise the measured planet-star flux ratios from the $Spitzer$/IRS spectroscopy (Swain et al., 2008b), the $Spitzer$ broadband photometry (Knutson et al., 2008, D. Deming taken from Madhusudhan and Seager (2009)), and the HST/NICMOS spectrophotometry (S09b). A spectrum in red colour demonstrates the best-fit spectrum using the P-T profile with an isotherm, which is red-coloured in the left panel.

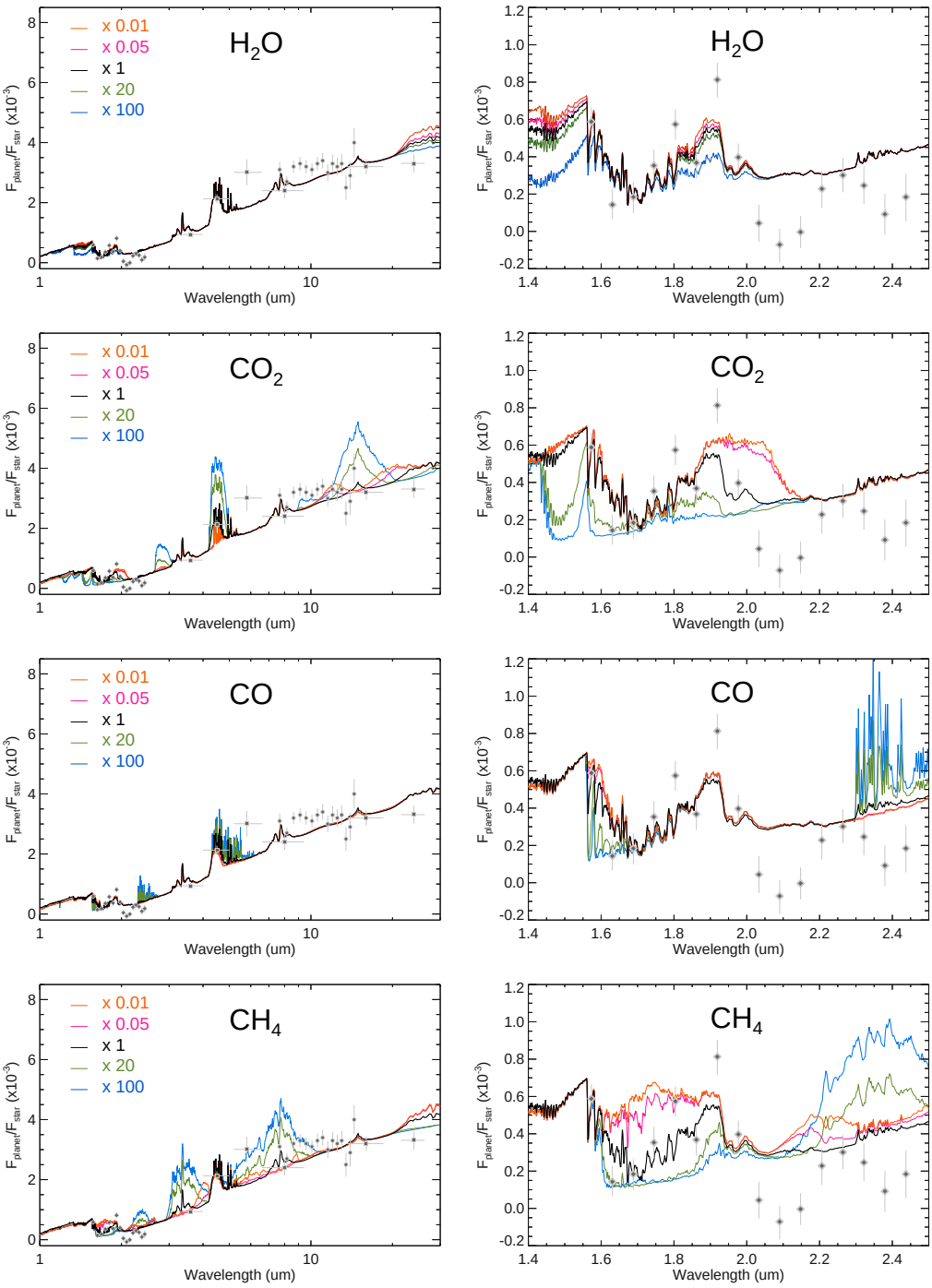

Figure 6.5: Fitted dayside emission spectra of HD 209458b. This is HD 209458b version of Figure 4.6. The black line shows the best-fit spectrum retrieved by the NEMESIS algorithm. Overlapped calculated spectra with various molecular abundances allow us to understand the regions of contribution of different molecules to the best-fit spectrum. For all cases, molecular abundances are varied 0.01, 0.05, 20.0, and 100.0 times from the abundance leading to the best-fit spectrum.

P-T profile. This helps to explain why an inversion at $>$1 mbar in the atmosphere of HD 209458b is only produced by certain channels. The P-T profiles used in the test are displayed in Figure 6.4.

Figure 6.6 shows the normalised contribution functions for these two P-T profiles. In the top panels, as a result of the isothermal structure above the troposphere (red profile in Figure 6.4), most of the contribution functions have their peaks at between 30 mbar to 1 bar, leading to absorption features at locations where strong emission features of CO_2 and CH_4 are seen in the best-fitting spectrum. The contribution function of the IRAC channel at 4.5 um has a dual modal profile. This is because this photometry channel has 1 μm bandwidth ranging from 4.0 and 4.5 μm, where the spectrum is reproduced by two different temperature levels. The spectrum at shortward of 4.3 μm comes from a deep atmosphere of 1 bar, which holds temperature warmer than 2000 K (i.e. high flux ratio), whereas the spectrum at longward of 4.3 μm is formed in a high atmosphere of 70 mbar, which is relatively colder temperature 1400 K. On the other hand, Figure 6.6 also shows that the observations are sensitive to the inverted P-T structure at 1 mbar in only a small number of the $Spitzer$ channels. These channels, at 3.6, 4.5, 7.7 and 14.3 μm, are the only ones which show sensitivity to the altitudes of the proposed temperature increase at $>$1 mbar, where the emission features are explicitly shown.

Contribution Functions for the Best-fitting Solution

By the latter case in the section above, we can see which channels contribute to different spectral regions if we consider the P-T profile with a temperature inversion above photosphere. The radiance contributions by the $Spitzer$ broadband channels are located at pressures between 20 mbar and $\sim$0.1 mbar whereas the function for the 16 μm IRS has a peak at 7 mbar. As described above, three $Spitzer$/IRAC channels at 3.6, 4.5, and 8.0 μm and two IRS channels at 7.7 and 8.1 μm provide the contributions for an inversion at higher altitude than the 1 mbar region, where strong CH_4 and CO_2 emissions are explicit. The thirteen $Spitzer$ IRS measurements have sequentially overlapped contribution functions between 4 and 100 mbar, from which an isothermal atmosphere is required to

reproduce the flat spectrum. The shorter wavelength channels of HST/NICMOS are used to constrain the temperature in the lower atmosphere (0.04–1.5 bar) whereas the channels in the wavelengths longward of 2.2 μm are responsible for the upper atmosphere at 1–4 mbar. The radiance from the lower atmosphere therefore characterises the temperatures at pressures where no contribution functions are covered by the $Spitzer$ channels.

In summary, fitting the broad spectral range covered by both HST and $Spitzer$, the P-T profile of the emission spectrum of HD 209458b can be constrained at broad pressure levels ranged from 0.1 mbar to 1.5 bar. However, due to the coarsely-spaced peaks of the contribution functions, it is expected that the constrained P-T profile has large uncertainty over most of the altitude range due to the high degeneracy between temperature and molecular abundances. The degeneracy issue will be discussed in Section 6.4.

6.3.7 Functional Derivatives

Inversion vs. No Inversion at >1 mbar

The resulted functional derivatives are the functions of the rate of change of the radiance with the retrieved atmospheric properties. Comparison between the vertical functional derivatives determined by two P-T profiles in Figure 6.4 can provide insight into the sensitivity of molecules at particular channels to the spectral regions showing emission features. Figure 6.7 shows the functional derivatives for all channels, being derived from the P-T profile with and without a temperature increase. The sensitivities are normalised to the highest peak of the functional derivatives for each measurement set. It is found here that when a P-T profile without a temperature increase is applied, all the channels (left panel in Figure 6.7) show negative sensitivities, which indicate absorption features on the spectrum, coming from a temperature-decreasing layer below an isotherm. In contrast, when a temperature increase layer is added at $\sim$1 mbar, a combination of positive and negative functional derivatives characterises molecular sensitivities to the fitted spectrum (right panel in Figure 6.7) by resulting emissions from stratosphere and absorptions from troposphere and isotherm. Consequently, we can find that the best-fitting spectrum is

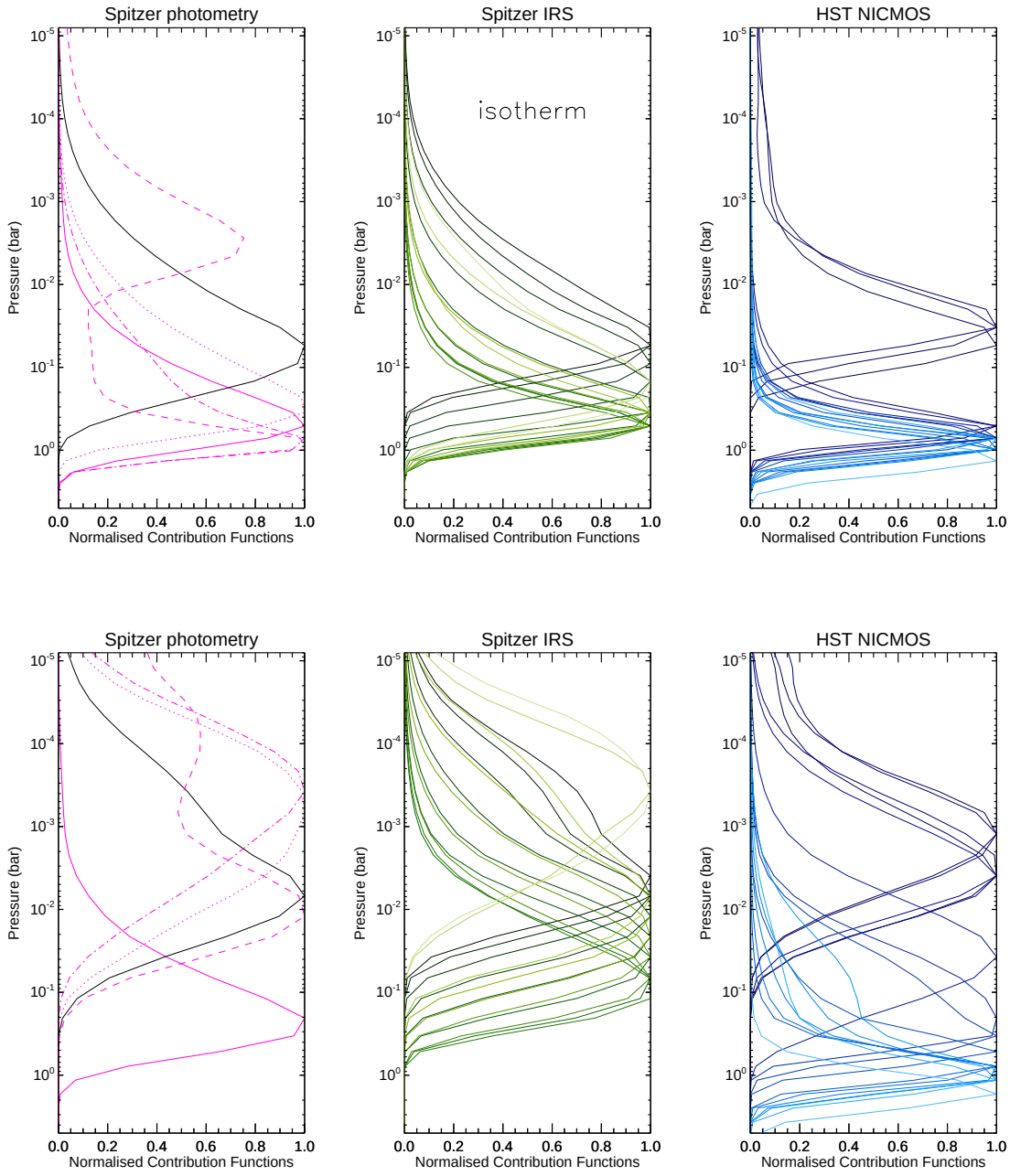

Figure 6.6: Two sets of contribution functions for the channels used for the HD 209458b dayside retrieval. The functions are resulted based on different P-T profiles that are displayed in Figure 6.4. For the $Spitzer$ broadband photometry channels, the solid, solid-black, dotted, dashed, dot-dashed lines correspond to the MIPS 24 μm, IRS 16 μm, IRAC 8.0 μm, 4.5 μm, and 3.6 μm channels. The brighter colours for the $Spitzer$/IRS and the HST/NICMOS channels denote the channels at the shorter wavelength. The top panels are yielded from a P-T profile without a temperature increase layer at $>$1 mbar. The functions are mostly peaked at between 30 mbar and 1.5 bar, where troposphere is located. On the other hand, the bottom panels, which come from a P-T profile with an inversion at above 1 mbar, show the radiance from the channels at 3.6, 4.5, 7.7, 8.0 and 14.3 μm characterises the emission features on the spectrum.

characterised by strong emission features of CO_2 at 4.5 and 14.3 μm and CH_4 at 3.6, 7.7, 8.0 and, even, $>$2–2.5 μm, where a weak emission is yielded, and the emissions at some wavelengths allow fitting the measurements better than the one with a non-inverted P-T profile at $>$1 mbar. Therefore, it is possible that these spectral features provide information concerning the presence or absence of a thermal inversion at any pressure level in the dayside of HD 209458b.

Functional Derivatives for the Best-fitting Solution

The molecular sensitivities for the best-fitting spectrum (right panel in Figure 6.7) are divided into three pressure levels, at $\sim$100 mbar, $\sim$1 mbar, and $>$0.1 mbar. The positive sensitivities at $>$0.1 mbar indicate emission features departing from the continuum, which is characterised by the absorptions of molecules at two lower layers, showing negative sensitivity for all cases.

From sensitivity for the $Spitzer$ photometry, the 24 μm MIPS channel is characterised by the absorption of H_2O, CO_2 and CH_4 at 100 mbar. Also, combinations of strong emission and weak absorption of CO_2 and CH_4 are dominant at the 16 μm IRS broadband channel and 3.6, 4.5 and 8.0 μm IRAC channels. The $Spitzer$/IRS channels are only sensitive to the CO_2 and CH_4 abundance, showing that the shorter and longer wavelengths are separately constrained by CH_4 and CO_2, of which emission features would produce high flux ratios at 7.7 and 14.3 μm. Sensitivity to all the molecules is seen in all the HST/NICMOS channels which show that the channels at 1.57–1.63 μm and 1.75–1.98 μm mainly constrain the H_2O abundance. The HST/NICMOS channels at $<$2.15 μm are sensitive to the CO_2 and its contributions are clustered in the 100 mbar region. The CO sensitivity is seen at both greater than 100 mbar and less than 0.1 mbar, being used to fit the spectrum at 1.57–1.75 μm and $>$2.32 μm. In the case of CH_4, high sensitivity is distributed at all altitudes, showing that a combination of the absorption at $<$2.03 μm and the emission at $>$2.09 μm of HST/NICMOS is able to constrain its abundance.

In summary, the functional derivatives show different sensitivities depending on the chosen temperature profile. This implies that there is a difference in our ability to de-

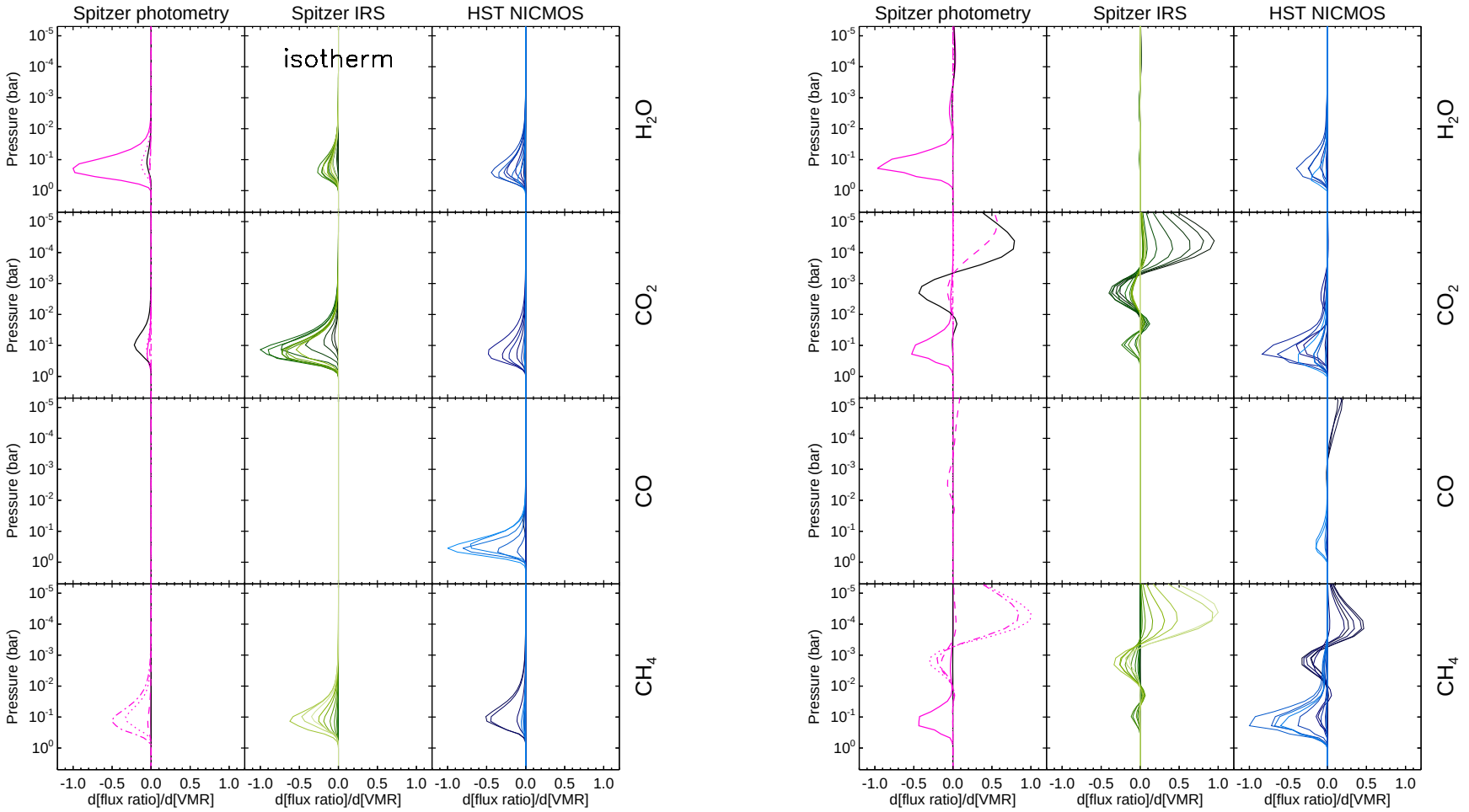

Figure 6.7: Two sets of functional derivatives for the $Spitzer$ and HST channels and molecules used for the retrieval of the dayside of HD 209458b. Two different panels are the results of the retrievals with the P-T profiles in Figure 6.4. The functional derivatives of molecules are normalised to the highest sensitivity between each measurement set. The applied colours are the same as those described in Figure 4.3 and each row shows the vertical sensitivity of radiance with respect to the abundances H_2O, CO_2, CO, and CH_4 (from top to bottom). The plots in the right panel show that strong CO_2 and CH_4 emissions originated from an inverted P-T profile fit the measurements at 2-2.5, 3.6, 4.5, 8.0, and 14.3 μm, which is a more-likely scenario than the fitted spectrum by a non-inversion P-T profile at $>$1 mbar (left panel).

termine the amount of molecular abundance depending on the thermal structure. For the best-fit case, the functional derivatives demonstrate that the absorption at 1 and 100 mbar and the emission at 0.1 mbar characterise the dayside emission spectrum of HD 209458b. The emission features are delivered by the CO_2 and CH_4 lines, where the spectra measured by *Spitzer* and *HST* provide enough sensitivity to constrain the abundances of these two species with low retrieval errors. The H_2O abundance is constrained by the 24 μm *Spitzer* MIPS channel with the additional *HST*/NICMOS channels at the shorter wavelengths (1.57–1.63 μm and 1.75–1.98 μm). Small sensitivity in the four *HST*/NICMOS channels (1.57–1.75 μm and $>$2.32 μm) are used to loosely constrain the CO abundance at 0.1–1 bar and the upper altitudes that 1 mbar. However, the *Spitzer*/IRS channels provide no sensitivity for constraining H_2O and CO abundances.

6.4 Temperature Degeneracy

Due to the large uncertainties inherent in the measurements and the lack of prior information, it is expected that the degree of degeneracy between the temperature and the molecular abundances will be significant for most pressures. Recalling the technique used to characterise the uncertainty explained in Section 4.4, the range of temperature uncertainty can be found by performing multiple retrievals with different molecular abundances, varying the molecular abundances in a wide range (10^{-7}–10^{-1}). Given the best fit *P-T* profile in Figure 6.3, the temperatures, as shown in Figure 6.8 (a), are severely degenerate with the abundance of molecules, of which the H_2O, CO_2, and CH_4 abundances show a strong correlation with temperature at lower altitudes than the 10-mbar level (maximum correlation function is $\sim$0.6). Of these molecules, CO_2 and CH_4 have secondary peaks at 0.2 mbar, which are negative, due to emission features. CO shows only a weak correlation with temperature. As a result, the cross-correlation functions show that the temperatures primarily have the largest correlations with the molecules at locations where the functional derivatives in Figure 6.6 peak.

In Figure 6.8 (b), it is shown that the temperature error range for $\Delta\chi^2$/N$<$0.5 origi-

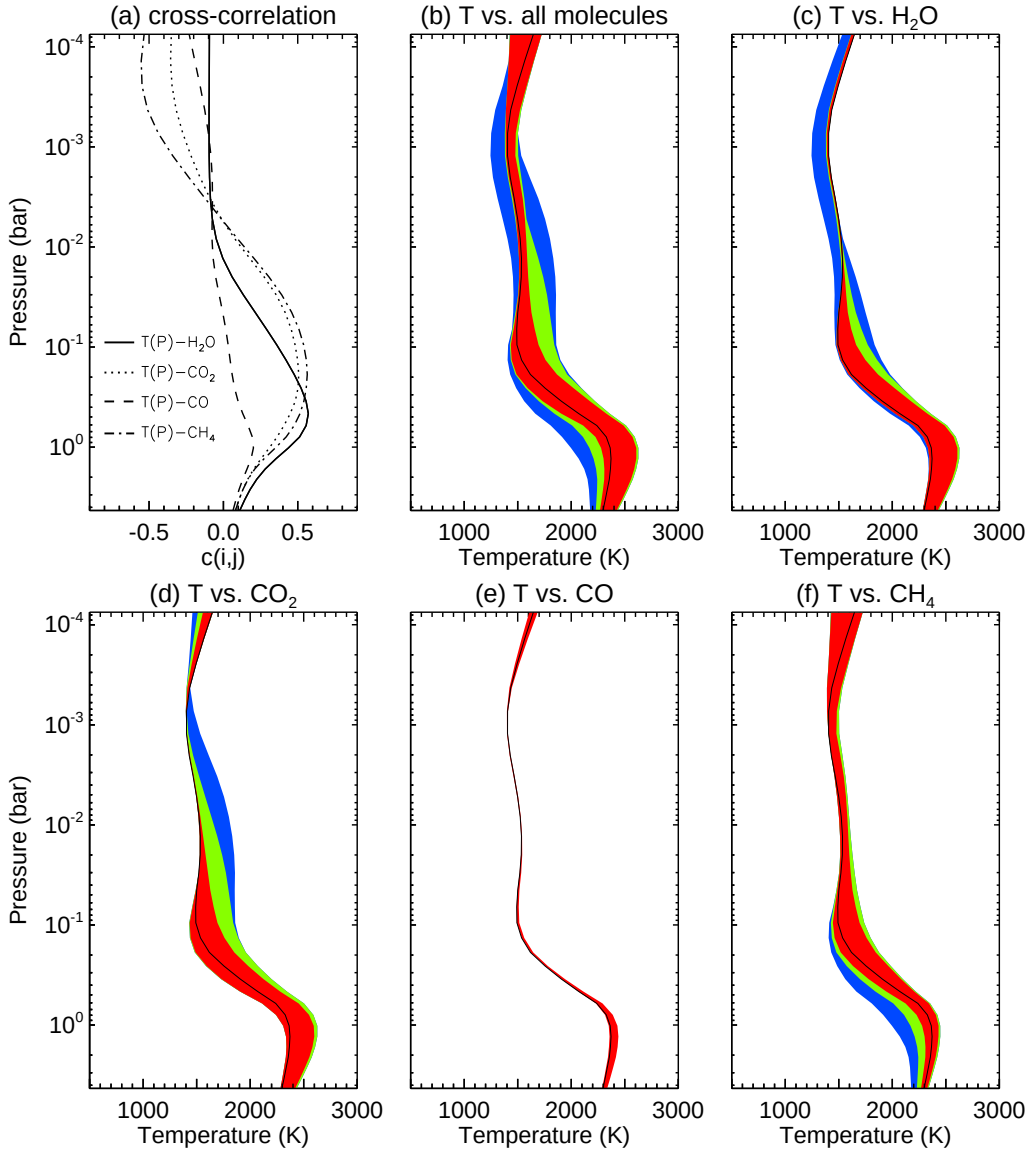

Figure 6.8: (a) The vertical structure of the cross-correlation functions. The high correlation with H_2O and CO_2 dominates the degeneracy of temperature at most pressures. (b-f) The retrieved P-T profiles of the dayside HD 209458b with various mixing ratios for each molecule are presented with $\Delta\chi^2$/N ranges. Each colour demonstrates $\Delta\chi^2$/N $<$0.5 (red), 1.0 (green), and 2.0 (blue), respectively. As a result, the large uncertainties of P-T profile are broadly distributed for all pressure levels, which implies that the inversion at the upper atmosphere is hardly constrained by the current measurements.

nates from the degeneracy with H_2O, CO_2, and CH_4, irrespective of the CO abundance. In particular, the temperatures above the 10 mbar altitude are mainly determined by spectral features of CH_4, which causes a high correlation between the two at the highest altitudes in the model. For $\Delta\chi^2$/N<0.5, the errors of temperature at 0.1 mbar, 10 mbar, and 1 bar are thus 270 K, 80 K, and 330 K, respectively. Unlike the dayside of HD 189733b, it is found that temperatures at high altitudes have rather broad errors, which implies that the inverted temperature above 1 mbar is weakly constrained and a solution without a temperature increase at this pressure is also able to explain the measurements within the uncertainty range $\Delta\chi^2$/N<0.5.

We expected that the pressure regions showing the greater correlations indicate the larger errors. For $\Delta\chi^2$/N<1.0 and 2.0, however, the temperature uncertainties that have large error at 4 mbar in Figure 6.9 (b) seem not to follow the cross-correlation. There are two reasons for this phenomenon: First, the vertical structure of the cross-correlation function varies with respect to the final P-T profile. In Figure 6.9, it is shown that the variations in the correlation between the temperature and molecules are even more significant for CO_2 and CH_4 when the temperature inversion is located deeper in the atmosphere (in photosphere). The more inverted temperature causes more distinctive emission features on the spectrum [Figure 6.9 (c)], which produces an equivalent effect with an enhancement in molecular abundance. On the other hand, in the atmosphere with an isotherm above 100 mbar, CO_2 and CH_4 are not strongly correlated with temperature at upper altitudes so that positive correlations are extended from the lower atmosphere to the 1 mbar region, where large temperature uncertainties are found. Therefore, temperature structure determines the degree of correlation with the molecular constituents, and vice versa, such that these figures should be treated as a guideline for the potential degeneracies.

In summary, the P-T profile of the dayside of HD 209458b can be determined with a broad uncertainty in all altitudes due to its strong degeneracy with the molecular abundances. This implies that the measurements, particularly the $Spitzer$/IRAC and IRS channels, are the only ones providing evidence for an inversion-like profile above photosphere, and that this is only weakly constraining. Therefore an atmosphere without an inverted

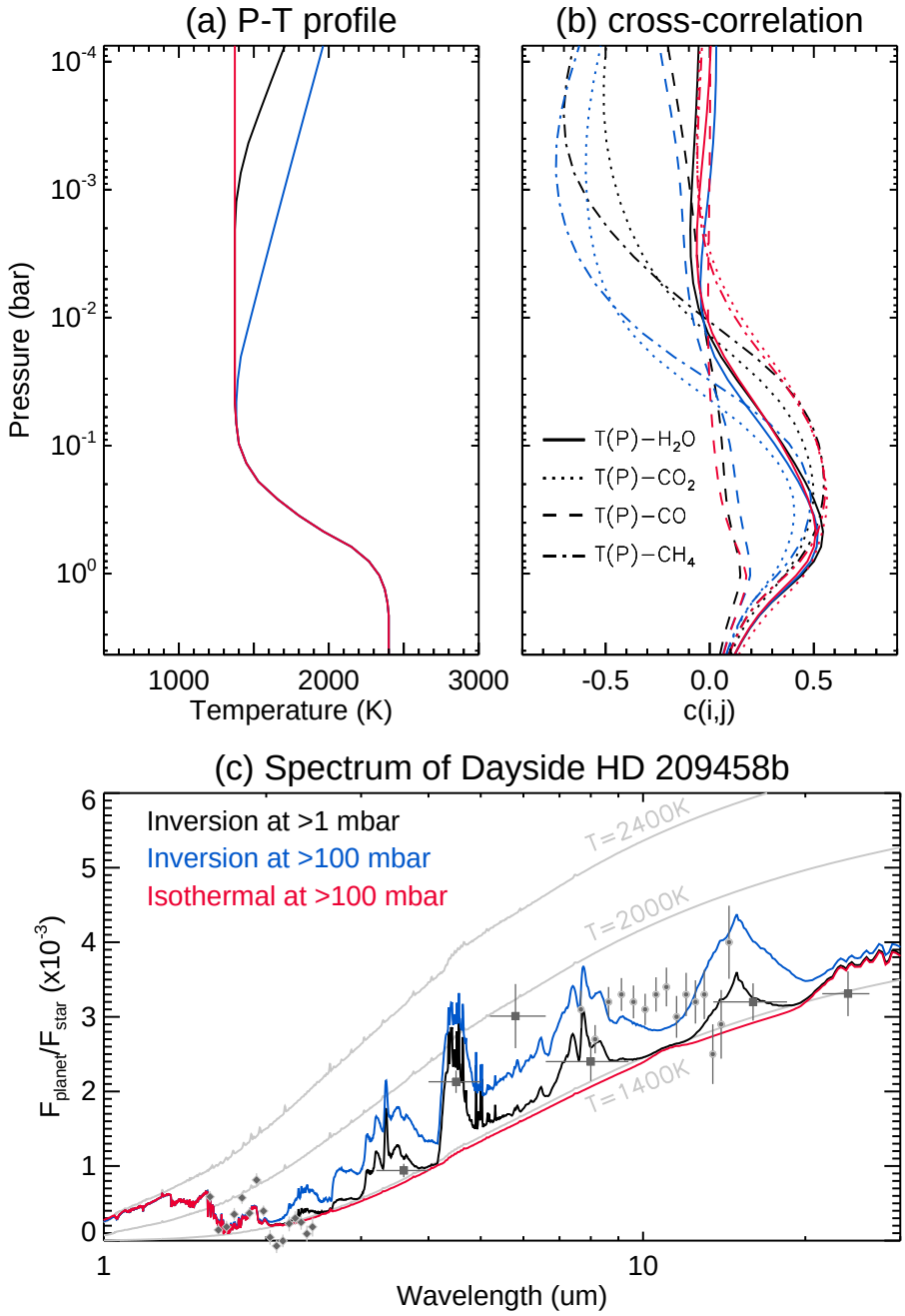

Figure 6.9: (b) Variation of vertical cross-correlation functions on account of (a) different P-T profiles; isothermal (red), inverted layer above 100 mbar (blue), and inverted layer above 1 mbar (black). Depending on the location of a temperature inverted layer, the temperature cross-correlation varies considerably. (c) Resulted synthetic spectra show how an inversion characterises emission features and how the cross-correlations are related to spectrum shape. Overall, the spectrum with a temperature increase with height located at above 1 mbar, which shows a similar appearance with the best-fit case [e.g. Figure 6.4 (b)], gives the best fitting quality among three cases.

temperature could fit the data if the measurement accuracy has been overestimated.

6.5 Retrieval of Molecular Abundances

Performing multiple retrievals by changing each molecular abundance while fixing the abundances of the other three molecules, we find that the molecular abundances have considerably large uncertainty due to the degeneracy with the temperature. As indicated in Figure 6.10, the uncertainty ranges of the four key molecules are much broader than the molecules in HD 189733b because there are half as many measurements (i.e. weaker constraints). For $\Delta\chi^2$/N$<$0.5, the data permit an upper limit on the H_2O mole fraction of 6×10^{-5} for H_2O, (0.06–150)$\times10^{-5}$ for CO_2, and (4–450)$\times10^{-4}$ for CH_4. The uncertainty range of the CO abundance can not be estimated with a certain $\Delta\chi^2$/N, owing to its marginal contribution to the spectrum. For $\Delta\chi^2$/N$<$1.0 and $<$2.0, the measurements determine only upper or lower boundary of the abundances of H_2O, CO_2 and CH_4.

In Table 6.1, there are a few orders of magnitude difference in mixing ratios between the retrieval studies. In particular, the mixing ratios for CH_4 and CO_2 estimated previously are considerably lower than the constrained values in this study. This is because the former models with an inversion layer needed 1) mostly H_2O and CH_4 to describe the spectrum (S09b) or 2) strong CO emission and weak spectral features from other molecules (MS10). In NEMESIS, these two molecules, however, struggle to fit the measurements that give high flux ratios and, as a result, strong emission leads to the large mixing ratios (4×10^{-3} for CO_2 and 8.7×10^{-5} for CH_4 for the best-fitting case). In contrast, S09b and MS10 proposed lower abundances of CO_2 [(1–10)$\times10^{-6}$ by S09b and 6×10^{-9} by MS10] and CH_4 [(1–20)$\times10^{-5}$ by S09b and 4×10^{-8} by MS10]; The fitted spectra by S09b require emission and absorption features from a small amount of CO_2 in order to produce the flux ratios at 1.95–2.2, 4.5 and 8–14.3 μm whereas MS10 found the depletion of CO_2 to fit the six $Spitzer$ broadband channels, which are primarily produced by CO. On the other hand, NEMESIS utilises a high abundance of CO_2 that results emissions, fitting the flux ratios at 1.9–2.15 μm (NICMOS), 4.5 μm (IRAC) and 11.5–16 μm

(IRS). The retrieved CH_4 abundance in MS10 is also depleted, again, because the major feature of the spectrum is characterised by CO. In S09b, the CH_4 abundance is determined with reliability using various constraints from most NICMOS channels, IRAC channels at 3.6 and 8.0 μm and IRS channels at 7–8 μm. Although the same constraints are adopted, NEMESIS constrains CH_4 to be at least $\sim$20 times higher than the others since our fitted spectrum explains the flux ratios from these channels with strong emissions by CH_4, which are the most distinct features with the CO_2 emissions compared to the spectra in the literature. Although both our study and S09 used identical measurements in the retrieval process, (again, MS10 adopted only the six broadband channels of $Spitzer$), the best-fitting solutions are different and the uncertainty ranges for molecular abundances by NEMESIS are much greater than those of S09b, leading us to suggest that there might be differences between two models: 1) the adopted line databases (e.g. CH_4 lines from STDS for this study or from Nassar and Bernath (2003) for S09b), 2) temperature dependency of lines, 3) partition functions, or 4) used physical parameters for planets and star. A direct comparison between the underlying forward models is required, but to date has not been available. For CO, retrieval cases in MS10 having an inversion layer constrained a high abundance, (3–700)$\times 10^{-4}$ with 3×10^{-2} as the best-fitting solution, by reproducing a strong emission feature at 4.5 μm. Likewise, this IRAC channel is mainly used to constrain a high CO abundance in this study (2×10^{-2} as the best-fitting solution) but the uncertainty of the CO abundance is not definitively determined due to the degeneracy, despite of the fact that we consider wider spectral coverage than MS10. Therefore, we found that the uncertainty on the CO result is much broader than that quoted by MS10, meaning that their models were being overestimated about the CO abundance

In Table 6.1, it is commonly shown for all studies that the chemistry in the dayside of HD 209458b is predominantly carbon-rich, high CH_4 or CO abundances except for a no-inversion case by MS10. If the warmer temperatures in the atmosphere of HD 209458b are enough to occur more abundant CO than CH_4, this leads to higher C/O ratio than the solar value (C/O=0.62). On the other hand, if the temperatures are sufficiently low to contain more CH_4 than CO, abundant CH_4 increases C/O ratio greater than 1. For both

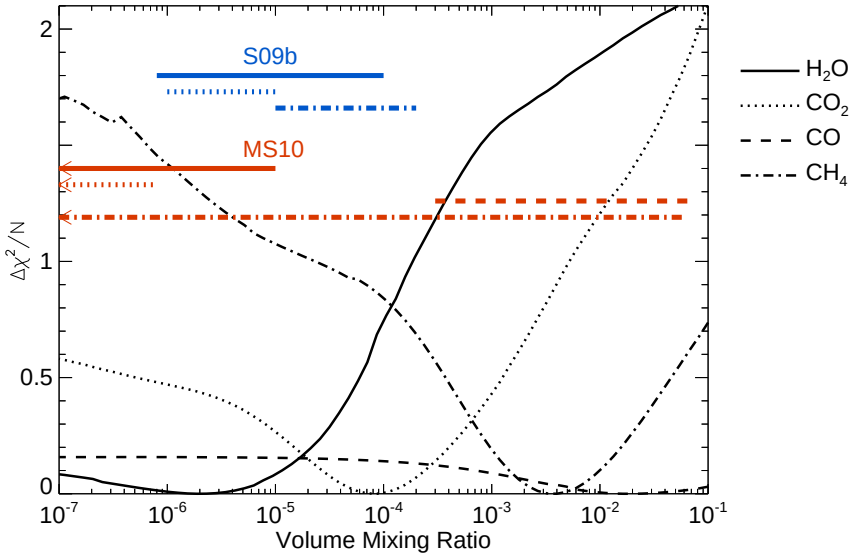

Figure 6.10: The degeneracy ranges of the molecular mixing ratios for H_2O, CO_2, CO, and CH_4. Each line shows the resultant $\Delta\chi^2$/N with respect to the given abundances. The $\Delta\chi^2$/N constrains the uncertainties of the molecular abundances, which are distributed around the best-fitting abundance of H_2O (1.9×10^{-6}), CO_2 (8.7×10^{-5}), CO (2.0×10^{-2}), and CH_4 (4.0×10^{-3}), respectively. Lower bounds of CO and CH_4 uncertainties are unconstrained due to their small contributions to the fitted spectrum. For comparison, the constrained molecular mixing ratios in S09b and MS10 are also displayed.

cases, we can find that these two carbon-bearing molecules play a key role in determining the C/O ratio of the dayside HD 209458b. This implies that, for some reason, the C/O ratio of HD 209458b appears to be highly enhanced unlike the result for HD 189733b. However, the large degeneracy as shown in Figure 6.10 means that the true abundance of CO remains undetermined and the lower limit of C/O ratio can be only provided.

6.6 Lapse Rate

In Figure 6.11, the retrieved temperatures of the dayside HD 209458b at pressures less than 100 mbar are characterised by the lapse rate ($\Gamma = dT/dz$), which shows a stratosphere where the temperature increases with altitude above a troposphere where the temperature decreases with altitude above 1 bar. In the troposphere, the atmosphere layer between 300–500 mbar is nearly a dry adiabatic [Dry Adiabatic Lapse Rate (DALR) = -0.72 K/km]. It also shows the location of the tropopause at 70 mbar, where the lapse rate

Table 6.1: Best estimated mixing ratios (ppm) for the dayside of HD 209458b. For the results of this study, Figure 6.10 shows why there is a broad range of values.

	H_2O	CO_2	CO	CH_4	C/O	Inversion layer	data source
Swain et al. (2009)	100	10	...	200		1 mbar	HST/NICMOS $Spitzer$/IRS $Spitzer$/IRAC
	10	5	...	60		10 mbar	
	10	5	...	60		No Inv.	
	0.8	1	...	10		100 mbar	
Madhusudhan & Seager (2010)	6	0.006	30000	0.04	1.0	100 mbar	$Spitzer$ Photometry
	40	0.00005	8	9	0.36	No Inv.	
	0.04–10	10^{-6}–0.8	300–70000	10^{-5}–60000	1-105	Inv.	$\chi^2/\mathrm{N} < 2.0$
This study	Best-fit value						
	1.9	87	20000	4000	1.2	>1 mbar	All measurements (excl. IRAC3 at 5.8 μm)
	Possible fit range						
	<60	0.6–1500	...	400–45000	>1.0		$\Delta\chi^2/\mathrm{N} < 0.5$
	<200	<5000	...	>25	>1.0		$\Delta\chi^2/\mathrm{N} < 1.0$
	<20000	<80000	...	>0.01	>0.5		$\Delta\chi^2/\mathrm{N} < 2.0$

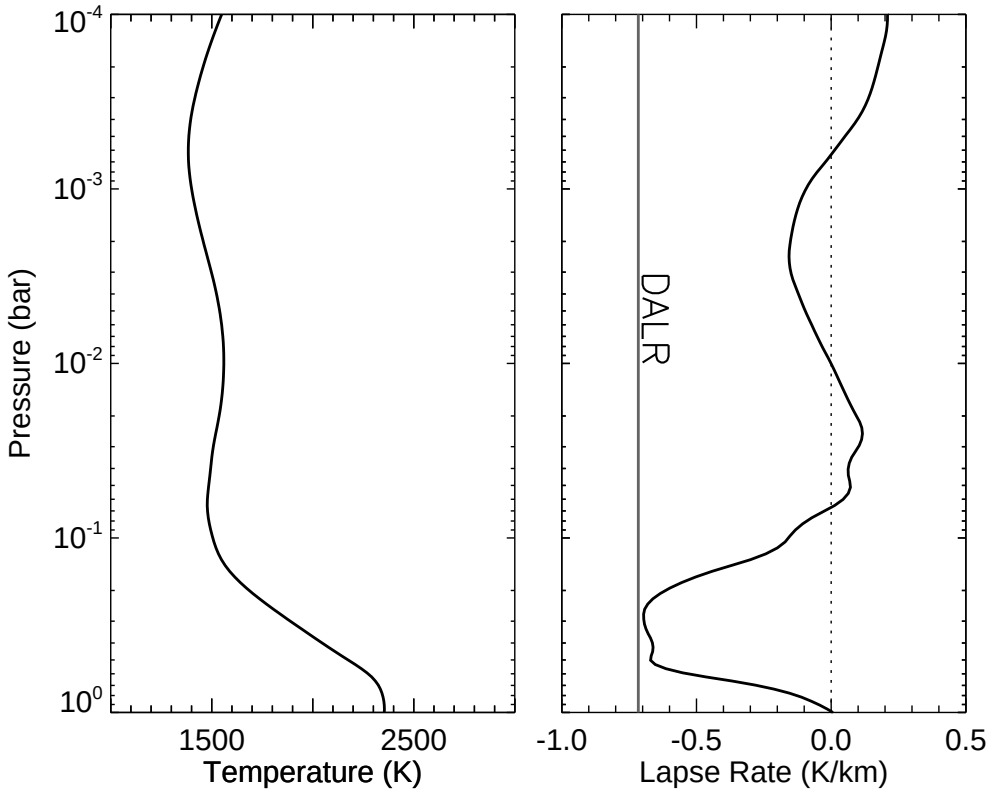

Figure 6.11: $(left)$ The retrieved thermal structure of the dayside HD 209458b and $(right)$ its lapse rate. The given pressures correspond to the levels covered by the contribution functions. The dry adiabatic lapse rate (DALR) is overlain in grey colour, assumed to be a constant (Γ=-0.72) over the altitude.

becomes zero. Above the troposphere, the lapse rate is close to zero (a quasi-isothermal layer) until we reach pressures of approximately 0.6 mbar. Above this height, the lapse rate is now consistently positive, owing to an inverted thermal structure, making a key distinguishing feature between HD 209458b and HD 189733b.

6.7 Additional Sources of Degeneracy

The planet-star radius ratio (R_p/R_*) is one of underlying assumptions made before establishing the retrieval model, which gives significant uncertainties for retrieved parameters, as discussed in Section 4.7. By varying R_p/R_* from 0.11 to 0.13, the retrievals were performed to find the variations in the molecular abundances and P-T profile. Figure 6.12 shows that the changes in molecular abundances are (1.1–4.4)$\times 10^{-6}$ for H_2O,

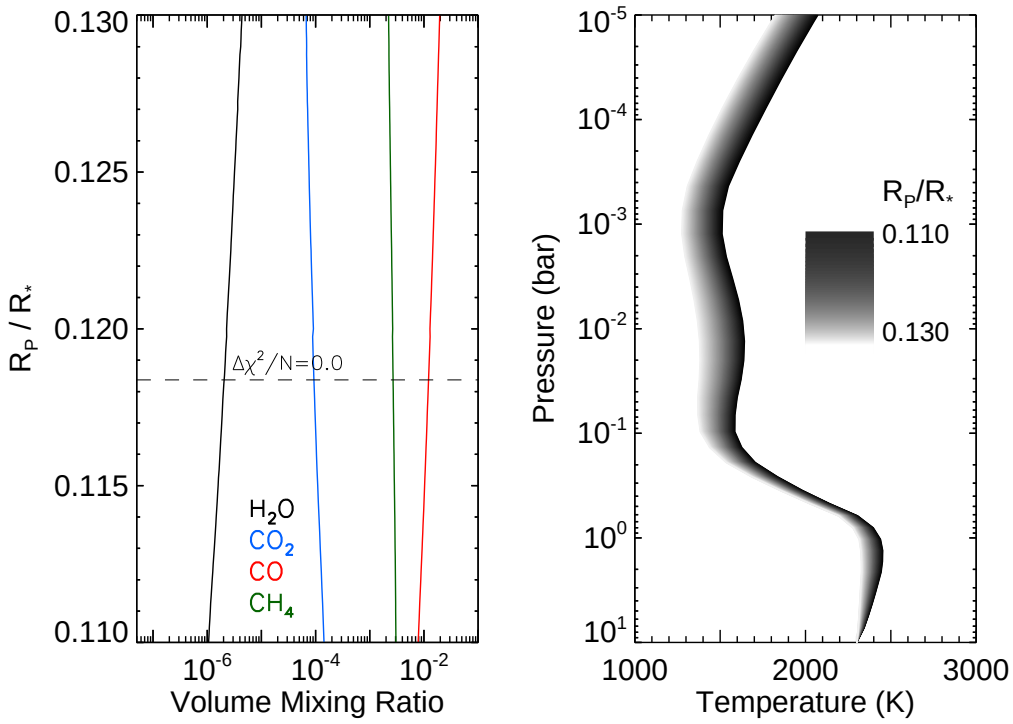

Figure 6.12: Uncertainty of composition ($left$) and temperature ($right$) being induced by the variation of planet-star radius ratio (R_p/R_*). Due to ∼0.02 change in R_p/R_* (0.11→0.13), the temperature profile shifts towards lower ∼250 K at 10 mbar whereas the fitting quality, $\Delta\chi^2$/N increases by ∼1.8.

(6.7–14)×10^{-5} for CO_2, (7.8–20)×10^{-3} for CO, and (2.2–3.0)×10^{-3} for CH_4. However, there seems that R_p/R_* is more degenerate with temperature as plotted in the right panel of Figure 6.12. The temperatures decrease by 170 K at 200 mbar, 260 K at 10 mbar, and 240 K at 1 mbar. Under the condition of an increase in R_p/R_* (0.11 to 0.13), the retrieval model achieves a best fit-like spectrum by taking correspondingly lower temperatures to reduce the flux ratio and finds an increase in $\Delta\chi^2$/N (∼1.8).

6.8 HD 189733b vs. HD 209458b

We find that the temperature profile of the dayside hemisphere of HD 209458b is likely to hold a temperature increasing layer above photosphere. This suggests that the thermal structure of HD 209458b above 1 mbar differs from the one of HD 189733b that is characterised by an isothermal temperature, even though the temperatures for two planets

commonly show tropospheric and isothermal structures at pressures between the 0.001–1 bar level. The evidence for an inverted layer at > 1 mbar in HD 209458b is that the strong emission features caused by CO_2 and CO are required to explain a high flux ratio at 4.5 μm, while the flux ratio of HD 189733b at the same channel is low, which can only be explained by absorption spectrum[1]. For HD 189733b, the observed spectrum at wavelengths longward of MIR is flat, meaning that an isothermal structure above troposphere is highly plausible (Fortney and Marley, 2007; Grillmair et al., 2008).

We also find that CO seems to be abundant in both atmospheres as this molecule is responsible for fitting high absorption (HD 189733b) or emission (HD 209458b) spectra. Although a high CO abundance scenario matches theoretical hypotheses (Liang et al., 2003; Line et al., 2010; Moses et al., 2011), this should be confirmed with more measurement constraints in order to reduce its large uncertainty and to increase reliability. On the other hand, the CO_2 amount in the equilibrium or disequilibrium chemistry models referred above is predicted to be $\sim 10^{-8}$–$\sim 10^{-7}$, which is a few orders of magnitude lower than the ones measured for the dayside atmosphere of HD 209458b ($\sim 10^{-4}$) and HD 189733b ($\sim 10^{-3}$). Since CO_2 is considered to only a minor constituent in the atmospheres of these hot Jupiters, this is the largest discrepancy between theory and observations. Thus an improvement in either chemical models or observational constraints in near future will help to solve this problem.

We see that the difference in the H_2O and CH_4 abundances in both dayside atmospheres are unexpectedly large. For CH_4, its high abundance in the dayside hemisphere of HD 209458b is acceptable if we assume that there is a strong atmospheric transport for vertical mixing, i.e. large eddy diffusion coefficient (K_{zz}) that causes quenching in low altitude and high mixing ratio in the quenching point, while K_{zz} in HD 189733b is small, leading to a low CH_4 abundance (Moses et al., 2011). However, H_2O mixing is not highly affected by vertical transport mechanisms and is produced by an analogous chemistry in both atmospheres (Moses et al., 2011). Therefore, we cannot suggest any plausible sce-

[1]This test was firstly proposed by Knutson et al. (2010) that whether or not an inversion in a hot Jupiter atmosphere exists can be assessed by measuring the slope between the flux ratios of the $Spitzer$/IRAC channels at 3.6 and 4.5 μm.

nario for the difference in H_2O with current theoretical models. We need to re-visit HD 209458b with the additional retrievals for the terminators or dayside in order to explain the mysterious atmosphere with a low H_2O abundance, as derived by S09b, MS10 and this study.

Consequently, we conclude that the atmospheres of the two hot Jupiters discussed above exhibit the characteristics that were specified by the hot Jupiter classification schemes such as 'Class IV' vs. 'Class V' (Sudarsky et al., 2000) or 'pL class' vs. 'pM class' (Fortney et al., 2008) (see Chapter 1.3). Some findings related to composition, however, cannot be explained by existing theoretical models, which were limited by a small number of measurements or lack of physical understanding of these atmospheres.

6.9 Conclusion

The current observations of the emission spectrum of the dayside of HD 209458b were able to constrain the atmospheric structure and composition. One of the key objectives for this study was searching for evidence for a thermal inversion caused by strong optical absorbers in the stratosphere. However, the small number of measurements and large measurement errors lead to broad uncertainties of the derived temperature and composition. Despite the current measurement uncertainties, this study derived three major findings from the measurement constraints.

First, it was shown that the measurements between 1.5–24 μm provide constraints for deriving a thermal structure at some pressure levels, including a temperature increase at the upper atmosphere at 1 mbar. Various studies have suggested that evidence for a temperature inversion layer can be found or has been found in a stratosphere of the dayside atmosphere of HD 209458b (Burrows et al., 2008; Knutson et al., 2007; Madhusudhan and Seager, 2009, 2010; Showman et al., 2009; Swain et al., 2009b), which was possibly generated by optical absorption by gaseous TiO/VO. In this context, the best-fit P-T profile, retrieved within the NEMESIS architecture, showed that a weakly increasing temperature layer lies at higher than photosphere ($\sim$1 mbar) to fit the $Spitzer$ broadband channels as

well as some IRS channels. However, no evidence for TiO/VO was found because dayside measurements do not probe below 1.5 μm. The retrieved best-fit spectrum at MIR is rather flat and the deep absorptions shown by S09b (cf. Figure 4 in S09b) are not necessary at any wavelength in order to fit high flux ratios of the $Spitzer$ measurements. As stated in Section 6.5, this is possibly due to the different forward models used for each study, with different line databases and parameters applied during retrievals.

To characterise the best-fit solution, we carried out additional retrievals for four different combinations of the available measurements. We found that the $Spitzer$/IRS channels require a featureless spectrum [Case (a) in Section 6.3.1], giving an unconstrained P-T profile, while the inclusion of all the $Spitzer$ broadband channels yields a broad inversion layer at 0.1–10 mbar [Case (b) in Section 6.3.1]. A thermal inversion is also constrained when high planet-star flux ratios in two $Spitzer$/IRAC channels (i.e. 3.6 and 4.5 μm) are involved in the retrieval [Case (d) in Section 6.3.1]. Just like the dayside of HD 189733b, the HST/NICMOS channels were used to constrain the tropospheric temperatures over a pressure between 100 mbar and 1 bar and a weak inversion at 1–100 mbar [Case (c) in Section 6.3.1]. None of these atmospheric models were capable of reproducing the 5.8 μm emission, which remains a mystery.

Secondly, the best estimated mixing ratio for H_2O agrees with the other retrieval models by S09b and MS10. The mixing ratios for CO_2 and CH_4 are, however, significantly enhanced compared to previous studies, showing strong emission at the $Spitzer$ MIR and FIR channels, which are the predominant features of the fitted spectrum. Although the driving force for the CO richness in both studies is the fitting of the flux ratio in the 4.5 μm $Spitzer$/IRAC channel, there is no strong evidence for a high amount of CO as suggested by MS10 due to the large uncertainty driven by the degeneracy problem. This is also applicable for the retrieval of the H_2O abundance. In this context, the compositional abundances for CO_2 and CH_4 can be constrained from the given measurements, leaving the uncertainty ranges of H_2O and CO much broader than those from the other authors.

Thirdly, the retrieved P-T profile has large uncertainties over the entire atmosphere. The high temperature correlations due to molecules are found at low altitudes, where all

molecules except CO are responsible for the degeneracy ($\sim$100 mbar) while the negative correlations at the altitudes higher than 1 mbar are mainly derived from CH_4 and CO_2. The degeneracy between the temperature and molecular abundances is considerable at the altitudes of the proposed temperature increasing layer with height, implying that the size of the thermal inversion is strongly dependent on the chosen vertical profile of cross-correlation for the emitting species. Thus the inference of an inversion in or above photosphere must be re-confirmed by further observations. Moreover, the uncertainties in the abundances are much wider than the case of HD 189733b. This is because of the smaller number of constraints for HD 209458b does not provide enough information to constrain the abundances with the error ranges as narrow as HD 189733b. Also, it is found that fewer constraints primarily increase the mixing ratio errors rather than the temperature errors.

The observations to date allow fitting to the data with various solutions, leading to extreme degeneracies between retrieval variables. Therefore, it is clear that the observations analysed here for the retrieval of the emission spectrum of the dayside HD 209458b are still in their infancy, which will need significant improvement to make progress in understanding this hot Jupiter atmosphere. In particular, additional measurements with high resolution and enhanced S/N are required from the future missions (e.g. EChO, Tinetti et al., 2012) in order to characterise the highly inflated atmosphere, not fully constrained in this study (i.e. the presence of an inversion and molecules such as H_2O and CO) with high reliability.

The observations for the transmission spectrum of HD 209458b is also available, as introduced in Chapter 1.3, measured in the $Spitzer$/IRAC and HST/STIS channels. However, we consider that the retrieval for the terminator regions may not provide sufficient information for the atmospheric structure of HD 209458b due to the small number of measurements and the large measurement uncertainty even though these datasets were used to find information for the evidence for TiO/VO (Désert et al., 2008). For this reason, we will investigate the terminators with more constraints when it is available in the future.

Chapter 7

Conclusion

7.1 Summary

7.1.1 Optimal Estimation Retrievals for Exoplanets

Transit spectroscopy has been providing the best chance of characterising the atmospheric structure and composition of planets around other stars. The current understanding of exoplanets implies great atmospheric diversity, requiring specialized software tools to overcome the degeneracy problem that is caused by the limits of available observations. In this sense, the aim of this study was to explore the family of plausible solutions for the atmospheric structure of known exoplanets by quantifying the uncertainties and correlation between the atmospheric temperature and composition. This study thus focused on answering the fundamental questions of "what lessons can or cannot be learned from the current measurements, and which scenarios give the most plausible atmospheric structure and composition?". Two solutions were suggested to overcome the limitations of previous methodologies:

- **Solving the inverse problem that is ill-posed and ill-conditioned** To solve the inverse problem inherent in modelling of exoplanetary atmospheres, the retrieval in this study adopted an optimal estimation architecture using an iterative scheme to maximise the probability of solutions to the available data based on a Bayesian

approach. By doing so we were able to achieve formal quantification of uncertainty from the small number of measurements given.

- **Fast and reliable radiative transfer calculations for rapid forward modelling** For high temperature applications, a forward model should address weak transitions as well as strong transitions at room temperatures, meaning that extreme computational resources are required during a line-by-line calculation. To improve forward modelling speed while retaining accuracy, this study adopted a correlated-k model, whose calculations can be orders of magnitude faster than a line-by-line calculation by incorporating the pre-integrated k-coefficients.

The complete versions of k-coefficients (between 300–30000 cm^{-1} with 5 cm^{-1} step) for molecules and elements have been tabulated from HITEMP2010 (Rothman et al., 2010) for H_2O and CO_2, HITEMP1995 for CO, STDS for CH_4, VALD for Na and K, and R.S.Freedman (private communication) for TiO and VO, respectively. The accuracy of the correlated-k approximation was tested via comparisons to line-by-line models, and the differences between them was found to be insignificant compared to the quality of existing exoplanetary measurements.

7.1.2 Disk-averaged Dayside Emission Spectrum of HD 189733b

HD 189733b is currently our best-characterised hot Jupiter and its 71 data points from various instruments on the HST and $Spitzer$ telescopes permit the retrieval of the P-T profile between 0.1 and 950 mbar in the dayside atmosphere of HD 189733b, wherein the structure with a linearly decreasing tropospheric temperature and an isothermal stratosphere can be constrained. Contribution functions showed atmospheric pressures where each channel of HST/NICMOS (8-950 mbar), $Spitzer$/IRS (0.4–250 mbar), and broadband photometry (0.1–500 mbar) provided constraints. Also, as shown in Figure 4.4, radiance with respect to molecular sensitivity indicated that the current measurements provide strong constraints for H_2O at $\sim$50–500 mbar, CO_2 at deeper than $\sim$100 mbar, and CO at 100 mbar. However, no strong evidence for CH_4 was found in the current

dayside spectra. The constrained best-fit volume mixing ratios were consistent with the values in the literature except for CO_2, which was constrained to a few magnitudes higher than other authors. This is because CO_2 in our model plays a critical role in fitting the channels in the visible and, particularly, longward of 9 μm where the H_2O spectrum dominates. Re-analysed flux ratio at 3.6 μm by Knutson et al. (2012) shows that the evidence for the H_2O and CH_4 may be no longer valid due to the fact that a strong CH_4 absorption may replace the H_2 spectrum at this wavelength. To constrain the uncertainties for temperature and composition, considering the degeneracy between retrieval parameters, the retrievals were repeated with the wide range of abundances for four molecules, finding the best-fit P-T profiles and tracing goodness-of-fit values. This allowed us to assess the uncertainties of the variables based on the quality of the measurements instead of simple Gaussian errors by the retrieval model. As a result, the temperature uncertainties are broad (540 K) at 800 mbar and narrow (50 K) at 2 mbar, which confirms the existence of an isothermal structure above the troposphere. Given the temperature uncertainty caused by the degeneracy with molecules and reported by previous studies, it was clearly shown that the retrieved temperature has a non-inverted layer possibly due to the absence of strong absorbers in stratosphere (i.e. TiO/VO), consistent with the expectations for a planet of this temperature, called a pL planet, whose spectrum shows abundant H_2O and alkali metals (Fortney et al., 2008). The significant degeneracy due to a 15 per cent increment in the input radius ratio (R_p/R_*) caused the temperature to decrease by 220 K at 1 mbar and variations in molecular abundances to increase (H_2O) and decrease (CO_2 and CO) by factor of 2 to 3.

7.1.3 Transmission Spectrum of HD 189733b

The transmission spectra of HD 189733b in the visible (0.55–1.05 μm) (Pont et al., 2008) and the NIR (1.5–2.5 μm) (Gibson et al., 2011; Swain et al., 2008b) were used to retrieve the properties of haze/cloud in the atmosphere and the volume mixing ratio for molecules. To interpret the featureless transmission spectrum of HST/ACS, the extinction effect by Rayleigh scattering of haze/cloud was inserted at pressures where the atmosphere is op-

tically thin. Since temperature only affects the scale height of the atmosphere during primary transit, the temperature profile was assumed to be the same as that determined on the dayside. We considered also that the haze/cloud of $MgSiO_3$ is responsible for the extinction in visible. By performing rigorous retrievals for a range of abundance and particle size of the condensate, plausible haze/cloud scenarios were constrained with particle size less than 0.25 μm only. Other properties such as haze/cloud lower deck pressure, density, thickness and nadir optical depth are highly correlated. The constrained H_2O abundance in the terminators ($2\times10^{-7}\sim3\times10^{-2}$) is relevant to the result from the dayside atmosphere ($1\times10^{-5}\sim2\times10^{-2}$ for $\Delta\chi^2$/N$<$1). The constrained properties of haze/cloud in the terminators matched up with the values in Lecavelier Des Etangs et al. (2008). By adding the HST/NICMOS spectra from Swain et al. (2008b) and Gibson et al. (2011), the molecular mixing ratios of H_2O and CH_4 were also constrained with broad uncertainties, either consistent with those by the previous studies (Madhusudhan and Seager, 2009; Swain et al., 2008b) or slightly underestimated compared to them due to an additional opacity source by hazes. Moreover, all haze solutions found from the transmission spectrum showed insignificant change in the dayside emission spectrum of HD 189733b. Even though the suggested scenarios are need to be confirmed by further studies using better constraints due to a lack of our knowledge on the cloud physics, we drew conclusions from the retrievals that molecular absorptions are required to reproduce the primary transit spectrum, and atmospheric scenarios with haze alone is insufficient. For further study, we suggested that the significance of the planetary radius to the retrieval results must be tested for constraining the atmospheric properties without being overinterpreted.

7.1.4 Disk-averaged Dayside Emission Spectrum of HD 209458b

As the second best characterised hot Jupiter in terms of the number and quality of the secondary eclipse measurements, the retrievals of the dayside emission spectrum of HD 209458b were performed with diverse combinations of the measurements by HST (1.45–2.5 μm for NICMOS) and $Spitzer$ (3.6, 4.5, 8.0, 16 and 24 μm for IRAC and MIPS, and 7.46–15.25 for IRS). Combining all the measurements together, the emission spectrum

of HD 209458b was able to constrain the atmospheric structure at pressures between 0.1 mbar and 1.5 bar of the dayside atmosphere. This deeper atmosphere than the case of HD 189733b is also retrievable because the temperature weighting functions in the NICMOS channels can reach higher pressure levels. We adopted all the datasets currently available except the $Spitzer$/IRAC channel at 5.8 μm, as there is no appropriate model to explain its high flux ratio. Given the P-T profile, it was found that an inverted thermal structure at altitudes higher than 1 mbar, wherein strong visible absorptions are likely active as in a pM class planet (Fortney et al., 2008), is only constrained from the $Spitzer$ channels. Also, we found that the retrieved thermal structure shows warmer temperatures ($\sim$300 K) than one from the dayside of HD 189733b, which is one of the primary differences between pM and pL or Class IV and V planets. However, due to large errors inherent in the measurements, broad uncertainties were found (300 K at 1 mbar and 700 K at 500 mbar) and did not allow us to tightly constrain the thermal structure at all pressure levels. Moreover, the temperature inversion above photosphere was only required by a small subset of the available channels (i.e. IRAC and IRS). Therefore, it is expected that larger errors driven by the degeneracy would likely rule out the need for the inversion in this atmosphere. It is shown that the mixing ratio of H_2O is constrained to values consistent with Swain et al. (2009a) and Madhusudhan and Seager (2010), while highly enhanced abundances of CO_2 and CH_4 were found compared to previous studies. This is because 1) the synthetic spectra by S09b are largely different from our best-fit spectrum due to different spectral modelling techniques used, and 2) the constrained abundances for two molecules by MS10 are only based on the six $Spitzer$ broadband channels, which would produce a very ill-conditioned retrieval. Unlike the result by MS10, strong evidence for CO was not discovered. Due to the degeneracy between retrieved parameters and the large temperature uncertainties, an inversion in the dayside of HD 209458b should be re-visited when further measurements at longer wavelengths become available. Also, the broad uncertainties of molecular abundances showed that our knowledge of the chemistry of this planet is extremely limited by the various error sources from the measurements. We found that an increment of 0.2 from R_p/R_*=0.11 leads to a temperature decrease by

260 K at 10 mbar and 3–4 times increase (H_2O and CO) or 1.5–2.0 times reduction (CO_2 and CH_4) in molecular abundances.

7.2 Discussion - Hot Jupiter Classification

A comparison between the retrievals for atmospheric structure and composition of HD 189733b and HD 209458b showed that these planets are likely to have thermal structures that were predicted by theoretical models for each hot Jupiter class. Based on measurement constraints, the dayside atmosphere of HD 189733b is characterised by an isothermal temperature ($\sim$1250 K) above 100 mbar that needs to fit the flat $Spitzer$/IRS spectrum, while a temperature inversion placed above the 1 mbar level was required to reproduce the high flux ratios of the dayside of HD 209458b measured in the $Spitzer$ MIR channels, although no evidence for TiO/VO or other visible absorbers have been discovered on either planet. The findings are consistent with hypothetical planets modelled by Fortney et al. (2008) (pL and pM) or Sudarsky et al. (2000, 2003) (class IV and class V).

However, caution must be taken when we apply these classifications to characterise hot Jupiters due to the uncertain mechanism producing an inversion (no strong observational evidence for an optical absorber is available). Currently, the thermal structures of a number of hot Jupiter atmospheres have been investigated using the $Spitzer$ broadband bandpasses and it is found that some of hot Jupiters [e.g. WASP-14 (Blecic et al., 2011) and WASP-19 (Anderson et al., 2011)] experiencing radiation from their parent stars that are as strong as HD 209458b show no emission features, which implies that some hot Jupiters that have atmospheres as warm as a Class V or pM class planet may not contain any absorbers to produce an inverted stratosphere. In contrast, a hot Jupiter, XO-1b (Machalek et al., 2008) having a cooler dayside than HD 189733b is well described by atmospheric models with a temperature inversion. These results suggest that the inversion hypothesis may not provide a clear description for the atmospheric structure of hot Jupiters.

Alternatively, Knutson et al. (2010) proposed that the presence of an inversion in a

hot Jupiter has a strong correlation with the chromospheric activity of the parent star. By estimating Lyman α fluxes from the host stars of hot Jupiters, they found that strong UV fluxes from the parent star destroy radiation absorbers in the upper atmosphere and make the atmosphere optically thin, leading to a thermal structure free from an inversion. Therefore, planets orbiting non-active stars ("quiet stars") in the UV (e.g. HD 209458b) are likely to have an inversion in high altitude atmosphere, while planets orbiting chromospherically active stars (e.g. HD 189733b) are unlikely to contain an inversion at altitudes. TrES-3 orbiting an active G-type star, for instance, exhibits no strong inversion, despite the fact that this planet has been considered to keep a warm enough atmosphere to have gaseous TiO (Fressin et al., 2010). On the other hand, XO-1b (Machalek et al., 2008) faces weak UV radiation from the quiet parent star that is possibly responsible for an inversion in its cool atmosphere.

The hot Jupiter atmospheres referred in Knutson et al. (2010), however, have been interpreted mostly based on the $Spitzer$/IRAC channels and limited to the small number of constraints, causing an increase in degeneracy in the atmospheric solution. For instance, even though WASP-12b orbits a chromospherically active star, the observed dayside spectrum is reproducible by any atmospheric model, irrespective of the presence of an inverted stratosphere, owing to the lack of constraint from available measurements (Croll et al., 2011; Madhusudhan and Seager, 2011). Moreover, the sampling number of hot Jupiters orbiting quiet and active stars are still insufficient to confirm a correlation between stratosphere and UV fluxes from host star. Therefore, we find that understanding of inversion mechanisms in hot Jupiter can be achieved with larger sampling number, along with comprehensive understanding of interactions between host star and planet.

7.3 Future Work

- **Retrieval for brown dwarfs** The atmospheres of hot Jupiters are analogous to those of substellar objects, specifically, L type (1400 K$< T_{eff} <$2200 K) or T type (500 K$< T_{eff} <$1400 K) brown dwarfs. Among them, the atmospheres of the T type

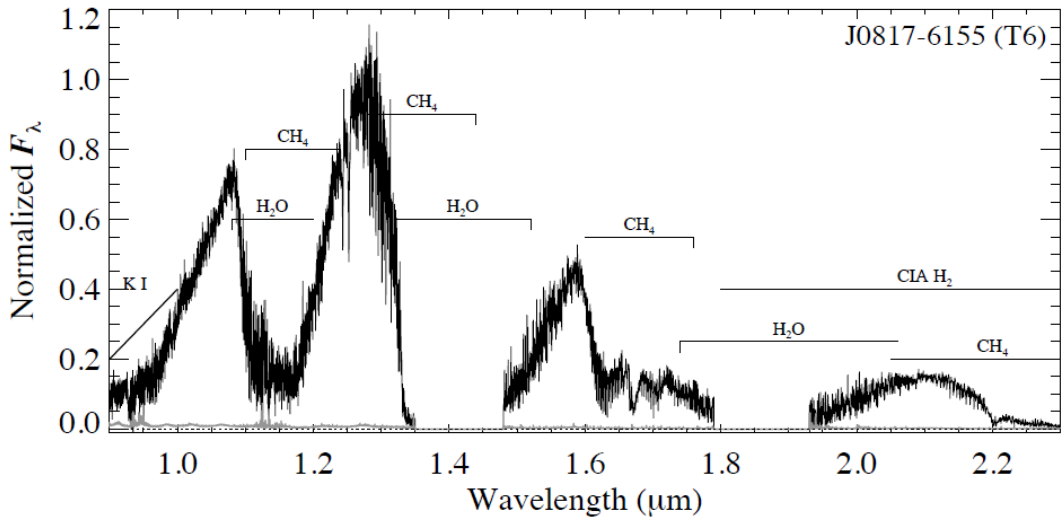

Figure 7.1: Spectral template of a T dwarf of J0817-6155. (Courtesy of A. Burgasser)

dwarfs show strong absorption features by the molecules similar to those present in a hot Jupiter's atmospheres. Moreover, emission spectra of brown dwarfs have been observed from spectrographs with a high S/N and resolution on the ground-based telescopes[1] (e.g. Figure 7.1) because they are strong IR emitters, not disturbed by any nearby companion. Thus the same modelling techniques developed here for the retrieval of atmospheric parameters from exoplanetary spectra could be straightforwardly applied to brown dwarf spectroscopy. By doing so, we will be able to determine the vertical temperature profile, compositional amounts, and cloud/haze properties within brown dwarf atmospheres.

- **Retrieval for direct imaged exoplanets** Likewise, there are multiple exoplanets orbiting around HR 8799 (Marois et al., 2008), a directly-imaged system, measured in high resolution spectroscopy (H and K bands) and broadband photometry (various channels between 1.03 and 4.7 μm). These exoplanets are intriguing objects in terms of understanding the evolution and formation of the planetary system. Currently, four planets (b, c, d, and e) have been studied (Barman et al., 2011; Skemer

[1]e.g. The IRTF Spectral Library - `http://irtfweb.ifa.hawaii.edu/~spex/IRTF_Spectral_Library/index.html`

et al., 2012) and it is expected that they will provide new insight into the chemistry and cloud structure of early-aged planet atmospheres.

- **Atmospheric Variability** One may argue that variability in these extreme atmospheres is large enough to change the emergent spectrum at some wavelengths. In Figure 7.2, two best fit spectra retrieved from different sets of the dayside measurement are displayed, the black spectrum taken from the best fit case in Chapter 4 and the red spectrum from a new compilation of results based on the original HST/NICMOS measurements, plus revised $Spitzer$ measurements: IRS including 16μm, IRAC (5.8μm), new IRAC (3.6, 4.5, and 8 μm), and new MIPS (24 μm) (Agol et al., 2010; Knutson et al., 2009, 2012). It is found that the best-fit spectrum yielded from the new $Spitzer$ broadband measurements needs temperatures in the troposphere approximately 100 K warmer. The reduced flux ratios at 3.6 and 4.5 μm support the existence of CH_4 in the dayside, which were not probed in the original case (Chapter 4). This implies two interpretations: 1) if the different levels of fluxes in the same channel have been determined because of different data analysis techniques used for each study, the retrieved temperature and molecular abundances tell us the uncertainties on the atmospheric parameters based on the measurements. On the other hand, 2) if the reduced flux ratios are the result of any type of time variation in the atmosphere itself, the retrieval is able to see a variability in the atmospheric structure in between. However, variability in the atmospheres of exoplanets has not been well studied and its detection is difficult due to huge uncertainties in the measurements (Agol et al., 2010; Knutson et al., 2011, 2012).

  Variations in disk-averaged flux within our own solar system is rather uncommon, and we would not necessarily expect the whole planetary flux to change so drastically. If the planet is changing with time, then the retrieval technique allows us to assess whether a change in temperature, composition, and haze/cloud is physically plausible.

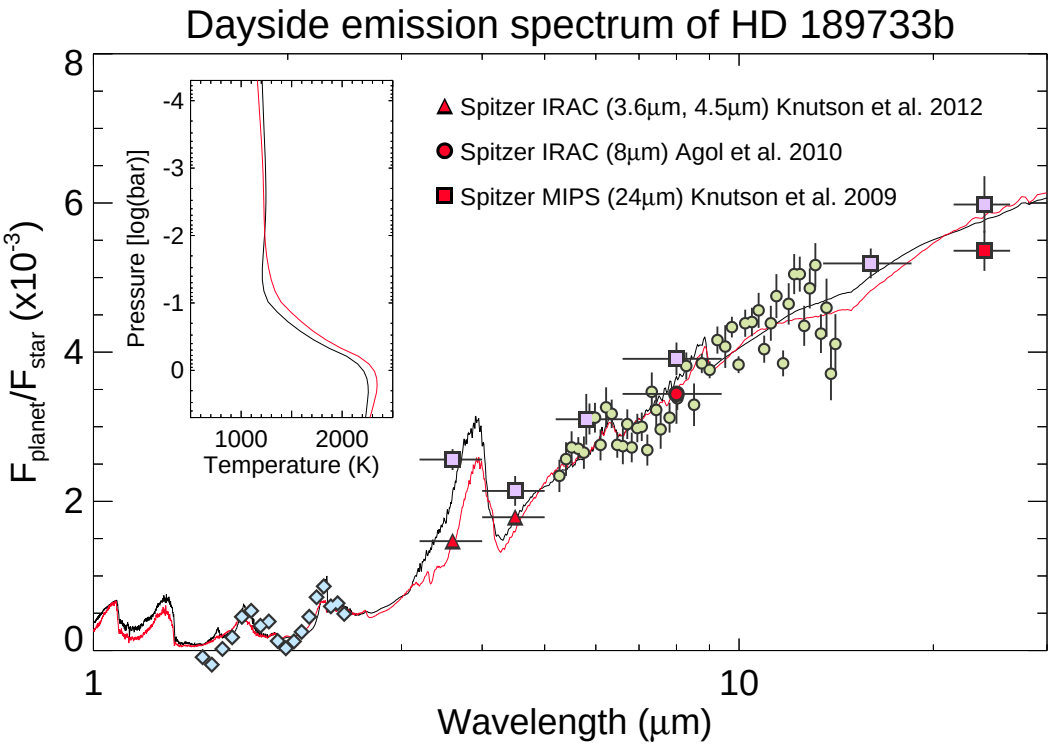

Figure 7.2: The best fit spectrum and P-T profile of emission spectra of HD 189733b (black colour) is retrieved from HST/NICMOS (light blue), $Spitzer$/IRS (green) and different sets of broadband channels (purple by Charbonneau et al. (2008)), while the other best fit case (red colour) is retrieved from same sets of measurement except the 4 $Spitzer$ photometry channels at 3.6, 4.5, 8, and 24 μm (Agol et al., 2010; Knutson et al., 2009, 2012).

- **Retrieval for Hot Neptune and Super Earth** In addition to hot Jupiters, the planets having smaller radius and mass becomes one of interesting targets in terms of the planetary diversity and habitability. Among them, $hot\ Neptunes$ (e.g. GJ 436b), which are tens of times more massive than the Earth but smaller than $hot\ Jupiters$ ($\sim$20 M_E) show an effective temperature of several hundreds Kelvins warmed up by the radiation from their parent stars (von Braun et al., 2012). Particularly, $hot\ Neptunes$ orbiting the M type dwarf stars become a main target of transit spectroscopy because high transit depths can be achieved with smaller and cooler planets, bringing us closer to the terrestrial regime. Until now $\sim$10 transiting $hot\ Neptunes$ have been discovered, mostly done by the recent $Kepler$ observations. As the smaller object, $super\text{-}Earths$ (e.g. GJ 1214b), which indicate the

planets $\sim$2-$\sim$10 times heavier than Earth analog planets, become intriguing targets because some of them orbiting around dwarf stars with a relatively low temperature enough for maintaining liquid water ("Goldilocks zone") are considered to hold a habitable environment. Further retrieval anaysis to constrain uncertainties of molecular abundances and P-T profile will be carried out for a $hot\ Neptune$ and a $super$-$Earth$.

- **Comparison to retrievals with a MCMC method** In Chapter 1, we showed that a Monte-Carlo Markov Chain (MCMC) scheme (e.g. Benneke and Seager, 2012) is widely used for retrieval studies for exoplanetray atmospheres, incorporating iterative forward modelling method. However, this method does not solve an inverse problem when finding the best-fitting solution and degeneracy uncertainty. The objective of this study is to demonstrate the difference in characterised atmospheres caused by the difference in methodologies applied (i.e. solving vs. not solving an inverse problem), to show how an optimal estimation can overcome the limitation of its counterpart and to discuss what lessons we can also learn from a MCMC method.

- **Retrieval for the dayside hemisphere of HD 209458b using the $Spitzer$ broadband channels** To compare retrievals achieved by different methods, the datasets applied for each scheme should be identical. One of comparable datasets is the dayside emission spectrum of HD 209458b measured in the $Spitzer$ broadband channels, with which Madhusudhan and Seager (2010) suggested the plausibility of a themal inversion in the dayside hemisphere and compositional amounts with broad error ranges. However, the results by these only six points might be over-interpreted as there might be a great number of solutions that are able to reproduce spectra within a certain goodness-of-fit. We will provide evidence for lack of reliability of retrievals with a small number of measurements and justify the importance of using full spectral range of datasets.

- **Further retrieval with haze/cloud** In Chapter 5, the presence of haze was sug-

gested to explain a smoothing out of the expected features in the HST/ACS spectral region, but the optical properties and composition of the haze require more detailed exploration. Therefore, a combination of the extinction by haze/cloud and molecular features in exoplanetary atmospheres should be applied to a broader spectral range than originally came from the ACS and NICMOS data. In particularly, to avoid a high degree of discrepancy between various observations, we didn't consider HST/STIS or $Spitzer$/IRAC data with the various transit observations available in between UV and FIR as seen in Figure 7.3. As a preliminary test, we show in Figure 7.3 that a compact haze layer at a high altitude do not provide an adequate fit to this extended spectrum as $MgSiO_3$ delivers very high optical depths at FIR caused by the unique refractive index in this wavelength region. This fact indicates that we could further constrain the properties of the haze layers by performing retrievals with different optical properties of the candidate grains. The goal of this further work will be to perform a retrieval over the entire spectral range covered by available measurements, including the smoothly varying spectrum in UV and visible, by applying the scattering calculation based on the Mie approximation. The effects of the optical properties will be tested for different haze candidates.

7.4 Conclusion

Exploration of atmospheres outside Earth provides a way to learn about the evolution of our own planet. Particularly, exploration of atmospheres outside our solar system allows us to widen our view to a broad ensemble of planetary atmospheres. Since the first detection of planets in other stellar system, observations and analysis of exoplanets spectra have been performed to understand the differences between the atmospheres of exoplanets and planets in our solar system. With the number of known exoplanets increasing rapidly, a number of techniques to characterise the atmospheres from spectroscopic measurements have been attempted to explain the diversity of planetary atmospheres and their chemistry but this field is still in its infancy. This is mainly due to the fact that the atmo-

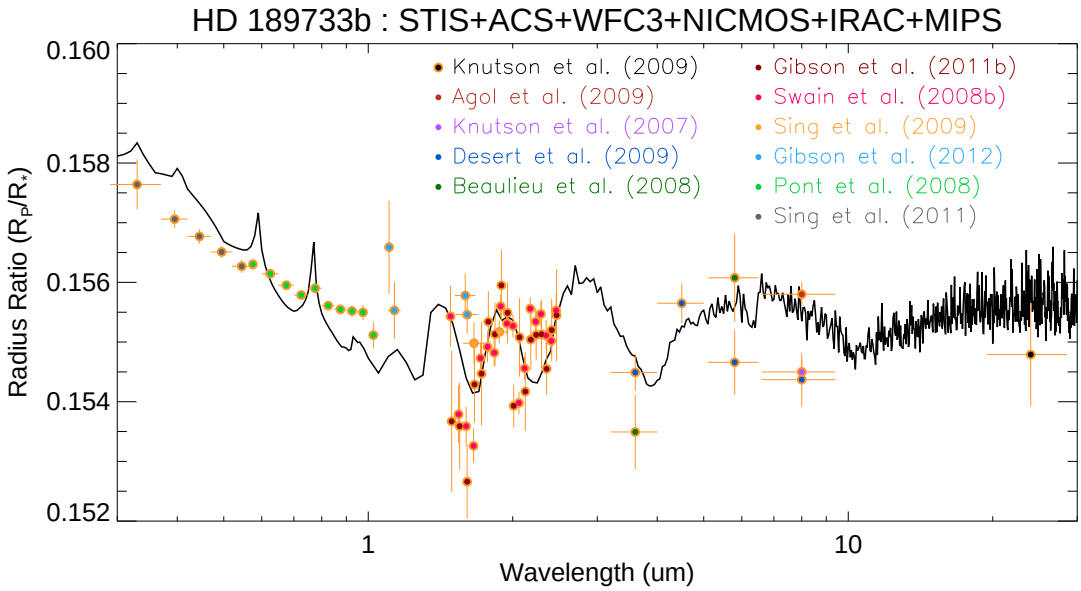

Figure 7.3: Available measurements for transmission spectrum of HD 189733b and a plausible fit. However, the best-fit atmosphere here does not provides an adequate fit to the whole spectrum. Further work is required to understand the properties of the hazes on the HD 189733b terminator regions.

spheric characterisations were based on poor-quality measurements. In this respect, this study contributed to proving a novel method to describe the structure of exoplanetary atmospheres from the limited information, which is based on the tools proven by a number of studies for the atmospheres in our solar system.

With the tools of optimal estimation and the correlated-k method, this study retrieved the best plausible scenarios for the atmospheric properties of known hot Jupiters from publicly available primary and secondary transit data. At the same time, our efficient model can explain the necessity of these tools that are able to analyse measurements quickly, which will be available via high resolution spectroscopy in near future. Moreover, this study attempted to remain conservative when reproducing the small number of available exoplanetary spectra, avoiding under- or overestimating any atmospheric features suggested in the literature. By constraining the overall shape of the spectrum, the HST and $Spitzer$ data of two different types of hot Jupiter allowed us to evaluate the vertical temperature structure and molecular abundances. Retrievals from other authors which have focussed on smaller wavelength ranges or fewer data points were subject to

broader uncertainties than were presented previously. This study was able to discuss the benefit of considering a wide spectral range for breaking these degeneracies and highlight the limitations of the data sets available today.

Appendix A

Available line lists for molecules and elements

Table A.1: Available line lists for molecule, element and continuum absorption.

	HITRAN08	GEISA09	HITEMP10	individual list
H_2O	✓	✓	✓	Patridge & Schwenke (1997) Barber et al. (2007) AMES SCAN
CO_2	✓	✓	✓	CDSD - Tashkun et al.(2003)
CO	✓	✓	✓	-
CH_4	✓	✓	✓	Strong et al.(1993) Brown et al.(1997) Karkoschka (1994) STDS - Wenger & Champion (1998) Nassar & Bernath (2003) Thievin et al.(2008)
TiO	-	-	-	Allard et al.(2000) Plez (1998)
VO	-	-	-	Plez (1998)
alkali metal				VALD NIST Atomic Spectra Database TOPbase
Collision-Induced Absoprtion				Borysow & Frommhold (1990), Zheng & Borysow (1995), Borysow et al.(1997) for H_2-H_2 Borysow et al.(1989), Borysow & Frommhold (1989) for H_2-He

Appendix B

Partition function

Table B.1: Polynomial form of partition function and coefficients

Species	poly. form	isotope no.	polynomial coefficients				
			a_0	a_1	a_2	a_3	a_4
H_2O	$\sum_{i=0}^{3} a_i T^i$	161	-1.69592e+2	1.29367e+0	-5.21098e-4	6.24887e-7	
		626	-2.49458e+3	1.38585e+1	-1.65451e-2	8.14385e-6	
		636	-5.46924e+3	3.02257e+1	-3.62677e-2	1.77051e-5	
		628	-5.47892e+3	3.03745e+1	-3.63434e-2	1.78286e-5	
CO_2		627	-3.14590e+4	1.74564e+2	-2.08653e-1	1.02504e-4	
		638	-1.20742e+4	6.65827e+1	-8.00806e-2	3.89456e-5	
		637	-6.91181e+4	3.81536e+2	-4.53835e-1	2.23323e-4	
		828	-3.00858e+3	1.66473e+1	-1.99591e-2	9.75994e-6	
CO		26	1.17133e+1	3.01374e-1	5.68592e-5	1.10085e-8	
		36	2.52449e+1	6.25271e-1	1.26461e-4	2.28110e-8	
		28	1.27037e+1	3.13604e-1	6.37930e-5	1.14406e-8	
		27	7.33570e+1	1.84636e+0	3.62534e-4	6.73937e-8	
		38	2.74350e+1	6.51846e-1	1.42248e-4	2.37446e-8	
		38	1.50771e+2	3.88593e+0	7.33075e-4	1.41758e-7	
CH_4(<1000K)		211	-3.14109e+2	4.59494e+0	-8.39981e-3	1.19895e-5	
			-6.28187e+2	9.18943e+0	-1.67991e-2	2.39779e-5	
			-2.54542e+3	3.71886e+1	-6.79955e-2	9.70626e-5	
			-2.60101e+5	6.48085e+2	-5.45139e-1	1.64916e-4	
CH_4(1000∼2000K)		311	-5.20196e+5	1.29615e+3	-1.09025e+0	3.27821e-4	
			-2.10531e+6	5.24595e+3	-4.41287e+0	1.32696e-3	
			-1.19710e+7	1.68635e+4	-8.07604e+0	1.33856e-3	
CH_4(>2000K)		212	-2.39334e+7	3.37157e+4	-1.61471e+1	2.67637e-3	
			-9.68816e+7	1.36480e+5	-6.53634e+1	1.08341e-2	
TiO	$log_{10}Q(T) = \sum_{i=0}^{4} a_i l_\theta^i$		5.3051	-2.3739	0.8940	-0.3641	
VO			5.0687	-2.2186	0.9545	-0.4592	
Na	$log_{10}Q(T) = \sum_{i=0}^{4} a_i l_\theta^i$		0.30955	-0.17778	1.10594	-2.42847	1.70721
K			0.34419	-0.048157	1.92563	-3.17826	1.83211

Bibliography

E. Agol, N.B. Cowan, J. Bushong, H. Knutson, D. Charbonneau, D. Deming, and J.H. Steffen. Transits and secondary eclipses of hd 189733 with spitzer. In *IAU Symposium*, volume 253, page 209, 2009.

E. Agol, N.B. Cowan, H.A. Knutson, D. Deming, J.H. Steffen, G.W. Henry, and D. Charbonneau. The climate of hd 189733b from fourteen transits and eclipses measured by spitzer. *The Astrophysical Journal*, 721:1861, 2010.

R. Alonso, T.M. Brown, G. Torres, D.W. Latham, A. Sozzetti, G. Mandushev, J.A. Belmonte, D. Charbonneau, H.J. Deeg, E.W. Dunham, et al. Tres-1: The transiting planet of a bright k0 v star. *The Astrophysical Journal*, 613:L153, 2004.

E. Anders and N. Grevesse. Abundances of the elements-meteoritic and solar. *Geochimica et Cosmochimica Acta*, 53:197, 1989.

D.R. Anderson, A.M.S. Smith, A.A. Lanotte, T.S. Barman, A. Collier Cameron, C.J. Campo, M. Gillon, J. Harrington, C. Hellier, P.F.L. Maxted, et al. Thermal emission at 4.5 and 8 mum of wasp-17b, an extremely large planet in a slightly eccentric orbit. *Monthly Notices of the Royal Astronomical Society*, 416:2108, 2011.

G.Á. Bakos, J. Lázár, I. Papp, P. Sári, and EM Green. System description and first light curves of the hungarian automated telescope, an autonomous observatory for variability search. *Publications of the Astronomical Society of the Pacific*, 114:974, 2002.

A. Baranne, D. Queloz, M. Mayor, G. Adrianzyk, G. Knispel, D. Kohler, D. Lacroix, J.P. Meunier, G. Rimbaud, and A. Vin. Elodie: A spectrograph for accurate radial velocity measurements. *Astronomy and Astrophysics Supplement Series*, 119:373, 1996.

R.J. Barber, J. Tennyson, G.J. Harris, and R.N. Tolchenov. A high-accuracy computed water line list. *Monthly Notices of the Royal Astronomical Society*, 368(3):1087, 2006.

T. Barman. Identification of absorption features in an extrasolar planet atmosphere. *The Astrophysical Journal*, 661:L191, 2007.

T.S. Barman, B. Macintosh, Q.M. Konopacky, and C. Marois. Clouds and chemistry in the atmosphere of extrasolar planet hr8799b. *The Astrophysical Journal*, 733:65, 2011.

N.M. Batalha, J.F. Rowe, S.T. Bryson, T. Barclay, C.J. Burke, D.A. Caldwell, J.L. Christiansen, F. Mullally, S.E. Thompson, T.M. Brown, et al. Planetary candidates observed by kepler, iii: Analysis of the first 16 months of data. *arXiv preprint arXiv:1202.5852*, 2012.

J.P. Beaulieu, S. Carey, I. Ribas, and G. Tinetti. Primary transit of the planet hd 189733b at 3.6 and 5.8 μm. *The Astrophysical Journal*, 677(2):1343, 2008.

J.P. Beaulieu, D.M. Kipping, V. Batista, G. Tinetti, I. Ribas, S. Carey, J.A. Noriega-Crespo, C.A. Griffith, G. Campanella, S. Dong, et al. Water in the atmosphere of hd 209458b from 3.6–8 μm irac photometric observations in primary transit. *Monthly Notices of the Royal Astronomical Society*, 409(3):963, 2010.

V.J.S. Béjar, M.R.Z. Osorio, A. Pérez-Garrido, C. Álvarez, EL Martín, R. Rebolo, I. Villó-Pérez, and A. Díaz-Sánchez. Discovery of a wide companion near the deuterium-burning mass limit in the upper scorpius association. *The Astrophysical Journal Letters*, 673(2):L185, 2008.

G.F. Benedict, B.E. McArthur, T. Forveille, X. Delfosse, E. Nelan, R.P. Butler, W. Spiesman, G. Marcy, B. Goldman, C. Perrier, et al. A mass for the extrasolar planet gliese 876b determined from hubble space telescope fine guidance sensor 3 astrometry and high-precision radial velocities. *The Astrophysical Journal*, 581:L115, 2002.

B. Benneke and S. Seager. Atmospheric Retrieval for Super-Earths: Uniquely Constraining the Atmospheric Composition with Transmission Spectroscopy. *The Astrophysical Journal*, 753:100, July 2012. doi: 10.1088/0004-637X/753/2/100.

D.D. Bennett. Exoplanets: detection, formation, properties, habitability, 2008.

B.A. Biller, M. Kasper, L.M. Close, W. Brandner, and S. Kellner. Discovery of a brown dwarf very close to the sun: A methane-rich brown dwarf companion to the low-mass star scr 1845–6357. *The Astrophysical Journal Letters*, 641(2):L141, 2008.

J. Blecic, J. Harrington, N. Madhusudhan, K.B. Stevenson, R.A. Hardy, C.J. Campo, W.C. Bowman, S. Nymeyer, P. Cubillos, and D.R. Anderson. Thermal emission of wasp-14b revealed with three spitzer eclipses. *arXiv preprint arXiv:1111.2363*, 2011.

I.A. Bond, N.J. Rattenbury, J. Skuljan, F. Abe, R.J. Dodd, J.B. Hearnshaw, M. Honda, J. Jugaku, P.M. Kilmartin, A. Marles, et al. Study by moa of extrasolar planets in gravitational microlensing events of high magnification. *Monthly Notices of the Royal Astronomical Societ*, 333:71, 2002.

I.A. Bond, A. Udalski, M. Jaroszynski, N.J. Rattenbury, B. Paczynski, I. Soszynski, L. Wyrzykowski, M.K. Szymanski, M. Kubiak, O. Szewczyk, et al. Ogle 2003-blg-235/moa 2003-blg-53: A planetary microlensing event. *The Astrophysical Journal*, 606:L155, 2004.

W.J. Borucki, D.G. Koch, J.J. Lissauer, G.B. Basri, J.F. Caldwell, W.D. Cochran, E.W. Dunham, J.C. Geary, D.W. Latham, R.L. Gilliland, et al. The kepler mission: a wide-field-of-view photometer designed to determine the frequency of earth-size planets around solar-like stars. In *Society of Photo-Optical Instrumentation Engineers (SPIE) Conference Series*, volume 4854, page 129, 2003.

W.J. Borucki, D.G. Koch, G. Basri, N. Batalha, T.M. Brown, S.T. Bryson, D. Caldwell, J. Christensen-Dalsgaard, W.D. Cochran, E. DeVore, et al. Characteristics of planetary candidates observed by kepler. ii. analysis of the first four months of data. *The Astrophysical Journal*, 736(1):19, 2011.

A. Borysow. Collision-induced absorption coefficients of h pairs at temperatures from 60 k to 1000 k. *Astronomy and Astrophysics*, 390(2):779, 2002.

A. Borysow and L. Frommhold. Collision-induced infrared spectra of h2-he pairs at temperatures from 18 to 7000 k. ii-overtone and hot bands. *The Astrophysical Journal*, 341:549, 1989.

A. Borysow and L. Frommhold. A new computation of the infrared absorption by h2 pairs in the fundamental band at temperatures from 600 to 5000 k. *The Astrophysical Journal*, 348:L41, 1990.

A. Borysow, L. Frommhold, and M. Moraldi. Collision-induced infrared spectra of h2-he pairs involving 0-1 vibrational transitions and temperatures from 18 to 7000 k. *The Astrophysical Journal*, 336:495–503, 1989.

A. Borysow, J. P. Champion, U. G. Jørgensen, and C. Wenger. Preliminary CH_4 Line List Data for Stellar Atmospheres. In I. Hubeny, D. Mihalas, and K. Werner, editors, *Stellar Atmosphere Modeling*, volume 288 of *Astronomical Society of the Pacific Conference Series*, page 352, 2003.

F. Bouchy, S. Udry, M. Mayor, C. Moutou, F. Pont, N. Iribarne, R. Da Silva, S. Ilovaisky, D. Queloz, N.C. Santos, et al. Elodie metallicity-biased search for transiting hot jupiters. *Astronomy and Astrophysics*, 444(1):15, 2005.

L. R. Brown, J. P. Champion, J. C. Hilico, M. Loete, A. Nikitin, O. Ouardi, and V. G. Tyuterev. Line parameters of methane and deuterated methane from 2 to 10 mu m. In *AAS/Division for Planetary Sciences Meeting Abstracts #29*, volume 29 of *Bulletin of the American Astronomical Society*, page 1010, 1997.

A. Burrows and CM Sharp. Chemical equilibrium abundances in brown dwarf and extrasolar giant planet atmospheres. *The Astrophysical Journal*, 512:843, 1999.

A. Burrows, I. Hubeny, J. Budaj, H.A. Knutson, and D. Charbonneau. Theoretical spectral models of the planet hd 209458b with a thermal inversion and water emission bands. *The Astrophysical Journal*, 668:L171, 2007.

A. Burrows, J. Budaj, and I. Hubeny. Theoretical spectra and light curves of close-in extrasolar giant planets and comparison with data. *The Astrophysical Journal*, 678(2): 1436, 2008.

D. Charbonneau, T.M. Brown, R.W. Noyes, and R.L. Gilliland. Detection of an extrasolar planet atmosphere. *The Astrophysical Journal*, 568:377, 2002.

D. Charbonneau, H.A. Knutson, T. Barman, L.E. Allen, M. Mayor, S.T. Megeath, D. Queloz, and S. Udry. The broadband infrared emission spectrum of the exoplanet hd 189733b. *The Astrophysical Journal*, 686(2):1341, 2008.

G. Chauvin, A.M. Lagrange, C. Dumas, B. Zuckerman, D. Mouillet, I. Song, J.L. Beuzit, and P. Lowrance. A giant planet candidate near a young brown dwarf. *Astronomy and Astrophysics*, 425(2):29, 2004.

G. Chauvin, A.M. Lagrange, B. Zuckerman, C. Dumas, D. Mouillet, I. Song, J.L. Beuzit, P. Lowrance, and M.S. Bessell. A companion to ab pic at the planet/brown dwarf boundary. *Astronomy and Astrophysics*, 438(3):29, 2005.

J.L. Christiansen, S. Ballard, D. Charbonneau, N. Madhusudhan, S. Seager, M.J. Holman, D.D. Wellnitz, D. Deming, M.F. A'Hearn, and T. EPOXI. Studying the atmosphere of the exoplanet hat-p-7b via secondary eclipse measurements with epoxi, spitzer, and kepler. *The Astrophysical Journal*, 710:97, 2010.

J.L. Christiansen, S. Ballard, D. Charbonneau, D. Deming, M.J. Holman, N. Madhusudhan, S. Seager, D.D. Wellnitz, R.K. Barry, T.A. Livengood, et al. System parameters, transit times, and secondary eclipse constraints of the exoplanet systems hat-p-4, tres-2, tres-3, and wasp-3 from the nasa epoxi mission of opportunity. *The Astrophysical Journal*, 726:94, 2011.

M. Clampin. Status of the james webb space telescope (jwst). In *Society of Photo-Optical Instrumentation Engineers (SPIE) Conference Series*, volume 7010, page 19, 2008.

B. Croll, L. Albert, R. Jayawardhana, E.M.R. Kempton, J.J. Fortney, N. Murray, and H. Neilson. Broadband transmission spectroscopy of the super-earth gj 1214b suggests a low mean molecular weight atmosphere. *The Astrophysical Journal*, 736(2):78, 2011.

I.J.M. Crossfield, H. Knutson, J. Fortney, A.P. Showman, N.B. Cowan, and D. Deming. Spitzer/mips 24 mum observations of hd 209458b: Three eclipses, two and a half transits, and a phase curve corrupted by instrumental sensitivity variations. *The Astrophysical Journal*, 752:81, 2012.

W. Cunto and C. Mendoza. The opacity project-the topbase atomic database. *Revista Mexicana de Astronomia y Astrofisica, vol. 23*, 23:107, 1992.

W. Cunto, C. Mendoza, F. Ochsenbein, and C.J. Zeippen. Topbase at the cds. *Astronomy and Astrophysics*, 275:L5, 1993.

A.R. Curtis. Discussion of a statistical model for water vapor absorption. *Quaterly Journal of Royal Meteorological Society*, 78:165, 1952.

R.J. de Kok and D.M. Stam. The influence of forward-scattered light in transmission measurements of (exo)planetary atmospheres. *Icarus*, 221(2):517, 2012. ISSN 0019-1035. doi: 10.1016/j.icarus.2012.08.020. URL `http://www.sciencedirect.com/science/article/pii/S0019103512003399`.

D. Deming, J. Harrington, S. Seager, and L. J. Richardson. Strong Infrared Emission from the Extrasolar Planet HD 189733b. *The Astrophysical Journal*, 644:560, June 2006. doi: 10.1086/503358.

B.O. Demory, S. Seager, N. Madhusudhan, H. Kjeldsen, J. Christensen-Dalsgaard, M. Gillon, J.F. Rowe, W.F. Welsh, E.R. Adams, A. Dupree, et al. The high albedo of the hot jupiter kepler-7 b. *The Astrophysical Journal*, 735:L12, 2011.

J.M. Désert, A. Vidal-Madjar, A. Lecavelier Des Etangs, D. Sing, D. Ehrenreich, G. Hébrard, and R. Ferlet. Tio and vo broad band absorption features in the optical spectrum of the atmosphere of the hot-jupiter hd 209458b. *Astronomy and Astrophysics*, 492(2):585, 2008.

J.M. Désert, A.L. Des Etangs, G. Hébrard, D.K. Sing, D. Ehrenreich, R. Ferlet, and A. Vidal-Madjar. Search for carbon monoxide in the atmosphere of the transiting exoplanet hd 189733b. *The Astrophysical Journal*, 699(1):478, 2009.

J.M. Désert, D. Charbonneau, B.O. Demory, S. Ballard, J.A. Carter, J.J. Fortney, W.D. Cochran, M. Endl, S.N. Quinn, H.T. Isaacson, et al. The hot-jupiter kepler-17b: Discovery, obliquity from stroboscopic starspots, and atmospheric characterization. *The Astrophysical Journal Supplement Series*, 197:14, 2011.

I. Dobbs-Dixon and D.N.C. Lin. Atmospheric dynamics of short-period extrasolar gas giant planets. i. dependence of nightside temperature on opacity. *The Astrophysical Journal*, 673:513, 2008.

M. Dominik, M.D. Albrow, J.P. Beaulieu, J.A.R. Caldwell, D.L. DePoy, B.S. Gaudi, A. Gould, J. Greenhill, K. Hill, S. Kane, et al. The planet microlensing follow-up network: results and prospects for the detection of extra-solar planets. *Planetary and Space Science*, 50:299, 2002.

David Ehrenreich, Guillaume Hébrard, Alain Lecavelier Des Etangs, David K Sing, Jean-Michel Désert, François Bouchy, Roger Ferlet, and Alfred Vidal-Madjar. A spitzer search for water in the transiting exoplanet hd 189733b. *The Astrophysical Journal Letters*, 668(2):L179, 2008.

A. Einstein. Lens-like action of a star by the deviation of light in the gravitational field. *Science*, 84:506, 1936.

G.G. Fazio, J.L. Hora, L.E. Allen, M.L.N. Ashby, P. Barmby, L.K. Deutsch, J.S. Huang, S. Kleiner, M. Marengo, S.T. Megeath, et al. The infrared array camera (irac) for the spitzer space telescope. *The Astrophysical Journal Supplement Series*, 154:10–17, 2004.

J.J. Fortney. The effect of condensates on the characterization of transiting planet atmospheres with transmission spectroscopy. *Monthly Notices of the Royal Astronomical Society*, 364:649, 2005.

J.J. Fortney and M.S. Marley. Analysis of spitzer spectra of irradiated planets: Evidence for water vapor? *The Astrophysical Journal*, 666:L45, 2007.

J.J. Fortney, D. Saumon, M.S. Marley, K. Lodders, and R.S. Freedman. Atmosphere, interior, and evolution of the metal-rich transiting planet hd 149026b. *The Astrophysical Journal*, 642:495, 2006.

J.J. Fortney, K. Lodders, M.S. Marley, and R.S. Freedman. A unified theory for the atmospheres of the hot and very hot jupiters: two classes of irradiated atmospheres. *The Astrophysical Journal*, 678(2):1419, 2008.

J.J. Fortney, M. Shabram, A.P. Showman, Y. Lian, R.S. Freedman, M.S. Marley, and N.K. Lewis. Transmission spectra of three-dimensional hot jupiter model atmospheres. *The Astrophysical Journal*, 709(2):1396, 2010.

F. Fressin, H.A. Knutson, D. Charbonneau, F.T. O'Donovan, A. Burrows, D. Deming, G. Mandushev, and D. Spiegel. The broadband infrared emission spectrum of the exoplanet tres-3. *The Astrophysical Journal*, 711:374, 2010.

M. Fridlund. The darwin mission. In *Earth-like planets and moons*, volume 514, pages 31–37, 2002.

J.R. Fuhr and W.L. Wiese. Crc handbook of chemistry and physics, ed. dr lide, 1998.

R.R. Gamache and J.M. Hartmann. An intercomparison of measured pressure-broadening and pressure-shifting parameters of water vapor. *Canadian journal of chemistry*, 82(6): 1013, 2004.

R.R. Gamache and A.L. Laraia. N2-, o2-, and air-broadened half-widths, their temperature dependence, and line shifts for the rotation band of h216o. *Journal of Molecular Spectroscopy*, 257:116, 2009.

B.S. Gaudi and J.N. Winn. Prospects for the characterization and confirmation of transiting exoplanets via the rossiter-mclaughlin effect. *The Astrophysical Journal*, 655:550, 2007.

N.P. Gibson, S. Aigrain, S. Roberts, T.M. Evans, M. Osborne, and F. Pont. A gaussian process framework for modelling instrumental systematics: application to transmission spectroscopy. *Monthly Notices of the Royal Astronomical Society*, 1:1868, 2011.

N.P. Gibson, F. Pont, and S. Aigrain. A new look at nicmos transmission spectroscopy of hd 189733, gj-436 and xo-1: no conclusive evidence for molecular features. *Monthly Notices of the Royal Astronomical Society*, 411:2199, 2011b.

N.P. Gibson, S. Aigrain, F. Pont, D.K. Sing, J.M. Désert, T.M. Evans, G. Henry, N. Husnoo, and H. Knutson. Probing the haze in the atmosphere of hd 189733b with hubble space telescope/wfc3 transmission spectroscopy. *Monthly Notices of the Royal Astronomical Society*, 1:2666, 2012.

G.F. Gilmore, M.A. Perryman, L. Lindegren, F. Favata, E. Hoeg, M. Lattanzi, X. Luri, F. Mignard, S. Roeser, and P.T. de Zeeuw. Gaia: origin and evolution of the milky way. In *Society of Photo-Optical Instrumentation Engineers (SPIE) Conference Series*, volume 3350, page 541, 1998.

R. Gilmozzi and J. Spyromilio. The 42m european elt: status. In *Society of Photo-Optical Instrumentation Engineers (SPIE) Conference Series*, volume 7012, page 43, 2008.

W.L. Godson. The computation of infrared transmission by atmospheric water vapor. *Journal of Atmospheric Sciences*, 12:272, 1955.

A. Gomboc, C. Guidorzi, C.G. Mundell, A. Melandri, A. Monfardini, D. Bersier, M.F. Bode, D. Carter, S. Kobayashi, C.J. Mottram, et al. A review of early-time optical follow-ups with 2 m robotic telescopes. *Nuovo Cimento B Serie*, 121:1303, 2006.

R.M. Goody and Y.L. Yung. *Atmospheric Radiation: Theoretical Basis, 1989*. Oxford University Press, New York, 1989.

A. Gould and A. Loeb. Discovering planetary systems through gravitational microlenses. *The Astrophysical Journal*, 396:104, 1992.

P.C. Gregory. A bayesian periodogram finds evidence for three planets in hd 11964. *Monthly Notices of the Royal Astronomical Society*, 381:1607, 2007.

C.J. Grillmair, A. Burrows, D. Charbonneau, L. Armus, J. Stauffer, V. Meadows, J. Van Cleve, K. Von Braun, and D. Levine. Strong water absorption in the dayside emission spectrum of the planet hd 189733b. *Nature*, 456(7223):767, 2008.

J. Harrington, B.M. Hansen, S.H. Luszcz, S. Seager, D. Deming, K. Menou, J.Y.K. Cho, and L.J. Richardson. The phase-dependent infrared brightness of the extrasolar planet upsilo andromedae b. *Science*, 314:623, 2006.

P.H. Hauschildt, E. Baron, and F. Allard. Parallel implementation of the phoenix generalized stellar atmosphere program. *The Astrophysical Journal*, 483:390, 1997.

C. Helling and P. Woitke. Dust in brown dwarfs. v. growth and evaporation of dirty dust grains. *Astronomy and Astrophysics*, 455:325, 2006.

K. Heng, W. Hayek, F. Pont, and D.K. Sing. On the effects of clouds and hazes in the atmospheres of hot jupiters: semi-analytical temperature-pressure profiles. *Monthly Notices of the Royal Astronomical Society*, 420:20, 2012.

C. Henry, O.P. Lay, M. Aung, S.M. Gunter, S. Dubovitsky, and G.H. Blackwood. Terrestrial planet finder interferometer: architecture, mission design, and technology development. In *Society of Photo-Optical Instrumentation Engineers (SPIE) Conference Series*, volume 5491, page 265, 2004.

W.B. Hubbard, J.J. Fortney, J.I. Lunine, A. Burrows, D. Sudarsky, and P. Pinto. Theory of extrasolar giant planet transits. *The Astrophysical Journal*, 560:413, 2001.

K.P. Huber and G. Herzberg. Molecular structure and molecular spectra iv: constants of diatomic molecules. *Van Rostrand-Reinhold, New York*, 1979.

P.G.J Irwin, N.A. Teanby, R. de Kok, L.N. Fletcher, C.J.A. Howett, C.C.C. Tsang, C.F. Wilson, S.B. Calcutt, C.A. Nixon, and P.D. Parrish. The nemesis planetary atmosphere radiative transfer and retrieval tool. *Journal of Quantitative Spectroscopy and Radiative Transfer*, 109(6):1136, 2008.

N. Jacquinet-Husson, N.A. Scott, A. Chédin, L. Crépeau, R. Armante, V. Capelle, J. Orphal, A. Coustenis, C. Boonne, N. Poulet-Crovisier, et al. The geisa spectroscopic database: Current and future archive for earth and planetary atmosphere studies. *Journal of Quantitative Spectroscopy and Radiative Transfer*, 109:1043, 2008.

M. Johns, J.R.P. Angel, S. Shectman, R. Bernstein, D.G. Fabricant, P. McCarthy, and M. Phillips. Status of the giant magellan telescope (gmt) project. In *Society of Photo-Optical Instrumentation Engineers (SPIE) Conference Series*, volume 5489, page 441, 2004.

U.G. Jørgensen. Cool star models. *Molecules in Astrophysics: Probes and Processes*, (178):441, 1997.

E. Karkoschka. Spectrophotometry of the jovian planets and titan at 300-to 1000-nm wavelength: The methane spectrum. *Icarus*, 111(1):174, 1994.

N. E. Kassim and W. C. Erickson. Meter- and decameter-wavelength array for astrophysics and solar radar. In T. G. Phillips, editor, *Society of Photo-Optical Instrumentation Engineers (SPIE) Conference Series*, volume 3357 of *Society of Photo-Optical Instrumentation Engineers (SPIE) Conference Series*, pages 740–754, July 1998.

N. E. Kassim, T. J. W. Lazio, P. S. Ray, P. C. Crane, B. C. Hicks, K. P. Stewart, A. S. Cohen, and W. M. Lane. The low-frequency array (LOFAR): opening a new window on the universe. *Planetary and Space Science*, 52:1343–1349, December 2004. doi: 10.1016/j.pss.2004.09.013.

H.A. Knutson, D. Charbonneau, L.E. Allen, J.J. Fortney, E. Agol, N.B. Cowan, A.P. Showman, C.S. Cooper, and S.T. Megeath. A map of the day–night contrast of the extrasolar planet hd 189733b. *Nature*, 447(7141):183, 2007.

H.A. Knutson, D. Charbonneau, L.E. Allen, A. Burrows, and S.T. Megeath. The 3.6-8.0 μm broadband emission spectrum of hd 209458b: Evidence for an atmospheric temperature inversion. *The Astrophysical Journal*, 673(1):526, 2008.

H.A. Knutson, D. Charbonneau, N.B. Cowan, J.J. Fortney, A.P. Showman, E. Agol, G.W. Henry, M.E. Everett, and L.E. Allen. Multiwavelength constraints on the day-night circulation patterns of hd 189733b. *The Astrophysical Journal*, 690:822, 2009.

H.A. Knutson, A.W. Howard, and H. Isaacson. A correlation between stellar activity and hot jupiter emission spectra. *The Astrophysical Journal*, 720:1569, 2010.

H.A. Knutson, N. Madhusudhan, N.B. Cowan, J.L. Christiansen, E. Agol, D. Deming, J.M. Désert, D. Charbonneau, G.W. Henry, D. Homeier, et al. A spitzer transmission spectrum for the exoplanet gj 436b, evidence for stellar variability, and constraints on dayside flux variations. *The Astrophysical Journal*, 735(1):27, 2011.

H.A. Knutson, N. Lewis, J.J. Fortney, A. Burrows, A.P. Showman, N.B. Cowan, E. Agol, S. Aigrain, D. Charbonneau, D. Deming, et al. 3.6 and 4.5 mum phase curves and evidence for non-equilibrium chemistry in the atmosphere of extrasolar planet hd 189733b. *The Astrophysical Journal*, 754:22, 2012.

F.G. Kupka, T.A. Ryabchikova, N.E. Piskunov, H.C. Stempels, and W.W. Weiss. Vald-2–the new vienna atomic line database. *Baltic Astronomy*, 9:590, 2000.

R. Kurucz. Stellar model and associated spectra, 2006. URL `http://kurucz.harvard.edu/grids.html`.

A.A. Lacis and V. Oinas. A description of the correlated k distribution method for modeling nongray gaseous absorption, thermal emission, and multiple scattering in vertically inhomogeneous atmospheres. *Journal of Geophysical Research*, 96(D5):9027, 1991.

D. Lafrenière, R. Jayawardhana, and M.H. van Kerkwijk. The directly imaged planet around the young solar analog 1rxs j160929. 1-210524: Confirmation of common proper motion, temperature, and mass. *The Astrophysical Journal*, 719:497, 2010.

D. Lafrenière, R. Jayawardhana, M. Janson, C. Helling, S. Witte, and P. Hauschildt. Discovery of an˜ 23 m jup brown dwarf orbiting˜ 700 au from the massive star hip 78530 in upper scorpius. *The Astrophysical Journal*, 730:42, 2011.

A.M. Lagrange, D. Gratadour, G. Chauvin, T. Fusco, D. Ehrenreich, D. Mouillet, G. Rousset, D. Rouan, F. Allard, É. Gendron, et al. A probable giant planet imaged in the beta pictoris disk. vlt/naco deep l'-band imaging. *Astronomy and Astrophysics*, 493:L21, 2009.

A.L. Laraia, R.R. Gamache, J. Lamouroux, I.E. Gordon, and L.S. Rothman. Total internal partition sums to support planetary remote sensing. *Icarus*, 215:391, 2011.

A. Lecavelier Des Etangs, F. Pont, A. Vidal-Madjar, and D. Sing. Rayleigh scattering in the transit spectrum of hd 189733b. *Astronomy and Astrophysics*, 481:L83, 2008.

J.-M. Lee, L.N. Fletcher, and P.G.J. Irwin. Optimal estimation retrievals of the atmospheric structure and composition of HD 189733b from secondary eclipse spectroscopy. *Monthly Notices of the Royal Astronomical Society*, 420:170–182, 2012. doi: 10.1111/j.1365-2966.2011.20013.x.

K. Levenberg. A method for the solution of certain problems in least squares. *Quarterly of applied mathematics*, 2:164, 1944.

M.C. Liang, C.D. Parkinson, A.Y.T. Lee, Y.L. Yung, and S. Seager. Source of atomic hydrogen in the atmosphere of hd 209458b. *The Astrophysical Journal*, 596:L247, 2003.

M.C. Liang, S. Seager, C.D. Parkinson, A.Y.T. Lee, and Y.L. Yung. On the insignificance of photochemical hydrocarbon aerosols in the atmospheres of close-in extrasolar giant planets. *The Astrophysical Journal*, 605:L61, 2004.

M.R. Line, M.C. Liang, and Y.L. Yung. High-temperature photochemistry in the atmosphere of hd 189733b. *The Astrophysical Journal*, 717(1):496, 2010.

M.R. Line, G. Vasisht, P. Chen, D. Angerhausen, and Y.L. Yung. Thermochemical and photochemical kinetics in cooler hydrogen-dominated extrasolar planets: A methane-poor gj436b? *The Astrophysical Journal*, 738:32, 2011.

M.R. Line, X. Zhang, G. Vasisht, V. Natraj, P. Chen, and Y.L. Yung. Information content of exoplanetary transit spectra: An initial look. *The Astrophysical Journal*, 749(1):93, 2012.

K. Lodders. Alkali element chemistry in cool dwarf atmospheres. *The Astrophysical Journal*, 519:793, 1999.

P. Machalek, P.R. McCullough, C.J. Burke, J.A. Valenti, A. Burrows, and J.L. Hora. Thermal emission of exoplanet xo-1b. *The Astrophysical Journal*, 684:1427, 2008.

N. Madhusudhan and S. Seager. A temperature and abundance retrieval method for exoplanet atmospheres. *The Astrophysical Journal*, 707(1):24, 2009.

N. Madhusudhan and S. Seager. On the inference of thermal inversions in hot jupiter atmospheres. *The Astrophysical Journal*, 725(1):261, 2010.

N. Madhusudhan and S. Seager. High metallicity and non-equilibrium chemistry in the dayside atmosphere of hot-neptune gj 436b. *The Astrophysical Journal*, 729(1):41, 2011.

N. Madhusudhan, J. Harrington, K.B. Stevenson, S. Nymeyer, C.J. Campo, P.J. Wheatley, D. Deming, J. Blecic, R.A. Hardy, N.B. Lust, et al. A high c/o ratio and weak thermal inversion in the atmosphere of exoplanet wasp-12b. *Nature*, 469(7328):64, 2010.

N. Madhusudhan, A. Burrows, and T. Currie. Model atmospheres for massive gas giants with thick clouds: Application to the hr 8799 planets and predictions for future detections. *The Astrophysical Journal*, 737:34, 2011.

S. Mao and B. Paczynski. Gravitational microlensing by double stars and planetary systems. *The Astrophysical Journal*, 374:L37, 1991.

C. Marois, B. Macintosh, T. Barman, B. Zuckerman, I. Song, J. Patience, D. Lafrenière, and R. Doyon. Direct imaging of multiple planets orbiting the star hr 8799. *Science*, 322(5906):1348, 2008.

C. Marois, B. Zuckerman, Q.M. Konopacky, B. Macintosh, and T. Barman. Images of a fourth planet orbiting hr 8799. *Nature*, 468(7327):1080, 2010.

D.W. Marquardt. An algorithm for least-squares estimation of nonlinear parameters. *Journal of the Society for Industrial & Applied Mathematics*, 11(2):431, 1963.

M. Mayor and D. Queloz. A jupiter-mass companion to a solar-type star. *Nature*, 378 (6555):355–, 1995.

M. Mayor, F. Pepe, D. Queloz, F. Bouchy, G. Rupprecht, G. Lo Curto, G. Avila, W. Benz, J.L. Bertaux, X. Bonfils, et al. Setting new standards with harps. *The Messenger*, 114: 20, 2003.

M. Mayor, X. Bonfils, T. Forveille, X. Delfosse, S. Udry, J.L. Bertaux, H. Beust, F. Bouchy, C. Lovis, F. Pepe, et al. The harps search for southern extra-solar planets. *Astronomy and Astrophysics*, 507(1):487, 2009.

P.R. McCullough, J.E. Stys, J.A. Valenti, S.W. Fleming, K.A. Janes, and J.N. Heasley. The xo project: Searching for transiting extrasolar planet candidates. *Publications of the Astronomical Society of the Pacific*, 117:783, 2005.

B. Mennesson, R.L. Akeson, E. Appleby, J. Bell, A. Booth, M.M. Colavita, S. Crawford, M.J. Creech-Eakman, W. Dahl, J. Fanson, et al. Long baseline nulling interferometry with the keck telescopes: a progress report. In *IAU Colloq. 200: Direct Imaging of Exoplanets: Science & Techniques*, volume 1, page 227, 2006.

S. Metchev, C. Marois, and B. Zuckerman. Pre-discovery 2007 image of the hr 8799 planetary system. *The Astrophysical Journal Letters*, 705(2):L204, 2009.

J.I. Moses, C. Visscher, J.J. Fortney, A.P. Showman, NK Lewis, C.A. Griffith, S.J. Klippenstein, M. Shabram, A.J. Friedson, M.S. Marley, et al. Disequilibrium carbon, oxygen, and nitrogen chemistry in the atmospheres of hd 189733b and hd 209458b. *The Astrophysical Journal*, 737:15, 2011.

R. Nassar and P. Bernath. Hot methane spectra for astrophysical applications. *Journal of Quantitative Spectroscopy and Radiative Transfer*, 82(1):279, 2003.

J. Nelson and G.H. Sanders. The status of the thirty meter telescope project. In *Society of Photo-Optical Instrumentation Engineers (SPIE) Conference Series*, volume 7012, page 44, 2008.

R. Neuhäuser and T.O.B. Schmidt. Direct imaging of extra-solar planets-homogeneous comparison of detected planets and candidates. *arXiv preprint arXiv:1201.3537*, 2012.

R. Neuhäuser, E.W .Guenther, G. Wuchterl, M. Mugrauer, A. Bedalov, and P.H. Hauschildt. Evidence for a co-moving sub-stellar companion of gq lup. *Astronomy and Astrophysics*, 435(1):13, 2005.

S. Nymeyer, J. Harrington, R.A. Hardy, K.B. Stevenson, C.J. Campo, N. Madhusudhan, A. Collier-Cameron, T.J. Loredo, J. Blecic, W.C. Bowman, et al. Spitzer secondary eclipses of wasp-18b. *The Astrophysical Journal*, 742:35, 2011.

F.T. O'Donovan, D. Charbonneau, J. Harrington, N. Madhusudhan, S. Seager, D. Deming, and H.A. Knutson. Detection of planetary emission from the exoplanet tres-2 using spitzer/irac. *The Astrophysical Journal*, 710:1551, 2010.

Y. Ohta, A. Taruya, and Y. Suto. The rossiter-mclaughlin effect and analytic radial velocity curves for transiting extrasolar planetary systems. *The Astrophysical Journal*, 622: 1118, 2005.

S. Perruchot, D. Kohler, F. Bouchy, Y. Richaud, P. Richaud, G. Moreaux, M. Merzougui, R. Sottile, L. Hill, G. Knispel, et al. The sophie spectrograph: design and technical key-points for high throughput and high stability. In *Society of Photo-Optical Instrumentation Engineers (SPIE) Conference Series*, volume 7014, page 17, 2008.

F. Pont, H. Knutson, RL Gilliland, C. Moutou, and D. Charbonneau. Detection of atmospheric haze on an extrasolar planet: the 0.55–1.05 μm transmission spectrum of hd 189733b with the hubble space telescope. *Monthly Notices of the Royal Astronomical Society*, 385(1):109, 2008.

F Pont, DK Sing, NP Gibson, S Aigrain, G Henry, and N Husnoo. The prevalence of dust on the exoplanet hd 189733b from hubble and spitzer observations. *arXiv preprint arXiv:1210.4163*, 2012.

S.H. Pravdo and S.B. Shaklan. An ultracool star's candidate planet. *The Astrophysical Journal*, 700:623, 2009.

S. Redfield, M. Endl, W.D. Cochran, and L. Koesterke. Sodium absorption from the exoplanetary atmosphere of hd 189733b detected in the optical transmission spectrum. *The Astrophysical Journal Letters*, 673(1):L87, 2008.

L.J. Richardson, J. Harrington, S. Seager, and D. Deming. A spitzer infrared radius for the transiting extrasolar planet hd 209458b. *The Astrophysical Journal*, 649:1043–1047, 2006.

G.H. Rieke, E.T. Young, C.W. Engelbracht, D.M. Kelly, F.J. Low, E.E. Haller, J.W. Beeman, K.D. Gordon, J.A. Stansberry, K.A. Misselt, et al. The multiband imaging photometer for spitzer (mips). *The Astrophysical Journal Supplement Series*, 154:25, 2004.

C.D. Rodgers. *Inverse Methods for Atmospheric Sounding: Theory and Practice World Scientific*. Singapore, 2000.

L.S. Rothman, R.B. Wattson, R. Gamache, J.W. Schroeder, and A. McCann. Hitran hawks and hitemp: high-temperature molecular database. In *SPIE's 1995 Symposium on OE/Aerospace Sensing and Dual Use Photonics*, page 105. International Society for Optics and Photonics, 1995.

L.S. Rothman, I.E. Gordon, A. Barber, D.C. Benner, P.F. Bernath, M. Birk, V. Boudon, L.R. Brown, A. Campargue, J.P. Champion, et al. The¡ i¿ hitran¡/i¿ 2008 molecular spectroscopic database. *Journal of Quantitative Spectroscopy and Radiative Transfer*, 110(9):533, 2009.

L.S. Rothman, I.E. Gordon, R.J. Barber, H. Dothe, R.R. Gamache, A. Goldman, V.I. Perevalov, S.A. Tashkun, and J. Tennyson. Hitemp, the high-temperature molecular spectroscopic database. *Journal of Quantitative Spectroscopy and Radiative Transfer*, 111(15):2139, 2010.

A.J. Sauval and J.B. Tatum. A set of partition functions and equilibrium constants for 300 diatomic molecules of astrophysical interest. *The Astrophysical Journal Supplement Series*, 56:193, 1984.

T.O.B. Schmidt, R. Neuhäuser, A. Seifahrt, N. Vogt, A. Bedalov, C. Helling, S. Witte, and P.H. Hauschildt. Direct evidence of a sub-stellar companion around ct chamaeleontis. *Astronomy and Astrophysics*, 491(1):3110, 2008.

T.O.B. Schmidt, R. Neuhäuser, M. Mugrauer, A. Bedalov, and N. Vogt. New astrometry and photometry for the companion candidates of ct cha. In *AIP Conference Proceedings*, volume 1094, page 852, 2009.

A. Scott and W.W. Duley. Ultraviolet and infrared refractive indices of amorphous silicates. *The Astrophysical Journal Supplement Series*, 105:401, 1996.

S. Seager. Exoplanet transit spectroscopy and photometry. *Space Science Reviews*, 135 (1):345, 2008.

S. Seager. *Exoplanet atmospheres: physical processes*. Princeton University Press, 2010.

S. Seager. *Exoplanets*. University of Arizona Press, 2011.

S. Seager and D. Deming. Exoplanet atmospheres. *Annual Review of Astronomy and Astrophysics*, 48:631, 2010.

S. Seager and G. Mallén-Ornelas. A unique solution of planet and star parameters from an extrasolar planet transit light curve. *The Astrophysical Journal*, 585:1038, 2003.

S. Seager and D.D. Sasselov. Theoretical transmission spectra during extrasolar giant planet transits. *The Astrophysical Journal*, 537:916, 2000.

M. Shabram, J.J. Fortney, T.P. Greene, and R.S. Freedman. Transmission spectra of transiting planet atmospheres: Model validation and simulations of the hot neptune gj 436b for the james webb space telescope. *The Astrophysical Journal*, 727(2):65, 2011.

C.M. Sharp and A. Burrows. Atomic and molecular opacities for brown dwarf and giant planet atmospheres. *The Astrophysical Journal Supplement Series*, 168:140, 2007.

A.P. Showman, C.S. Cooper, J.J. Fortney, and M.S. Marley. Atmospheric circulation of hot jupiters: Three-dimensional circulation models of hd 209458b and hd 189733b with simplified forcing. *The Astrophysical Journal*, 682(1):559, 2008.

A.P. Showman, J.J. Fortney, Y. Lian, M.S. Marley, R.S. Freedman, H.A. Knutson, and D. Charbonneau. Atmospheric circulation of hot jupiters: Coupled radiative-dynamical general circulation model simulations of hd 189733b and hd 209458b. *The Astrophysical Journal*, 699:564, 2009.

D.K. Sing, A. Vidal-Madjar, A.L. Des Etangs, J.M. Désert, G. Ballester, and D. Ehrenreich. Determining atmospheric conditions at the terminator of the hot jupiter hd 209458b. *The Astrophysical Journal*, 686(1):667, 2008.

D.K. Sing, J.M. Désert, A. Lecavelier Des Etangs, G.E. Ballester, A. Vidal-Madjar, V. Parmentier, G. Hebrard, and G.W. Henry. Transit spectrophotometry of the exoplanet hd 189733b. *Astronomy and Astrophysics*, 505(2):891, 2009.

D.K. Sing, F. Pont, S. Aigrain, D. Charbonneau, J.M. Désert, N. Gibson, R. Gilliland, W. Hayek, G. Henry, H. Knutson, et al. Hubble space telescope transmission spectroscopy of the exoplanet hd 189733b: high-altitude atmospheric haze in the optical and near-ultraviolet with stis. *Monthly Notices of the Royal Astronomical Society*, 416 (2):1443, 2011.

A.J. Skemer, P.M. Hinz, S. Esposito, A. Burrows, J. Leisenring, M. Skrutskie, S. Desidera, D. Mesa, C. Arcidiacono, F. Mannucci, et al. First light lbt ao images of hr 8799 bcde at 1.6 and 3.3 μm: New discrepancies between young planets and old brown dwarfs. *The Astrophysical Journal*, 753(1):14, 2012.

A.M.S. Smith, D.R. Anderson, N. Madhusudhan, J. Southworth, A. Collier-Cameron, J. Blecic, J. Harrington, C. Hellier, P.F.L. Maxted, D. Pollacco, et al. Thermal emission from wasp-24b at 3.6 and 4.5 mum. *Astronomy and Astrophysics*, 545:93, 2012.

I.A.G. Snellen, R.J. De Kok, E.J.W. de Mooij, and S. Albrecht. The orbital motion, absolute mass and high-altitude winds of exoplanet hd [thinsp] 209458b. *Nature*, 465 (7301):1049, 2010.

K.B. Stevenson, J. Harrington, S. Nymeyer, N. Madhusudhan, S. Seager, W.C. Bowman, R.A. Hardy, D. Deming, E. Rauscher, and N.B. Lust. Possible thermochemical disequilibrium in the atmosphere of the exoplanet gj 436b. *Nature*, 464(7292):11614, 2010.

K.A. Strand. 61 cygni as a triple system. *Publications of the Astronomical Society of the Pacific*, 55:29, 1943.

R.A. Street, D.L. Pollaco, A. Fitzsimmons, F.P. Keenan, K. Horne, S. Kane, A. Collier Cameron, T.A. Lister, C. Haswell, A.J. Norton, et al. Superwasp: Wide angle search for planets. In *Scientific Frontiers in Research on Extrasolar Planets*, volume 294, page 405, 2003.

K. Strong, F.W. Taylor, S.B. Calcutt, J.J. Remedios, and J. Ballard. Spectral parameters of self-and hydrogen-broadened methane from 2000 to 9500 cm¡ sup¿-1¡/sup¿ for remote sounding of the atmosphere of jupiter. *Journal of Quantitative Spectroscopy and Radiative Transfer*, 50(4):363, 1993.

D. Sudarsky, A. Burrows, and P. Pinto. Albedo and reflection spectra of extrasolar giant planets. *The Astrophysical Journal*, 538:885, 2000.

D. Sudarsky, A. Burrows, and I. Hubeny. Theoretical spectra and atmospheres of extrasolar giant planets. *The Astrophysical Journal*, 588:1121, 2003.

M.R. Swain, J. Bouwman, R.L. Akeson, S. Lawler, and C.A. Beichman. The mid-infrared spectrum of the transiting exoplanet hd 209458b. *The Astrophysical Journal*, 674(1): 482, 2008a.

M.R. Swain, G. Vasisht, and G. Tinetti. The presence of methane in the atmosphere of an extrasolar planet. *Nature*, 452(7185):329, 2008b.

M.R. Swain, G. Tinetti, G. Vasisht, P. Deroo, C. Griffith, J. Bouwman, P. Chen, Y. Yung, A. Burrows, L.R. Brown, et al. Water, methane, and carbon dioxide present in the dayside spectrum of the exoplanet hd 209458b. *The Astrophysical Journal*, 704(2): 1616, 2009a.

M.R. Swain, G. Vasisht, G. Tinetti, J. Bouwman, P. Chen, Y. Yung, D. Deming, and P. Deroo. Molecular signatures in the near-infrared dayside spectrum of hd 189733b. *The Astrophysical Journal*, 690:L114, 2009b.

M.R. Swain, P. Deroo, C.A. Griffith, G. Tinetti, A. Thatte, G. Vasisht, P. Chen, J. Bouwman, I.J. Crossfield, D. Angerhausen, et al. A ground-based near-infrared emission spectrum of the exoplanet hd 189733b. *Nature*, 463(7281):637, 2010.

S.A. Tashkun and V.I. Perevalov. Cdsd-4000: High-resolution, high-temperature carbon dioxide spectroscopic databank. *Journal of Quantitative Spectroscopy and Radiative Transfer*, 112:1403, 2011.

S.A. Tashkun, V.I. Perevalov, J.L. Teffo, A.D. Bykov, and N.N. Lavrentieva. Cdsd-1000, the high-temperature carbon dioxide spectroscopic databank. *Journal of Quantitative Spectroscopy and Radiative Transfer*, 82(1):165, 2003.

Y. Terzian and J. Lazio. The Square Kilometre Array. In *Society of Photo-Optical Instrumentation Engineers (SPIE) Conference Series*, volume 6267 of *Society of Photo-Optical Instrumentation Engineers (SPIE) Conference Series*, July 2006. doi: 10.1117/12.673512.

A. Thatte, P. Deroo, and M.R. Swain. Selective principal component extraction and reconstruction: a novel method for ground based exoplanet spectroscopy. *Astronomy and Astrophysics*, 523, 2010.

G. Tinetti, M.C. Liang, A. Vidal-Madjar, D. Ehrenreich, A. Lecavelier des Etangs, and Y.L. Yung. Infrared transmission spectra for extrasolar giant planets. *The Astrophysical Journal*, 654:L99, 2007a.

G. Tinetti, A. Vidal-Madjar, M.C. Liang, J.P. Beaulieu, Y. Yung, S. Carey, R.J. Barber, J. Tennyson, I. Ribas, N. Allard, et al. Water vapour in the atmosphere of a transiting extrasolar planet. *Nature*, 448(7150):169, 2007b.

G. Tinetti, J.P. Beaulieu, T. Henning, M. Meyer, G. Micela, I. Ribas, D. Stam, M. Swain, O. Krause, M. Ollivier, et al. Echo. *Experimental Astronomy*, page 1, 2012.

K. Todorov, D. Deming, J. Harrington, K.B. Stevenson, W.C. Bowman, S. Nymeyer, J.J. Fortney, and G.Á. Bakos. Spitzer irac secondary eclipse photometry of the transiting extrasolar planet hat-p-1b. *The Astrophysical Journal*, 708:498, 2010.

G. Torres, J.N. Winn, and M.J. Holman. Improved parameters for extrasolar transiting planets. *The Astrophysical Journal*, 677(2):1324, 2008.

R.G. Tull. High-resolution fiber-coupled spectrograph of the hobby-eberly telescope. In *Society of Photo-Optical Instrumentation Engineers (SPIE) Conference Series*, volume 3355, page 387, 1998.

A. Udalski. The optical gravitational lensing experiment. real time data analysis systems in the ogle-iii survey. *Acta Astronomica*, 53:291, 2003.

P. Van de Kamp. Astrometric study of barnard's star from plates taken with the 24-inch sproul refractor. *The Astronomical Journal*, 68:515, 1963.

T. Viard, P. Bodin, A. Magnan, and A. Baglin. Corot telescope: Corotel. In *Society of Photo-Optical Instrumentation Engineers (SPIE) Conference Series*, volume 6693, page 11, 2007.

A. Vidal-Madjar, A. Lecavelier des Etangs, J.M. Désert, G.E. Ballester, R. Ferlet, G. Hébrard, and M. Mayor. An extended upper atmosphere around the extrasolar planet hd209458b. *Nature*, 422(6928):143, 2003.

A. Vidal-Madjar, J.M. Désert, A. Lecavelier des Etangs, G. Hébrard, GE Ballester, D. Ehrenreich, R. Ferlet, J.C. McConnell, M. Mayor, and C.D. Parkinson. Detection of oxygen and carbon in the hydrodynamically escaping atmosphere of the extrasolar planet hd 209458b. *The Astrophysical Journal*, 604:L69, 2004.

C. Visscher and J.I. Moses. Quenching of carbon monoxide and methane in the atmospheres of cool brown dwarfs and hot jupiters. *The Astrophysical Journal*, 738:72, 2011.

C. Visscher, K. Lodders, and B. Fegley Jr. Atmospheric chemistry in giant planets, brown dwarfs, and low-mass dwarf stars. iii. iron, magnesium, and silicon. *The Astrophysical Journal*, 716:1060, 2010.

S.S. Vogt, S.L. Allen, B.C. Bigelow, L. Bresee, B. Brown, T. Cantrall, A. Conrad, M. Couture, C. Delaney, H.W. Epps, et al. Hires: the high-resolution echelle spectrometer on the keck 10-m telescope. In *Society of Photo-Optical Instrumentation Engineers (SPIE) Conference Series*, volume 2198, page 362, 1994.

K. von Braun, T.S. Boyajian, S.R. Kane, L. Hebb, G.T. van Belle, C. Farrington, D.R. Ciardi, H.A. Knutson, A. Theo, M. López-Morales, et al. The gj 436 system: Directly determined astrophysical parameters of an m dwarf and implications for the transiting hot neptune. *The Astrophysical Journal*, 753(2):171, 2012.

L. Weber, A. Blecha, G. Davignon, C. Maire, D. Queloz, G.B. Russiniello, and G. Simond. Fully automated high-resolution spectroscopy at swiss 1.2 m la silla telescope. In *Society of Photo-Optical Instrumentation Engineers (SPIE) Conference Series*, volume 4009, page 61, 2000.

C. Wenger and J.P. Champion. Spherical top data system (stds) software for the simulation of spherical top spectra. *Journal of Quantitative Spectroscopy and Radiative Transfer*, 59(3):471, 1998.

A Wolszczan and DA Frail. A planetary system around the millisecond pulsar psr1257+ 12. *Nature*, 355:145–147, 1992.

J. Yoo, D.L. DePoy, A. Gal-Yam, B.S. Gaudi, A. Gould, C. Han, Y. Lipkin, D. Maoz, E.O. Ofek, B.G. Park, et al. Ogle-2003-blg-262: Finite-source effects from a point-mass lens. *The Astrophysical Journal*, 603:139, 2004.

C. Zheng and A. Borysow. Rototranslational collision-induced absorption by h2-h2 pairs at temperatures from 600 to 7000 k. *The Astrophysical Journal*, 441:960, 1995.